ZERO DEGREE HADRON PRODUCTION FROM AN ALUMINUM TARGET AT 300 GEV

Thesis by

Thomas Humphrey

In Partial Fulfillment of the Requirements
For the Degree of
Doctor of Philosophy

California Institute of Technology
Pasadena, California
1975
(Submitted February 26, 1975)

ACKNOWLEDGMENTS

The experiment described in this thesis was one facet of a larger experiment designed to study high energy neutrino interactions. No one part of the experiment could have been accomplished without the combined efforts of all members of the group.

Frank J. Sciulli and Barry C. Barish conceived the experiment and directed its operation. I am particularly indebted to Frank Sciulli for his constant guidance and many fruitful suggestions. Other members of the group also assisted during set-up, data taking, and analysis. These include: J.F. Bartlett, Dave Buchholz, Gene Fisk, George Krafczyk, Frank Merritt, Yori Nagashima, Denny Shields, and Hank Suter.

For financial support, I am indebted to the National Science Foundation, the Atomic Energy Commission, the California Institute of Technology, and the State of California.

ABSTRACT

The hadronic yields from proton-Aluminum collisions into a 455 μsr-% beam centered at 0° have been measured at a laboratory proton energy of 300 Gev and secondary momenta of 95, 120, 145 and 170 Gev/c.

$$p + Al \rightarrow \left\{ \begin{array}{c} \pi^{\pm} \\ K^{\pm} \\ p \end{array} \right\} + \text{anything} \qquad (1)$$

The pion and kaon component of the hadron beam provided, through decay, a dichromatic beam of neutrinos used in the study of neutrino interactions at 38 and 108 Gev. The measured neutrino total cross sections have been found(26) to have an energy dependence consistent with a linear rise in cross section with increasing neutrino energy for both neutrino and antineutrino beams. Knowledge of the slope of this linear rise is imperative in order to compare the cross section data with current models. The experiment described in this thesis provided the beam flux normalization necessary to measure the slope absolutely.

Using the data from this experiment we have also been able to make a study of the inclusive production of hadrons from an Aluminum target. An inclusive interaction is one in which only a single particle is detected after the initial interaction. The undetected

particles are all grouped under 'anything' in equation (1)

The total hadron flux in this beam was measured with an ionization chamber, and particle ratios were extracted from Cerenkov counter pressure curves. The Cerenkov counter used in this experiment was novel at the time of its use. At high energies, Cerenkov counters must be long in order to have an efficiency close to 100%. For this experiment, our counter would have had to be about 180 feet long in order to be 95% efficient. Instead of constructing such a long counter, we used a 6 foot counter. The efficiency was low (typically less than 20%) but the efficiency is a geometrical effect and therefore the same for all particles producing Cerenkov light at the same angle. Thus, while particle fluxes are not reliably measured with this counter, particle ratios may be obtained. Both of these devices (ionization chamber and Cerenkov counter) were situated 400 m. from the production target.

The results and conclusions of this experiment fall into the two above mentioned categories: the study of neutrino interactions and the study of inclusive hadron production from Aluminum with a 300 Gev proton beam.

The measured neutrino and antineutrino total cross sections have an energy dependence consistent with a linear rise. In parton models(27) the sum of the slopes of these cross sections provide a measurement of the mean-square charge of the constituents of the nucleon. Our measurement gives a value $\langle q^2 \rangle = 0.27 \pm 0.05$ for this mean-square charge. The simplest quark model gives $\langle q^2 \rangle = 5/18 = 0.28$.

Parton models employing V-A scattering from spin $\frac{1}{2}$ constituents predict that the ratio of the slopes (antineutrino/neutrino) is equal to 1/3. Deviation from a ratio of 1/3 is a measure of the antiquark (antiparton) component in the nucleon. We measure a slope ratio equal to 0.33 ± 0.08. The results of our measurements of the normalized neutrino and antineutrino total cross sections therefore are consistent with the predictions of a model employing fractionally charged spin $\frac{1}{2}$ constituents and little antiquark component.

The study of the inclusive production of hadrons is interesting as a test of theoretical models of hadron production and also as a test of the more general model of hadronic scaling.

The most comprehensive model of high energy hadron production is the Thermodynamic Model of Hagedorn and Ranft.(8-10) Comparing our data with the predictions of this model, we find consistency in some momentum regions and discrepancies as large as a factor 2 in other momentum regions.

In a simple model of hadronic scaling,(1) one assumes that cross sections can be parameterized using the scaling variables x and P :

$$\frac{d^2\sigma}{d\Omega\, dp} = E_0\, f_1(x)\, f_2(P_\perp) \qquad (59)$$

E_0 = beam energy

$P_\parallel$ = longitudinal momentum

$x = P_\parallel / E_0$

$P_\perp$ = transverse momentum

$f_2(P_\perp) \sim$ exp (-P /200 Mev/c) (14)

$f_1(x)$ is then energy-independent. To test this predicted energy independence, we have extracted $f_1(x)$ from our data and compared it to the $f_1(x)$ extracted from similar data at 19.2 Gev. We find agreement to 30% for the production of $\pi^\pm$ and protons. For $K^\pm$ the 300 Gev $f_1(x)$ is consistently larger than the 19.2 Gev $f_1(x)$ by as much as a factor 3.

Therefore, over the momentum region covered in this experiment, one can predict our results from scaling almost as reliably as the Thermodynamic Model.

To Kate, Kris, Mike, and Bobby

TABLE OF CONTENTS

TABLE OF CONTENTS (cont.)

I. Introduction

This thesis is a study of the reaction:

$$p + Al \rightarrow \left\{ \begin{matrix} \pi^{\pm} \\ K^{\pm} \\ P \end{matrix} \right\} + \text{anything} \qquad (1)$$

from a 12" Aluminum target at a beam energy of 300 Gev. The experiment was conducted at the Fermilab synchrotron. The hadrons were produced in the forward direction into a beam with a momentum bite of ± 16.5% and an overall acceptance of 455 μsr-%. The beam was constructed in order to provide the dichromatic source of high energy neutrinos from π and K decay used in the study of neutrino interactions. The flux of neutrinos was determined by measurement of the hadron flux. This experiment measured the total hadron flux with an ionization chamber and the differential flux with a low efficiency Freon-13 differential Cerenkov counter.

In Chapter II we will describe the characteristics of the hadron beam used in this experiment. The hadrons accepted by this beam were allowed to travel 345 meters in a decay pipe at partial vacuum before being absorbed in a beam dump. This drift space allowed for hadron decay. The decay mode which interested us was $\pi \rightarrow \mu\nu$ and $K \rightarrow \mu\nu$ because these decays provided the dichromatic neutrino beam used in our study of neutrino interactions.

Not all the pions and kaons decayed. For example, at a hadron energy of 120 Gev 5.0% of the pions and 20.7% of the kaons decayed through this mode. The target for these neutrinos was 160 tons of steel. Even with such a massive target, the probability of a neutrino interaction was typically 10^{-9}. Therefore, we wanted a hadron beam with as large an acceptance as possible without compromising the dichromaticity of the beam. The acceptance of our beam (455 μsr-%) is about five orders of magnitude larger than a typical(22) beam used to provide hadrons with sharp momentum definition.

The hadronic ratios in this beam were measured at the end of the 345 meter decay pipe with a Freon-13 Cerenkov counter. Chapter III describes the experimental setup used to define the hadron beam at this location and the procedure used to identify the different hadron components in the beam. In an earlier attempt to analyze the hadron composition of the beam, the Cerenkov counter was placed at the upstream end of the decay pipe. In this configuration the beam stop for the primary proton beam was only 25 meters upstream of the Cerenkov counter. This beam stop acted as a secondary source of hadrons. These secondary hadrons increased our accidental rates and reduced the signal-to-noise ratio. Since this background was unfocused, we decided to move the

Cerenkov counter downstream so as to get a cleaner sample of hadrons produced in the 12" target.

The maximum efficiency that a Cerenkov counter can have and still separate pions and kaons is given by:

$$\mathcal{E}_{MAX} = 1 - \mathrm{EXP}\left\{ -kL \frac{(m_K^2 - m_\pi^2)}{p^2} \right\} \qquad (2)$$

L = length of counter

k = constant determined by light collection efficiency, bandpass of photocathode, quantum efficiency, etc.

m_K = mass of kaon

m_π = mass of pion

p = hadron momentum

At high energy the efficiency is reduced unless the length of the counter grows like p^2. A Cerenkov counter operating in a 100 Gev hadron beam must be about 117 feet long in order to be 95% efficient. In a 200 Gev beam the length must increase to 468 feet. However, if one inserts a light-absorbing iris in front of the photocathode so that the pion Cerenkov light cannot reach the photocathode past kaon threshold, the resulting pressure curve can be integrated to yield particle ratios without the necessity of high efficiency or even knowledge of the efficiency. This is the approach we took, using a six foot Cerenkov counter with efficiency typically less than 20%. This measurement was then complemented by a measurement of the overall hadron flux using an ionization chamber. This approach was novel at the time of this experiment and it proved successful. In Chapter IV we describe in detail the characteristics of our low efficiency Cerenkov counter.

When conducting the neutrino experiment with this beam, we always ran with the highest possible flux of incident protons. Intensities were as high as 5×10^{12} protons per accelerator cycle. In order to measure particle ratios with the Cerenkov counter we needed to reduce the intensity to less than 10^{10} protons per pulse. Lower intensities would have been desirable , but they were impossible to achieve. An electrostatic septum was used to shave off a small fraction of the extracted proton beam for use in our beam line. This method could reduce the beam intensity by at most a factor 100. Reduction of the intensity inside the main ring made the beam position monitors in the ring useless.

As a result of this high intensity, accidental rates in our counter telescope were non-negligible and we were forced to apply an accidental subtraction to the data. This subtraction did not remove all of the background from the data sample. In Chapter III we describe various techniques(veto counters, shower counters, hadron calorimeter, pulse height discrimination, etc.) utilized to increase the signal-to-noise ratio. In Chapter V we discuss corrections made on the pressure curves themselves, in particular the subtraction of backgrounds still present in the pressure curves.

The pressure curves contain more information than just particle ratios. They also provide several checks on our measuring technique. For example, the efficiency of the counter must vary with pressure, $\mathbb{P}$, in a well-defined way:

$$\text{Efficiency} = 1 - \exp(-k\mathbb{P}) \qquad (3)$$

where k is a constant. Moreover, the overall integral of the entire curve provides a relative measure of the quantum efficiency of the Cerenkov counter phototube. Angular misalignment of the counter and the cutoff angle provided by the light-absorbing iris may also be extracted from the curves. These checks are described in Chapter VI.

Our measurements did not provide only particle ratios in the beam but also absolute flux. A description of the technique used to measure these fluxes is contained in Chapter VII.

The results and conclusions of this experiment fall into two categories: the study of inclusive hadron production from Aluminum with a 300 Gev proton beam, and the study of high energy neutrino interactions. An inclusive interaction is one in which only a single particle is detected after the initial interaction. The undetected particles are all grouped under 'anything' in equation (1).

There is considerable interest in the inclusive production of hadrons at high energy that goes beyond the standard yield measurements accompanying the birth of a new accelerator (in our case, the Fermilab synchrotron). Comprehensive discussions may be found in the literature.(1-2) Examples of attempts to parameterize or predict high energy behavior are found in the models of Cocconi, Koester, and Perkins,(3) Trilling,(4) Sanford-Wang,(5-6) Benecke et al.,(7) and Hagedorn-Ranft.(8-10) Independent of production mechanism, the common thread running through most of these models is the idea of 'scaling'.

We are speaking here of 'hadronic scaling', also called 'Feynman scaling' or 'longitudinal scaling'. This kind of scaling concerns itself with the momentum distribution of final state hadrons produced in hadronic collisions. In Feynman's radiation picture of hadronic scaling(11) the interacting hadrons in the initial state are pictured in the center of mass frame as Lorentz contracted spheres (discs) which at the time of collision act as a stationary radiative source with a disc shape. The longitudinal momentum distribution of the radiated hadrons is the Fourier transform of the spatial distribution of sources inside this disc. If the only effect of a change in the energy of the initial particles is to contract this source, then the width of the momentum distribution grows like the energy of the initial particles, but the shape is the same when plotted as a function of $x = 2P_{\parallel}/\sqrt{s}$ where

$P_{\parallel}$ = longitudinal momentum of produced hadron in the center of mass frame

$\sqrt{s}$ = total energy of system in the center of mass frame

Lorentz contraction does not occur for the transverse momentum, $P_{\perp}$, so the variables used to describe inclusive hadronic production in a scaling model are x and $P_{\perp}$

The expressions for the cross sections in scaling models may be written in different ways to emphasize various features:

a) $dP_{\parallel}/P_{\parallel}$ radiation similar to Bremsstrahlung

$$\frac{d^2\sigma}{dP_{\parallel}\,dP_{\perp}^2} = \frac{f(x,P_{\perp})}{P_{\parallel}\sqrt{1+\frac{m^2+P_{\perp}^2}{P_{\parallel}^2}}} = \frac{f(x,P_{\perp})}{E} \qquad (4)$$

b) Lorentz Invariance

$$E\frac{d^3\sigma}{d^3\vec{p}} = f(x, P_\perp) \qquad (5)$$

c) Laboratory Yields

$$\frac{d^2\sigma}{dp\,d\Omega} = E_0 f(x, P_\perp) \qquad (6)$$

$f(x,P_\perp)$ = universal scaling function

$P_\parallel$ = longitudinal hadron momentum

$P_\perp$ = transverse hadron momentum

E_0 = beam energy

$x = P_\parallel / E_0$

There is a second type of scaling which is not purely hadronic. This type is called 'deep inelastic scaling' or 'transverse scaling' and is concerned with the interactions between leptons and hadrons. The processes studied are those which are deeply inelastic, i.e. involve small impact parameters. The lepton is used as a probe of the substructure of the nucleon. It has been found(28) that these inclusive deep-inelastic lepton-hadron interactions can be described in terms of the scaling variable

$$\omega = 2m\nu/Q^2 \qquad (7)$$

m = mass of proton

ν = energy transfer from lepton to hadron

Q^2 = four-momentum transfer

Without scaling the processes would depend upon both ν and Q^2 ,not just their ratio. In this thesis we do not consider this type of scaling.

The most comprehensive model of high energy hadron production is the Thermodynamic Model of Hagedorn and Ranft. This model incorporates the general features of hadronic scaling and, in addition, specifies the shape of the momentum distribution of produced hadrons. We outline the characteristics of this model in Chapter VIII.

In Chapter IX we discuss the data from the point of view of absolute yields and particle ratios. The results are compared with lower energy data in order to reach a conclusion concerning the validity of hadronic scaling. The results are also compared with the predictions of the Thermodynamic Model.

The neutrino total cross section measurement would not have been possible without the normalization provided by this experiment. In Chapter X we discuss the results of our measurement of this cross section.

Finally, in Chapter XI we make suggestions for possible improvements in the experimental method.

II. Description of Hadron and Neutrino Beams

A. Description of Hadron Beam

The secondary hadron beam used in this experiment is a simple defocus-bend-focus-bend system designed to provide momentum analysis, vertical and horizontal point-to-parallel focusing, and momentum recombination. A lenslike representation of the beam is shown in fig. 2.1

In the thin lens approximation to this optical system, quadrupoles are characterized simply by a focal length, f, and dipoles by a bend angle, ϑ.
Using this thin lens approximation and accompanying lens diagrams, we will show how the beam accomplishes its objectives: vertical and horizontal point-to-parallel focusing, and momentum recombination.

The vertical focusing action of the quadrupoles is depicted in fig. 2.2. Quadrupole OFT defocuses in such a way that all the rays emanating from the target appear to have originated from a point a distance $\gamma_1 = l_1/\left(1+\frac{l_1}{f_1}\right)$ in front of OFT. Quadrupole ODT then forms a parallel beam from these diverging rays if it has a focal length, f_2, equal to $\gamma_1 + l_2 + l_3$. This constraint for vertical point to parallel focusing is summarized by:

Vertical point-to-parallel focusing

$$\left\{1+\frac{l_1}{f_1}\right\}\left\{\frac{l_2+l_3-f_2}{f_2}\right\}+\frac{l_1}{f_2}=0 \qquad (8)$$

The horizontal focusing action of the quadrupole doublet is shown in fig. 2.3. Behaving like a convex lens, quadrupole OFT forms an image of the target at a distance $l_2 + l_3 + \delta_2$. Before the image is formed, the rays are intercepted by ODT and the image is moved to infinity, i.e. a parallel beam. This is accomplished only if f_2, the focal length of ODT is equal to δ_2 This constraint may be written:

Horizontal point-to-parallel focusing

$$\left\{1-\frac{l_1}{f_1}\right\}\left\{f_2+l_2+l_3\right\}+l_1=0 \qquad (9)$$

In fig. 2.1 we see that the incident proton beam strikes the target with a 6 mr. inclination with respect to the horizontal. This feature was imposed on the beam in order to reduce low energy neutrino contamination of our high energy neutrino beam. It will be discussed later.

Because of this orientation of the incident beam, the two dipole bends are unequal. The first bend, θ_1, deflects the beam down 12 mr. and the second bend, θ_2, returns the beam to the horizontal with a weaker bend of 6 mr. Without the quadrupole ODT, this would leave the beam with a net dispersion of 0.06 mr/%, e.g. a ray with a momentum 10% larger than the central momentum would be inclined by +0.6 mr. after leaving this beam. By placing ODT strategically between the dipoles (see fig. 2.4), the combination of OPT-A and ODT behave like an equivalent dipole with a 6 mr. bend. The bend introduced by OPT-A is equal to $\vartheta_1 \, \Delta P/P_0$ where ϑ_1 = 12 mr. and $\Delta P/P_0$ is the fractional deviation from the central momentum. ODT introduces a bend in the opposite direction equal to $\vartheta_1 \, \Delta P/P_0 \; l_3/f_2$. If the difference in these two bends equals $\vartheta_2 \, \Delta P/P_0$ where ϑ_2 = 6 mr., we can achieve a parallel beam in spite of the unequal bends. This condition is simply:

Momentum Recombination

$$\frac{\vartheta_2}{\vartheta_1} = 1 - \frac{l_3}{f_2} \qquad (10)$$

Most of the beam elements are actually comprised of more than one physical magnet. These are labeled 1,2... where appropriate in the ray traces for a point target (figs 2.5, 2.6).

Having discussed the optical objectives of this beam, we now consider quantitatively the parameters describing its capabilities. These parameters (first-order transfer matrix elements) are listed in Table 2.1

The purpose of the angular collimators OCTAT and OCTAB (see fig. 2.1) is to provide vertical angular collimation of this beam. The incident proton beam has a finite spot size, so there is not a one-to-one correlation between angle at the target and angle at the collimator. Furthermore, the defocusing action of OFT magnifies the production angle of particles leaving the target. These two effects combine to yield a position-angle correlation at the collimator of 1.33 cm/mr and a magnification equal to 1.6. The spot size was typically ± 1.5 mm while the vertical angular acceptance extended from -1.25 mr to +2.5 mr. A 1.5 mr ray, therefore, reaches the angular collimator at 2 cm ± 0.24 cm.

At the momentum slit, OCTP, the dispersion is 0.23 cm/%, but the magnification is 3.65 and the position-angle correlation is 4.22 cm/mr. Fig. 2.7 shows the resulting position-momentum correlation for our beam. Using a narrow momentum slit is not sufficient to insure sharp momentum definition. This lack of momentum definition at the momentum slit results from the lack of an intermediate point focus at the position of the slit. An intermediate focus requires a longer beam and we were constrained by space limitations when the beam was constructed.

Fig. 2.8 shows the correlation between momentum and vertical position at the angular collimators, OCTAT and OCTAB. The high momentum tail on the momentum distribution can be eliminated by collimating from below with OCTAB (see fig. 2.8). Collimation from above will not narrow the momentum acceptance and it will unnecessarily reduce the flux. Momentum distributions for various settings of OCTAB are shown in figs. 2.9 through 2.12. We chose to run the experiment with collimator settings: OCTAT = +1½", OCTAB = -½". This leads to a momentum acceptance of ± 16.5% (RMS).

Collimating in this asymmetric fashion affects not only the magnitude of the acceptance of the beam, but also the midpoint of the vertical angular acceptance. Fig. 2.13 shows that collimating with the bottom half of the collimator, OCTAB, alone indeed results in a larger overall acceptance than symmetric collimation (OCTAB = -OCTAT). The midpoint of the angular acceptance however is now 0.25 mr.

While this beam was designed to achieve point-to-parallel focusing in both vertical and horizontal planes, finite spot size at the target does lead to angular divergence at the exit from the beam. In Table 2.1 we see a vertical angular divergence equal to -0.24 mr/cm and a horizontal angular divergence equal to -2.92 mr/cm. This difference of more than an order of magnitude in the angular divergences can be understood by studying figs. 2.14 and 2.15. Each of these lens systems can be described by a single equivalent convex lens. The focal length of the equivalent lens, f_{eq}, is given by:

$$\frac{1}{f_{eq}} = \frac{-1}{f_1} + \frac{(l_2+l_3)}{f_1 f_2} + \frac{1}{f_2} \qquad \text{Vertical focussing} \quad (11)$$

$$\frac{1}{f_{eq}} = \frac{1}{f_1} + \frac{(l_2+l_3)}{f_1 f_2} - \frac{1}{f_2} \qquad \text{Horizontal focussing} \quad (12)$$

and the target is positioned a distance f_{eq} in front of the equivalent lens. The closer the target is to the lens, the greater the angular divergence will be for rays originating off-center at the target. In fact, the angular divergence is proportional to $1/f_{eq}$. One can graphically show the qualitative difference between our horizontal focusing and vertical focusing. In fig. 2.14 the solid line represents a typical vertical trajectory for a particle originating off-center in the target. If we extrapolate the initial trajectory of the particle (before entering the beam), the point at which this extrapolated trajectory intersects the exit trajectory is the position of the equivalent convex lens. For vertical focusing the equivalent lens is downstream of the second quadrupole. In fig. 2.15 we show a typical horizontal trajectory for a particle originating off-center in the target. If we extrapolate both the entrance trajectory and exit trajectory, the point of intersection is the position of the equivalent convex lens. For horizontal focusing, the equivalent lens is close to the first quadrupole.

Thus, the different order of the quadrupoles (defocus-focus for vertical, and focus-defocus for horizontal) leads to the vastly different positions of the equivalent lenses. For vertical focusing, the equivalent lens is far from the target and the angular divergence is small. For horizontal focusing, the equivalent lens is close to the target and the angular divergence is larger by more than a factor 10. The choice to defocus first in the vertical direction was motivated by the fact that the dipole gaps in our beam were 5" high by 1 1/4" wide. Defocusing in the vertical means focusing in the horizontal direction, and this choice increased our angular acceptance.

In Table 2.2 we summarize the parameters describing the acceptance of this beam. In figs. 2.16 through 2.18 histograms show the shape of the acceptance functions for this beam. Figs. 2.19 through 2.22 show the profile and angular divergence of the beam at the position of the Cerenkov counter. In figs. 2.23 and 2.24 we show the correlation between momentum and position of the beam at the Cerenkov counter.

If our beam were amenable to description by first-order optics alone, all acceptance distributions would be symmetric. The lack of symmetry in the distributions is due to second-order effects, i.e. chromatic aberrations. These aberrations occur in both quadrupoles and dipoles. In quadrupoles the focal length is not independent of momentum, but rather is proportional to momentum. In dipoles, the bend angle is not simply $\vartheta \frac{\Delta P}{P_0}$ where θ equals the bend in the central trajectory, but rather the bend angle is given by $\vartheta \frac{\Delta P}{P_0} / \left(1+\frac{\Delta P}{P_0}\right)$. By design our beam had large angular and momentum acceptances, and the chromatic aberrations therefore skewed the acceptance distributions visibly.

B. Description of Neutrino Beam

The hadrons produced in the Aluminum target and accepted by our 455 μ sr-% beam served as the source of the dichromatic neutrino beam through the decay modes $\pi \to \mu\nu$ and $K \to \mu\nu$. In view of the small cross section for neutrino interactions (about 10^{-36} cm^2/nucleon for our experiment), our objective was to produce as many hadrons as possible. The large acceptance of our beam serves well in this regard, but we needed also to maximize the number of hadrons produced in the target, i.e. maximize the probability of interaction for an incident proton. Too short a target results in a small probability for interaction. Too long a target will absorb most of the produced hadrons before they leave the target. The probability of interaction with subsequent escape from the target is given approximately by:

$$\text{Probability} = (L/X)\, e^{-(L/X)} \qquad (13)$$

L = target length

X = collision length

This probability is maximized when L = X and it achieves a value between 30% and 40% depending on the material used. We used approximately one collision length (12") of Aluminum to maximize the hadron flux.

The hadrons produced in the target do not wait until they reach the decay region (the 345 m. following the beam) before they decay. They begin decaying immediately; some decay before the beam can select their charge and momentum. These early decays result in neutrinos with energies ranging from 30 Mev up to almost the incident beam energy (in our case, 300 Gev). They clearly do not constitute a neutrino beam with a well-defined energy.

In order to prevent these neutrinos from early decay from entering our neutrino-detecting apparatus 875 m. downstream, we oriented the optical axis of our beam so that for the most part it was inclined from the horizontal (see fig. 2.1). The proton beam struck the target with a + 6 mr inclination. The first bend directed the beam to - 6 mr and only after the last 6 mr bend was the beam returned to the horizontal.

The hadrons decaying in the 345 m. decay pipe thus became the predominant source of neutrinos. The probability of decay into a neutrino is given by:

$$\text{Probability} = 1 - \exp(-345/\lambda) \qquad (14)$$

$$\lambda = \frac{p}{m} c\tau$$

m = meson mass

p = meson momentum

$c\tau$ = 7.8 m. for pions

5.56 m. for kaons

At a hadron energy of 120 Gev, 5.0% of the pions decay into neutrinos and 20.7% of the kaons decay into neutrinos.

The selection of only the high energy neutrinos from these decays was accomplished geometrically. Fig. 2.25 shows qualitatively the correlation between the angle and energy of the neutrinos resulting from π and K decay. Our apparatus subtends a small angle ($<$ 1 mr) when viewed from the decay region. Neutrinos travelling at angles greater than about 1 mr. do not strike our apparatus. This angular cutoff (shown in the dashed line in fig. 2.25) eliminates low energy neutrinos, resulting in a double-humped (dichromatic) energy spectrum of neutrinos striking our apparatus. The maximum neutrino energy resulting from pion decay is 43% of the pion energy. The maximum neutrino energy resulting from kaon decay is 96% of the kaon energy.

Neutrino interactions in our apparatus were identified by the presence of a produced muon and observable energy from a shower of hadrons. When observed in this way, we measured the sum of the muon and hadron energies with about 25% resolution and reconstructed the energy spectrum of incident neutrinos. This reconstructed spectrum is shown in fig. 2.26 with the desired two peak structure.

III. Data Taking Procedure

Particle ratios in this beam were determined by use of a low efficiency Freon-13 Cerenkov counter (described in Chapter IV) in conjunction with a beam-defining telescope of scintillation counters (see figs. 3.1 and 3.2). Freon-13 was chosen as the gas to be used in this counter because its index of refraction increases more rapidly with pressure than do the indices of other common Cerenkov counter gases. The Freon-13 index increases 60% more rapidly than CO_2, more than twice as rapidly as N_2, and 20 times as rapidly as Helium. This enabled us to detect particles with momenta as low as 25 Gev/c without raising the gas pressure above one atmosphere.

The entire detection array was situated 345 m. downstream of the hadron beam (described in Chapter II) and immediately behind a 20 foot steel beam collimator. The collimator allowed passage of a 4" by 4" beam.

The objectives of this array of detectors were twofold: to define the hadron component of the beam (eliminating muons, electrons, photons and neutrinos) without introducing biases for or against any particular type of hadron, and to separate the hadronic components of the beam using the velocity selection of the Cerenkov counter. The amount of Cerenkov light produced by a particle passing through the Cerenkov counter depends upon the particle velocity as follows:(20)

$$\text{Amount of light} \sim 1 - \frac{1}{n^2\beta^2} \qquad (15)$$

v = particle velocity

c = speed of light

$\beta = v/c$

n = index of refraction of the gas

The primary definition of the hadron beam was achieved by demanding a coincidence in the three scintillation counters B1, B2, and B3. The distance between B1 and B3 was about 70 feet. Each of these counters measured 3" by 3".

Due to the presence of the 4" by 4" steel collimator, it was anticipated that hadrons scraping off the side of the collimator might produce accompanying particles which could either trigger the system or produce Cerenkov light. To avoid this error, we positioned veto counters, V1 and V2, around B1. See fig. 3.2 . This arrangement would geometrically remove about 95% of this spurious type of event. During the running we compared the data with and without vetoes and found no appreciable difference.

The presence of the veto counters reduced the effective dimensions of B1 to 2 7/8" by 2 7/8". The profile of the beam was measured at the position of B1 and found to extend vertically from -6" to +6" and horizontally from -7" to +7". This is consistent with the Monte Carlo vertical profile shown in fig. 2.21, but somewhat narrower than the Monte Carlo horizontal profile shown in fig. 2.22. Thus, we sampled only a portion of the beam at the Cerenkov counter. Monte Carlo calculations using Hagedorn-Ranft particle distributions (see Chapter VIII) concluded that we sampled the central 55% of our beam.

Figs. 2.23 and 2.24 show that there is a correlation between particle momentum and position at the Cerenkov counter. This is due to the chromatic aberrations in the beam, discussed in Chapter II. Because of this correlation particle fluxes and ratios were expected to vary slightly with lateral position in the beam. This bias, brought about by the undersized counters, requires correction. This correction will be discussed in Chapter V.

The light pipes on counters B1, B2, B3, V1 and V2 were air light pipes with Aluminum foil interiors. Plastic light pipes were not used because particles passing through the plastic produce Cerenkov light. Air light pipes insured that we were observing a 2 7/8" x 2 7/8" beam. Scintillation counters with air light pipes cannot take advantage of total internal reflection in plastic and, therefore, have lower light collection efficiencies than counters with plastic light pipes. To compensate for this lower light collection efficiency, counter B1 had two light pipes, one on either side, and was viewed by two phototubes.

In a further attempt to avoid circumstances where two particles traversed the Cerenkov counter at the same time (within a time resolution of about 5 ns.) we vetoed the trigger whenever the pulse height in either B1 or B2 was greater than twice minimum-ionizing. In addition, counter B2 was preceded by three radiation lengths of lead in order to discriminate against electrons and photons in the beam. The three radiation lengths of lead also discriminated against knock-on electrons with energy greater than 30 Mev produced upstream of B2. Discriminating against electrons and photons in the beam introduces no biases against the hadron component. Discrimination against knock-ons is not entirely without bias. While mesons and protons produce low energy knock-ons with the same probability, a proton is much more likely than a meson to produce a knock-on in the forward direction.(29) Fortunately the probability of forward-going knock-on production by a proton is low, about 10^{-6} /Gev/(gm/cm^2). This veto, then, affects all hadrons equally within the statistics of our measurements.

The effect of the B1 veto, which vetoes on twice minimum-ionizing pulse heights without lead, was negligible. The B2 veto, incorporating the lead, reduced the signal by about 25%. This vetoing of electrons is desirable because they produce Cerenkov light in the same pressure interval as pions. The vetoing technique, furthermore, does not bias our measurement of hadronic ratios.

The dipoles 1WO-1 and 1WO-2 (see fig. 3.1) are part of the existing Fermilab muon beam. For our purposes, they functioned as sweeping magnets. Since our beam is momentum-selected (and not mass-selected), the sweeping action of these magnets affected all hadronic components equally. These magnets remove from our beam all particles with momentum less than 22% of the beam-selected momentum.

The counters SH1-SH5 (see fig. 3.1) were separated by 6" of steel between adjacent counters. Each of these counters measured 14" high by 10" wide and, unlike the beam-defining and veto counters, they utilized plastic light pipes. The purpose of this arrangement (5 counters and 24" of steel) was to eliminate muons from the beam. Muons do not lose very much energy when passing through the steel. Their typical loss is 1.5 Mev/(gm/cm^2). Hadrons, on the other hand, interact strongly and produce a shower of hadrons cascading through the array. The gain on the phototubes for SH1-SH5 was set with the steel removed. It was adjusted such that minimum-ionizing particles produced a 3 mV signal in each counter. The experiment was run with the steel replaced and the signals from the five counters were summed. Muons produced a typical 15 mV signal in this sum, whereas hadrons produced signals as much as 100 times larger. Muon rejection was estimated to be close to 100% efficient. Assuming that pion and kaon decay in the 345 m. decay pipe is the dominant source of muons, we expect a μ/π ratio typically less than 15%. 93% muon rejection is sufficient to reduce this muon contamination to 1% of the pion signal.

A radiation length in steel is about 1.8 cm. Photons and electrons in the beam, therefore, either give large summed pulse heights like hadrons, or else are totally absorbed and never reach B3.

The above discussion of rationale and procedure for defining the hadron beam is summarized in the logic diagram of fig. 3.3 The definition of a hadron in the beam was a BEAM = B1•B2•B3•SH•$\overline{V}$ coincidence. The type of hadron was identified by FLUX = C•BEAM, i.e. the coincidence of BEAM with a pulse from the

Cerenkov counter. The details of the Cerenkov counter operation are discussed in Chapter IV.

Early running made it apparent that accidentals and spurious coincidences in the FLUX = Č•BEAM signal were to be the largest source of error in the pressure curves. Uncorrelated accidentals were monitored by delaying the Č signal by an integral number of R-F spacings (18.93 ns spacing). This accidental rate was then subtracted from the raw signal. The subtraction was always substantial, at times comprising almost 90% of the raw signal. The size of the subtraction was, in part, due to the high intensity of the incident proton beam, always greater than 10^9 protons/pulse. It was impossible to operate either the accelerator or the external beam lines at a lower intensity.

The subtraction of these uncorrelated accidentals did not entirely remove the background from underneath the pressure curves. There remained both a background at zero pressure and a background rising with pressure. These backgrounds were studied and subtracted in the curve fitting stage of the analysis. They will be discussed in Chapter V.

Since this counter was not operated as a threshold counter, we did not need to know the exact pressure at the position of any data point. However, it was imperative to insure that the pressure increment between points was a constant differential. This requirement was satisfied by the use of a constant volume-constant pressure gas line to add uniform quantities of Freon-13 to the counter volume using a remotely operated solenoid switch (see fig. 3.4). Using the notation in fig. 3.4 , the change in pressure, δP, per fill is:

$$\delta P = P_L \frac{\Delta V}{V} \qquad (16)$$

where $\Delta V/V \approx 10^{-3}$ for our Cerenkov counter and gas line.

The volume of our gas line could be varied by using three solenoid valves, any one of which could define the end of the line. These three sections were calibrated against two separate pressure gauges.

Pressure curves were thus taken by the sequential addition of constant amounts of gas and measurement of Cerenkov efficiency for each new pressure.

IV. Details of Cerenkov Counter Operation

The particulars of the hadron beam (i.e. focusing and dispersive properties, acceptance, chromatic aberrations etc.) have been described in a previous section. In this section we describe in detail the technique implemented in the yield measurements of forward-going hadrons.

Particle differentiation is accomplished by means of a Freon-13 gas Cerenkov counter designed to have low efficiency. The optics of this counter are shown in fig. 4.1. The photocathode of the Cerenkov counter phototube is placed 80" from the parabolic mirror (measured along a ray which reflects off the 45° mirror). The focal length, f, of the mirror, of course, is also 80". This optical arrangement was chosen because of the fact that Cerenkov light, emitted along the path of a particle passing through the counter, is focused into a zero-width ring of light at a distance f from the mirror. The above statement is true independent of the angle and/or position of the trajectory. In fig. 4.2 consider the cone of light emitted from point X_o at angle ϕ The reflected light behaves as though it emanates at angle $\phi' = \frac{X_o}{X_i}\vartheta_c$ from a virtual source a distance X_i behind the mirror. The relationship between X_o and X_i can be found in the lensmakers equation:

$$X_i = \frac{f X_0}{f - X_0} \qquad (17)$$

The reflected light also has a circular cross section and, at a distance f from the mirror, the radius of this circle is:

$$R = \phi'\left\{f + X_i\right\} = \frac{X_0}{X_i}\,\phi\left\{f + \frac{f X_0}{f - X_0}\right\} = \phi\, X_0 \left\{\frac{f - X_0}{f X_0}\right\}\left\{\frac{f^2}{f - X_0}\right\} = \phi f \qquad (18)$$

independent of X_0, i.e. all Cerenkov light from all points on the particle's trajectory is in this ring. The center of the ring at the focal length is not the same for all trajectories. If the trajectory makes an angle α with respect to the axis of symmetry, the center of the ring is displaced by an amount αf at the focal length. However, it is easy to show that the Cerenkov light is still focused into a concentric ring if the particle's trajectory is off-axis but parallel to the axis of symmetry.

In order to understand further the behavior of this counter, we need to make an estimate of its efficiency. The total number of photons, N , emitted in the wavelength interval $[\lambda_1, \lambda_2]$ and in a distance l is given by: (20)

$$N = 2\pi\alpha l \left\{\frac{1}{\lambda_1} - \frac{1}{\lambda_2}\right\} \sin^2\phi \qquad (19)$$

The quantum efficiency of an RCA-8850 phototube(21) is approximately 0.25 between $\lambda_1 = 2800\ \text{Å}$ and $\lambda_2 = 5000\ \text{Å}$ If we assume 75% light collection efficiency, K, and a flight path, l, of 70", we can calculate the mean number of photoelectrons, $\bar{n}$, as a function of Cerenkov angle ϕ

$$\bar{n} = 2\pi\alpha l Q K\left\{\frac{1}{\lambda_1}-\frac{1}{\lambda_2}\right\}\sin^2\phi = 0.024\,\phi^2\{mr\} \qquad (20)$$

Q = quantum efficiency = 0.25
K = light collection efficiency = 0.75
l = radiating length = 70"
α = 1/137
λ_1 = 2800 Å
λ_2 = 5000 Å

The efficiency of the counter is then given by:

$$\eta = 1 - e^{-\bar{n}} \approx \bar{n} - \frac{\bar{n}^2}{2} = 0.024\,\phi^2 - 0.00029\,\phi^4 \qquad (21)$$

The estimate of 75% light collection efficiency is based on the following. The Cerenkov light is reflected from two mirrors, both of which have a Beryllium-Aluminum alloy coating. Consulting fig. 4.3, one finds an average reflection coefficient of about 90% in the range 2800-5000 Å. The light must also pass through two quartz windows: one separating the gas volume from the phototube and one on the face of the phototube. The quartz window on the entrance face of the counter has a quarter-wave coating of MgF_2 which attempts to eliminate reflection. See fig. 4.4 for reflectivity versus index of refraction of the coating. However, the exit face still has only 96% transmission. The window on the phototube causes the light to suffer 4% loss at both entrance and exit. Consequently:

Collection Efficiency = (.9)(.9)(.96)(.96)(.96) = 0.75

From fig. 4.5 we see that if the Cerenkov angle is limited to a small value, η rises almost linearly with ϕ^2

If we write the index of refraction of the gas in the form $n = 1 + \epsilon \mathbb{P}$ where $\mathbb{P}$ = pressure in atmospheres and $\epsilon = 0.00075 \text{ atm}^{-1}$ for Freon-13 ($CClF_3$), then

$$\phi^2 = 2\epsilon\mathbb{P} - M^2/p^2 \qquad (22)$$

M = mass of particle traversing the counter

p = particle momentum

i.e. ϕ^2 has a linear dependence on the pressure, $\mathbb{P}$. Hence, for small enough Cerenkov angles, the counter efficiency is proportional to $\mathbb{P} - \mathbb{P}_0$ where $\mathbb{P}_0$ is the threshold pressure and is given by:

$$\mathbb{P}_0 = \text{threshold pressure} = M^2/2\epsilon p^2 \qquad (23)$$

Furthermore, if we establish a cutoff angle by inserting a light-absorbing iris as in fig. 4.1, we find that the pressure difference between threshold and cutoff, $\Delta\mathbb{P}=\mathbb{P}_c-\mathbb{P}_0$ is independent of either the particle or its momentum. This pressure difference depends only on the index of refraction of the gas and the cutoff angle:

$$\Delta\mathbb{P} = \theta_c^2/2\epsilon \qquad (24)$$

Hence, for a monoenergetic beam of pions, kaons, and protons, and low efficiency, we end up with the ideal Cerenkov pressure curve of fig. 4.6. Each of the triangular curves has the same width baseline, and particle ratios may be obtained by comparing peak values, integrals, or slopes.

In view of the fact that the width of an individual pressure curve is independent of momentum, and the fact that the threshold varies as M^2/p^2, it is important to decrease the iris opening with increasing momentum, lest two neighboring curves begin to overlap. Figs. 4.7-4.11 show the regions of usefullness for five different iris sizes. The filled-in regions represent the pressure interval within which the designated particle will produce observable Cerenkov light at the given momentum.

In actual practice the situation is not as simple as the above would imply. We have already seen that an angular divergence (or, equivalently, an angular misalignment in the Cerenkov counter) moves the ring of Cerenkov light so that its center no longer lies on the symmetry axis of the iris. This, of course, smears out the cutoff. The shape of the pressure curves resulting from angular misalignment is shown in fig. 4.12. The effect is geometrical and does not depend on the mass of the particle involved. One can show that the pressure curve resulting from this misalignment has the functional form:

$$f(\phi) \sim \mathrm{SIN}^2\phi \quad \text{FOR} \quad \phi + \alpha \leq \vartheta_c \tag{25}$$

$$f(\phi) \sim \mathrm{SIN}^2\phi \left\{ 1 - \frac{1}{\pi} \mathrm{ARCTAN} \left[\frac{\left\{ 2\phi^2(\vartheta_c^2+\alpha^2) - (\vartheta_c^2-\alpha^2)^2 - \phi^4 \right\}^{\frac{1}{2}}}{(\vartheta_c^2 - \alpha^2 - \phi^2)} \right] \right\} \tag{26}$$

$$\text{FOR} \quad \phi + \alpha > \vartheta_c$$

ϕ = Cerenkov angle

ϑ_c = cutoff angle

α = misalignment angle

In first order for a point target, this beam focuses point to parallel. Finite spot size and the inherent chromatic aberrations compromise this feature and lead to a beam with a small angular divergence at the exit from the train. See figs. 2.19 and 2.20 Because of this, meticulous alignment of the counter is not enough to guarantee the triangular shape of the pressure curves. In general the curves will resemble the shapes shown in the lower half of fig. 4.12.

An immediate consequence of this change in shape is the effect upon the integral of the pressure curve. For the same particle yield, the integral increases with increasing misalignment. Hence we must apply a correction factor to regain the 'no misalignment' integral. This correction factor is shown in fig. 4.13 as a function of misalignment angle for various iris apertures. Fortunately, the misalignment correction does not depend upon what particle goes through the counter, so the correction can be ignored if one is interested only in the ratios of particle yields.

Recall that the pressure threshold for particle detection is given by:

$$\mathbb{P}_0 = M^2/2\epsilon p^2 \qquad (27)$$

M = particle mass

n = index of refraction = $1+\epsilon\mathbb{P}$

p = particle momentum

and the width of a curve is given by:

$$\Delta\mathbb{P} = \vartheta_c^2/2\epsilon \qquad (28)$$

ϑ_c^2 = cutoff angle

Thus, the change in threshold due to a change in the momentum is $\delta\mathbb{P}_0 = \frac{M^2}{\epsilon p^2}\frac{\delta p}{p}$. For a beam with a finite momentum bite, the smearing of the curve is given to first order by:

$$S = \frac{\delta\mathbb{P}_0}{\Delta\mathbb{P}} = \frac{2M^2}{p^2}\frac{\delta p}{p}\frac{1}{\vartheta_c^2} \qquad (29)$$

Obviously the proton curve is severely smeared in most cases, while the pion curve remains relatively insensitive to this effect. Figs. 4.14 through 4.16 show pressure curve shapes resulting from an assumed triangular momentum distribution. Despite the radical nature of this distortion, the integrals of these pressure curves are independent of the amount of smearing.

V. Integration of Pressure Curves and Extraction of Particle Ratios

The raw data from the Cerenkov counter pressure curves are shown in figs. 5.1 through 5.10 with the kaon contribution to the curve magnified. Because of the large momentum acceptance of this beam (± 16.5%) particle ratios could not be gleaned from pressure curves by either the slope or peak-value methods. These methods apply only to ideal Cerenkov curves (see fig. 4.6) with triangular shape. Therefore, the ratios were abstracted from the pressure curves by the integral method. We have stated in a previous section (Chapter IV) that the ratio of the integral of one particle's curve to another's is a direct measure of the particle ratios independent of beam divergence, counter misalignment, and momentum bite. Therefore, particle ratios are theoretically easy to measure by integration. Two features of the data persuaded us to extend the analysis to include curve fitting of the pion and kaon curves. These features are: 1) the non-negligible background, and 2) the overlap of signal from neighboring portions of the curve.

We have mentioned before (in Chapter III) that the uncorrelated accidental background represented, at times, 90% of the raw signal from the Cerenkov counter. Some background remained even after the

subtraction of this uncorrelated background. The size and shape of the remaining background are consistent with the size and shape of backgrounds resulting from knock-on electrons and scattered Cerenkov light.
We shall discuss these backgrounds in the following pages.

A. Extraction of Integrals from Negative Cerenkov Curves

Magnified views of the Cerenkov curves for negatively charged particles (figs. 5.1 through 5.4) indicate a background with a zero offset and a linear rise with pressure. If the same background mechanism is operative for all four curves, the background functional form must be universal. The 'efficiency' of the Cerenkov counter at vacuum level for the four curves is shown below:

Energy	Vacuum Level 'Efficiency'	Iris Setting	Iris Area
-95	$(.495 \pm 0.0389) \times 10^{-3}$	3.393 mr.	1.493 cm^2
-120	$(.471 \pm 0.0435) \times 10^{-3}$	2.583 mr.	0.865 cm^2
-145	$(.515 \pm 0.0453) \times 10^{-3}$	2.161 mr.	0.606 cm^2
-170	$(.500 \pm 0.0500) \times 10^{-3}$	2.424 mr.	0.762 cm^2

The mean of these four values is:

Mean Vacuum Level 'Efficiency' = $(.494 \pm 0.022) \times 10^{-3}$

and the four values are consistent with a constant value for the vacuum level efficiency.

The existence and value of the background at vacuum level can be explained by delta rays (knock-on electrons) produced by hadrons as they pass through the 1/8" Aluminum entrance window to the Cerenkov counter. The probability of hadrons producing delta rays is:(29)

$$\text{Probability} = 0.15\, m_e \frac{dE'}{(E')^2} \quad \text{per gm/cm}^2 \qquad (30)$$

m_e = mass of electron

E' = energy of delta ray

We are considering here delta rays which are produced in the Aluminum window and are directed toward the quartz window separating the interior of the Cerenkov counter from the light-tight box housing the Cerenkov counter phototube. These delta rays will have energy between 0.19 Mev and 0.57 Mev. We use the larger value (0.57 Mev) to calculate a lower estimate on the probability of producing such knock-ons. The probability, P, is:

$$\frac{dP}{dE'dx} = \frac{0.236}{\text{MeV-gm/cm}^2} \qquad (31)$$

where $dE' = 0.375$ Mev

and $dx = 0.857$ grams of Aluminum

The solid angle subtended by the window and the correction for absorption and multiple scattering in the Aluminum introduce a correction factor of approximately 0.004. Combining all the factors we arrive at a probability for producing a knock-on which strikes the quartz window equal to 3.0×10^{-4}. These knock-ons produce Cerenkov light in the quartz window at an angle of approximately 48° and the quartz window becomes an efficient detector of delta rays, both because of the large Cerenkov angle and becuse of its proximity to the phototube.

Thus, delta ray production predicts a vacuum level efficiency of approximately 3.0×10^{-4}. This is very close to the vacuum level efficiencies observed for both positive and negative beams.

When gas is added to the counter, the back ground rises linearly, proportional to the amount of gas in the counter, i.e. proportional to the pressure. The slope of this background is not the same for all curves. However, the ratio of the slope to the iris area is a constant. Thus, we have found the empirical rule that the pressure dependent background rises linearly with pressure and quadratically with cutoff angle. One functional form fits all the negative curves.

These considerations lead to a universal background for the negative curves:

$$\text{Background 'Efficiency'} = 4.9454 \times 10^{-4} + 5.3546 \times 10^{-3}\,\mathbb{P}\,\vartheta_c^2$$

$\mathbb{P}$ = pressure in matm.

ϑ_c = cutoff angle in mr.

This background is shown in figs. 5.1 through 5.4.

In order to demonstrate in a more straightforward manner that the pressure-dependent background contribution is proportional to the iris area, we measured the efficiency of the counter for a variety of iris openings in pressure ranges where signal to background ratio was small. The results of these measurements are shown in fig. 5.11 and the data clearly support a background with a linear dependence on iris area.

After subtracting the background from the data, the curves were fit using the functional forms described in Chapter IV and a Hagedorn-Ranft Monte Carlo momentum distribution. These fits are shown in figs. 5.12 through 5.19 and the values of the integrals are listed in Table 5.1

In the fit of the pion curve at 95 Gev (fig. 5.12) there is a small portion of the curve at the very end of the falling edge that is not accounted for by the fit. This extra tail comes from the angular divergence in the beam. It is found in all of the pion curve fits and it represents less than 1% of the total integral. Its contribution was included in calculating the integrals.

B. Extraction of Integrals from Positive Cerenkov Curves

The vacuum level efficiencies for the positive Cerenkov curves are listed below:

Energy	Vacuum Level 'Efficiency'
+95	$(3.775 \pm 1.07) \times 10^{-4}$
+120I	$(3.725 \pm .932) \times 10^{-4}$
+120II	$(1.51 \pm .631) \times 10^{-4}$
+120III	$(2.92 \pm .464) \times 10^{-4}$
+145	$(0.5 \pm 1.58) \times 10^{-4}$
+170	$(2.04 \pm .678) \times 10^{-4}$

The mean of these six values is:

Mean Vacuum Level 'Efficiency' = $(2.412 \pm 0.291) \times 10^{-4}$

We have already shown in section A of this chapter that this vacuum level background can be understood semi-quantitatively in terms of delta rays. The variation in vacuum level background for the positive curves does not rule out delta rays. In fig. 5.20 the points labelled 'data' are the vacuum level efficiencies for the positive curves. None of these points is any more than 1½ standard deviations removed from the average value of 2.412×10^{-4}. It is expected that the average value of the vacuum level efficiency for the positive curves be lower than the corresponding value for negative curves because the quantum efficiency of the phototube used for the positive curves was lower than the quantum efficiency of the phototube used for the negative curves by about a factor 2.36. This change in quantum efficiency is discussed in Chapter VI.

Nonetheless, in order to ascertain the error introduced by the uncertainty in this constant background, three independent methods were used to 'predict' the value of this background from the rest of the data.

Method #1: The low pressure section of the pion curve (before cutoff) has a shape which depends only on the momentum distribution of the pions and the index of refraction of the gas. Using a simple parameterization of this distribution (Monte Carlo acceptance folded into exponential yields with one adjustable parameter) one can obtain a minimum-χ^2 fit which predicts the background level. The predictions from this method are shown in fig. 5.20

Method #2: Rather than parameterizing the momentum distribution, we used Hagedorn-Ranft predictions for the spectrum. Once again, the χ^2-minimization then predicts a background. (see fig 5.20)

Method #3: Once the cutoff and misalignment angles have been established from the pion fit, the shape of the kaon curve depends only on background and normalization. χ^2-minimization for the kaon fit leads to a new prediction for the constant background level.

This uncertainty in the constant background level is the largest source of error in the positive integrals.

The parameterization of that portion of the background which rises linearly with pressure can be achieved by restudying the negative Cerenkov curves. If we try the same parameterization that was used for the negative curves, it produces a background much too large, even at the same pressure where it was measured for the negative curves. However, in the case of the negatives, the beam population was dominated by pions. It was, therefore, impossible to conclude whether the pressure-dependent background was produced by the entire beam (e.g. scintillation) or by the pions only (e.g. scattered Cerenkov light). Both of these sources increase linearly with pressure.

If we assume that the background is due to scattered Cerenkov light, then there are three contributions to this background, π, K and proton Cerenkov light, each with its own threshold. To parameterize each of these contributions we use the parameterization for the negative curves multiplied by the appropriate particle fractions, i.e.

$$B = B\{0\} + \sum_{i=1}^{3} \{\mathbb{P} - \mathbb{P}_{0i}\} \theta_c^2 f_i \times 5.5488 \times 10^{-3} \qquad (32)$$

$\mathbb{P}$ = pressure in matm.

$\mathbb{P}_{0i}$ = pressure threshold for particle i
i=1 π
i=2 K
i=3 p

θ_c = cutoff angle

f_i = fraction of particle i in the beam

The most likely obstacle capable of scattering Cerenkov light from the path determined by the optics is the quartz window separating the interior of the Cerenkov counter from the light-tight box surrounding the phototube. Recent tests have shown that this window does indeed scatter light. Thus the quartz window becomes the offender for both the pressure-independent and the pressure-dependent backgrounds. Since the path to this window relies upon reflection from the 45°

mirror, there should be a geometrical cutoff to the background when the Cerenkov cone is larger than the mirror. This occurs at about 14.5 mr. Using the above three part background with geometrical cutoff, we arrived at the background subtraction shown in figs. 5.5 through 5.10. With the resulting background-subtracted data, we fitted the curves for the pion and kaon integrals, and simply integrated the larger proton curve. The fits are shown in figs. 5.21 through 5.31 and the values of the integrals are listed in Table 5.1.

The integrals of the pressure curves require the application of several correction factors before they represent the measure of particle ratios in our beam.

The counters used to define the beam were smaller than the actual beam (they sampled about 55% of the beam). Since the yields of pions, kaons, and protons do not have the same momentum dependence, and since our beam had chromatic aberrations (momentum-dependent aberrations), the particle ratios have a small dependence on lateral position in the beam. Table 5.2 shows the factor to be applied to the measured ratios in order to achieve the ratios for the entire beam. This table is the result of a Monte Carlo analysis of our beam assuming Hagedorn-Ranft momentum and angular distributions.

In order to test the validity of this calculated correction for the lateral dependence of particle ratios, we raised the pressure in the Cerenkov counter until we achieved maximum detection efficiency for 120 Gev pions. We then swept the beam vertically in order to measure variations in the pion fraction as a function of vertical position of the beam. This variation in pion fraction is shown as a function of the height of the beam centroid in fig. 5.32. The solid line is the Monte Carlo prediction for the expected variation in pion fraction. Our calculated correction is consistent with this measurement.

Since our detection apparatus was located 400 m. from the target, a non-negligible fraction of the pions and kaons decayed in flight. The correction for this decay is largest for 95 Gev/c hadrons where 43% of the kaons and 7.2% of the pions decay. This standard correction was also applied to the data.

The resulting particle ratios are listed in Table 5.3

VI. Further Checks on the Measuring Technique

The shape of a pion Cerenkov curve between threshold and geometrical cutoff is a direct measure of the Cerenkov angle dependence of the efficiency of the counter. Fig. 6.1 shows such a curve taken with π^- at 170 Gev with a large (6.25 mr.) cutoff. This energy was chosen because the K^- contribution under the pion curve is small ($K/\pi \approx 0.07$). A log plot of the efficiency (fig. 6.2) shows a) the efficiency of the counter is less than the calculation of section IV and b) there is a deviation from the expected exponential behavior of the efficiency. The lower efficiency is perhaps not surprising in view of the optimistic values used in the calculation, but it was, in fact, raised to its expected value by replacing the phototube. The reduced efficiency at large Cerenkov angles is most probably due to a variation in photocathode quantum efficiency with position of the Cerenkov ring on the photocathode. Note that in the region where we took data $\left\{\theta_{\pi^-}^{2} \leq 10\ \mathrm{mr}^{2}\right\}$ the efficiency does indeed have a strictly exponential behavior.

In order to have remote control of the cutoff angle and the ability to fully close the iris, we utilized a biplanar leaf iris driven by a stepping motor. (Single plane leaf irises cannot be fully closed). The position of the driving gears was monitored with a potentiometer. A vernier measurement of iris opening versus potentiometer reading is shown in fig.6.3. The results of the fitted pion curves show a somewhat larger opening than measured mechanically, but still with a linear dependence on potentiometer reading.

The shape of a pion Cerenkov pressure curve is given by formula (26). The integral of this curve depends on the cutoff angle, θ_c , and the misalignment angle, α , as per figure 6.4. We call this integral the 'Geometrical Efficiency', G.

$$G = \int f(\phi)\, d\mathbb{P} \qquad (33)$$

$$\phi^2 = 2\epsilon\mathbb{P} - m^2/p^2 \qquad (34)$$

$\mathbb{P}$ = pressure

m = particle mass

p = particle momentum

n = index of refraction = $1+\epsilon\mathbb{P}$

The measured integral of the pion curve is given by:

$$\int \pi\, d\mathbb{P} = QKf_\pi G \qquad (35)$$

Q = quantum efficiency

K = a constant depending on factors such as length of radiator, band pass of photocathode, mirror reflectivity, etc.

f_π = fraction of pions in the beam

G = geometrical efficiency

Since Cerenkov curves for kaons and protons are composed of overlapping curves of the type described by formula (26) the same arguments hold for them and we have:

$$\int \pi \, d\mathbb{P} = QKf_\pi G \qquad (36)$$

$$\int K \, d\mathbb{P} = QKf_K G \qquad (37)$$

$$\int P \, d\mathbb{P} = QKf_P G \qquad (38)$$

Adding the three contributions:

$$\int \{\pi + K + P\} \, d\mathbb{P} = QK \underbrace{\{f_\pi + f_K + f_P\}}_{1.0} G \qquad (39)$$

Since the geometrical efficiency is known once ϑ_c and α are gleaned from the pion curve, we can measure the relative quantum efficiencies for the various curves:

$$Q_r = \text{relative quantum efficiency} = \frac{\int \{\pi + K + P\} \, d\mathbb{P}}{G} \qquad (40)$$

These relative quantum efficiencies are shown in fig. 6.5 There is a clear jump between runs 6 and 7. An examination of the misalignment angle for the same runs also shows a jump between runs 6 and 7. Between runs 6 and 7 we changed phototubes from an RCA 8850 to a C31000M, a tube with a broader frequency pass and higher quantum efficiency. In the process of doing so we obviously moved the counter by about 140 microns.

The misalignment angle (before bumping) is seen to be about 0.4 mr. The angular divergence of the beam at the position of the Cerenkov counter has an RMS value of about 0.32 mr. In addition, our counter alignment technique was expected to be accurate to about 0.25 mr. These two sources are clearly consistent with the average value of 0.4 mr.

VII. Absolute Flux Measurements

In addition to the measurement of hadron ratios made with the Cerenkov counter, a measurement of the absolute flux of hadrons was also made with an ionization chamber (SIC) situated 10 feet upstream of the Cerenkov counter. The ionization chamber could not discriminate against muons, so we need new variables to describe the makeup of the beam as the SIC saw it.

Let:

f_π = fraction of pions in the hadron part of the beam at the Cerenkov counter

f_K = like fraction of kaons

f_p = like fraction of protons

$$f_\pi + f_K + f_p = 1 \qquad (41)$$

f'_π = fraction of pions in the total beam (including muons) at the Cerenkov counter

f'_K = like fraction of kaons

f'_p = like fraction of protons

f'_μ = like fraction of muons

$$f'_\pi + f'_K + f'_p + f'_\mu = 1 \qquad (42)$$

D_π = ratio of pions at target to pions at Cerenkov counter (decay correction)

D_K = ratio of kaons at target to kaons at Cerenkov counter

Using these variables, we find the following relationships:

$$f'_{\pi} = \frac{f_{\pi}}{f_{\pi} D_{\pi} + f_K D_K + f_p} \qquad (43)$$

$$f'_{K} = \frac{f_{K}}{f_{\pi} D_{\pi} + f_K D_K + f_p} \qquad (44)$$

$$f'_{p} = \frac{f_{p}}{f_{\pi} D_{\pi} + f_K D_K + f_p} \qquad (45)$$

$$f'_{\mu} = \frac{f_{\pi}\{D_{\pi}-1\} + f_K\{D_K-1\}}{f_{\pi} D_{\pi} + f_K D_K + f_p} \qquad (46)$$

The SIC was calibrated using a 200 Gev proton beam from the NAL synchrotron. Consequently, all ionization measurements have the units 'equivalent 200 Gev protons'. The actual ionization as a function of particle and energy is shown in fig. 7.1

If we define:

n = number of equivalent 200 Gev protons

N = actual number of particles passing through the SIC

β_i = ratio of ionization by particle i to ionization by a 200 Gev proton

then:

$$N = \frac{n}{f'_{\pi}\beta_{\pi} + f'_K\beta_K + f'_p\beta_p + f'_{\mu}\beta_{\mu}} \qquad (47)$$

The number of particle i produced at the target is then:

$$N_i = f_i' D_i N \qquad (48)$$

The results of these SIC measurements are shown in table 7.1

VIII. Thermodynamic Model of Hadron Production

The main ideas involved in the Thermodynamic Model of Particle Production have been discussed in the literature.(8-10) We shall describe briefly here some of the more important features.

The Thermodynamic Model is an extension of the two-fireball model(15) to a continuum of fireballs. It is a bootstrap model in the sense that:

A fireball is:

> a statistical equilibrium (hadronic blackbody radiation) of undetermined numbers of all kinds of fireballs, each of which, in turn, is considered to be

The multiplicity of fireballs within a fireball, $W(n,\varepsilon)$, is given by:

$$W(n,\varepsilon) \approx \frac{\bar{n}^{n}}{n!}\, e^{-\bar{n}} \qquad (49)$$

$$\bar{n}(\varepsilon) \xrightarrow[\varepsilon\to\infty]{} \alpha \ln\left(\frac{\varepsilon}{\varepsilon_0}\right) \qquad (50)$$

ε = energy density of decaying fireball

α = parameter used to vary this distribution if necessary because of conservation laws

$$\varepsilon_0 = 1\ \mathrm{GeV}/V_0 \qquad (51)$$

$$V_0 = \frac{4\pi}{3}\left(\frac{1}{m_\pi}\right)^3 \qquad (52)$$

Since there is a continuum of fireballs, they need a velocity distribution. Instead of using the velocity, β, as a parameter, the model uses λ:

$$\lambda = \mathrm{SIGN}(\beta)\, \frac{\gamma - 1}{\gamma_0 - 1} \qquad (53)$$

β = fireball velocity
β_0 = initial proton velocity
$\gamma = 1/\sqrt{1-\beta^2}$
$\gamma_0 = 1/\sqrt{1-\beta_0^2}$

λ is then the ratio of local kinetic energy density to incoming kinetic energy density. There are two velocity functions:

$F(\lambda)$ for newly created particles
$F_0(\lambda)$ for through-going particles

Each of the fireballs is a system of an indefinite number of particles, resonances, and other fireballs in equilibrium at temperature, T, where T is chosen such that $\langle E(T) \rangle$ = the energy of the fireball. The expression for $\langle E(T) \rangle$ will be given later.

The one-particle momentum spectrum for a particle of mass, m, participating in this system is:

$$f_m(\vec{p},T)\, d^3\vec{p} = \mathrm{CONST}\left\{ \mathrm{EXP}\left[\sqrt{\vec{p}\cdot\vec{p} + m^2}/T \right] \pm 1 \right\}^{-1} d^3\vec{p} \qquad (54)$$

i.e. isotropic with Planck Blackbody Radiation law.

In order to calculate $\langle E(T) \rangle$ for a fireball, we need the mass distribution of available particles, resonances, and fireballs. This is postulated to be:

$$\rho(m) \approx \frac{a_0}{(m_0^2+m^2)^{5/4}} e^{m/T_0} \qquad (55)$$

$a_0 = 2.63 \times 10^4$ Mev

$T_0 = 160$ Mev

$m_0 = 500$ Mev

This form fits onto the known mass distribution below 1200 Mev.

Integrating over $\vec{p}$ in equation (54), one finds:

$$\langle E(T)\rangle = \int_0^\infty f'(m,T)\, \rho(m)\, e^{-m/T}\, dm \qquad (56)$$

where $f'(m,T)$ is a well-behaved function. In order for this integral to be non-divergent, $T_0 = 160$ Mev $= 1.86 \times 10^{12}$ °K must be a limiting universal highest temperature. At this temperature, the addition of energy to a fireball results in more particles, not in more kinetic energy.

The only two functions which are left unpredicted by this model are $F(\lambda)$ and $F_0(\lambda)$. Using experimental data between 12 and 30 Gev, it was found that energy-independent forms could be used to reproduce all measured spectra in this region. These forms are:

$$F(\lambda) = \frac{1}{N}(1-\lambda)\, e^{-a\lambda} \qquad (57)$$

$$F_0(\lambda) = \frac{1}{N_0}\left[(1-\lambda)\, e^{-b\lambda} + d\lambda\, e^{-c(1-\lambda)}\right] \qquad (58)$$

where $a=5.6$

$b=20.8$

$c=2.4$

$d=7.1$

The Hagedorn-Ranft extrapolations to higher energies rely upon this assumption of energy independence for $F(\lambda)$ and $F_0(\lambda)$. It should be mentioned that this energy-independence for $F(\lambda)$ and $F_0(\lambda)$ is equivalent to the hypothesis of limiting fragmentation and Feynman's use of $x=P/E$ and $P_\perp$ in a scaling model. This equivalence is shown in ref. 16.

Before reviewing the first experimental tests of the Hagedorn-Ranft model, it is important to mention those difficulties which were anticipated.

The first difficulty is the kinematic cutoff. The theory is thermodynamical and has exponential distributions extending to infinity. Near kinematic cutoff the thermodynamics of the situation is less important than phase space restrictions. This cutoff was initially put in arbitrarily, and it was expected to need revision.

The second difficulty lies in the bootstrap characteristic of the model. In order to facilitate calculations, the final particles were assumed to come from the first fireballs rather than from a concatenation of fireballs. This resulted in an inability to predict particle multiplicities or absolute normalization. The forms of the spectra are, therefore, more reliable than the normalization.

The first test of the model was made against 19.2 Gev data from CERN(14) and 35, 43, 52 and 70 Gev data from Serpukhov.(17-18) The fits obtained for π^+, K^+ and proton spectra at 19.2 Gev were reasonably good without readjustment of the model. The predicted fits for K^-/π^- and $\bar{P}/\pi^-$ at 70 Gev were off by a factor 2 below x=0.7 and the disagreement was even worse above x=0.7. The model needed adjustment in order to gain consistency. The prediction for the absolute yields of π^-, however, were still high by a factor 5.

The only way to readjust the model was to introduce an energy-dependent $F(\lambda)$. This was not done for (at least) the following two reasons: 1) the experimental errors are ± 50%, and 2) If $F(\lambda)$ were reduced by a factor 5, the integral of the π^- spectra (i.e. π^- multiplicity) would be less than the known multiplicity at 30 Gev.

The latest versions of the Thermodynamic Spectra (the versions which we use for comparison to our data) are contained in ref. 19 . The plots are shown in figs. 8.1 through 8.6 and the input parameters to the computer program SPUKJ (30) are shown in Table 8.1

IX. Discussion of Data

A. Yields from this beam

The results of our measurements of hadron production from 300 Gev protons on a 12" Aluminum target are shown in figs. 9.1 and 9.2. These plots show the number of hadrons produced per incident proton and accepted by our beam as a function of x:

$x = P_{\parallel}/E_0$

$P_{\parallel}$ = longitudinal momentum of hadron

E_0 = beam energy

Measurement of these yields involved the implementation of three separate measuring devices: a secondary emission monitor (SEM) monitoring the flux of incident protons, the already-mentioned SIC measuring hadron flux, and the Freon-13 Cerenkov counter for particle differentiation. Foil irradiation calibration of the SEM gave agreement to 3%. The SIC was calibrated with a 200 Gev proton beam and showed a stability of 6.3%. The errors on the Cerenkov counter pressure curves are listed in Table 5.1 These errors include statistical fluctuations but are dominated by the indeterminacy of the background subtraction. We have applied both an empty target subtraction and decay correction to these yields. Empty target subtractions were small: less than 4%

for positive hadron beams, and less than 2% for negative hadron beams. The decay correction is calculable from known particle lifetimes and the distance from the Aluminum target to the Cerenkov counter. The largest decay correction necessary occurred for 95 Gev/c hadrons. At this momentum, 43% of the kaons and 7.2% of the pions decayed in flight.

It is important to note that these are yield measurements for our beam and not differential cross sections. Our beam has a large calculated acceptance (455 μsr-%) and utilized a thick target (12" Aluminum). Measurement of differential cross sections requires knowledge of this beam acceptance. The acceptance has been calculated but not measured.

B. Particle Ratios

Figures 9.3 through 9.8 show the particle ratios in the beam. These ratios do not depend upon SEM or SIC measurements, but only upon the Cerenkov counter integrals, the finite-sized counter correction, and the decay correction. For comparison in figs. 9.3 through 9.8 we have shown in the solid line the prediction resulting from folding Hagedorn-Ranft distributions into the calculated acceptance of our beam. At this point we will mention only that there is not complete agreement between the predictions and the data. We will go into more detail later.

Figures 9.9 through 9.11 show our particle ratios plotted along with the ISR results (p-p interactions)(12) and the results of the measurement of 3.6 mr. hadron production from Beryllium.(22) The ISR results are all at $P_\perp$ = 200 Mev/c, where $P_\perp$ is the transverse momentum of the produced hadron. Our data have maximal flux at $\theta \doteq 1.35$ mr. In each case $\left\{P/\pi^+, K^-/\pi^-, K^+/\pi^+\right\}$ the seven sets of data are in agreement to about a factor 2. The P/π^+ ratio rises almost exponentially. The K^-/π^- ratio is consistent with a constant, while the K^+/π^+ ratio shows a tendency to rise.

In making this comparison, we have compared data at six different energies from three different targets and very different transverse momenta. The major effect of thick targets (Aluminum and Beryllium) is to increase the π^+/p ratio over the ratio obtained from a proton target. This increase results from the fact that protons are more likely than pions to be reabsorbed in the targets. Rough calculations using a 24 mb total cross section for pion reabsorption and a 40 mb cross section for protons indicates that the π^+/p ratio from a thick target may be as much as 75% higher than the ratio from a proton target. The discrepancy is probably not this large, however, because about 25% of the protons scatter elastically and are not removed from the beam.

For 100 Gev/c hadrons, the ISR results were taken at $P_\perp$ = 200 Mev/c. Our measurements sampled a beam with a mean transverse momentum of 135 Mev/c, and the 3.6 mr data from Beryllium were taken at $P_\perp$ = 360 Mev/c. $P_\perp$-distributions are expected to be roughly exponential with $\langle P_\perp \rangle$ for pions = 320 Mev/c; for kaons $\langle P_\perp \rangle$ = 425 Mev/c and for protons $\langle P_\perp \rangle$ = 500 Mev/c. These values of $\langle P_\perp \rangle$ also have an x dependence. Thus, experiments conducted at differing values of $P_\perp$ are expected to give dissimilar results for particle ratios. In the case of the experiments we are considering, the results could differ by as much as a factor 2.

The factor 2 disagreement which we find in these ratios is thus consistent with thick target and transverse momentum corrections.

C. Corrections necessary for further analysis

In order to extend our analysis to include a simple test of scaling and a comparison with the Hagedorn-Ranft Thermodynamic Model, we need to make a correction for thick target absorption.

Figure 9.12 shows the relative flux per incident proton as a function of target thickness for a +120 Gev hadron beam. We have fitted the curve with the functional form:

$$\mathrm{FLUX} \sim \frac{L}{X} e^{-L/X} \qquad (13)$$

L = target length

X = interaction length

The fit results in X= 17.8" and a correction factor 0.344 (i.e. 34.4% of the incident protons produce observable hadrons). The fit is relatively insensitive to the choice of interaction length. Using X= 12.9", we obtain a correction factor 0.367. In applying this correction we have assumed that it is both energy and particle independent. The energy independence is most likely a good assumption since total cross sections are constant in the range 95 Gev to 170 Gev (the range of our measurements), but the particle independence is questionable, especially for protons. Our measurement is actually an average of the correction for mesons and protons in the beam. The error in this assumption may be as large as 30%.

D. Test of hadronic scaling with an Aluminum target between 19.2 Gev and 300 Gev

Using the data of Allaby et al.(14) for 12.5 mr. production of hadrons from Aluminum at 19.2 Gev incident proton energy, we have made a simple test of scaling.

(1)

We assume that the cross section has the functional form:

$$\frac{d^2\sigma}{d\Omega\, dp} = E_0\, f(x)\, f(P_\perp) \qquad (59)$$

E_0 = beam energy

$x = P_\parallel / E_0$

and that $f(P_\perp) \sim \mathrm{EXP}\{-P_\perp/200\} \qquad (60)$

We may then plot the 'universal' function f(x) measured by these two experiments (the Allaby experiment and the one described in this thesis). In order to do this it was necessary to use the thick target correction for our beam. The correction for differing $P_\perp$ was typically less than 15%.

Figures 9.13 through 9.17 show the f(x) determinations with a solid line drawn through the Allaby data. The horizontal error bars on our data merely point out the large momentum acceptance of our beam. They do not represent the error in the mean momentum. This comparison requires knowledge not only of the acceptance of our beam, but also of the momentum and angular distributions of the produced hadrons. These quantities were calculated for our beam using a Monte Carlo analysis with input from the Thermodynamic Model. The vertical errors represent only the statistical and systematic inaccuracies.

The f(x) discrepancy for π^- is never greater than

30 %. The π^+ agreement is even better. Our experiment shows a systematically higher yield of both K^- and K^+ than realized at 19.2 Gev. The proton data are in agreement. Given the indeterminacies both in the data and the method of comparison, one is free to say only that kaon fluxes have not yet reached a scaling plateau at 19.2 Gev.

The invariant cross sections at the ISR have also been compared to lower energy data(13) with a center of mass energy equal to 6.8 Gev. This comparison is shown in figs. 9.18 through 9.23 . The horizontal axis is the rapidity, y, of the observed particle in the lab:

$$y = \frac{1}{2} \ln \left\{ \frac{E+P_L}{E-P_L} \right\} \qquad (61)$$

P_L = center of mass longitudinal momentum of observed particle

E = center of mass energy of observed particle

In these variables:

$$x = 2P_L/\sqrt{s} \qquad (62)$$

$\sqrt{s}$ = total center of mass energy

What is most clear from these figures is that K^- and $\bar{p}$ production in p-p interactions has not reached the scaling region at 6.8 Gev.

Thus, our conclusions regarding hadronic scaling on Aluminum are essentially the same as those reached for p-p scaling from lower energy to ISR energies.

E. Comparison with the Thermodynamic Model

We have compared our yields and the yields at 3.6 mr(22) (Baker et al.) with the predictions from the Thermodynamic Model(8-10) for these beams. In figs. 9.24 through 9.28 we plot the ratio, R, of the measured yields to the predicted yields for the two experiments. The line R=1 indicates agreement between experiment and prediction.

Over the range of secondary momenta covered, the π^+ yields from the two experiments deviate from prediction in the same way, i.e. both sets of data points lie on the same R(x) curve. Furthermore, the yields from both experiments agree with the predictions to within 25%.

The K^+ yields from the Baker experiment are lower than predicted but agree to better than 25% with the prediction. Below a secondary momentum of 145 Gev/c our K^+ yields also agree to within 25%, but they are higher than predicted. Above 145 Gev/c, our K^+ yields may be higher than predicted by as much as a factor 2, but the error bars are large (the 170 Gev/c point is only an upper limit) and the 145 Gev/c point is only $1\frac{1}{2}$ standard deviations from the R=1 agreement line.

It is known that proton yields rise with increasing secondary momentum.(14) Both our data and the Baker data show this rise. The Baker data are consistent (within 2 standard deviations) with the Hagedorn-Ranft prediction for the 3.6 mr beam, but our data show a different functional dependence than the Thermodynamic Model. At 95 Gev/c secondary momentum, our yields are higher than the prediction by a factor 2, while at 170 Gev/c our yields are 15% lower than predicted, although statistically consistent.

The π^- yields from both experiments are unquestionably lower than predicted by nearly a factor 2 over the entire momentum range covered.

Our K^- yields, like our K^+ yields, agree with the Hagedorn-Ranft predictions to within 30% below a secondary momentum of 145 Gev/c and show a tendency to rise above prediction for momenta above 145 Gev/c. At the highest momentum measured, 170 Gev/c, the measured yield is twice the predicted yield and is almost three standard deviations removed from agreement. The Baker K^- data at 3.6 mr. are consistent with Hagedorn-Ranft predictions for their beam except at 70 Gev/c, where the yield is only 60% of the predicted value.

Thus, we find that for $\pi^\pm$ and proton production, the scaling predictions (section D of this chapter) are more reliable than the predictions of the Thermodynamic Model. For $K^{\pm}$, the Hagedorn-Ranft Model is more reliable than our scaling attempt to predict our yields.

X. Measurement of Neutrino Total Cross Section

The measurement of hadron fluxes and ratios described above provided the normalization (i.e. measurement of neutrino flux) necessary in order to conduct the measurement of the neutrino total cross sections at 38 Gev and 108 Gev.

The neutrino-detecting apparatus is situated 930 meters from the primary Aluminum target. This distance is comprised of a 55 m. beam (described in Chapter II), 345 m. of decay pipe, and 530 m. of muon shielding. The 1.5 m. by 1.5 m. target consists of 160 tons of steel interspersed with scintillation counters (used as a sampling calorimeter) and spark chambers (to follow the muon trajectory). A 5 foot diameter iron-core magnet, several spark chamber arrays, and trigger counters follow the target. See fig. 10.1 We detect reactions of the type:

$$\nu_\mu + N \to \mu^- + \text{HADRONS} \qquad (63)$$

$$\bar{\nu}_\mu + N \to \mu^+ + \text{HADRONS} \qquad (64)$$

The apparatus was triggered on either of the following conditions: (1) a muon traversing the magnet, as indicated by a signal in a scintillation counter located downstream of this magnet, or (2) energy deposition in the sampling calorimeter greater than that typical of a 6 Gev hadronic interaction.

The cross section may be calculated from the relation:

$$\sigma_{TOT} = \frac{1}{FB}\,\frac{T}{\epsilon} \qquad (65)$$

T = total number of observed interacting neutrinos with measured final muon energy

ϵ = efficiency for detection of final muon

F = total number of incident neutrinos

B = 3.087×10^{27} nucleons/cm^2

See Table 10.1 for the values of these quantities along with the systematic and statistical errors.

The efficiency of the apparatus for detecting final state muons was obtained from a Monte Carlo program using the quark model relations:

$$\frac{d^2N}{dx\,dy} = C F_2^{ed}(x)\left\{1 + a_\nu (1-y)^2\right\} \quad \text{FOR } \nu_\mu \qquad (66)$$

$$\frac{d^2N}{dx\,dy} = C F_2^{ed}(x)\left\{a_{\bar\nu} + (1-y)^2\right\} \quad \text{FOR } \bar\nu_\mu \qquad (67)$$

Previous neutrino data (23) give:

$$a_\nu = a_{\bar\nu} = 0.05^{+.25}_{-.17}$$

After correcting for efficiency, the muon angular distributions were compared with equations (66) and (67) We found good agreement with $a_\nu = 0.1^{+.4}_{-.2}$ $a_{\bar\nu} = 0.25^{+.5}_{-.2}$

For $a_\nu = a_{\bar{\nu}}$ we have an average $a_\nu = a_{\bar{\nu}} = 0.17^{+.3}_{-.15}$ Using this average value and its error in the Monte Carlo program, we obtained the best value for the efficiency, ϵ , and the associated systematic error, $(\Delta\epsilon/\epsilon)_{SYS}$

The total number of observed events, T , has an associated error resulting from Poisson statistics, $(\Delta T/T)_{STAT}$, and also a systematic error. The systematic error, $(\Delta T/T)_{SYS}$, comes from the uncertainty involved in the separation of pion neutrinos from kaon neutrinos. Fig. 2.26 demonstrates this overlap between the ν_π and ν_K components.

The flux of neutrinos, F , has a negligible statistical error (fluxes are of the order 10^{11} neutrinos), but it is subject to systematic error, $(\Delta F/F)_{SYS}$, from two sources: stability of the ion chamber (SIC) and uncertainties in the Cerenkov counter pressure curve integrals. The ionization chamber demonstrated a stability of ± 6.3% as a function of hadron beam steering. The systematic errors on the pressure curves are shown in Table 5.1

Our beam was not devoid of hadrons when the target was removed. Hadrons produced in the beam dump for the incident proton beam are surmised to constitute the majority of this 'empty target' contribution. The subtraction is small: 3.9% for the neutrino beam, and 1.6% for the antineutrino beam. These subtractions are expected to be dissimilar in view of the dissimilarity in beam dumping for positive and negative beams.

Fig. 10.2 shows the cross sections measured in this experiment with statistical errors extending to the inner horizontal error bars. The estimated systematic errors have been added in quadrature; the total errors are drawn to the outer horizontal bars. If we write:

$$\sigma_{TOT} = \alpha E \qquad E \text{ in GEV} \qquad (68)$$

the best fits are: $\alpha_{\nu} = 0.83 \pm 0.11 \times 10^{-38}\ \text{cm}^2/\text{GeV}$

$\alpha_{\bar{\nu}} = 0.28 \pm 0.055 \times 10^{-38}\ \text{cm}^2/\text{GeV}$

The data points are quite consistent with this assumed linear relationship intersecting the origin. Fig. 10.3 shows on a logarithmic scale the existing data on the neutrino total cross section.

This measurement of the total neutrino and antineutrino cross sections is an important test of quark and parton models:

1) In a model with spin ½ quarks and V-A coupling, $\alpha_{\bar{\nu}}/\alpha_{\nu} = \frac{1}{3}$ We measure:

$$\alpha_{\bar{\nu}}/\alpha_{\nu} = 0.33 \pm 0.08$$

See fig. 10.4

2) The quark/antiquark ratio in the nucleus is given in these models by:

$$\frac{\bar{Q}}{Q} = 0.37\left\{\frac{3\alpha_{\bar{\nu}}}{\alpha_{\nu}} - 1\right\}$$

We measure:

$$\frac{\bar{Q}}{Q} = 0.0 \pm 0.09$$

3) In parton models the mean-square-charge of the nuclear constituents is given by:

$$\langle q^2 \rangle = \frac{\int F_2^{\gamma N}(x)\,dx}{\frac{3\pi}{4G^2M}\left\{\alpha_{\nu} + \alpha_{\bar{\nu}}\right\}} \qquad (69)$$

where $\int F_2^{\gamma N}(x)\,dx = 0.15 \pm 0.02$ is the integral of the structure function measured in e-d scattering.(31) The simplest quark model gives $\langle q^2 \rangle = 5/18 = 0.28$. Averaging the data from this experiment, we obtain for $E > 30$ Gev:

$$\langle q^2 \rangle = 0.27 \pm 0.05$$

See figs. 10.4 and 10.5

In summary, the neutrino and antineutrino cross sections measured in this experiment are found to have slopes consistent with a simple quark model with little or no antiquark component.

XI. Suggested Changes and Improvement for Further Experiments of this type

The practicality of the use of a low efficiency Cerenkov counter in a high momentum beam has been demonstrated in this experiment. Clearly, the experiment would have been 'cleaner' if the resulting pressure curves more closely resembled the ideal curve of figure 4.6. We shall discuss first the factors possibly influencing the background under these curves and offer suggestions for improvement:

A) The vacuum level background is not due to light from within the counter, but rather to some other mechanism, such as knock-ons. Reducing the thickness of the entrance window reduces the probability of producing knock-ons. Our entrance window had approximately a 14½" diameter. If we reduce the diameter to 4", the thickness can be decreased by about a factor 3.6.

B) The knock-ons could produce the vacuum level background by producing Cerenkov light in the quartz window between the interior of the Cerenkov counter and the phototube, or in the glass window of the phototube. Moving the phototube farther away from the quartz window and farther away from the beam would decrease background produced by either of these mechanisms.

C) In our experiment we used only a lower-level discriminator on the Cerenkov counter signal. The use of an upper-level discriminator and/or pulse height analysis is an effective way of vetoing signals arising from large angle Cerenkov radiation in glass.

D) As mentioned before, the quartz window is known to scatter light which could be responsible for the pressure-dependent background. As with point B), this effect depends upon the solid angle subtended by the phototube. Moving the phototube farther away from the window would reduce this background.

In conjunction with attempts to remove the background, one should also be prepared to deal with existing background by curve fitting. We offer the following suggestions for improved curve fitting:

E) Due to the overlapping of neighboring portions of the Cerenkov curves, the background/signal ratio was high only at vacuum level and past the proton peak. Use of smaller iris settings would have exposed background contributions only between pions and kaons and between kaons and protons. This added information would be an obvious asset in parameterizing the background.

F) The acceptance of the beam was calculated, but not measured. Exact knowledge of the momentum acceptance and angular divergence, combined with exact (interferometric) knowledge of the pressure, completely determines everything about a pressure curve except normalization of the peaks. One then has only two effective parameters for use in curve fitting, i.e. normalization and background level.

G) In our experiment the misalignment angle plus angular divergence was measured with the falling portion of the pion curve. Even though the effect of misalignment upon the pressure curve is understood, it is an unnecessary nuisance and can be removed if the pitch and yaw of the Cerenkov counter are remotely controlled. One then operates on the falling edge of the pion curve and iterates the orientation to maximize the rate of fall of the curve.

H) The detailed fitting of any portion of the pressure curve depends upon an exact knowledge of the optics and geometry of the counter. A clean angular cutoff is best accomplished by using a fixed-radius circular aperture instead of a leaf-type (polygonal) biplaner iris, which is really two apertures in series.

XII. List of Tables

Table 2.1

Transfer Matrix Elements Describing Hadron Beam

y = vertical position (cm)
$\dot{y}$ = vertical angle (mr)
x = horizontal position (cm)
$\dot{x}$ = horizontal angle (mr)
$\Delta P/P_0$ = % deviation from central momentum
o subscript refers to coordinates at target

At Angular Collimator (OCTAT and OCTAB)

$$y = 1.6\, y_0 + 1.33\, \dot{y}_0$$

At Momentum Slit (OCTP)

$$y = 3.65\, y_0 + 4.22\, \dot{y}_0 + 0.23\, \Delta P/P_0$$

At exit from beam

$$\dot{y} = -0.24\, y_0$$

$$\dot{x} = -2.92\, x_0$$

Table 2.2

Beam Parameters

Horizontal Angular Acceptance = ± 1.5 mr (HWHM)

Vertical Angular Acceptance = ± 1.25 mr (HWHM)

Momentum Acceptance = ± 16.5% (RMS)

Full Acceptance = 720 μsr-%

Acceptance with OCTAB set to -½" = 455 μsr-%

Table 5.1

Integrals of pressure curves

Energy (Gev)	π		K		P	
+95	1.71×10^{-4}	2.17%	1.79×10^{-5}	6.59%	2.59×10^{-4}	8.0%
+120I	2.96×10^{-5}	1.72%	3.61×10^{-6}	10.7%	7.92×10^{-5}	7.0%
+120II	3.25×10^{-5}	2.20%	4.03×10^{-6}	12.5%	7.72×10^{-5}	7.0%
+120III	5.25×10^{-5}	1.70%	6.78×10^{-6}	4.25%	1.28×10^{-4}	7.0%
+145	1.42×10^{-5}	2.40%	2.31×10^{-6}	27.2%	5.97×10^{-5}	10.%
+170	4.77×10^{-6}	2.80%	$\le 9.21 \times 10^{-7}$		2.82×10^{-5}	10.%
-95	9.07×10^{-4}	0.37%	5.79×10^{-5}	5.92%		
-120	3.01×10^{-4}	0.96%	1.81×10^{-5}	7.07%		
-145	1.50×10^{-4}	0.59%	6.86×10^{-6}	14.6%		
-170	9.45×10^{-4}	0.56%	4.28×10^{-5}	16.2%		

All integrals are in units:

Fractional efficiency-atmospheres

Errors quoted are one standard deviation

Table 5.2

Correction factor for small counters

Energy (Gev)	P/π^+	K^+/π^+	K^-/π^-
95	1.0872	1.0108	1.0108
120	1.0972	1.004	1.0284
145	1.0873	0.984	1.0555
170	1.0673	0.9958	1.088

Table 5.3

Particle ratios at Aluminum production target

Energy (Gev)	K/π	π/p
-95	0.1093 (5.92%)	
-120	0.0945 (7.07%)	
-145	0.0694 (14.6%)	
-170	0.0676 (16.2%)	
+95	0.1757 (6.94%)	0.6548 (8.30%)
+120I	0.1830 (10.8%)	0.3629 (7.20%)
+120II	0.1862 (12.7%)	0.4084 (7.35%)
+120III	0.1939 (4.57%)	0.3968 (7.20%)
+145	0.2242 (27.3%)	0.2312 (10.3%)
+170	$\leq$ 0.2580 (2.83%)	0.1660 (10.4%)

Errors quoted are one standard deviation

Table 7.1

Number of hadrons produced on 12" Aluminum target
per incident 300 Gev proton

Energy (Gev)	π	K	P
+95	$2.40\mathrm{x}10^{-3}$ (8.83%)	$3.99\mathrm{x}10^{-4}$ (11.0%)	$3.65\mathrm{x}10^{-3}$ (11.7%)
+120	$2.15\mathrm{x}10^{-3}$ (8.60%)	$3.94\mathrm{x}10^{-4}$ (13.8%)	$5.45\mathrm{x}10^{-3}$ (11.0%)
+145	$1.99\mathrm{x}10^{-3}$ (9.00%)	$4.45\mathrm{x}10^{-4}$ (28.3%)	$8.62\mathrm{x}10^{-3}$ (13.1%)
+170	$1.80\mathrm{x}10^{-3}$ (9.00%)	$\leq 4.56\mathrm{x}10^{-4}$	$1.10\mathrm{x}10^{-2}$ (13.0%)
-95	$9.58\mathrm{x}10^{-4}$ (8.60%)	$1.00\mathrm{x}10^{-4}$ (11.3%)	
-120	$7.44\mathrm{x}10^{-4}$ (8.60%)	$6.70\mathrm{x}10^{-5}$ (11.0%)	
-145	$5.92\mathrm{x}10^{-4}$ (8.60%)	$3.90\mathrm{x}10^{-5}$ (16.9%)	
-170	$4.18\mathrm{x}10^{-4}$ (8.60%)	$2.71\mathrm{x}10^{-5}$ (18.2%)	

Errors quoted are one standard deviation

Table 8.1

Input parameters to computer program SPUKJ
used to calculate Thermodynamic Spectra

Parameter	π^-	K^-	π^+	K^+	P
A1	2.2866	0.0	1.815	2.768	1.815
A2	0.5	0.0	3.224	4.952	3.224
A3	0.0	5.4345	5.150	0.0	5.150
A4	0.0	0.5	0.0	0.0	0.182
A5	4.9604	4.9604	16.07	0.0	16.07
A6	0.4874	0.0	4.427	0.0	4.427
A7	0.572	0.572	0.8281	0.0	0.8281
A8	0.0	0.0	0.0	0.0	0.0
A9	0.0	0.0	0.0	0.0	0.0
A10	0.0	0.0	0.0	0.0	0.0

Table 10.1

Parameters used in cross section calculation

Parent Particle	Mean E_ν (GeV)	ϵ	$\left(\frac{\Delta\epsilon}{\epsilon}\right)_{sys}$	T (events)	$\left(\frac{\Delta T}{T}\right)_{sys}$	$\left(\frac{\Delta T}{T}\right)_{stat}$	$F\times10^{11}$ (neutrinos)	$\left(\frac{\Delta F}{F}\right)_{sys}$	σ_{tot} (10^{-38} cm^2)	$\Delta\sigma^{stat}$	$\Delta\sigma^{total}$
π^+	38	.326	.066	233.6	.073	.061	7.77	.13	29.9	1.8	5.2
K^+	107	.454	.052	102.8	.078	.092	.74	.16	98.6	9.1	20.4
π^-	38	.529	.164	97.6	.049	.097	5.02	.11	11.9	1.2	2.7
K^-	102	.647	.125	10.9	.181	.29	.24	.18	22.9	6.6	9.3

XIII. List of Figures

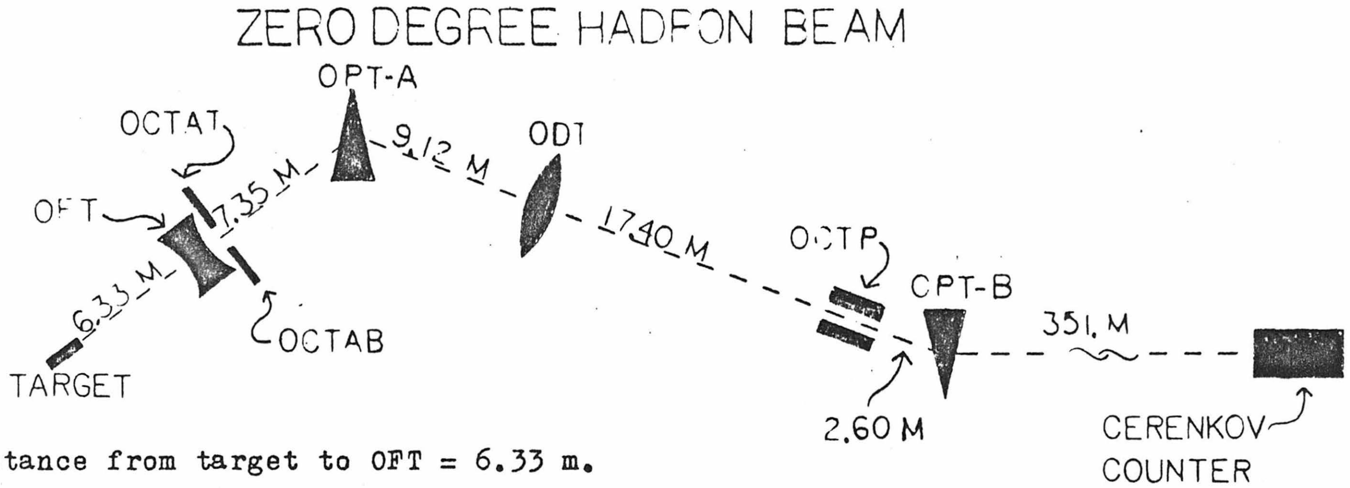

ℓ_1 = distance from target to OFT = 6.33 m.

ℓ_2 = distance from OFT to OPT-A = 7.35 m.

ℓ_3 = distance from OPT-A to ODT = 9.12 m.

f_1 = focal length of OFT = 5.38 m.

f_2 = focal length of ODT = 19.38 m.

θ_1 = first bend = 12 mr.

θ_2 = second bend = 6 mr.

TARGET - 12" Aluminum
OFT - Vertically defocusing quadrupole
OCTAT and OCTAB - Angular collimators
OPT-A and OPT-B - Serially-powered bending magnets
ODT - Vertically focusing quadrupole
OCTP - Momentum-selecting slit

Figure 2.1 Thin lens equivalent of hadron beam

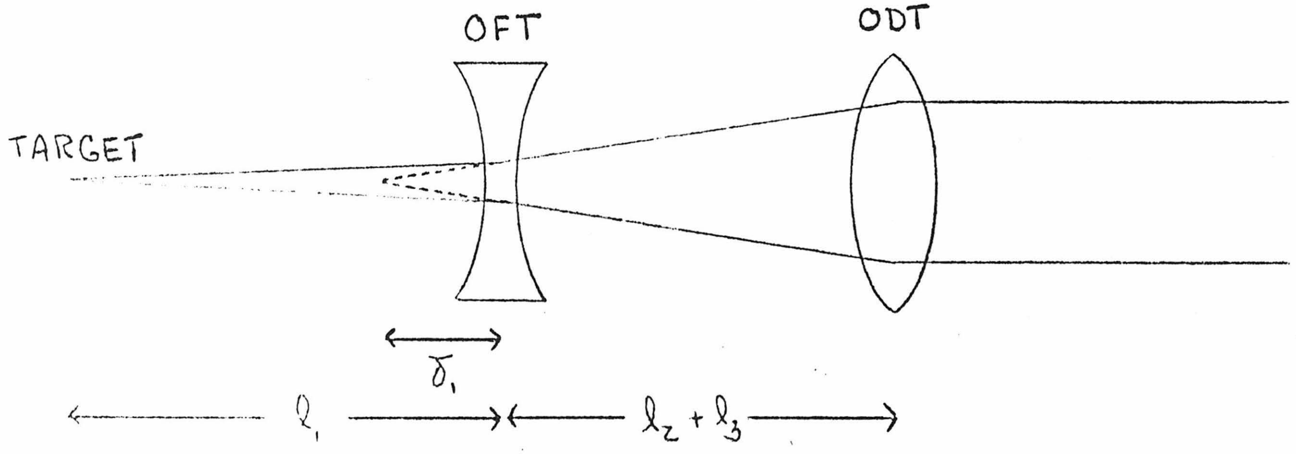

FIG 2.2 VERTICAL POINT-TO-PARALLEL FOCUSING

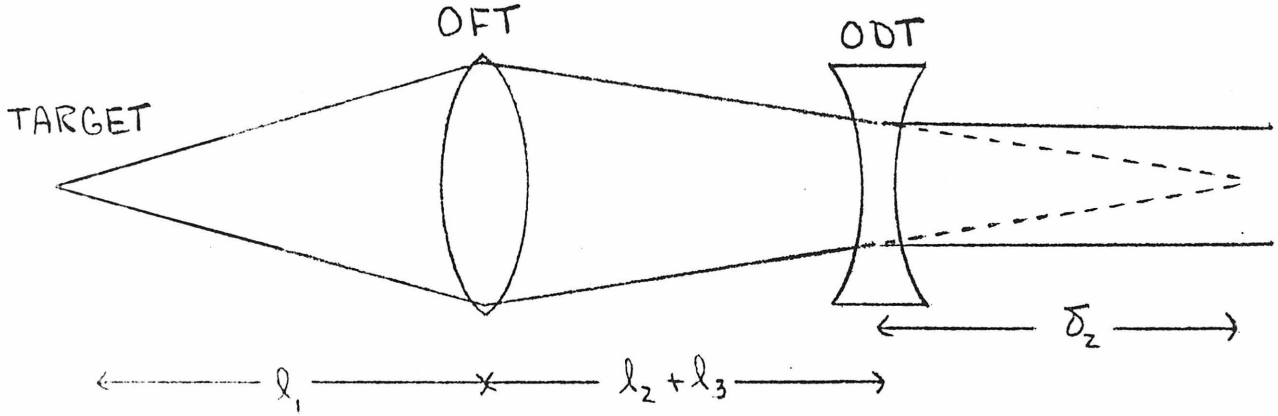

FIG. 2.3 HORIZONTAL POINT-TO-PARALLEL FOCUSING

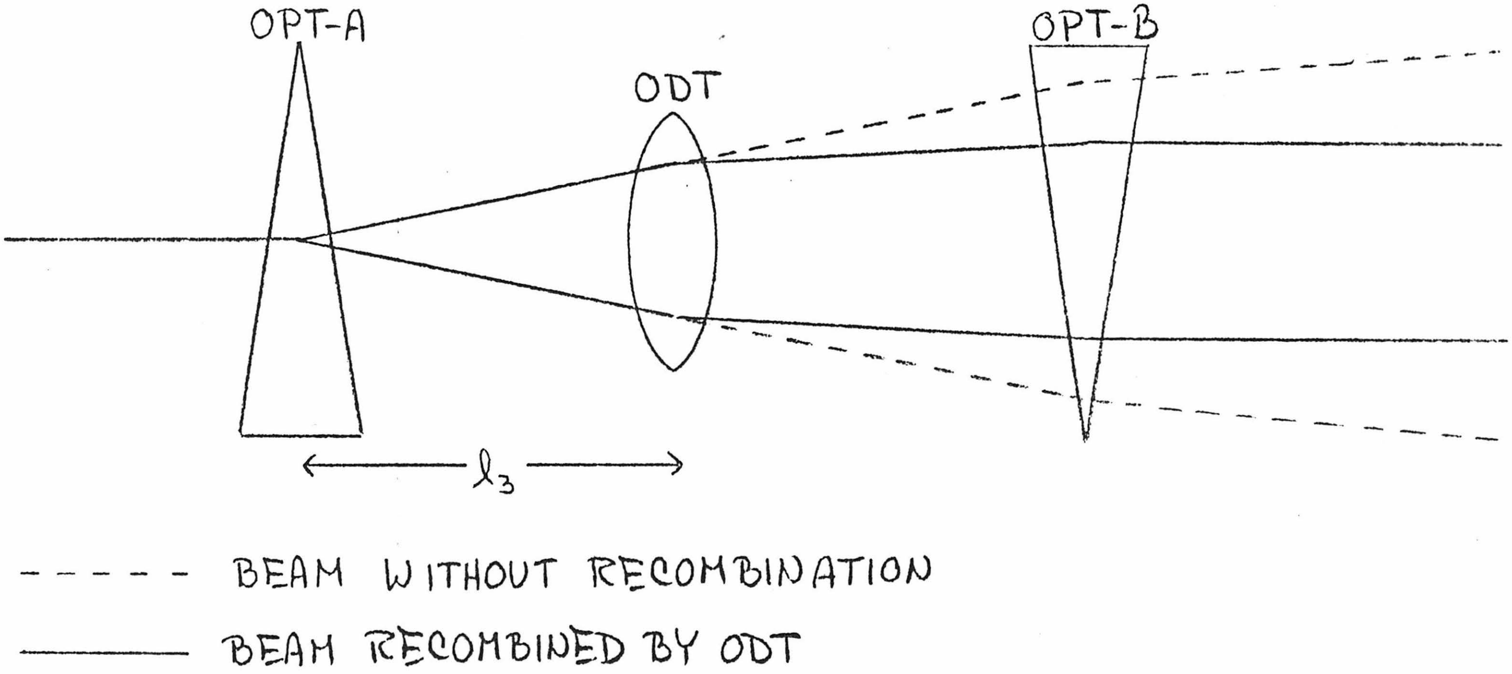

FIG. 2.4 MOMENTUM RECOMBINTION BY ODT

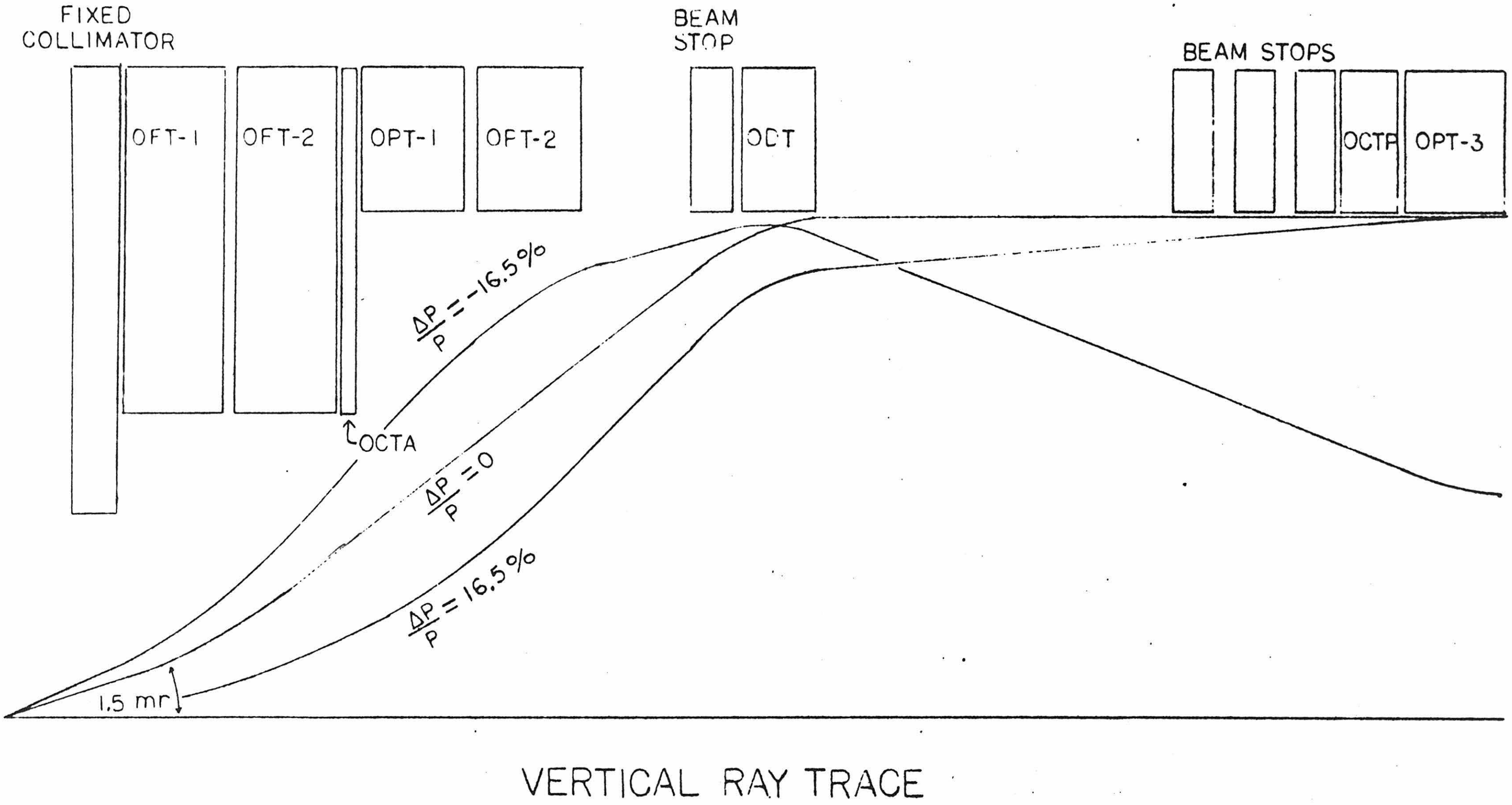

Figure 2.5 Vertical ray trace of hadron beam

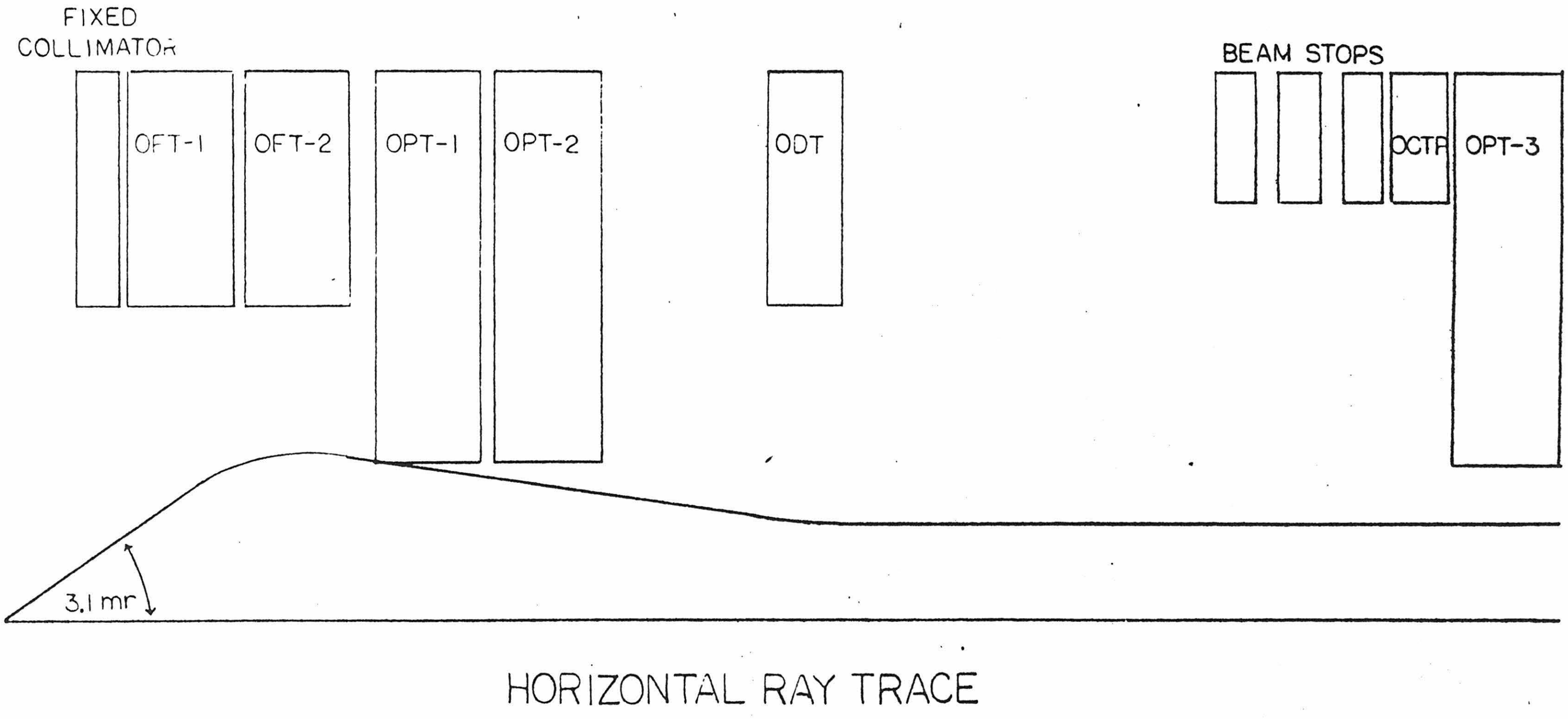

Figure 2.6 Horizontal ray trace of hadron beam.

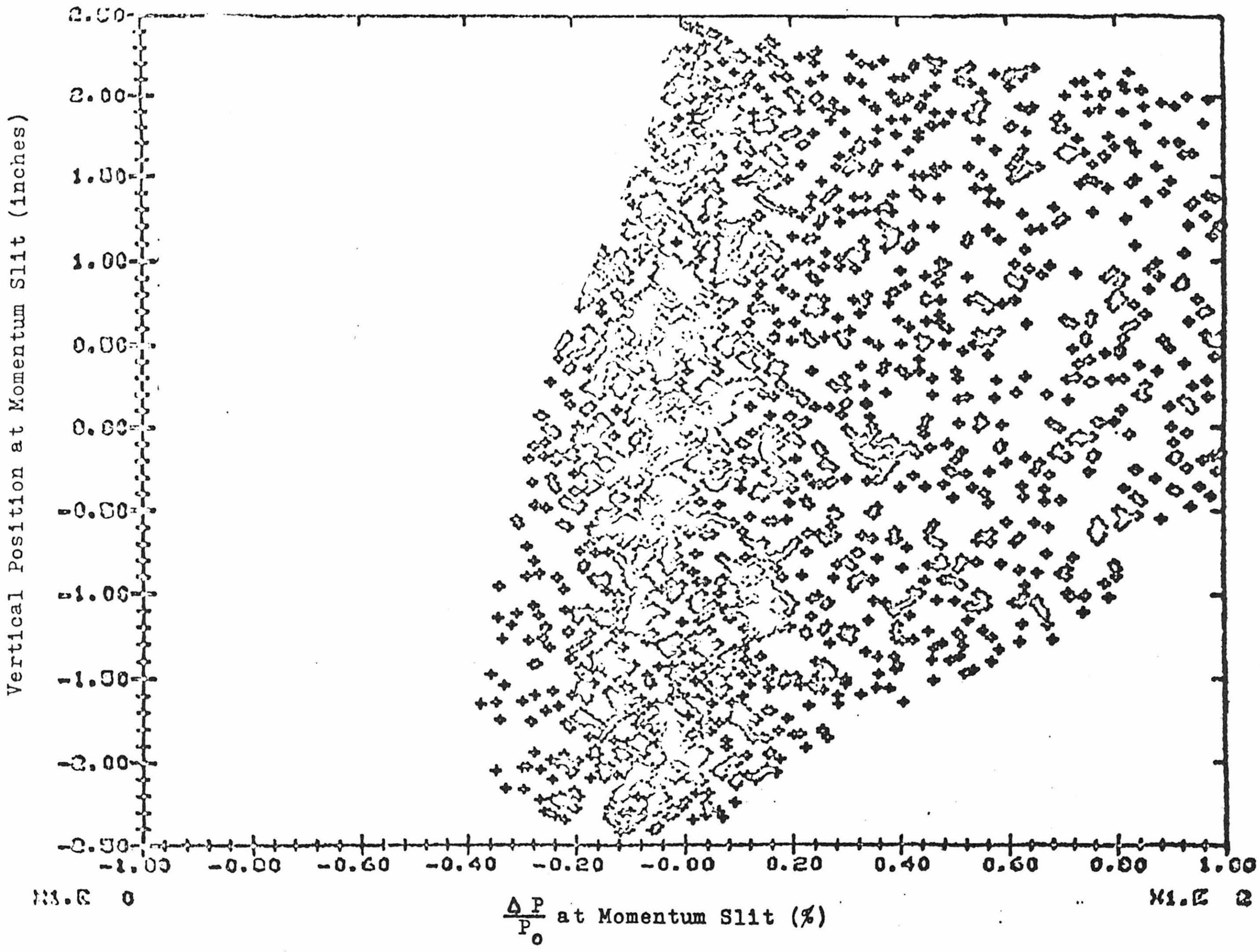

Figure 2.7 Momentum versus position at Momentum Slit

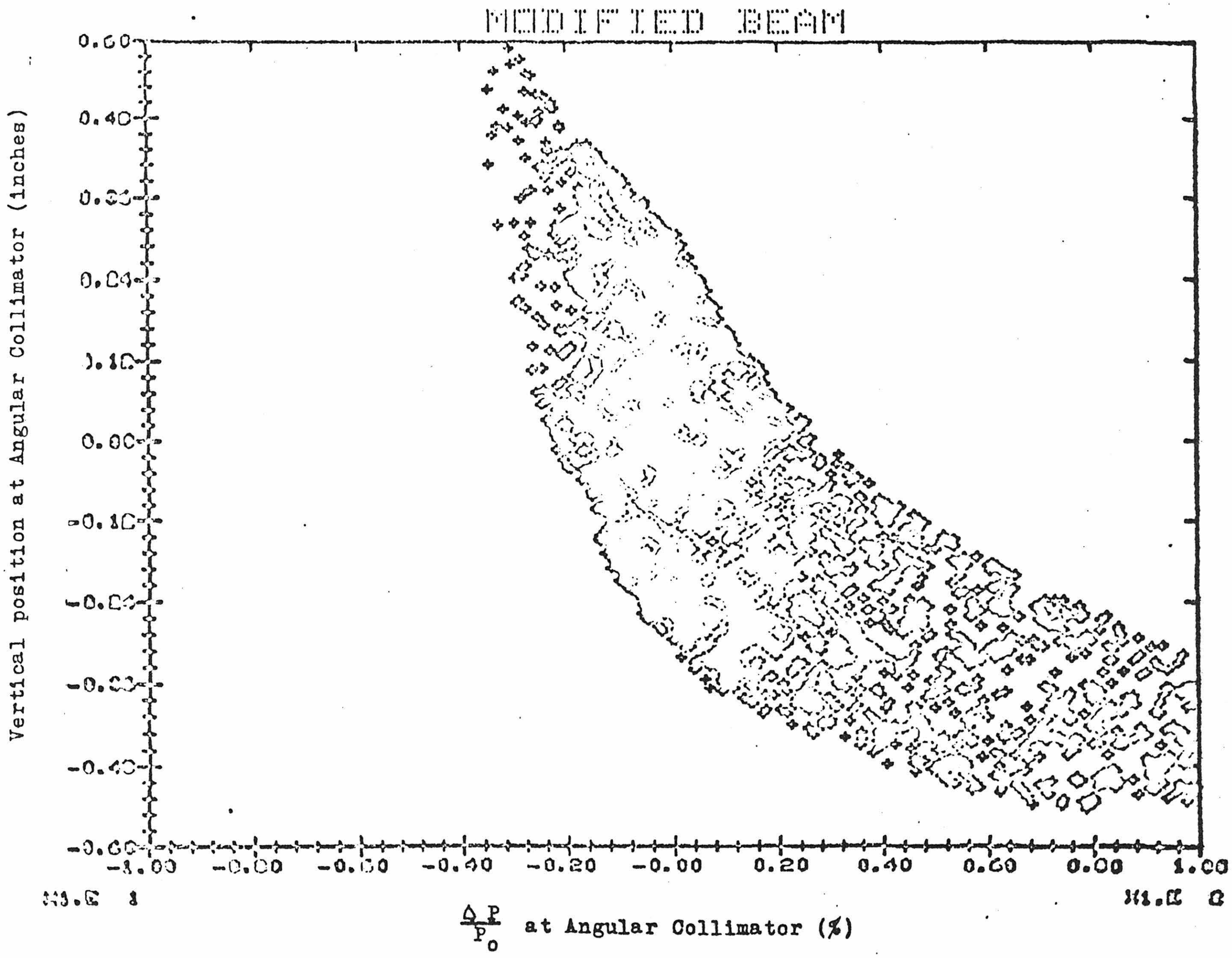

Figure 2.8 Momentum versus position at Angular Collimator

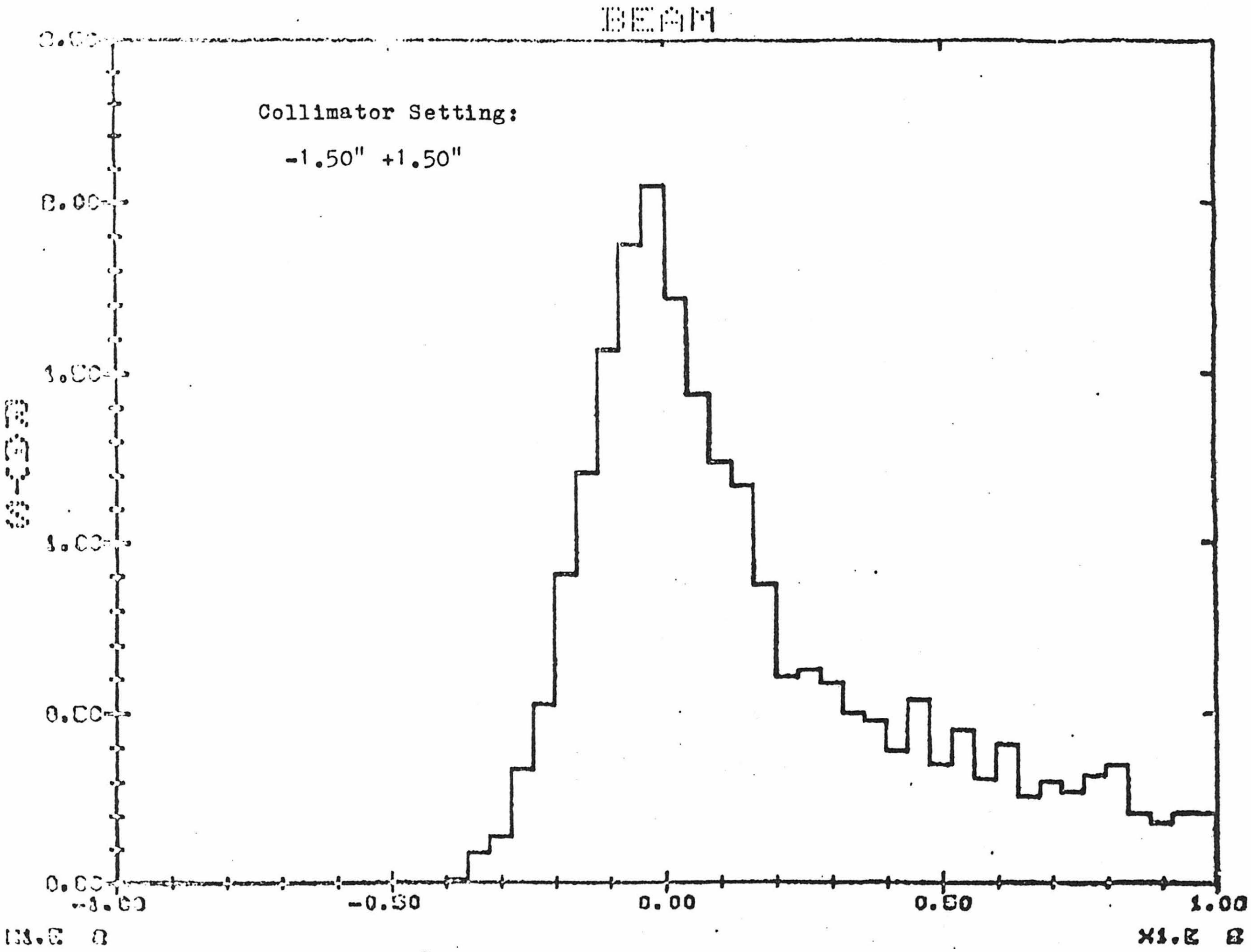

Figure 2.9 Momentum distribution with OCTAB = -1.50"

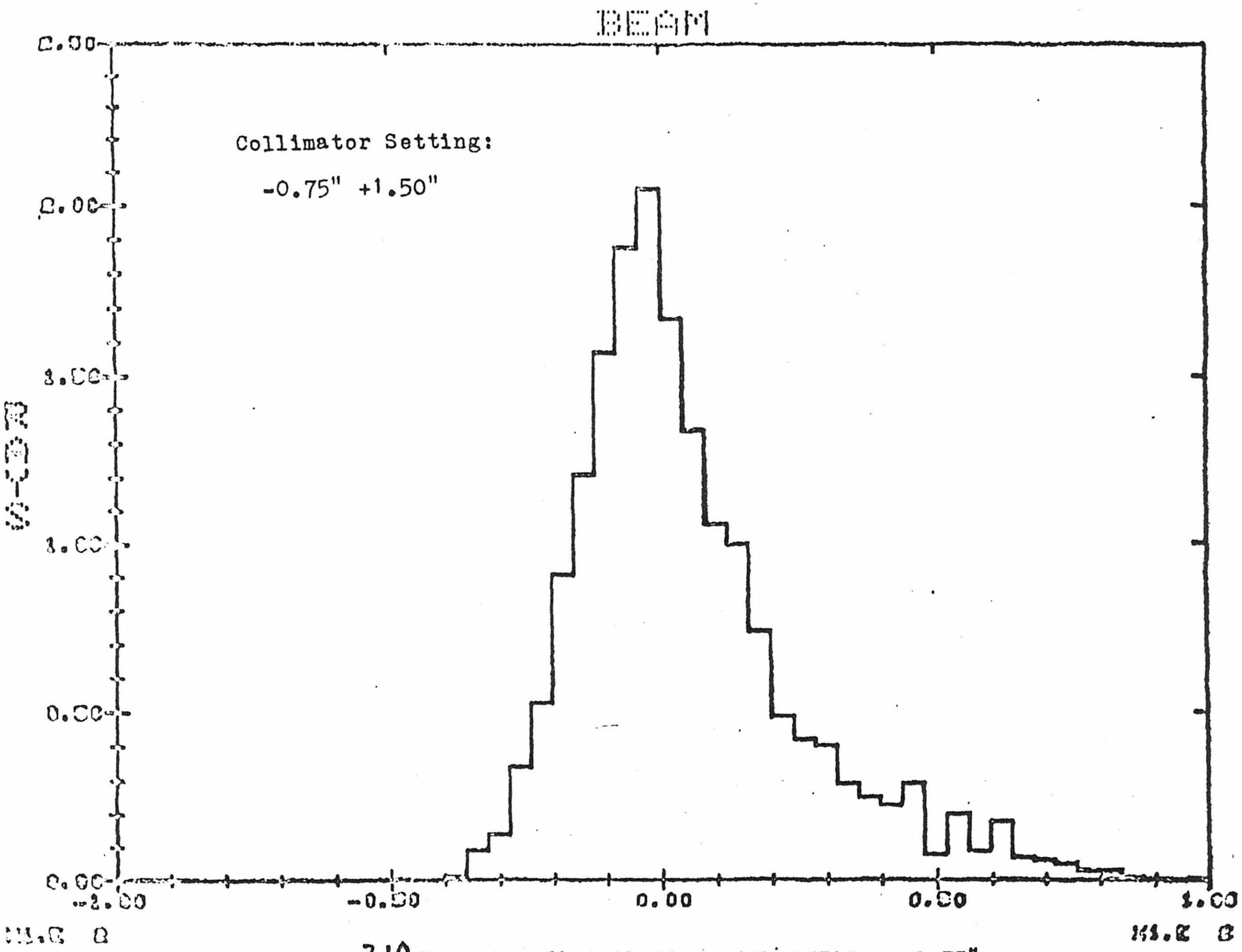

Collimator Setting:
-0.75" +1.50"

Figure 2.10 Momentum distribution with OCTAB = -0.75"

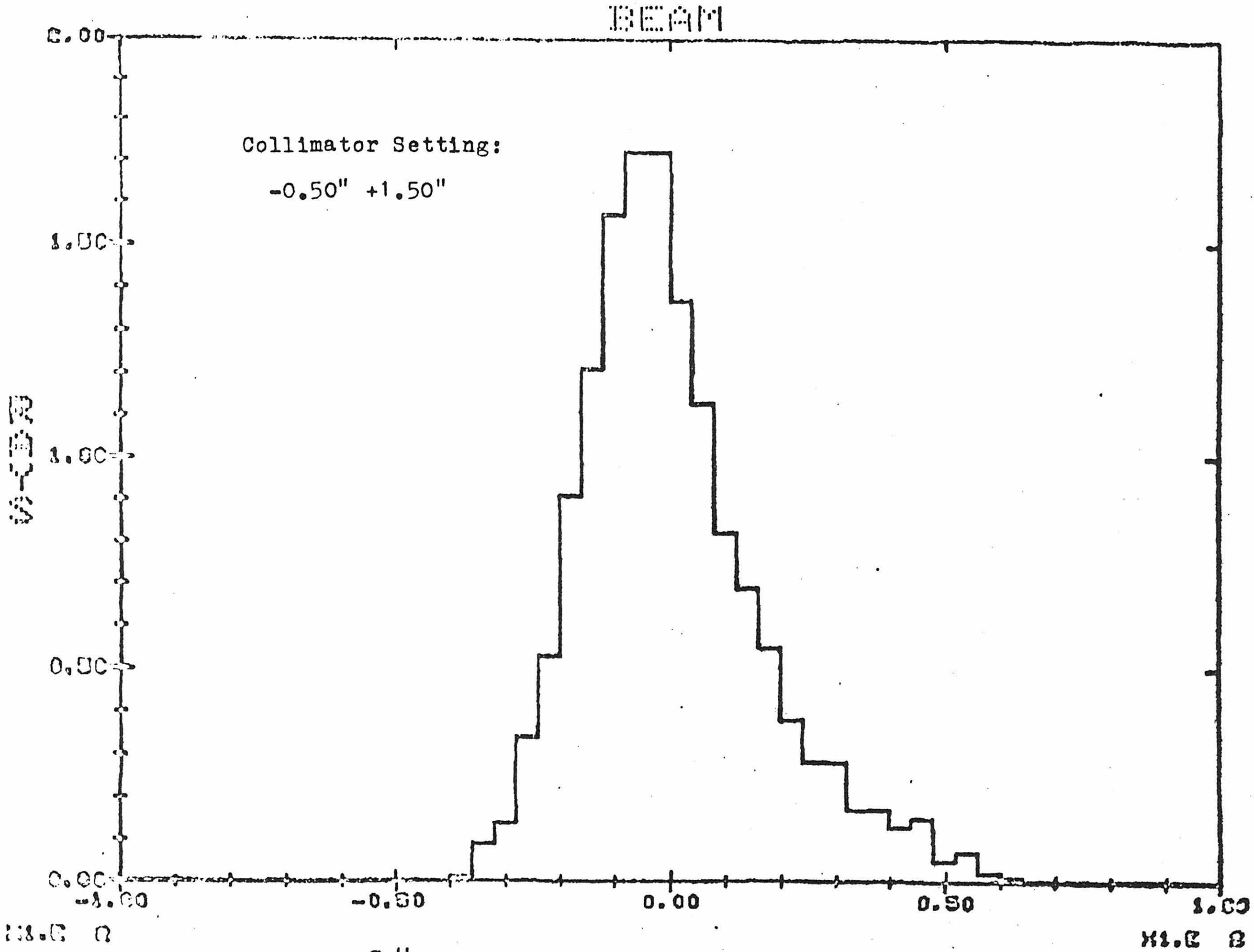

Figure 2.11 Momentum distribution with OCTAB = -0.50"

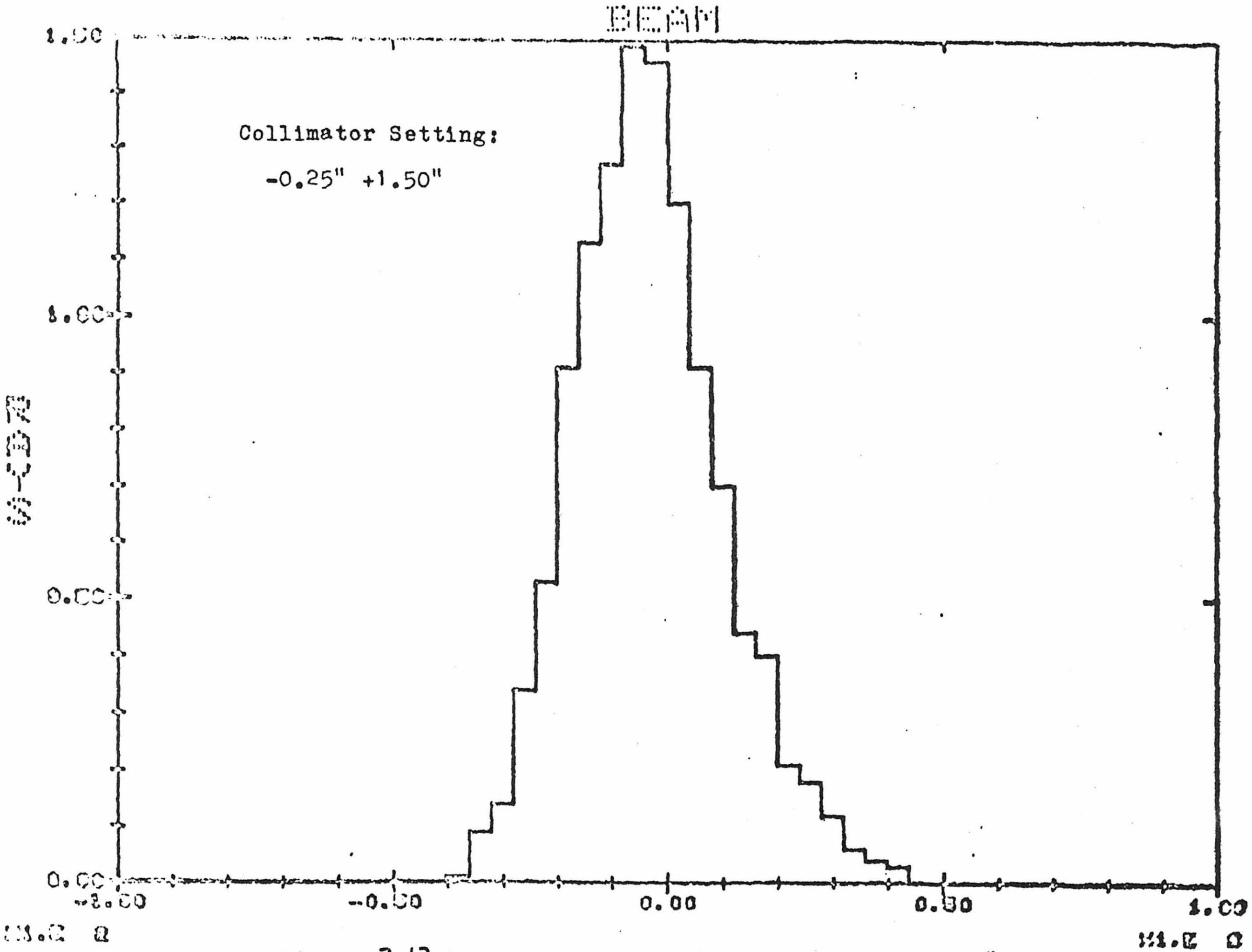

Collimator Setting:
-0.25" +1.50"

Figure 2.12 Momentum distribution with OCTAB = 0.25"

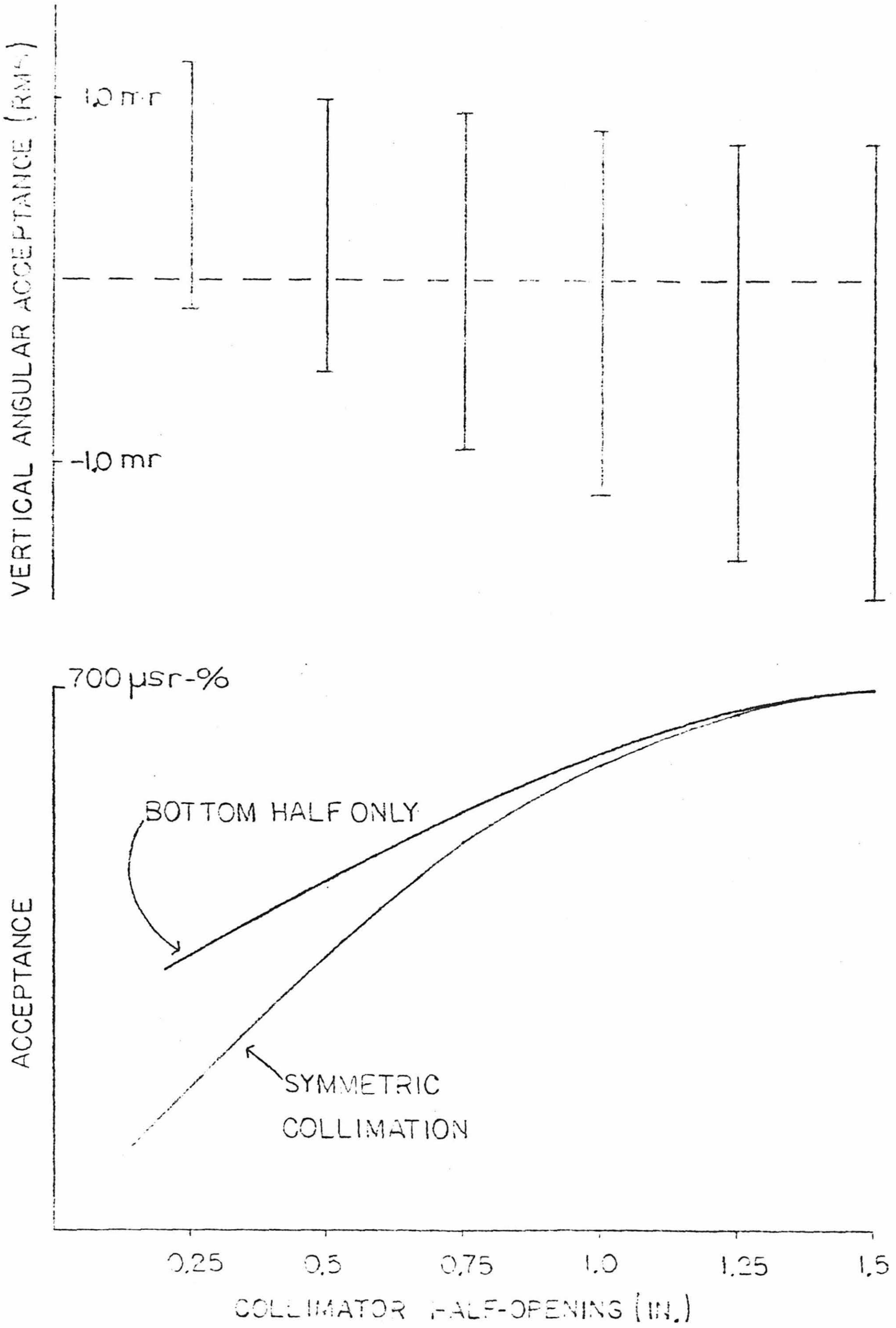

Figure 2.13 Acceptance versus Collimator Opening

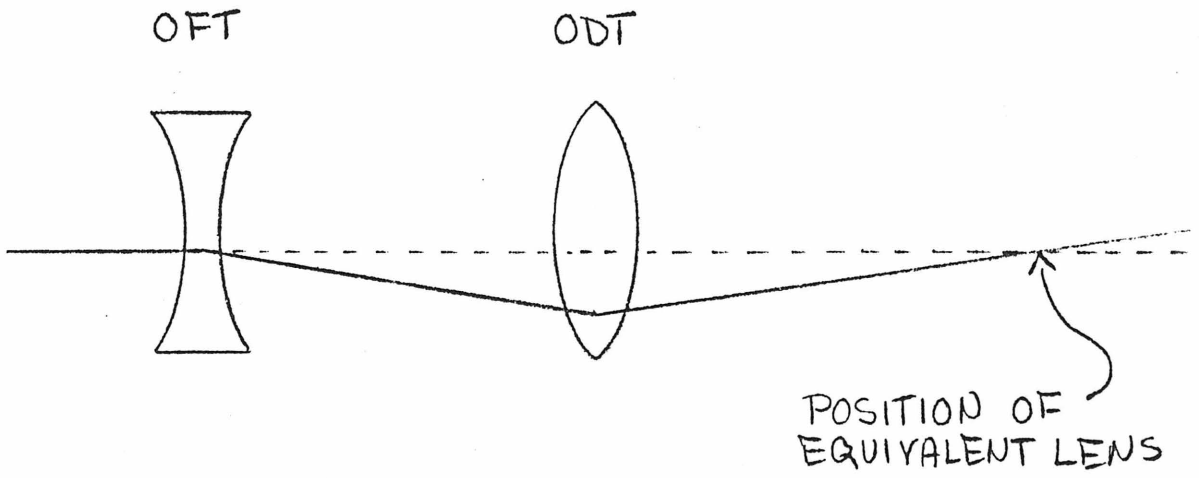

FIG 2.14 POSITION OF EQUIVALENT LENS FOR VERTICAL FOCUSING

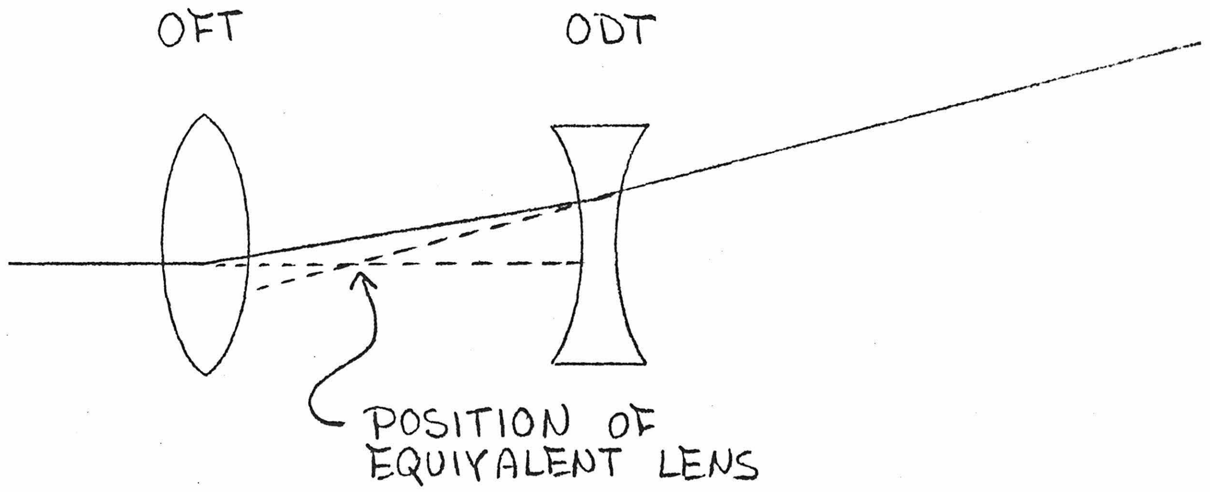

FIG 2.15 POSITION OF EQUIVALENT LENS FOR HORIZONTAL FOCUSING

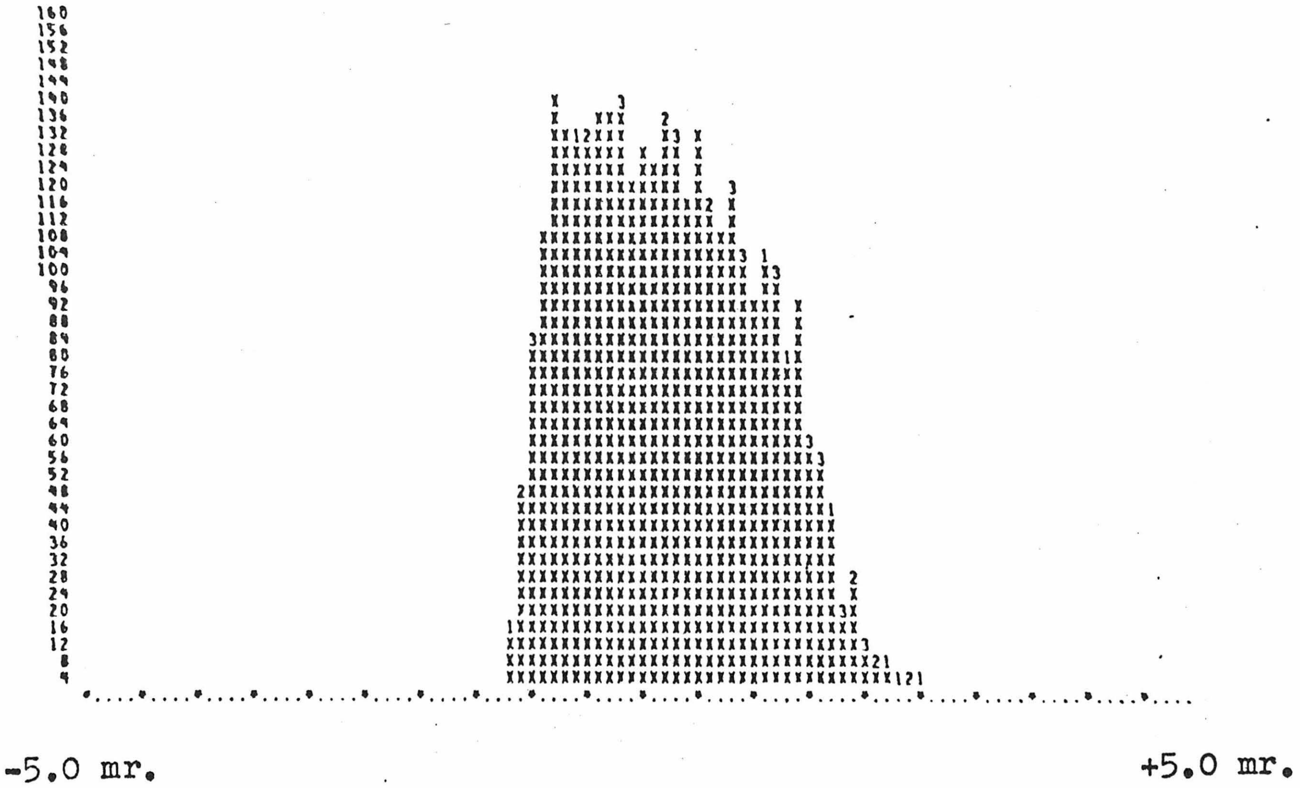

Figure 2.16 Vertical angular acceptance of this beam

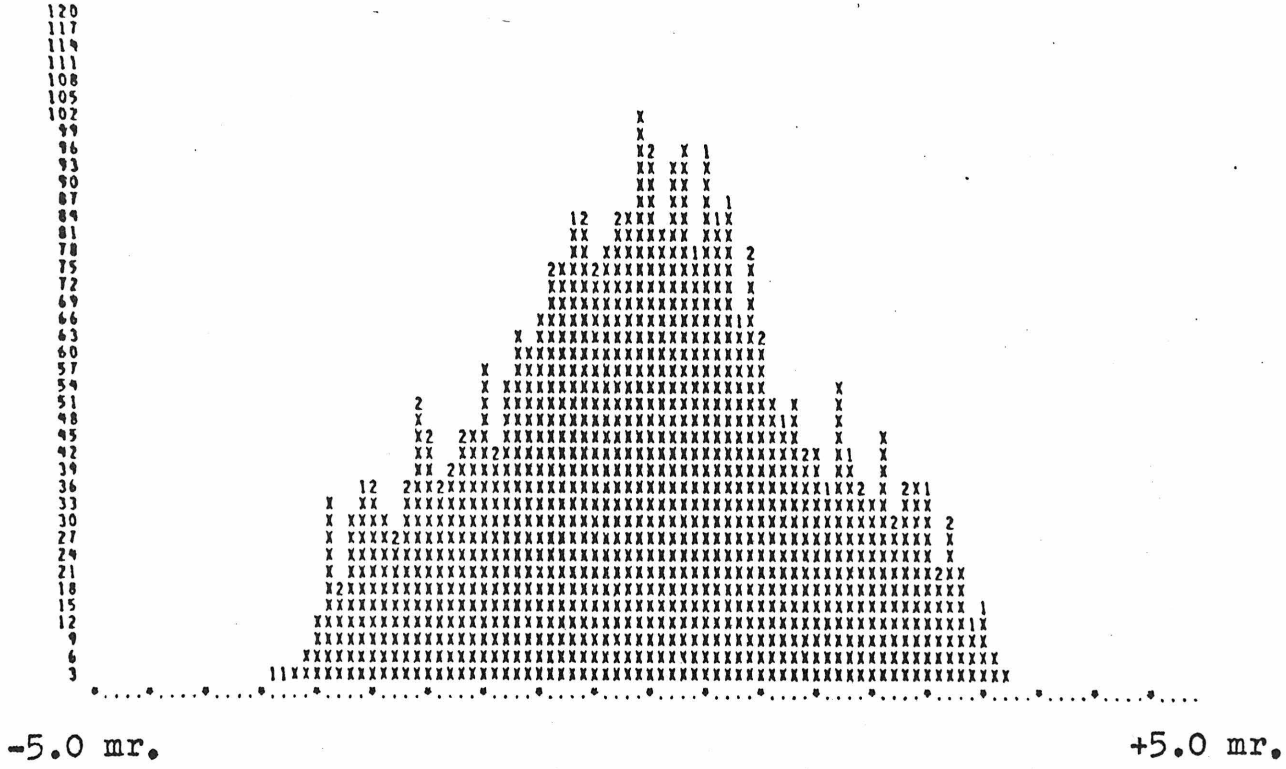

Figure 2.17 Horizontal angular acceptance of this beam

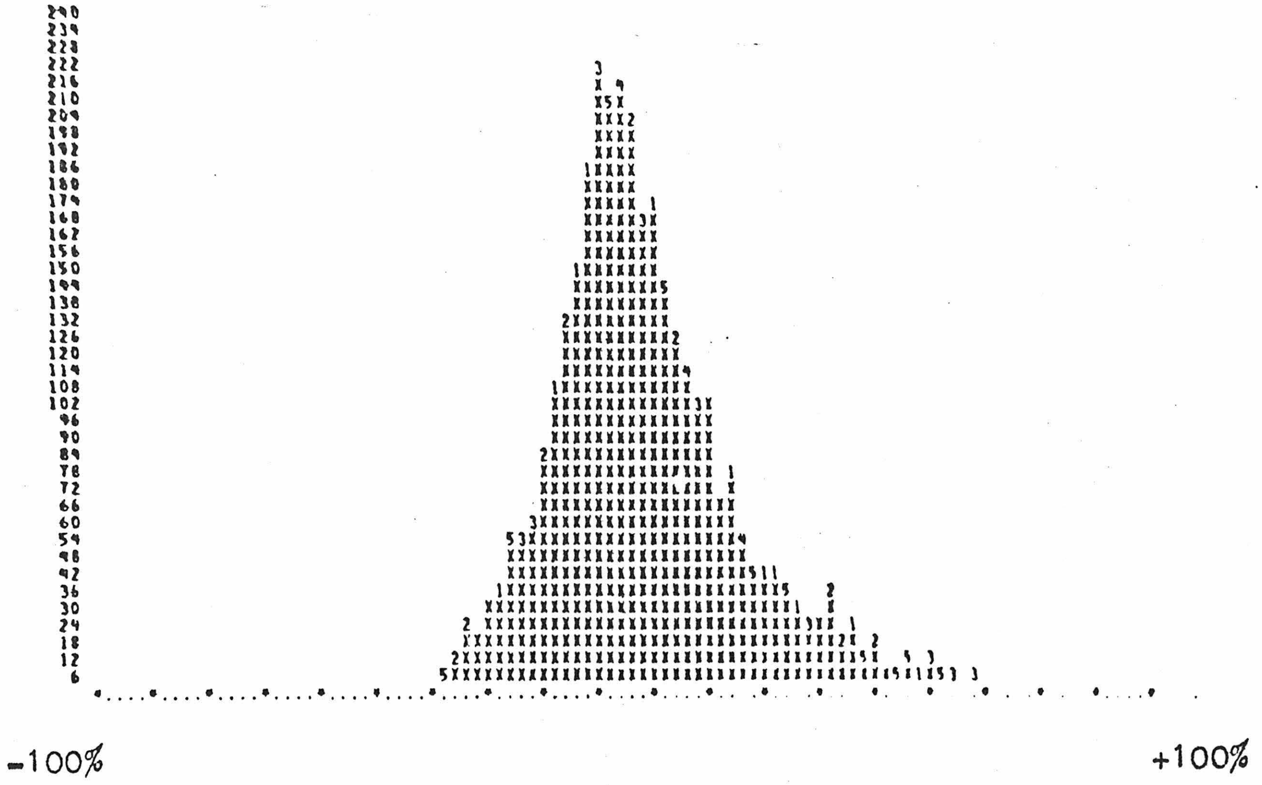

Figure 2.18 Momentum acceptance of this beam

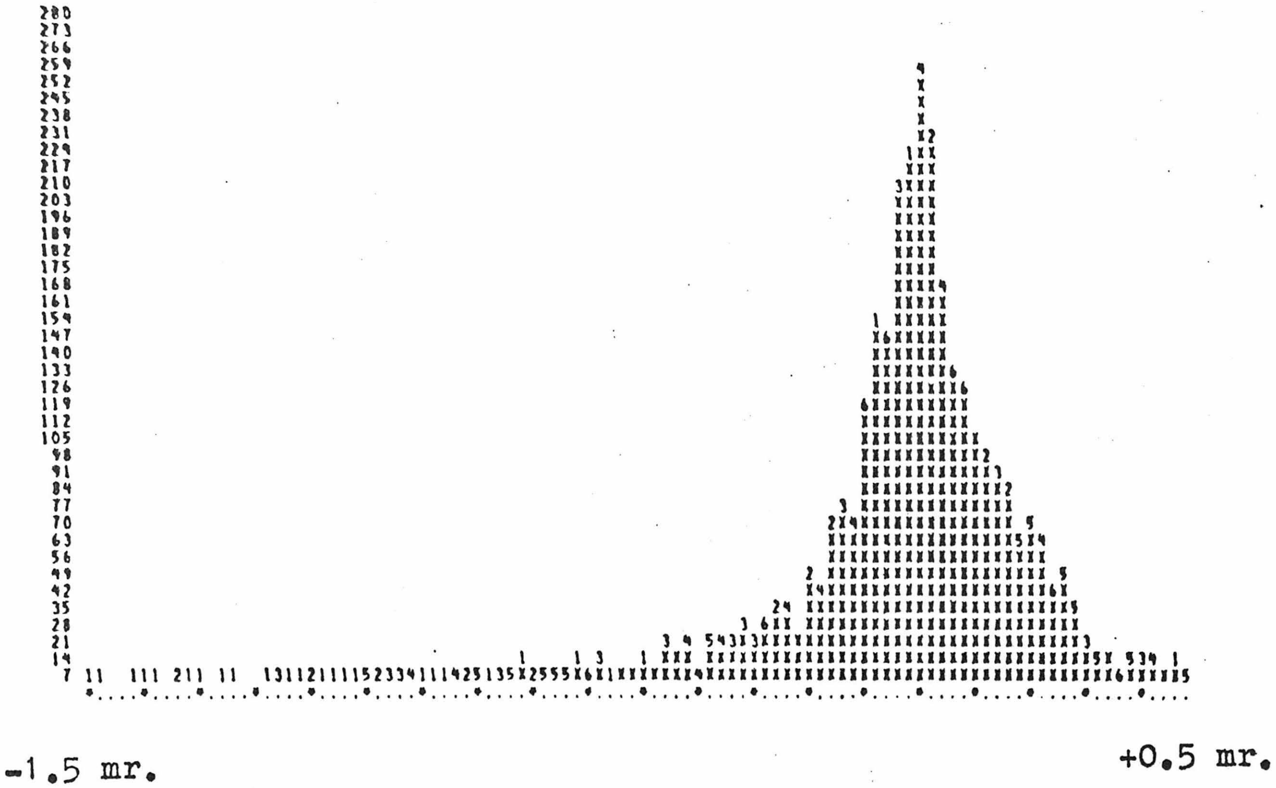

Figure 2.19 Vertical angular distribution at Cerenkov counter

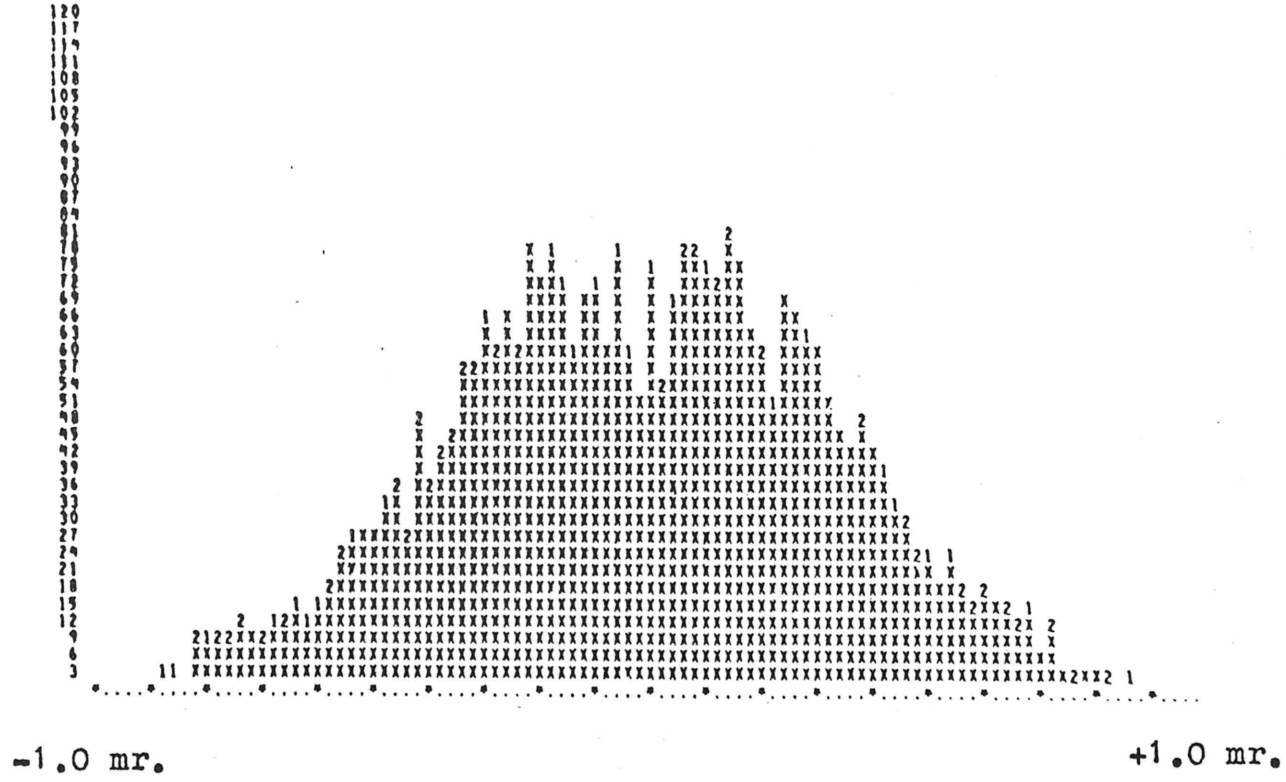

Figure 2.20 Horizontal angular distribution at Cerenkov counter

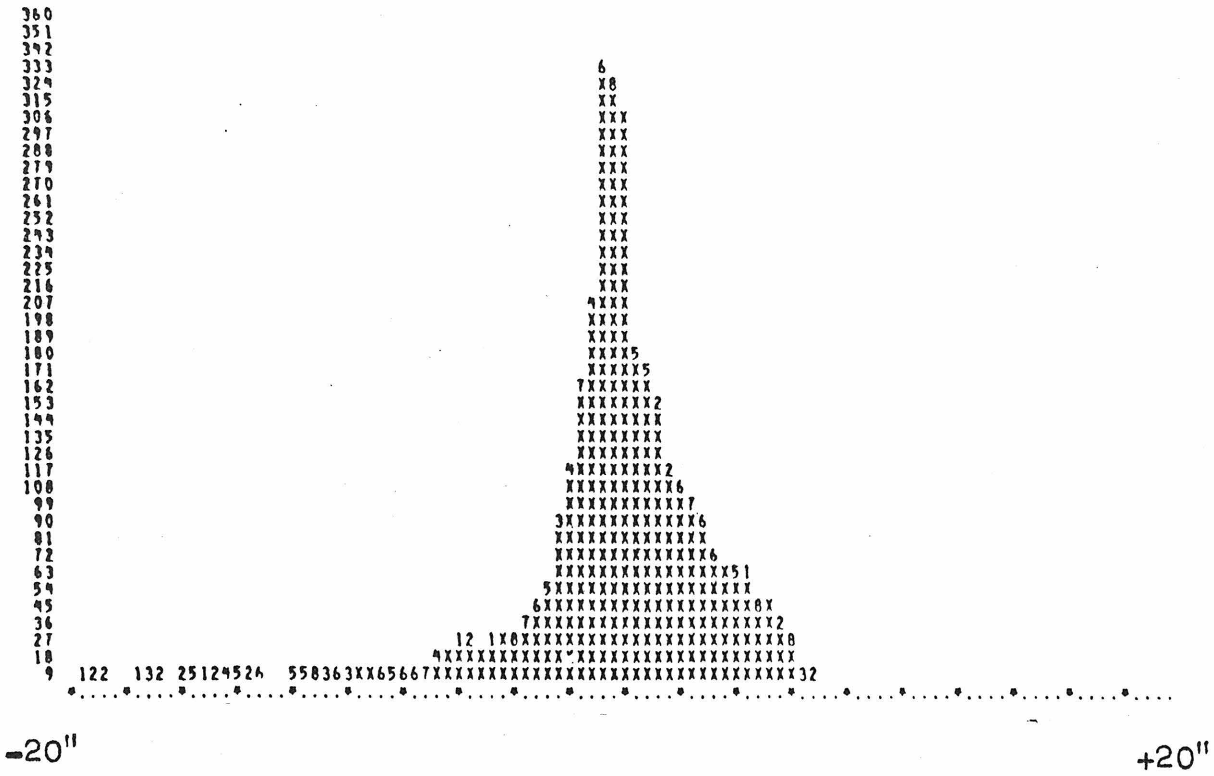

Figure 2.21 Vertical position distribution at Cerenkov counter

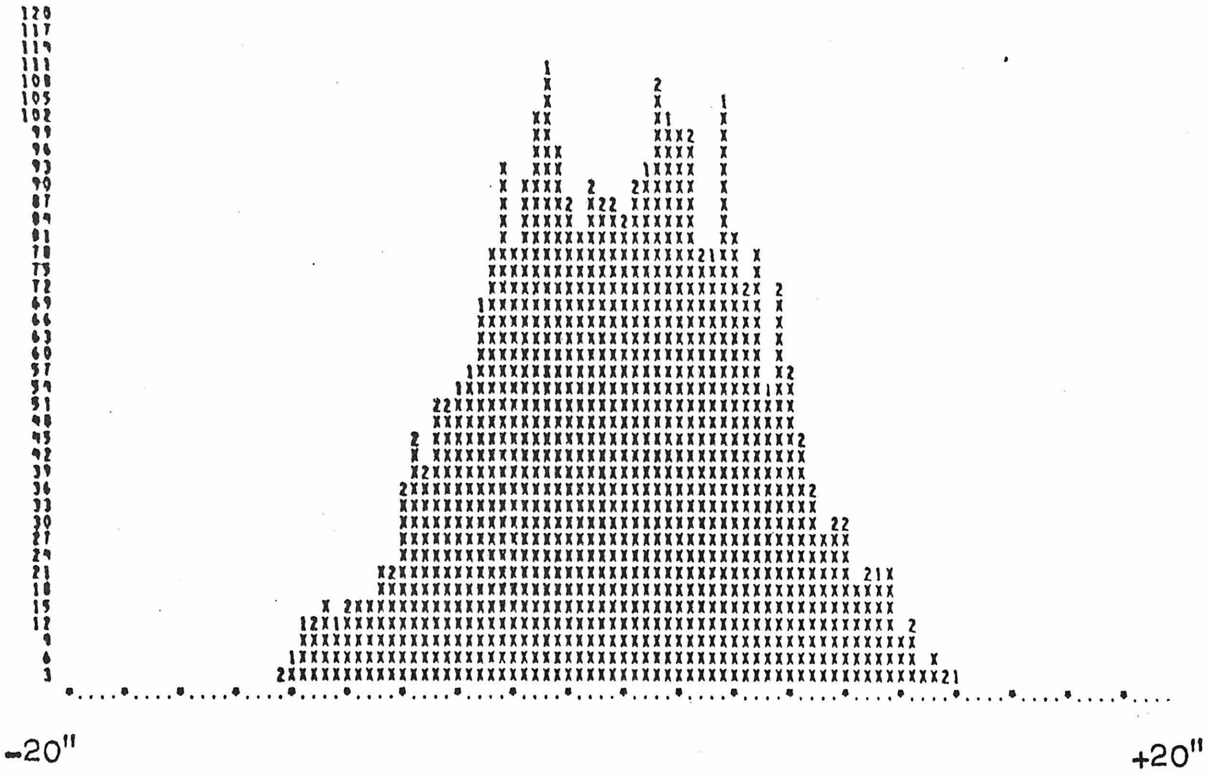

Figure 2.22 Horizontal position distribution at Cerenkov counter

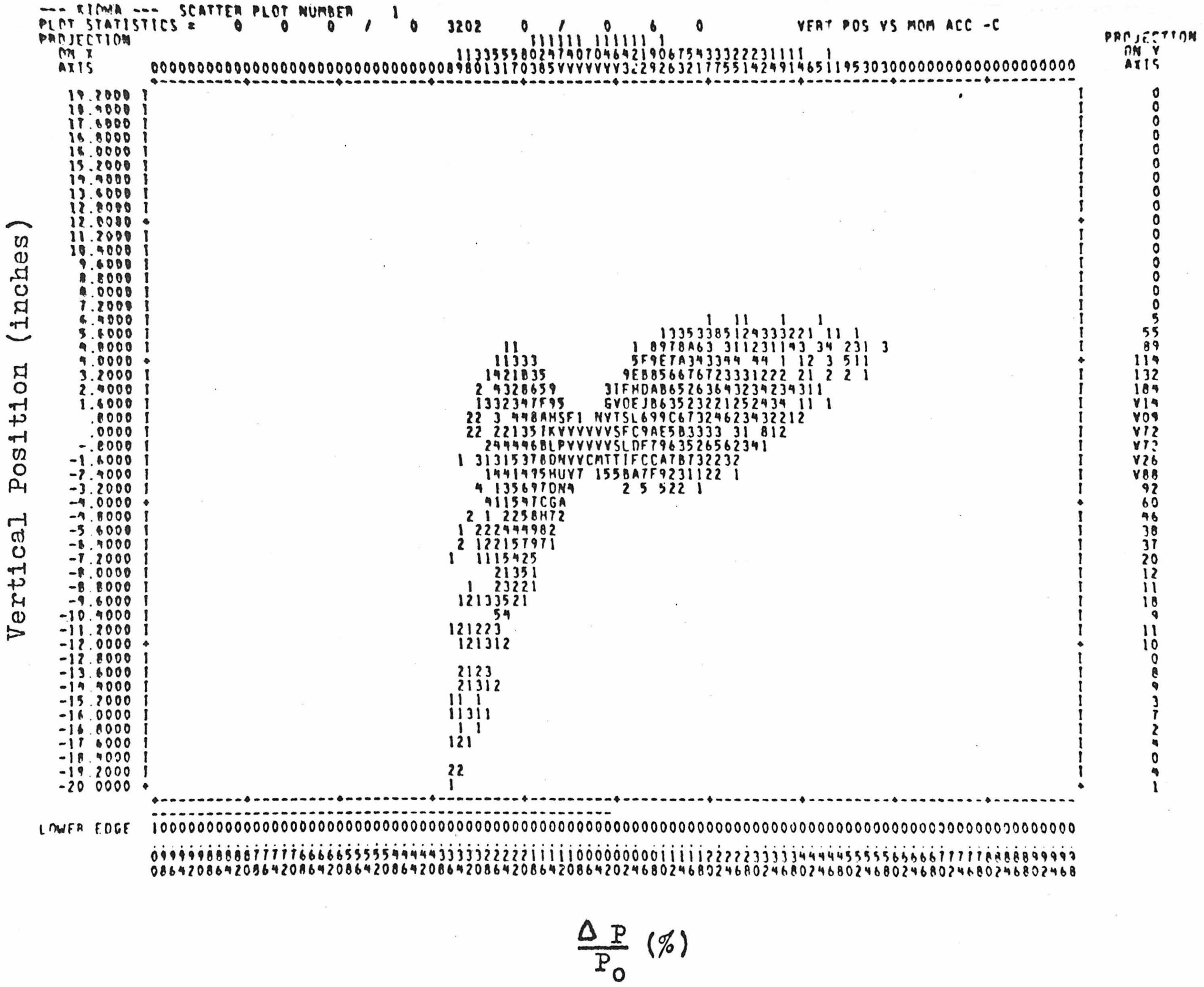

Figure 2.23 Vertical position versus momentum at Cerenkov counter

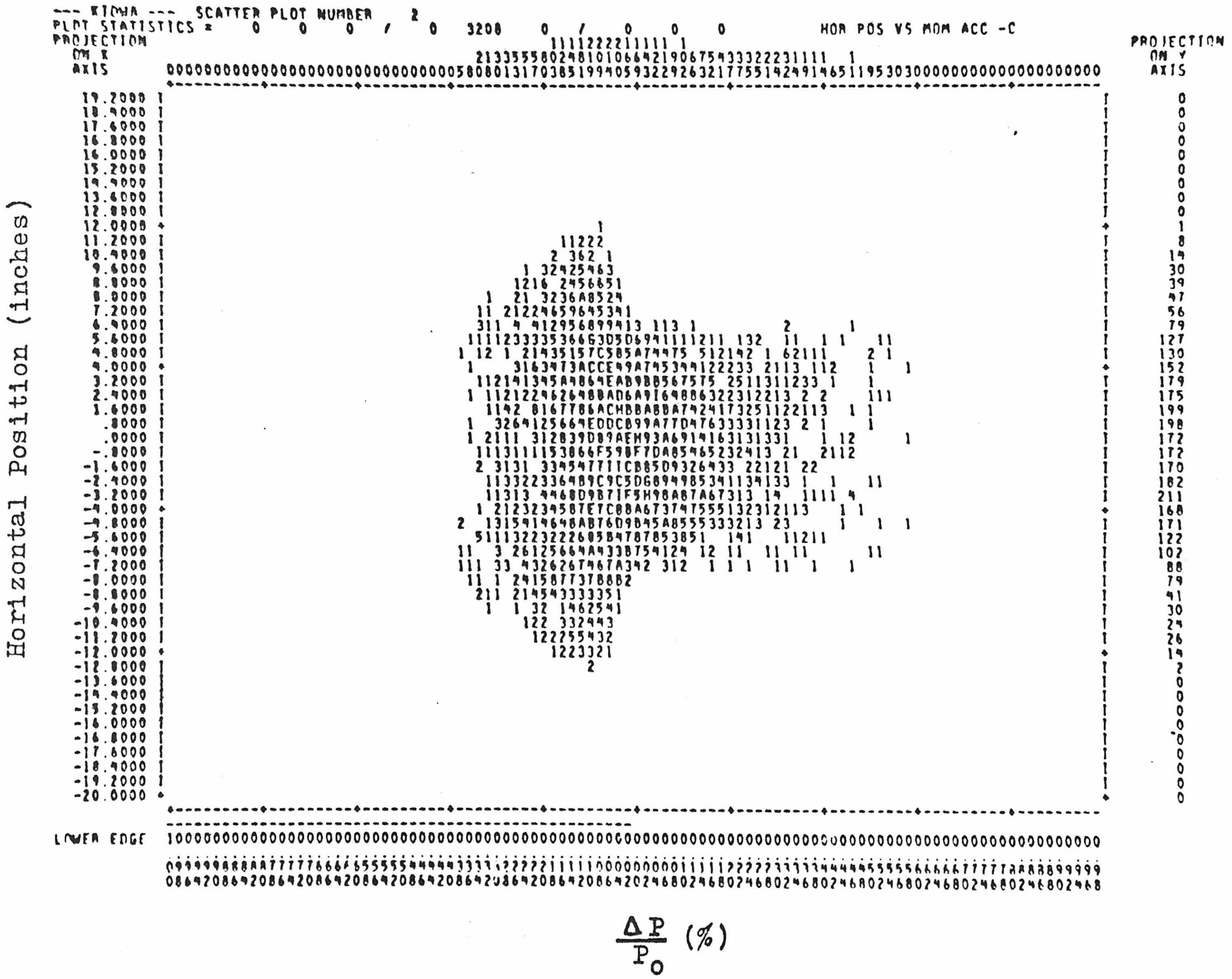

Figure 2.24 Horizontal position versus momentum at Cerenkov counter

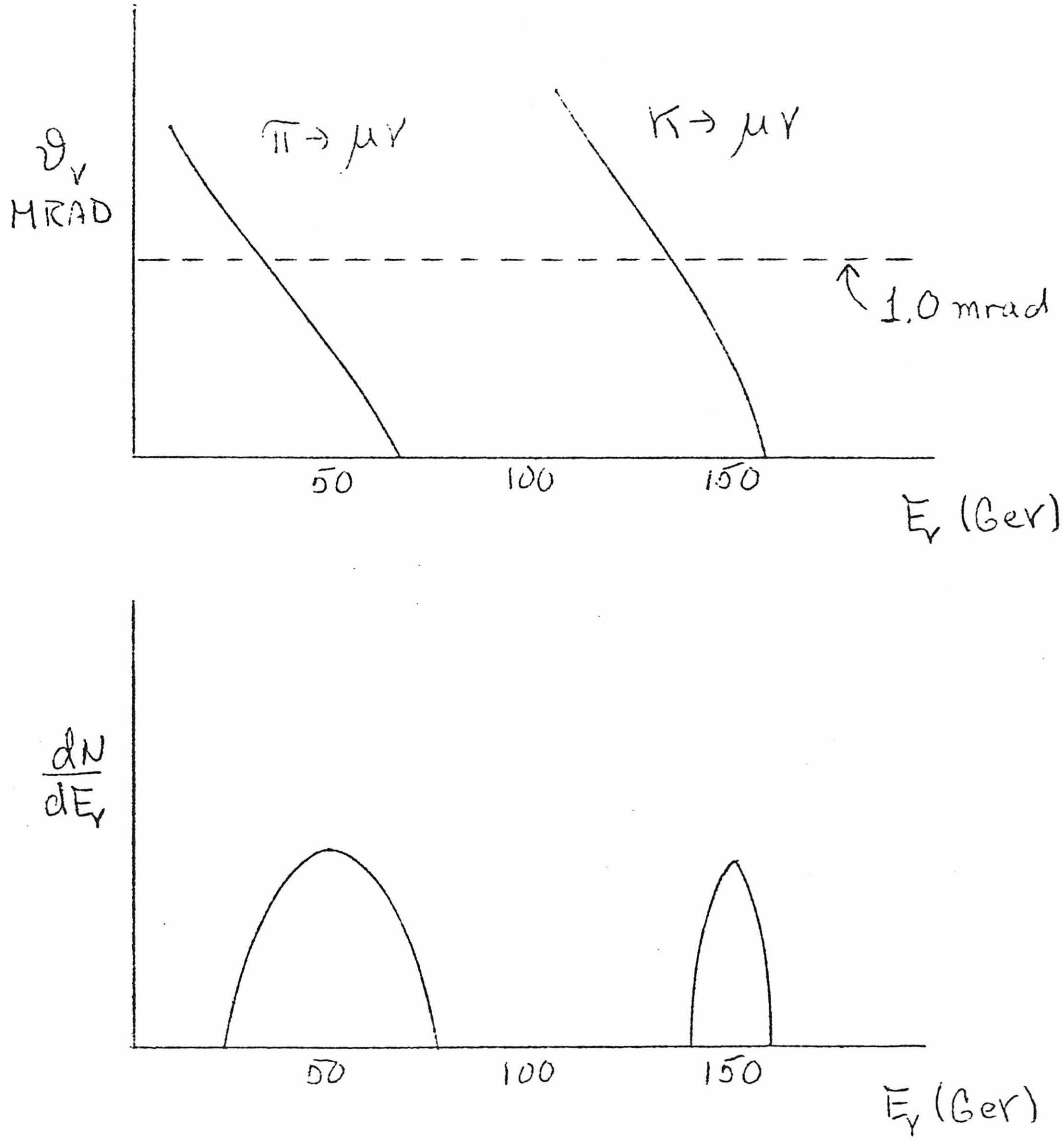

FIG 2.25 GEOMETRIC DETERMINATION OF DICHROMATIC NEUTRINO BEAM

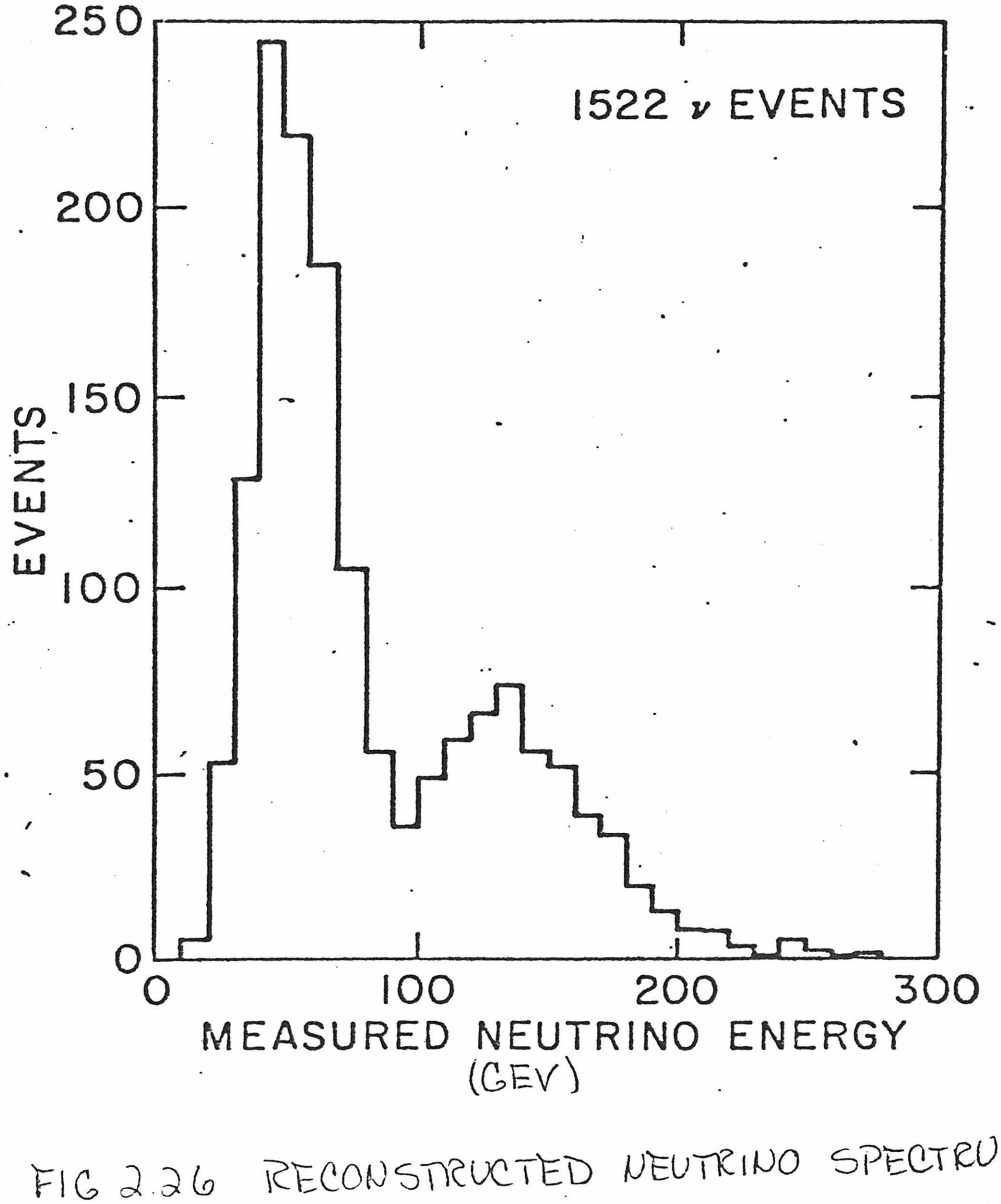

FIG 2.26 RECONSTRUCTED NEUTRINO SPECTRUM

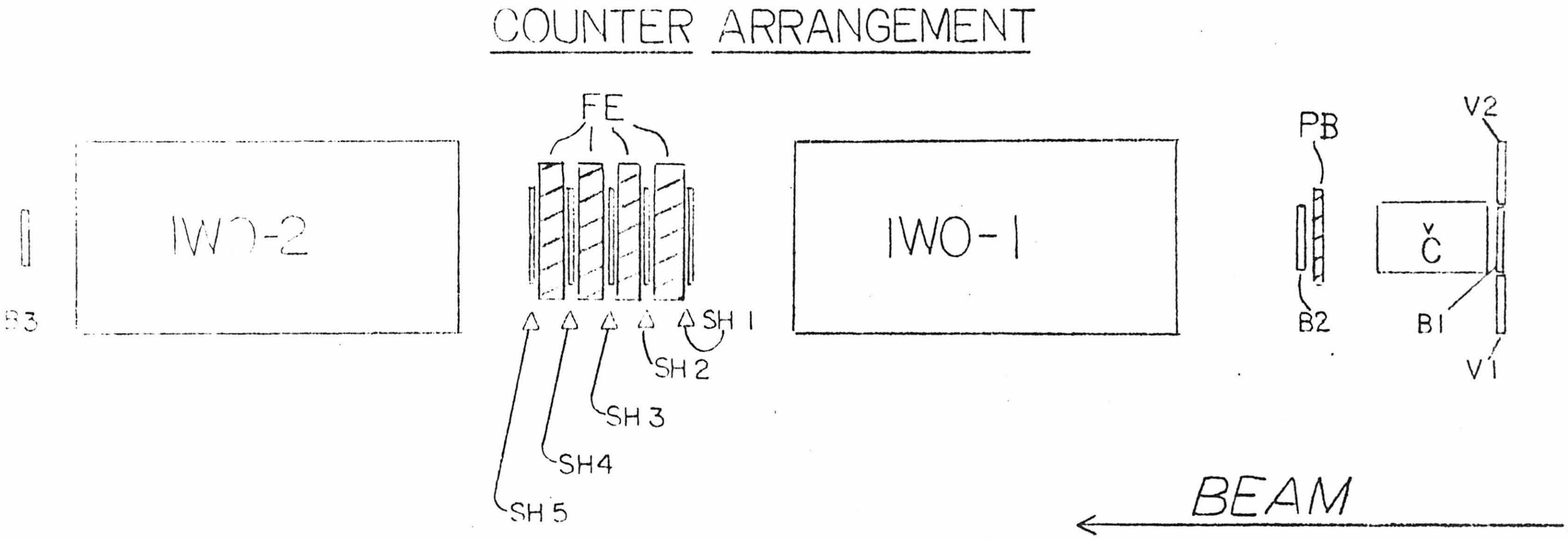

Figure 3.1 Counter arrangement

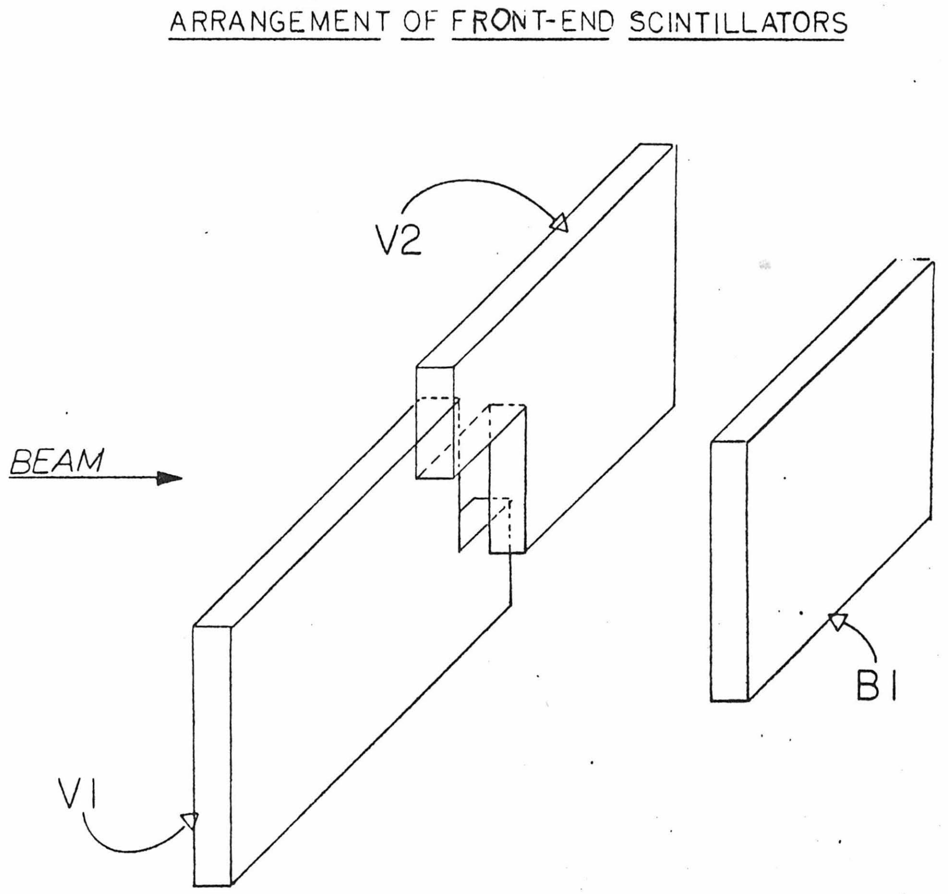

Figure 3.2 Arrangement of front-end scintillators

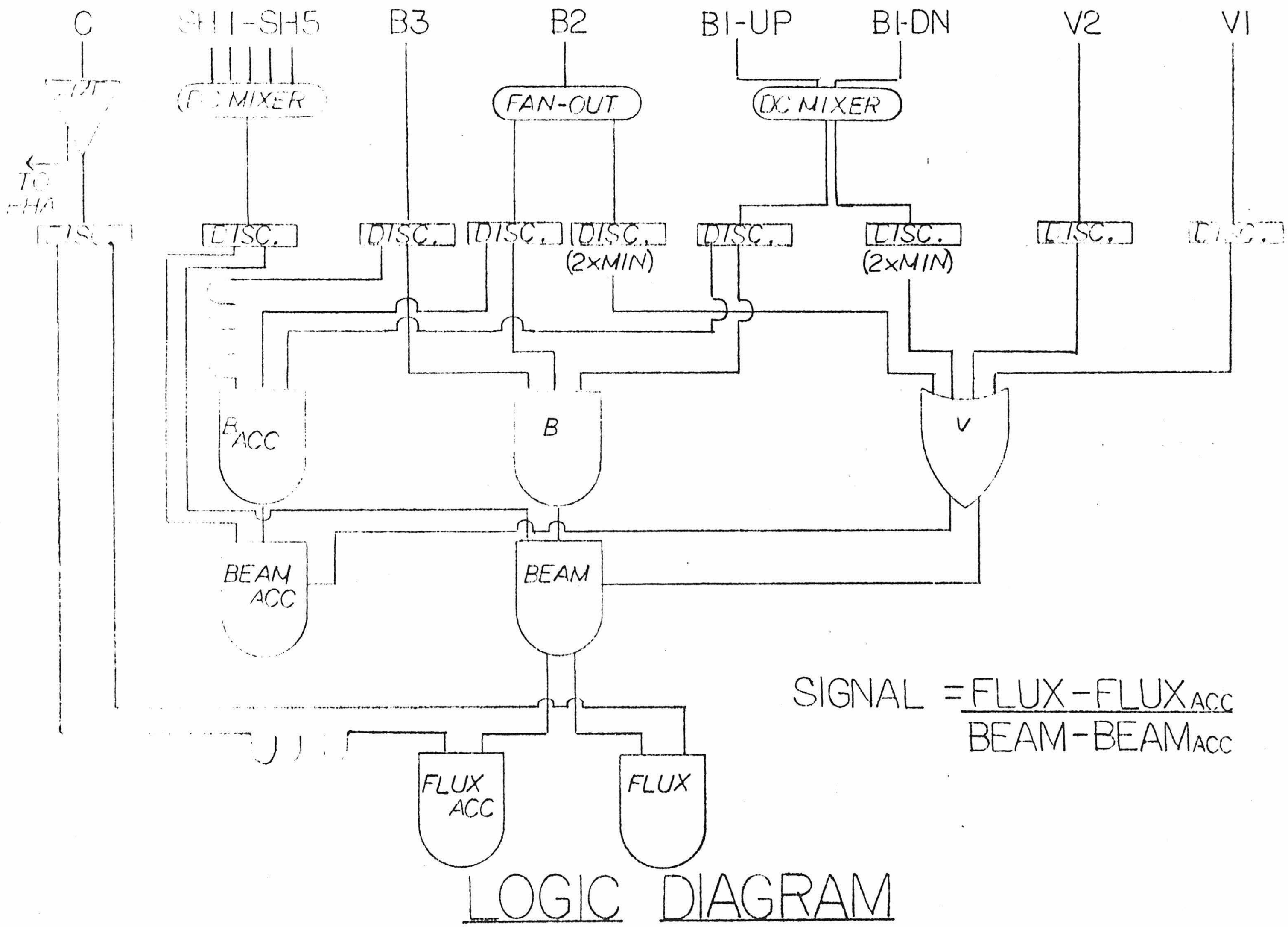

Figure 3.3 Logic diagram

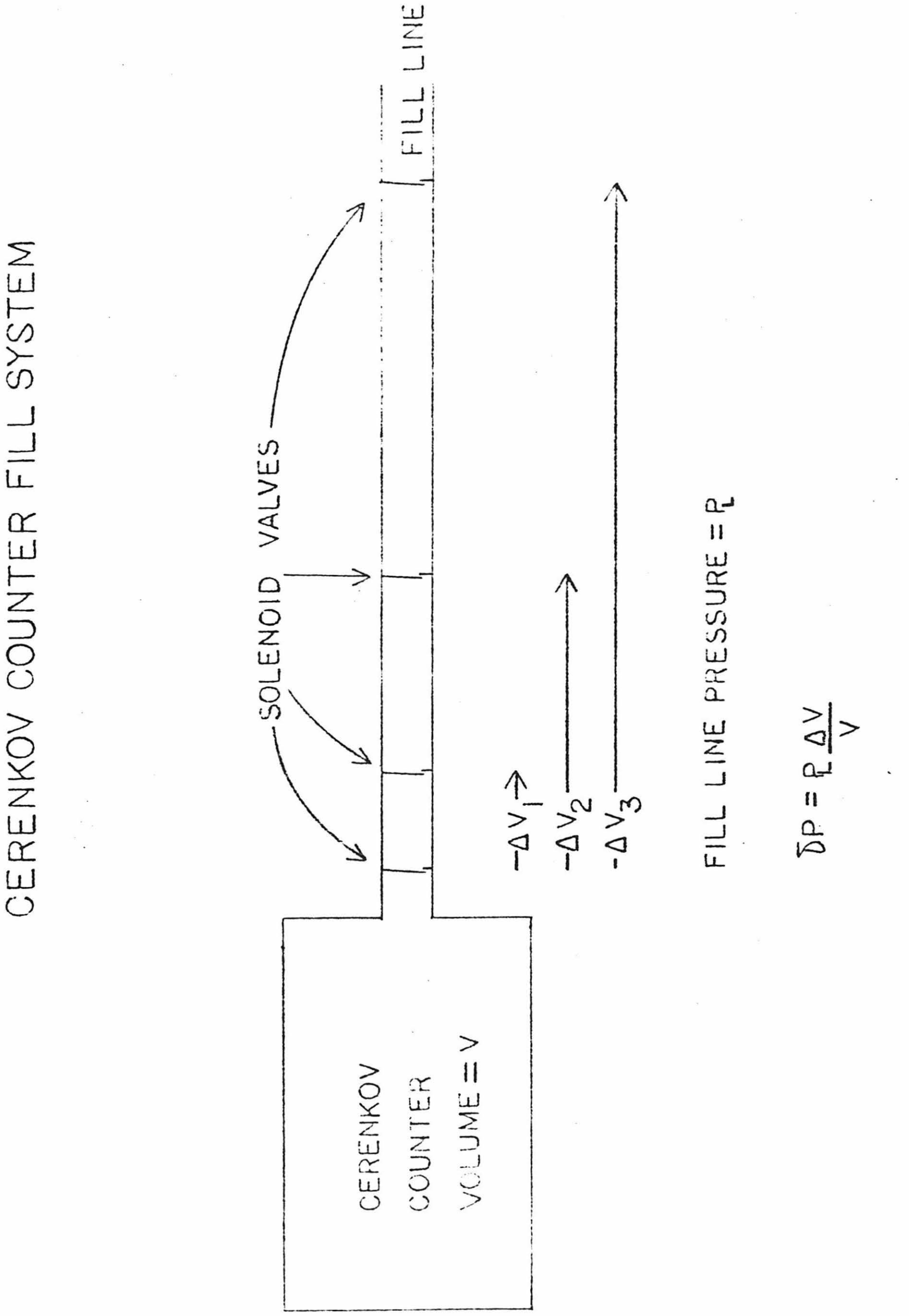

Figure 3.4 Cerenkov counter fill system

CERENKOV COUNTER OPTICS

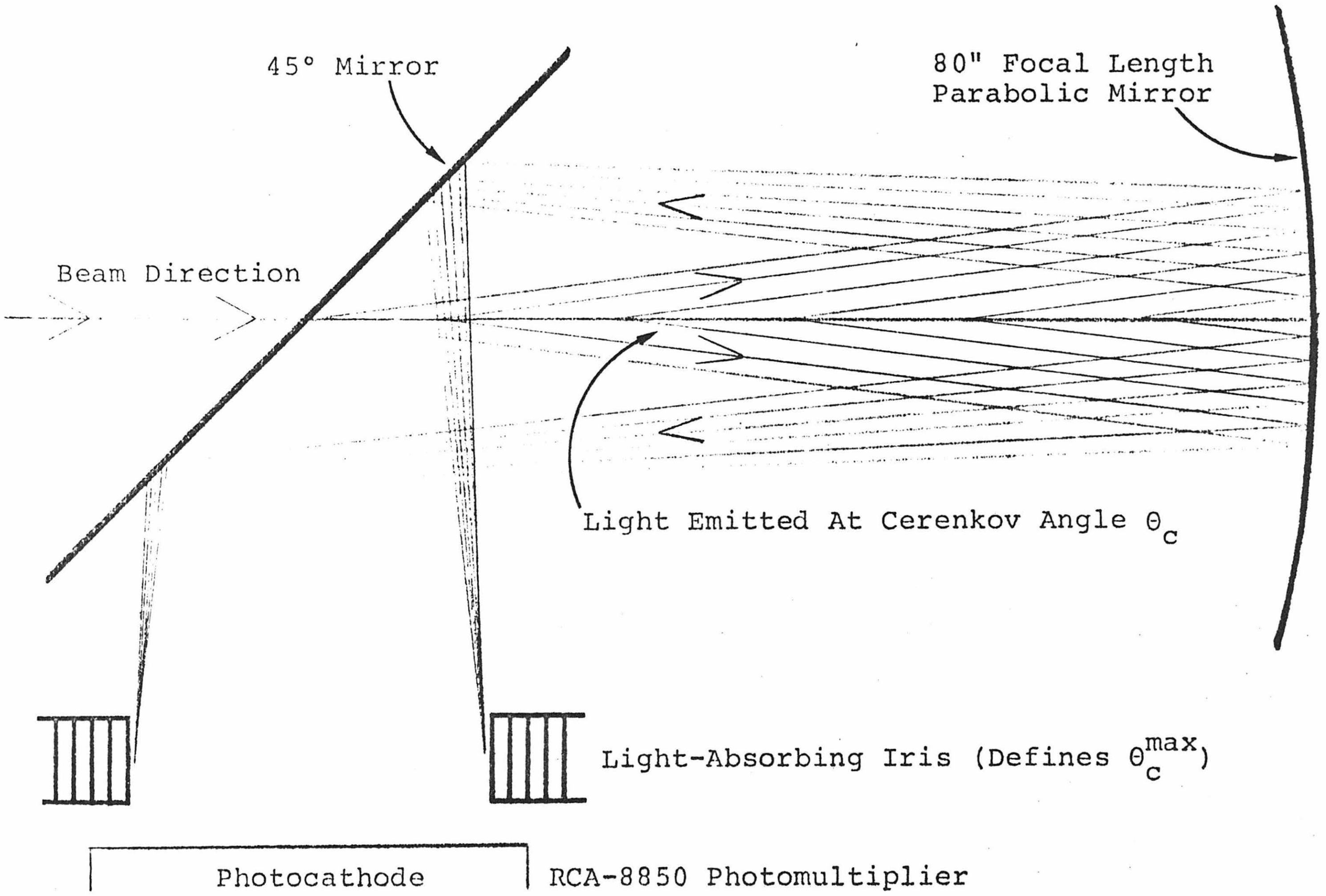

Figure 4.1 Cerenkov counter optics

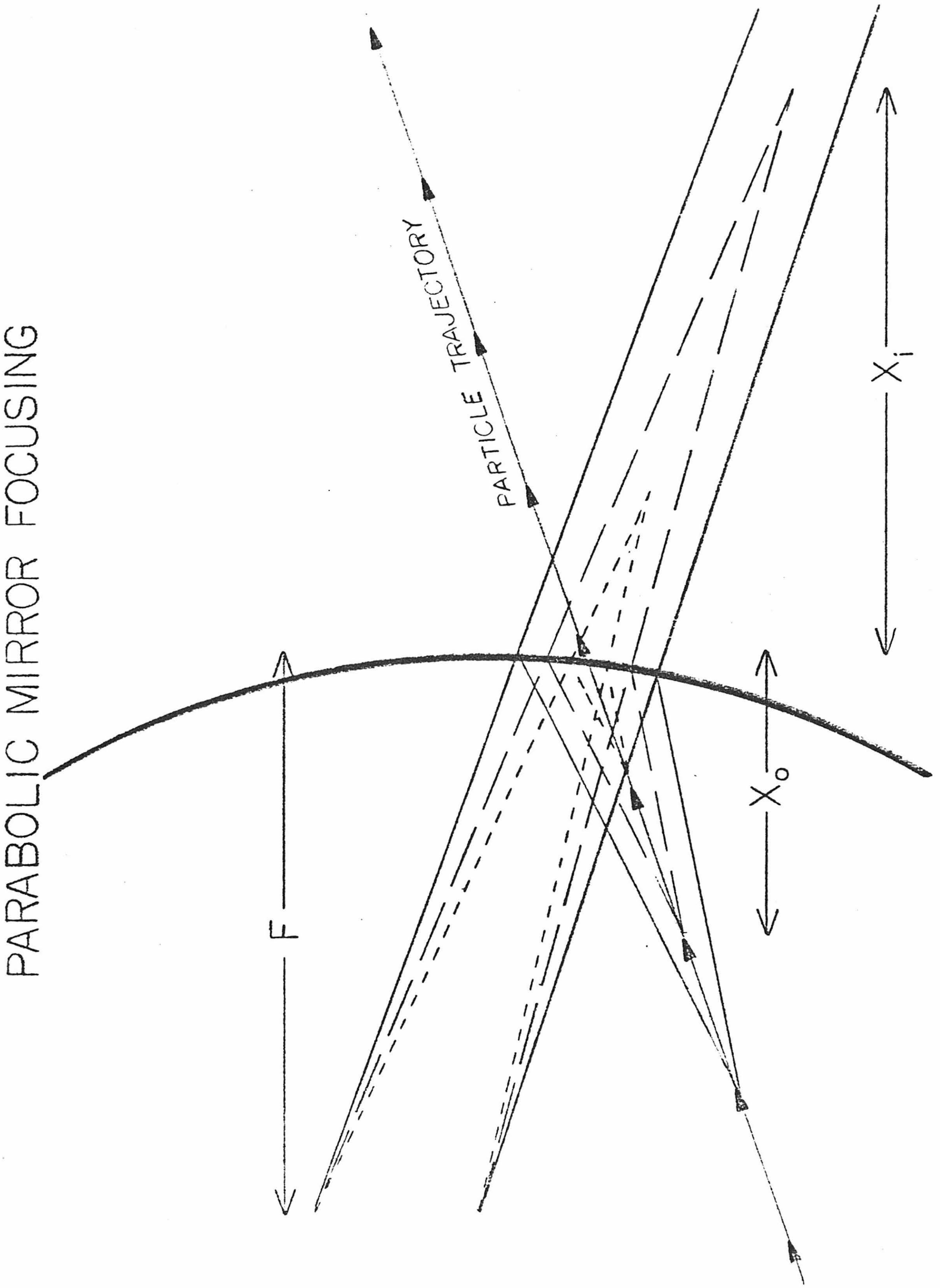

Figure 4.2 Parabolic mirror focusing

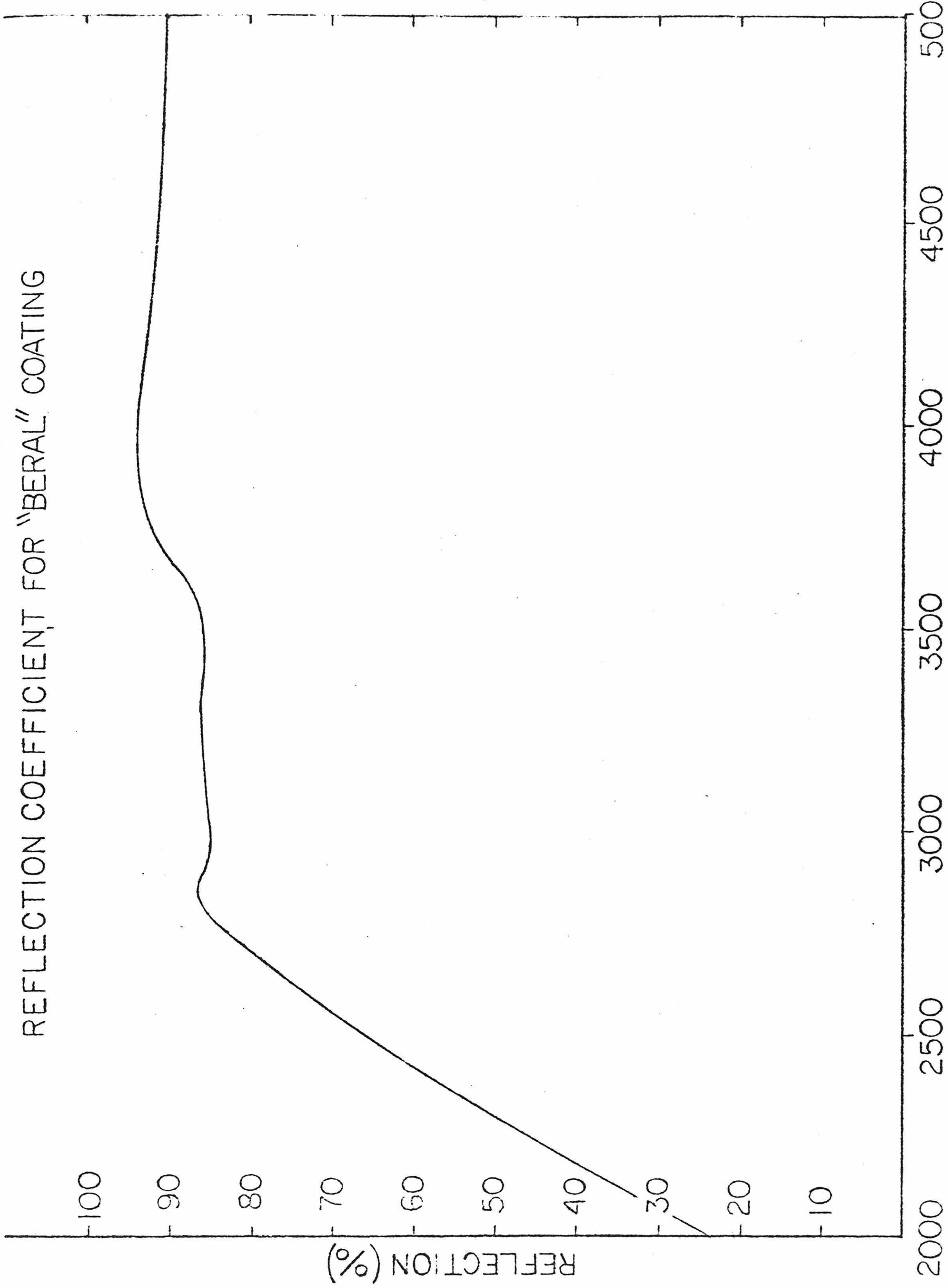

Figure 4.3 'Beral' reflection coefficient

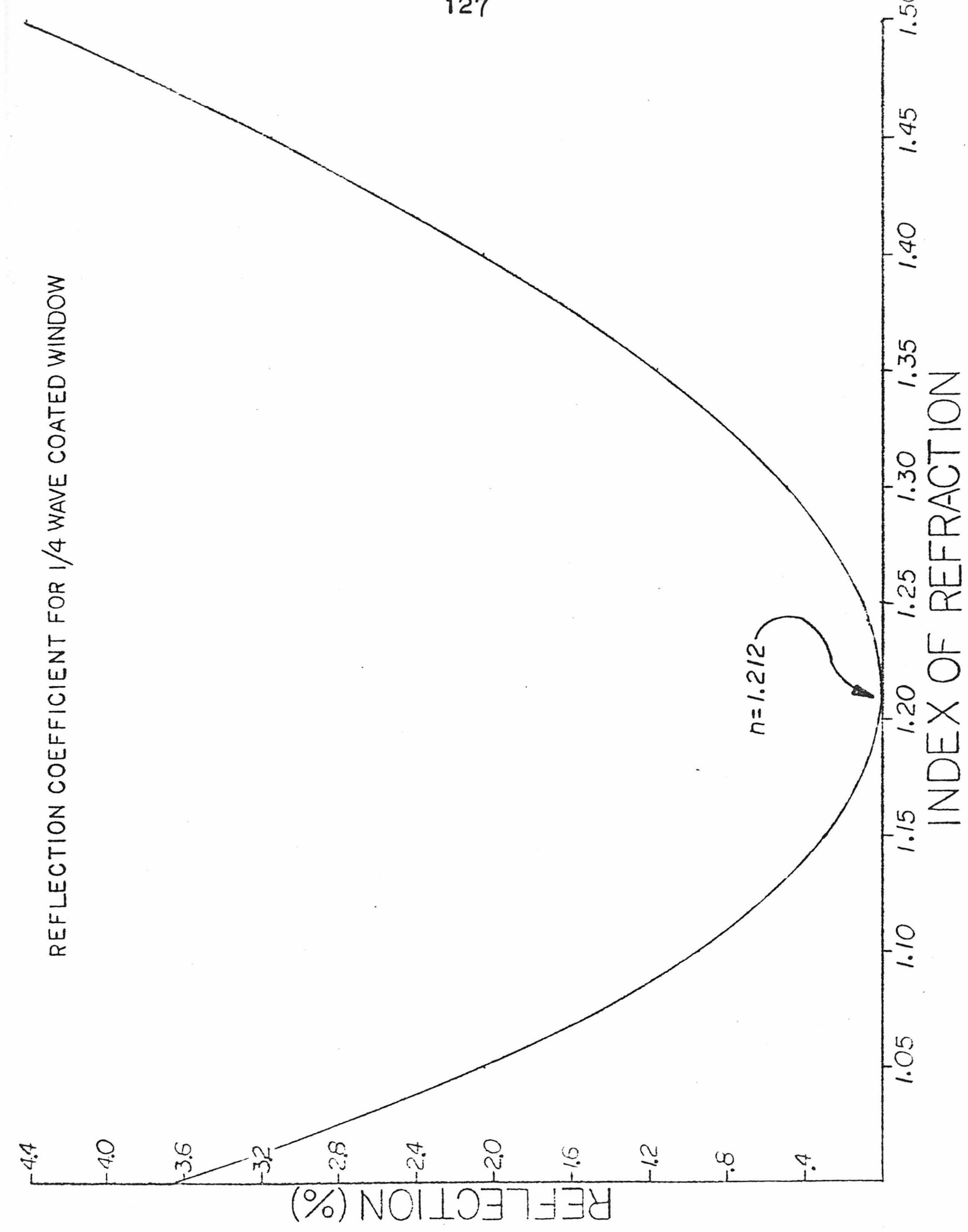

Figure 4.4 Reflection from quarter-wave coated glass

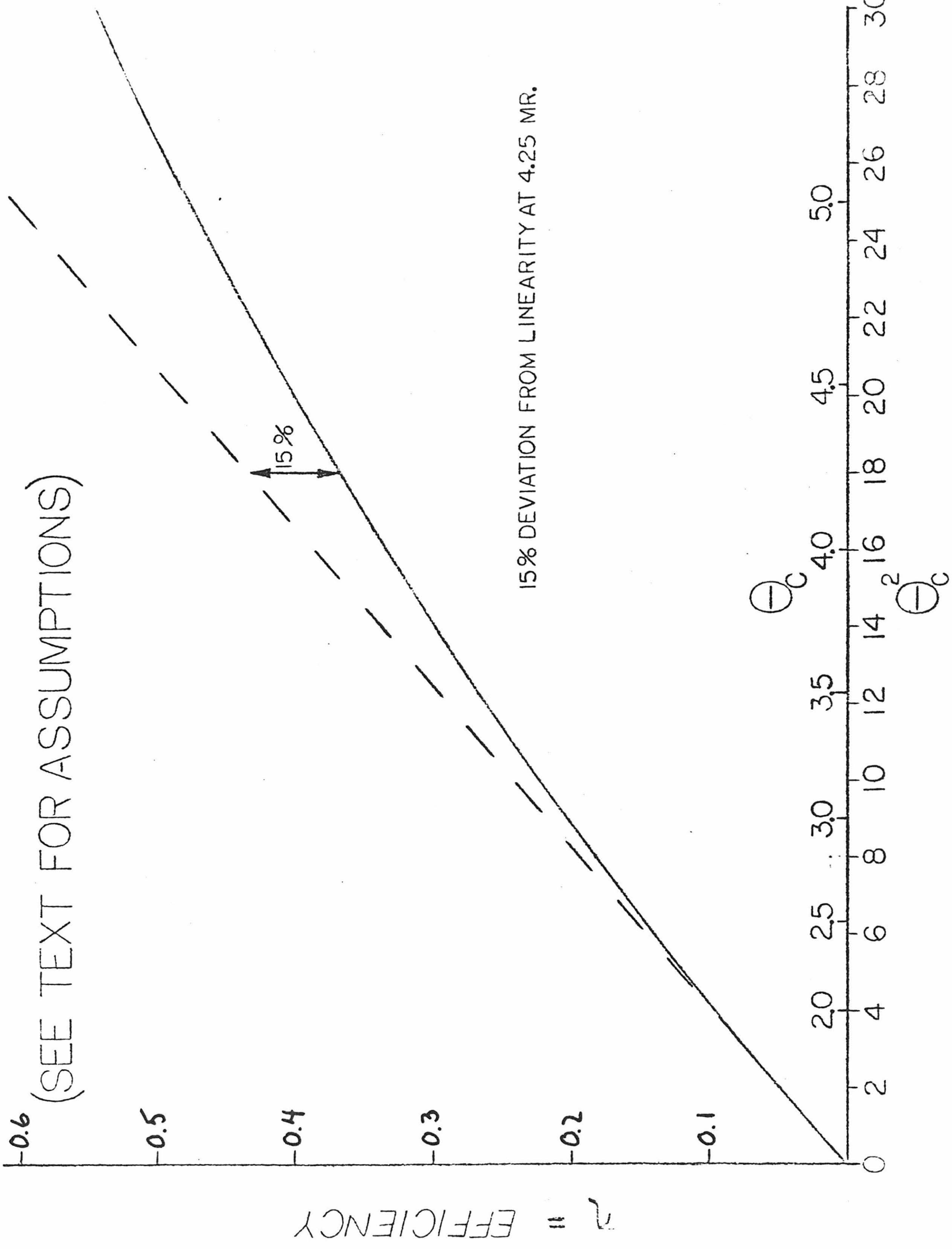

Figure 4.5 Efficiency estimate for our Cerenkov counter

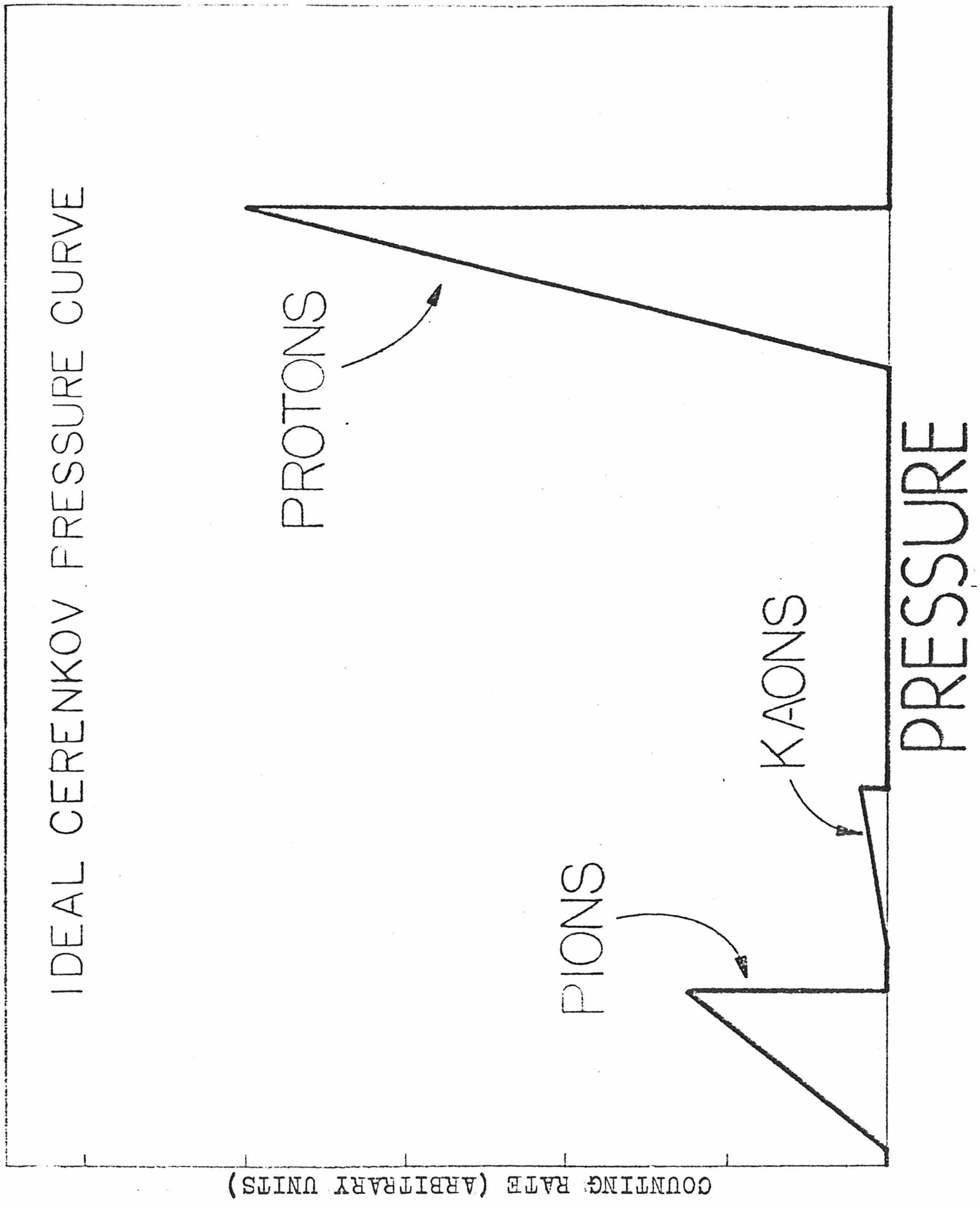

Figure 4.6 Ideal low efficiency pressure curve

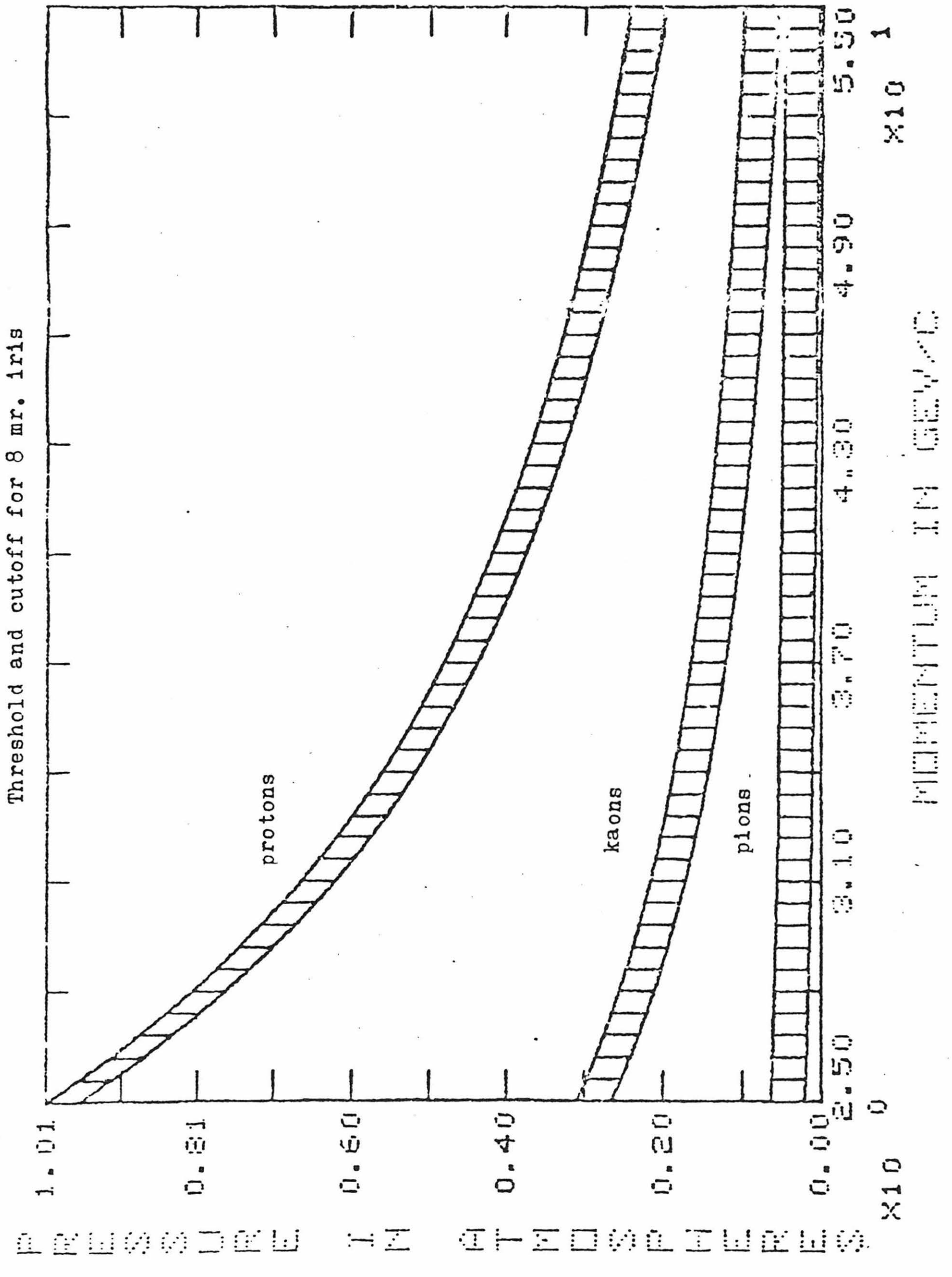

Figure 4.7 Separation of pion, kaon, and proton curves achieved by 8 mr. iris

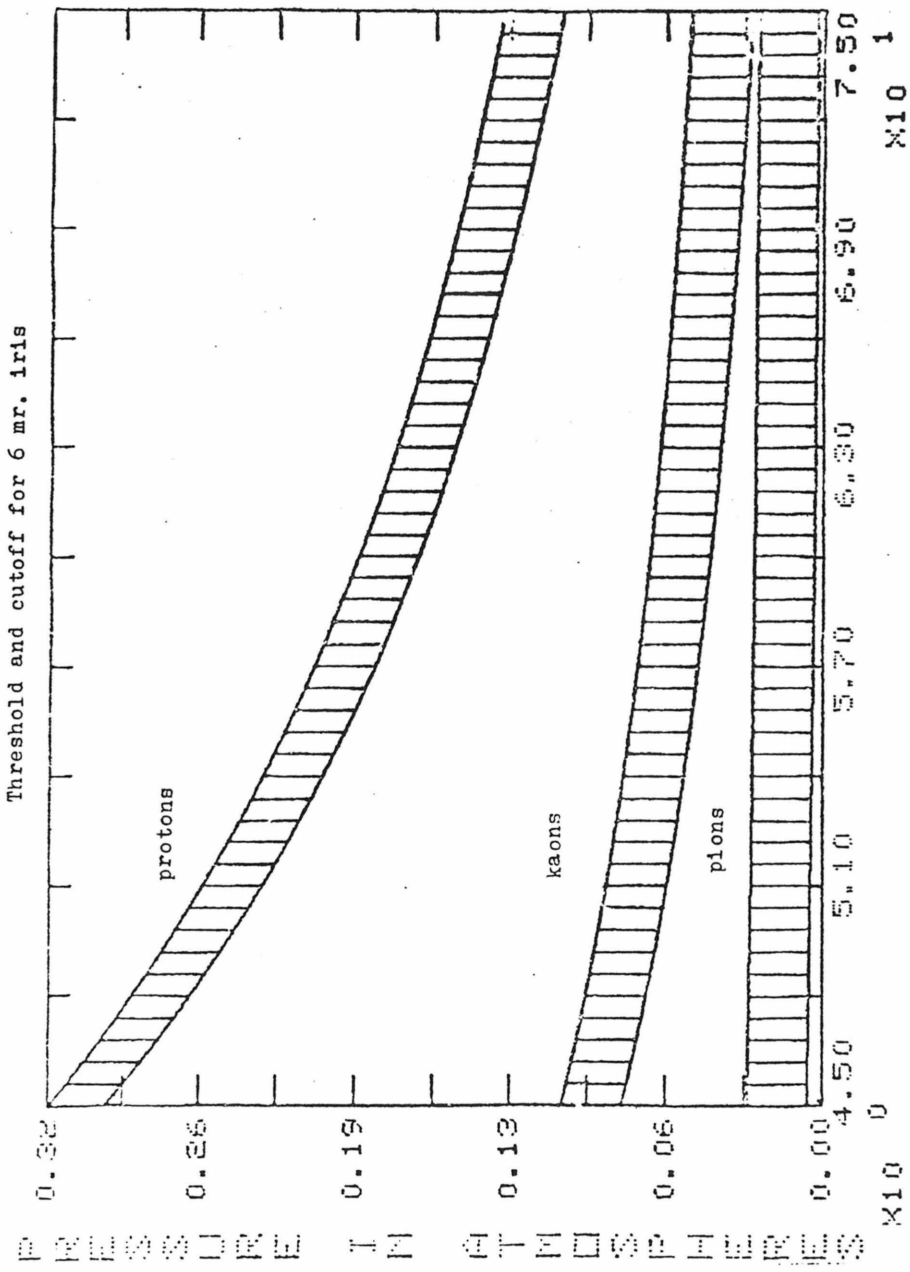

Figure 4.8 Separation of pion, kaon, and proton curves achieved by 6 mr. iris

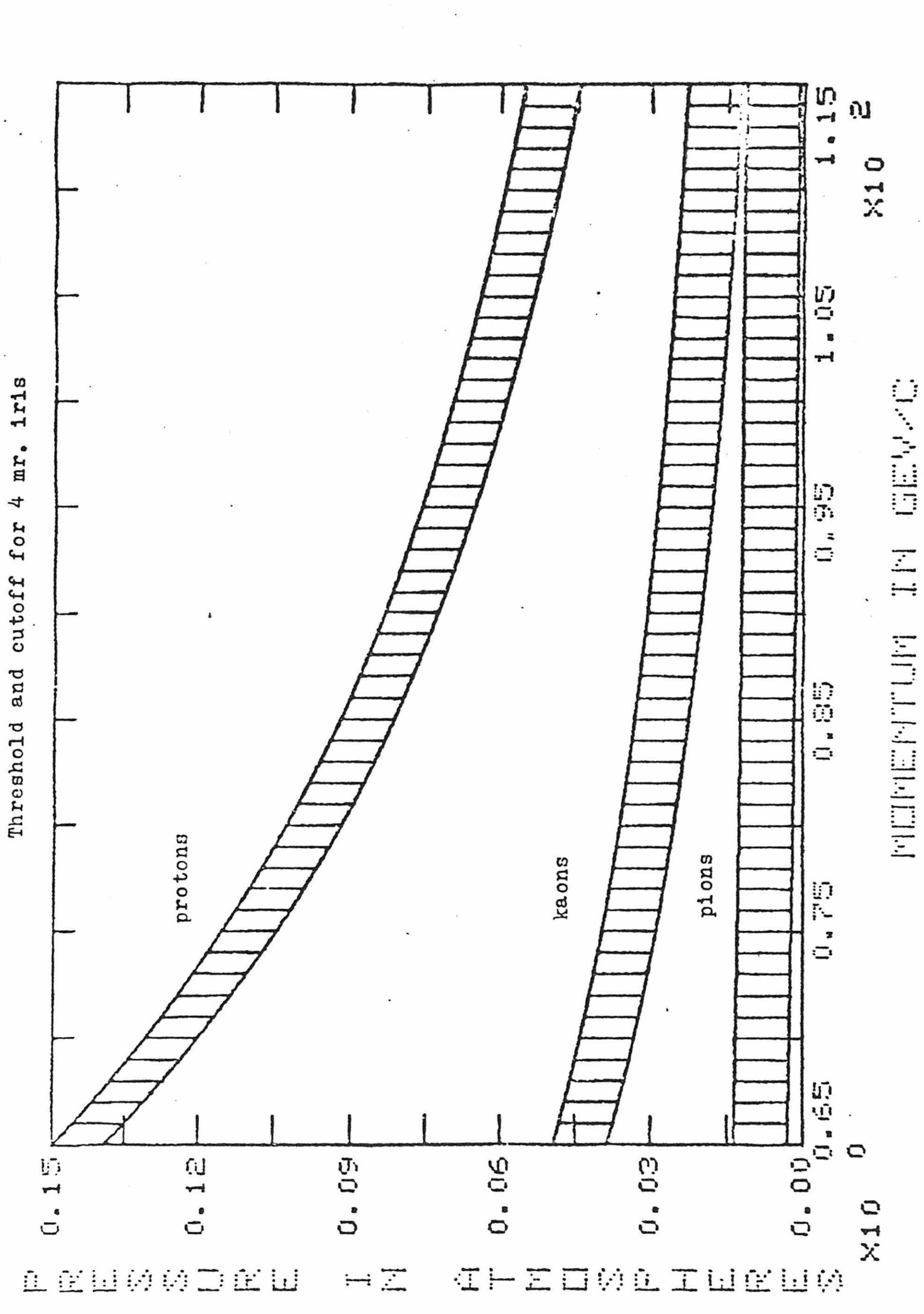

Figure 4.9 Separation of pion, kaon, and proton curves achieved by 4 mr. iris

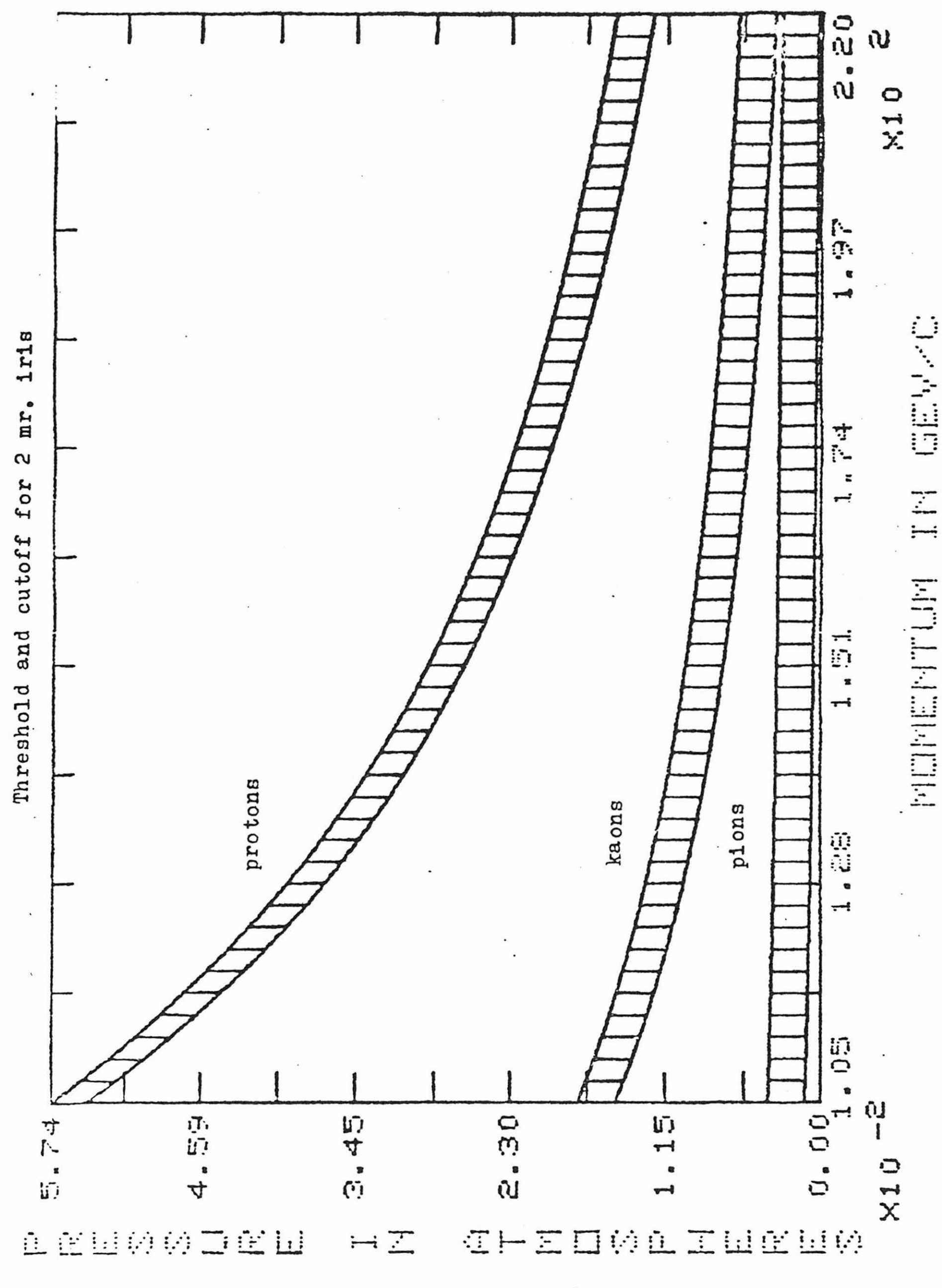

Figure 4.10 Separation of pion, kaon, and proton curves achieved by 2 mr. iris

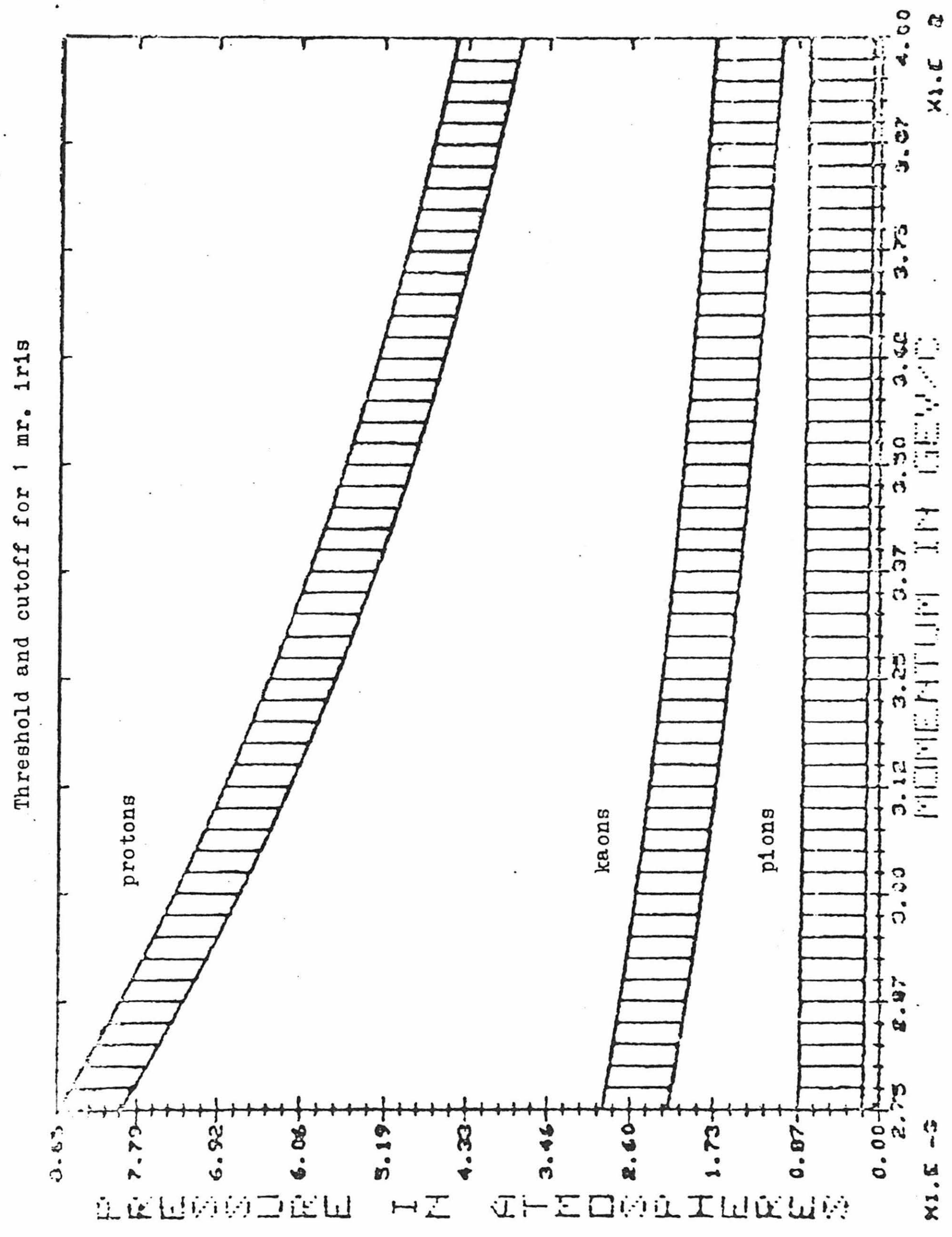

Figure 4.11 Separation of pion, kaon, and proton curves achieved by 1 mr. iris

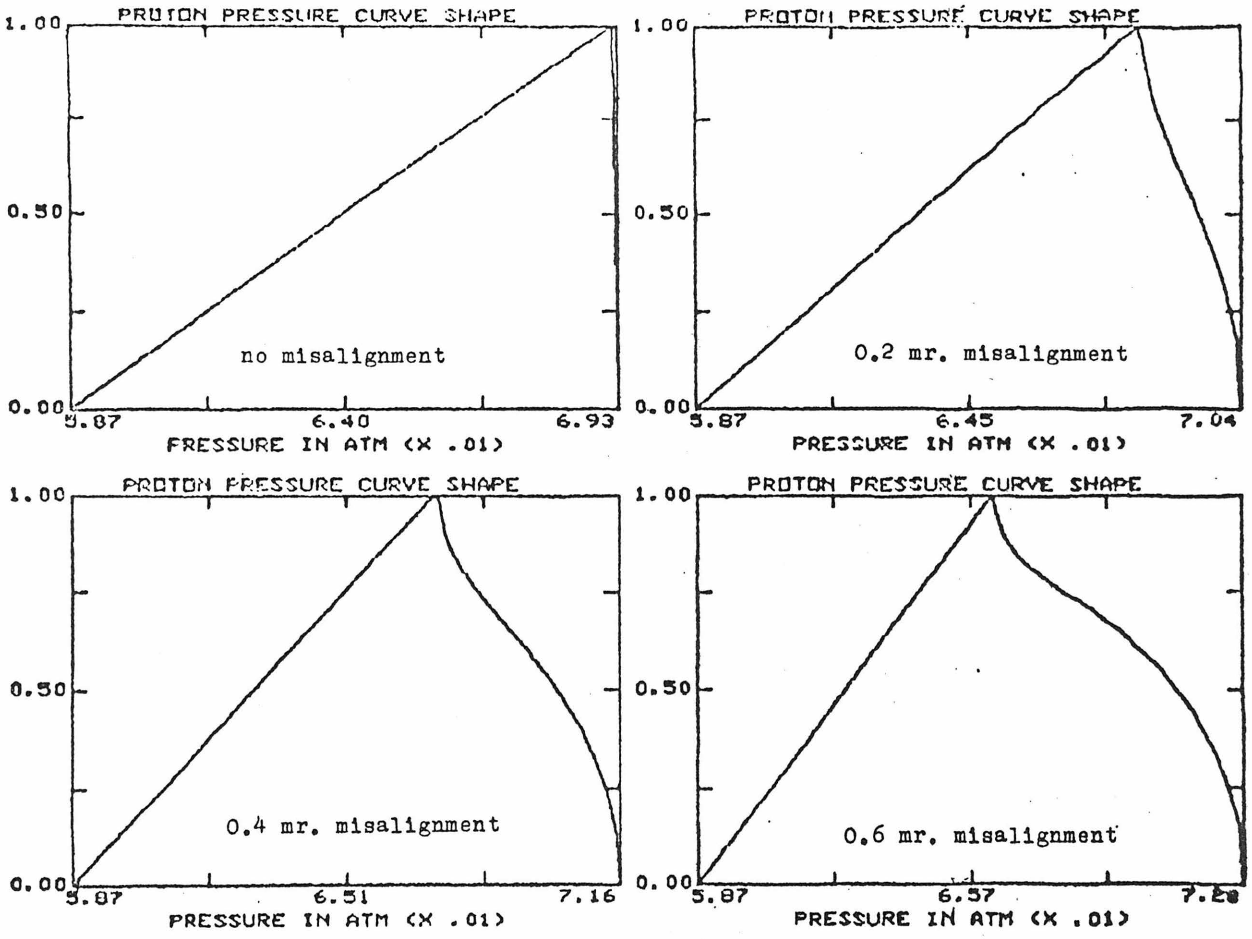

Figure 4.12 Effect of angular misalignment on pressure curves

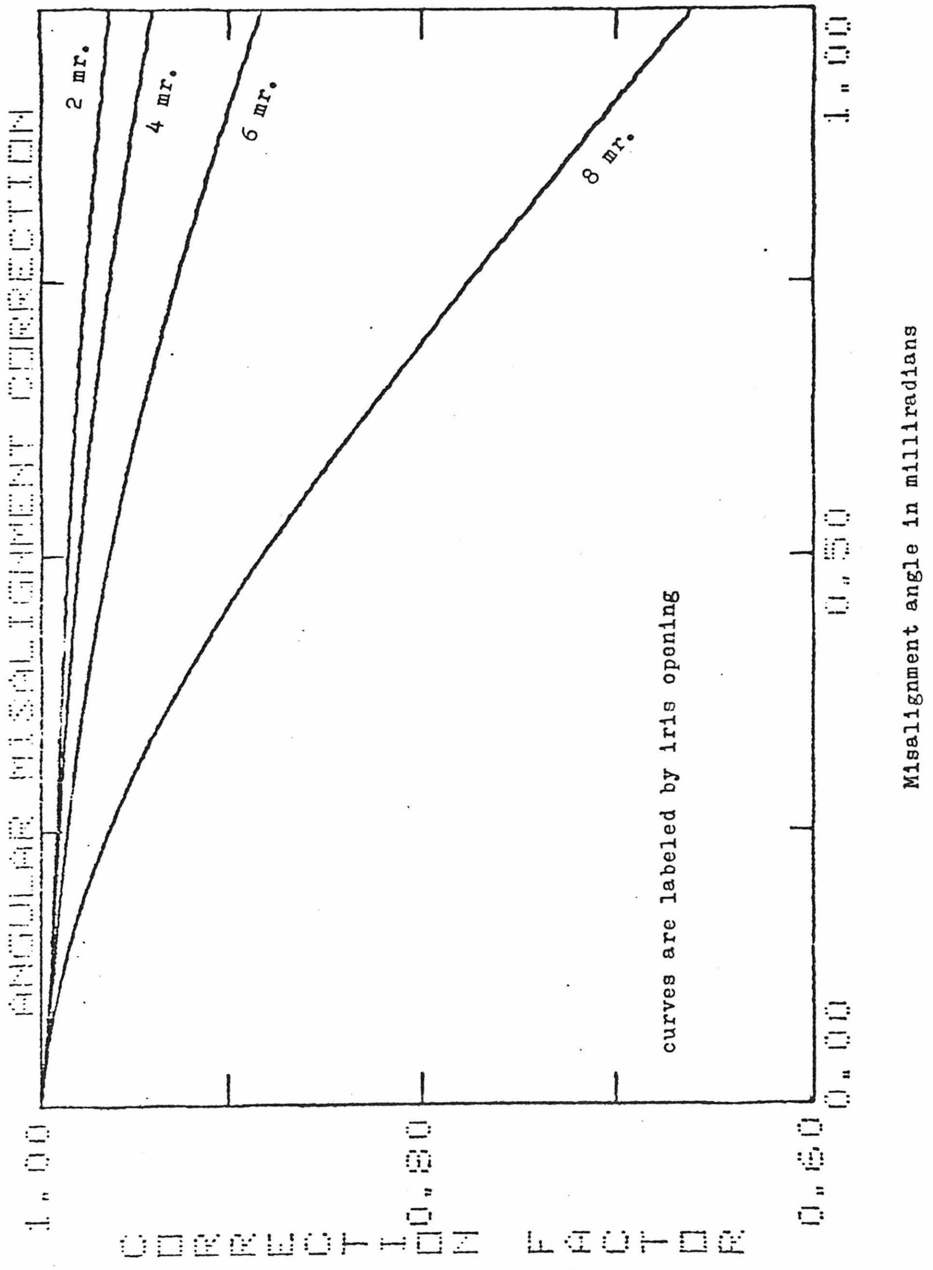

Figure 4.13 Ratio of the 'no misalignment' integral of a pressure curve to the integral with misalignment

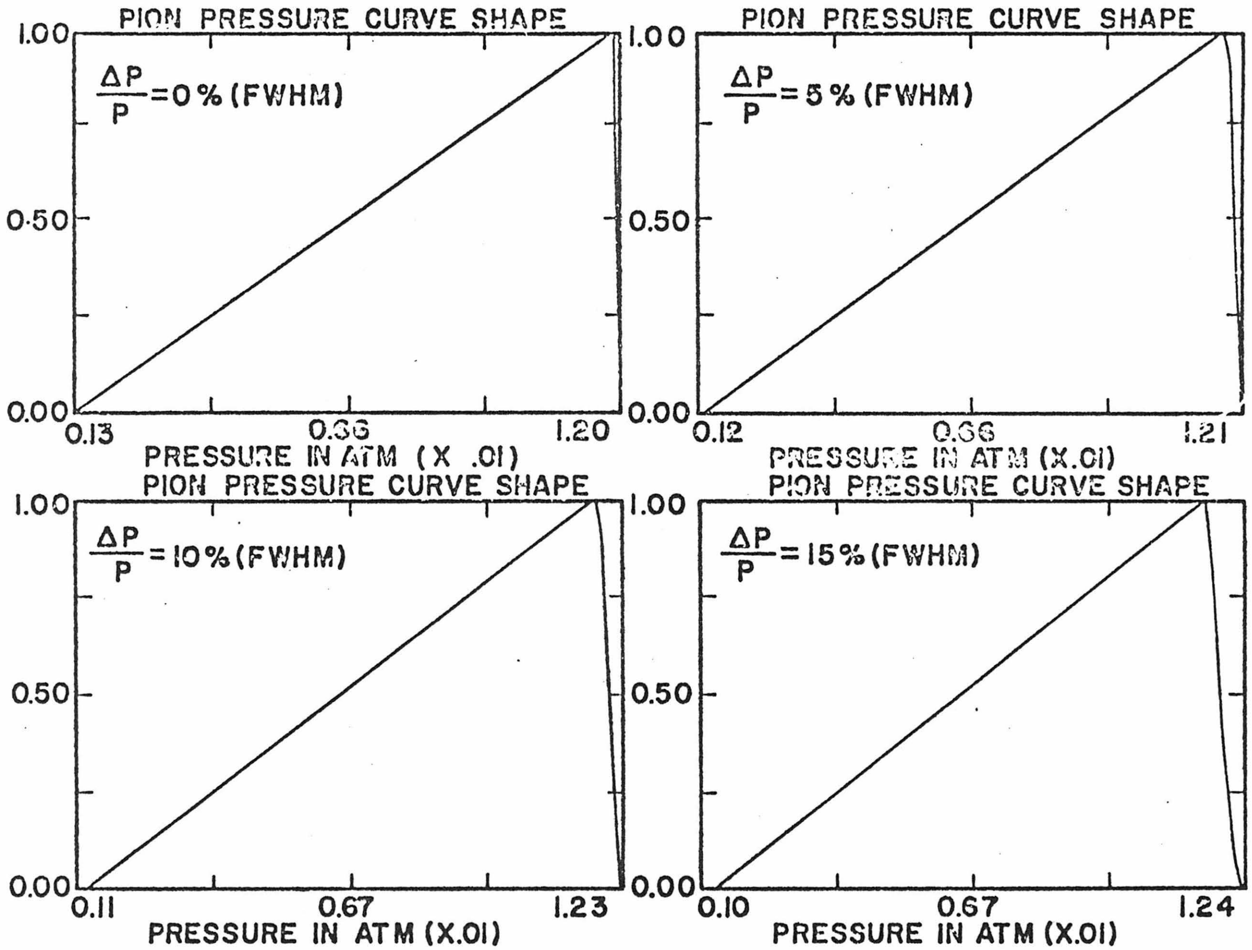

P = 100 GEV/C 4MR IRIS

Figure 4.14 Shape of pion curve versus momentum bite

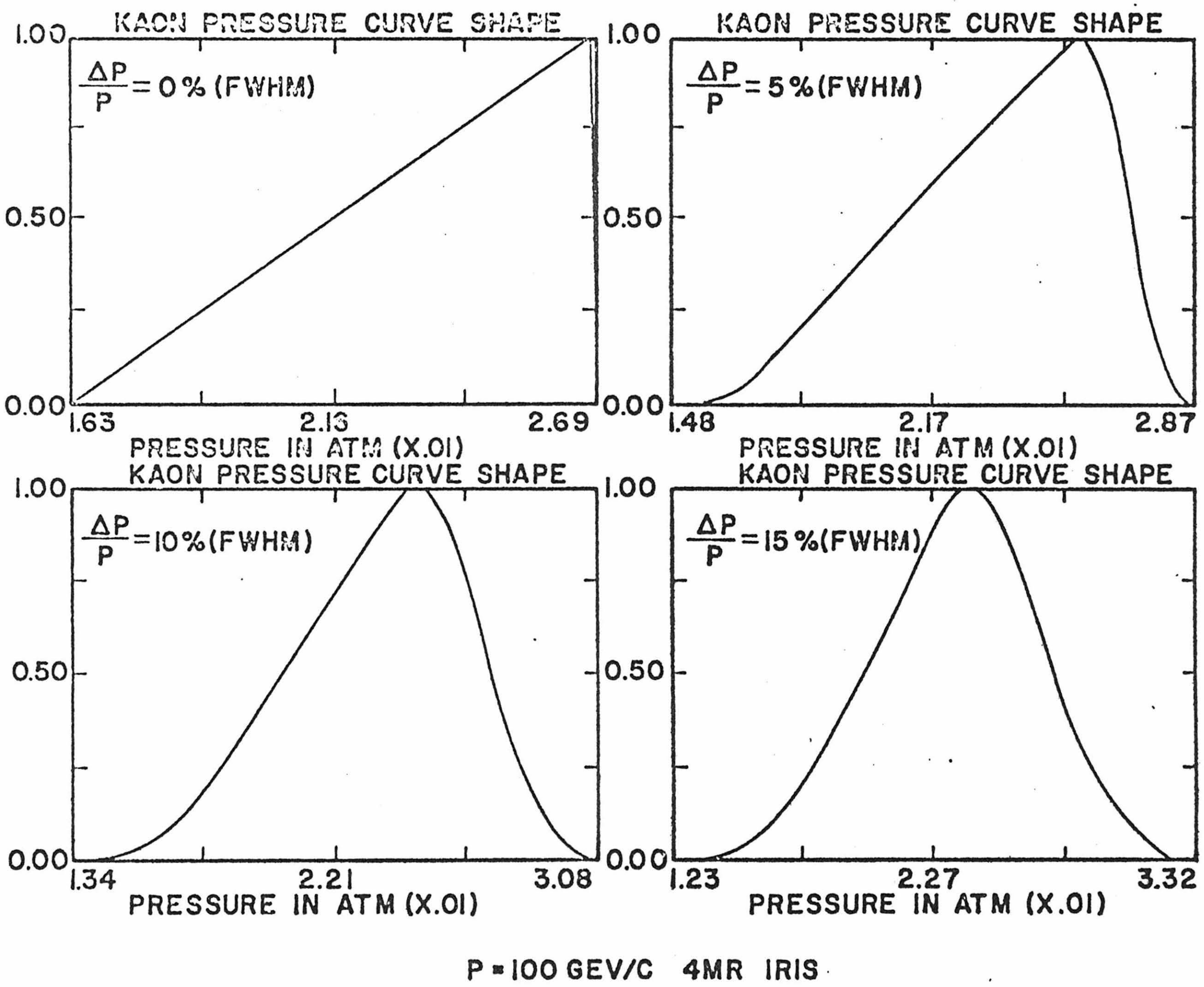

Figure 4.15 Shape of kaon curve versus momentum bite

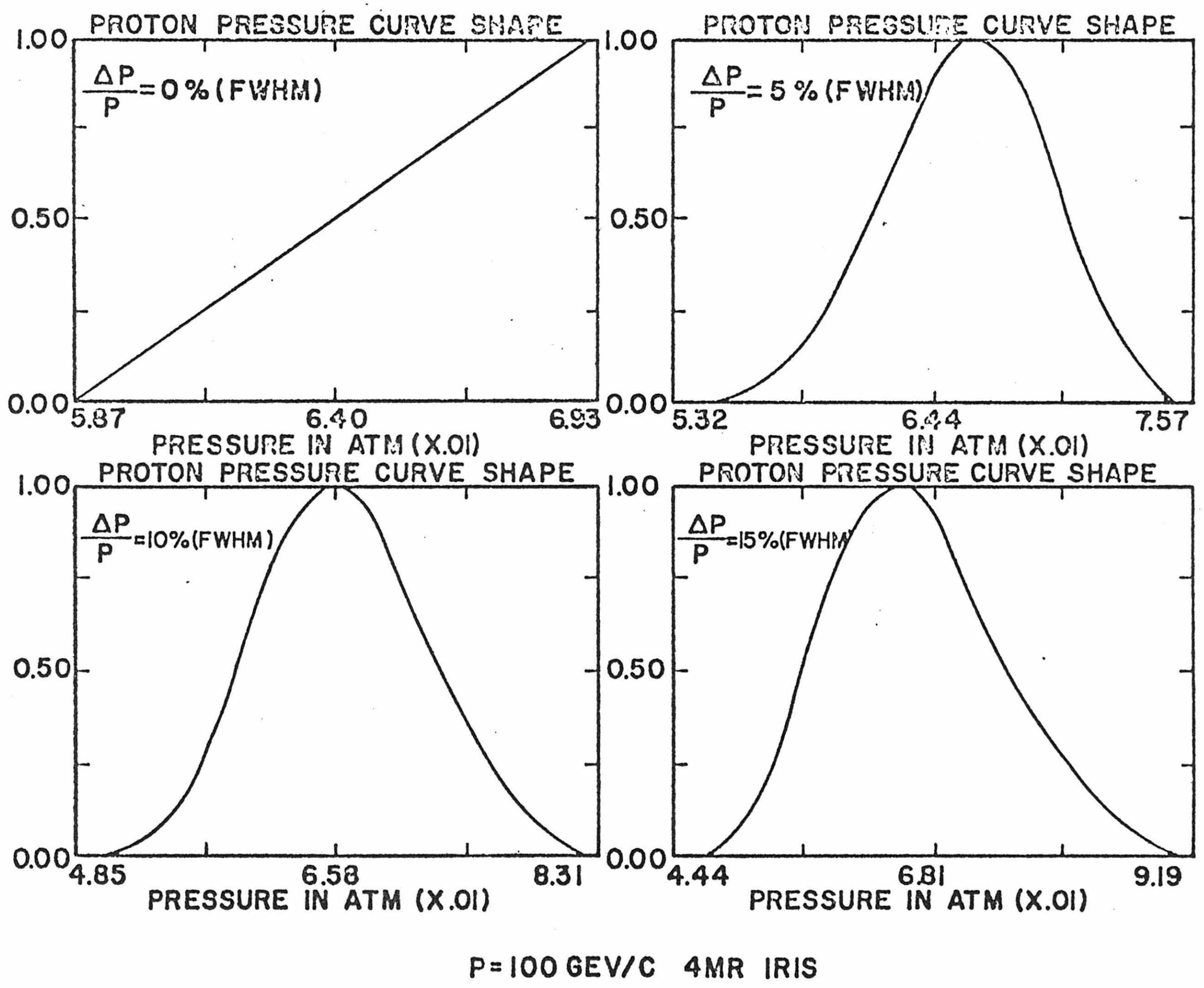

Figure 4.16 Shape of proton curve versus momentum bite

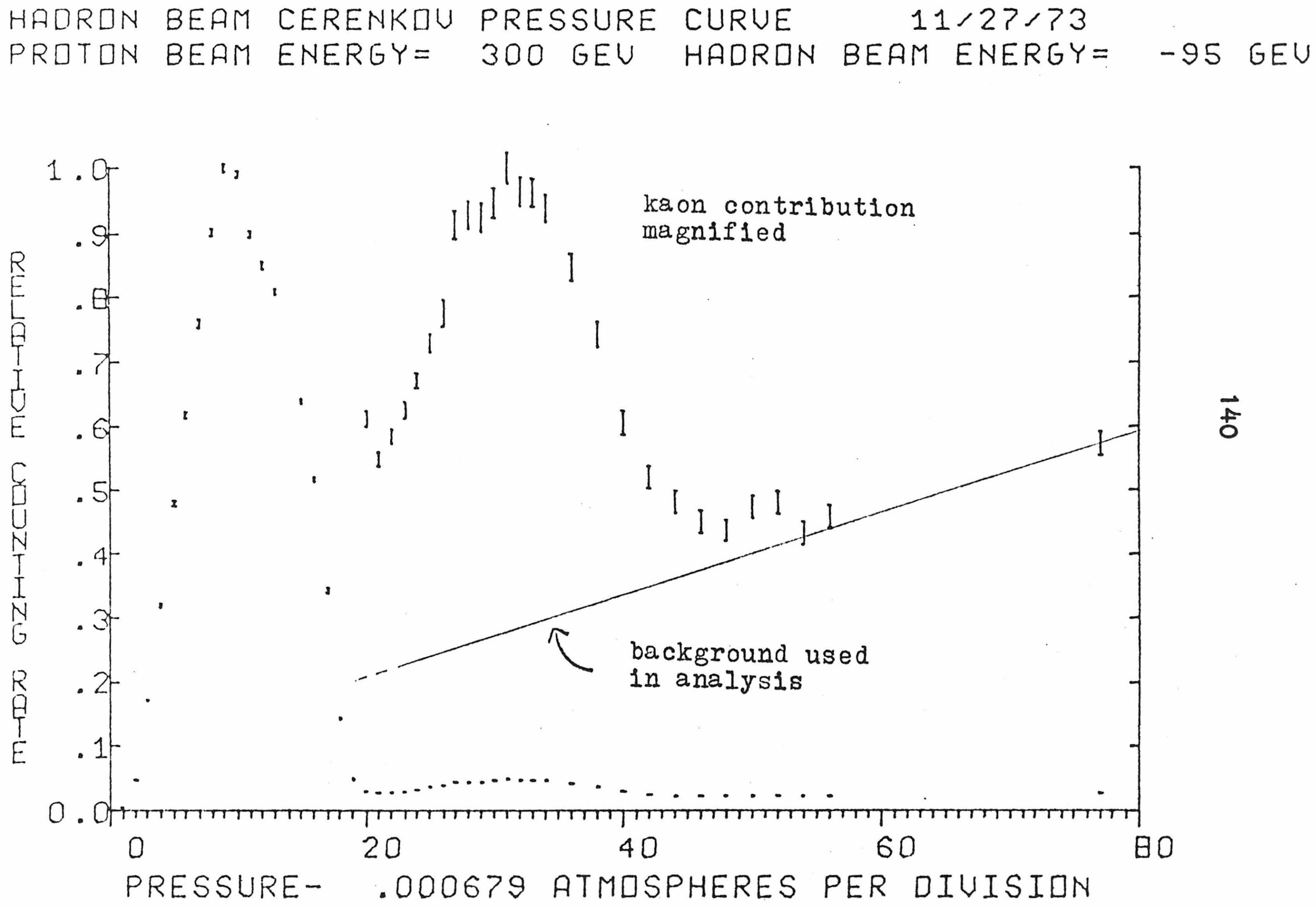

Figure 5.1 Cerenkov pressure curve at 95 Gev (negative)

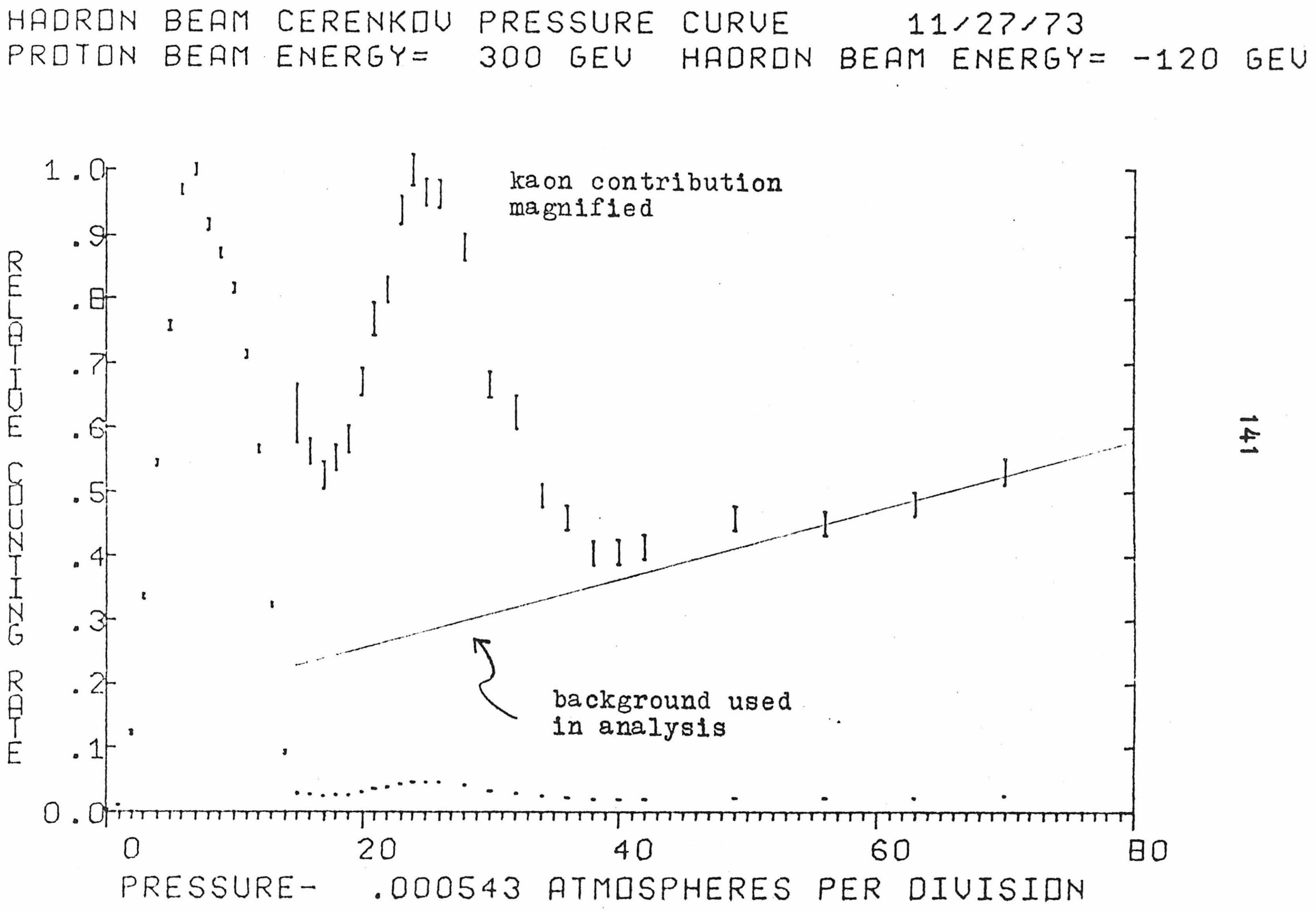

Figure 5.2 Cerenkov pressure curve at 120 Gev (negative)

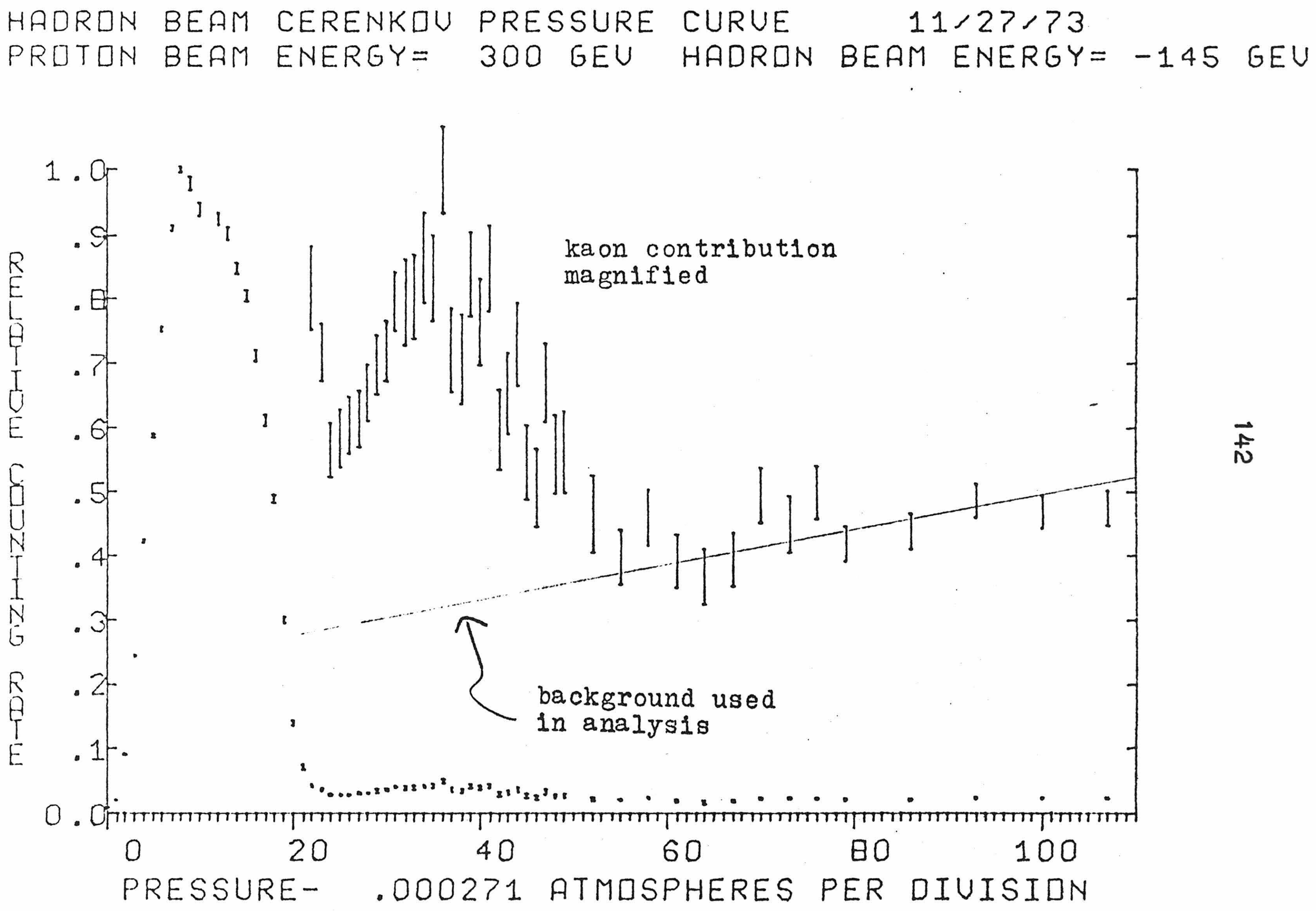

Figure 6.2 Cerenkov pressure curve at 145 Gev (negative)

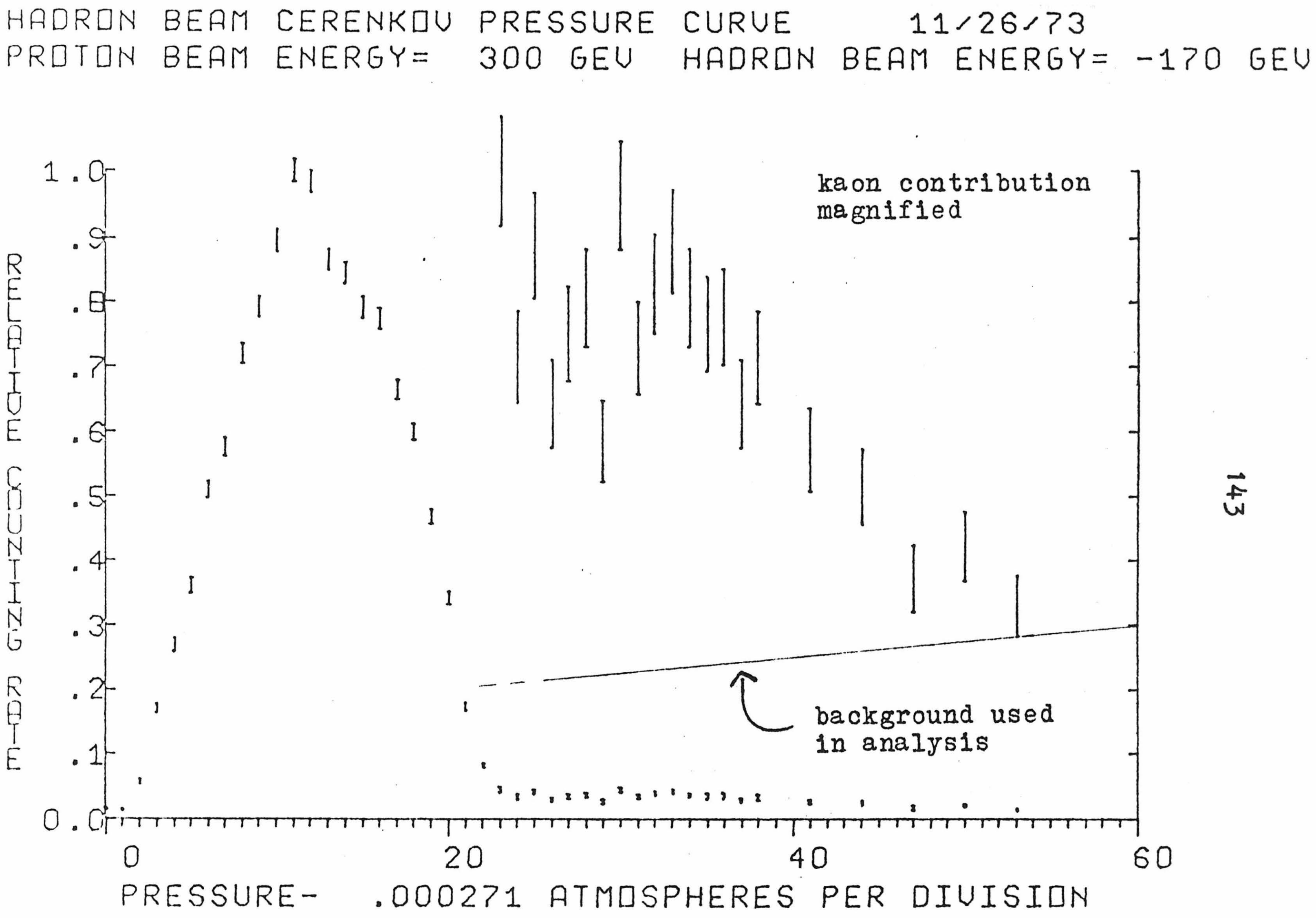

Figure 5.4 Cerenkov pressure curve at 170 Gev (negative)

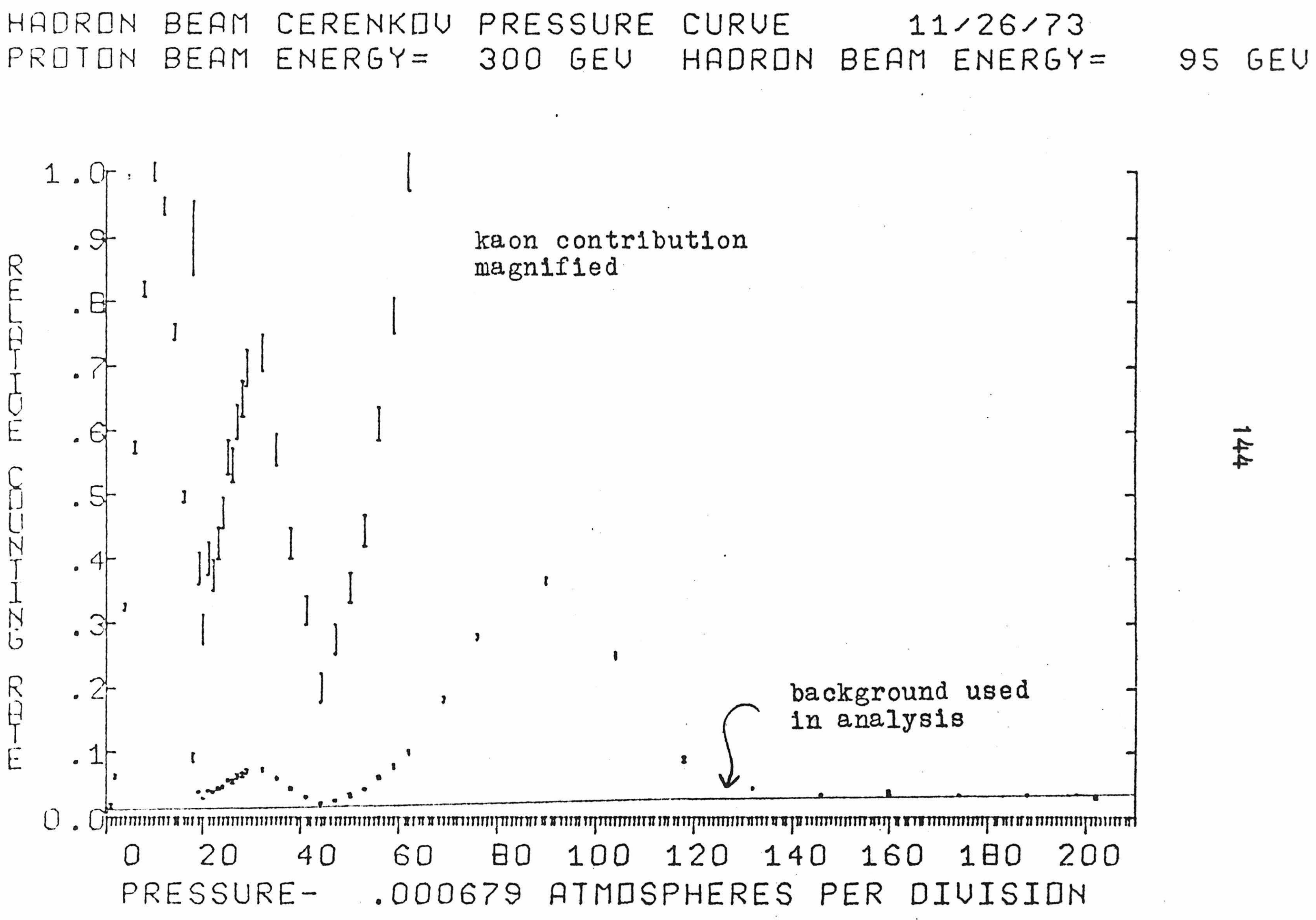

Figure 5.5 Cerenkov pressure curve at 95 GeV (positive)

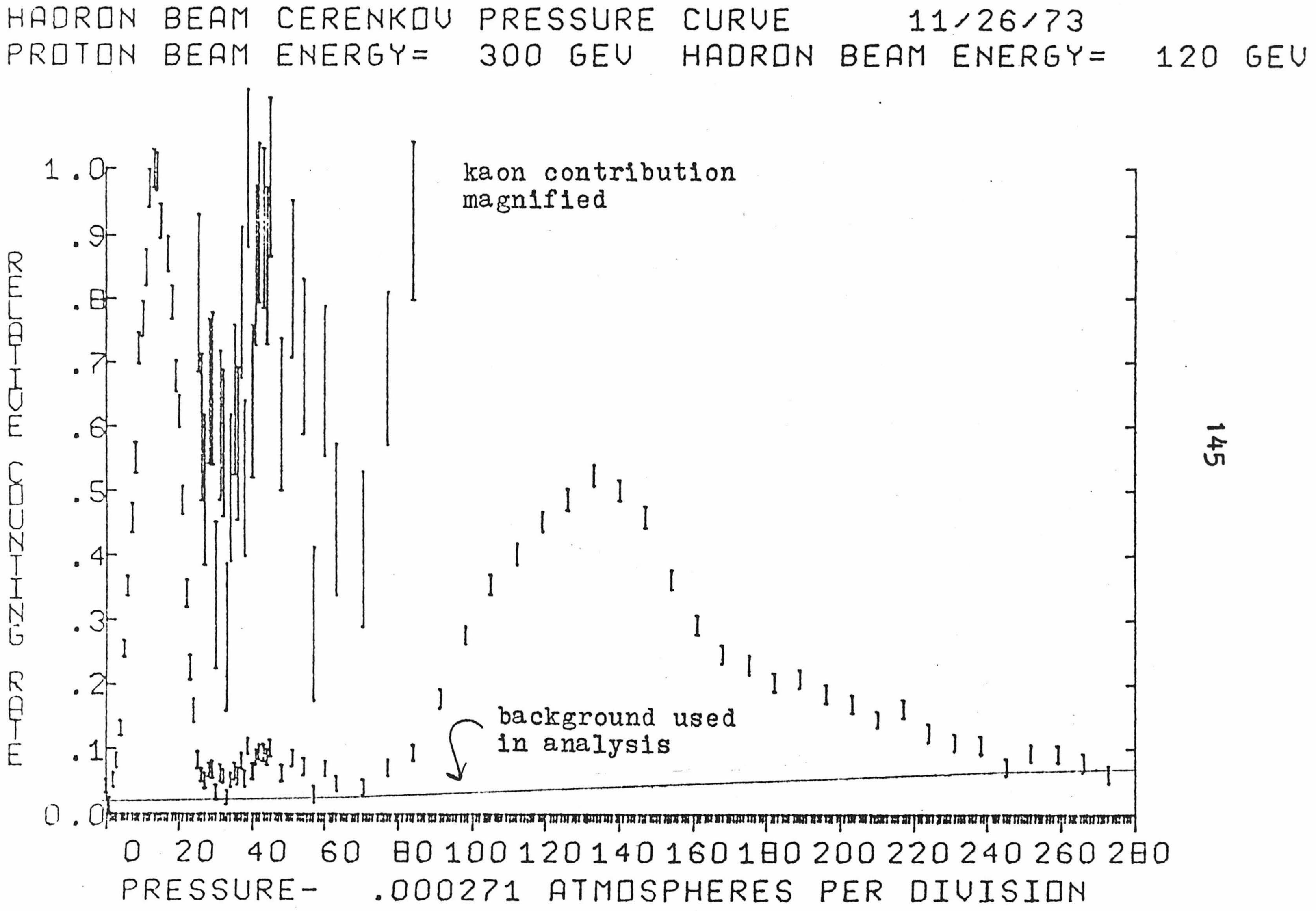

Figure 5.6 Cerenkov pressure curve at 120 Gev (positive) #1

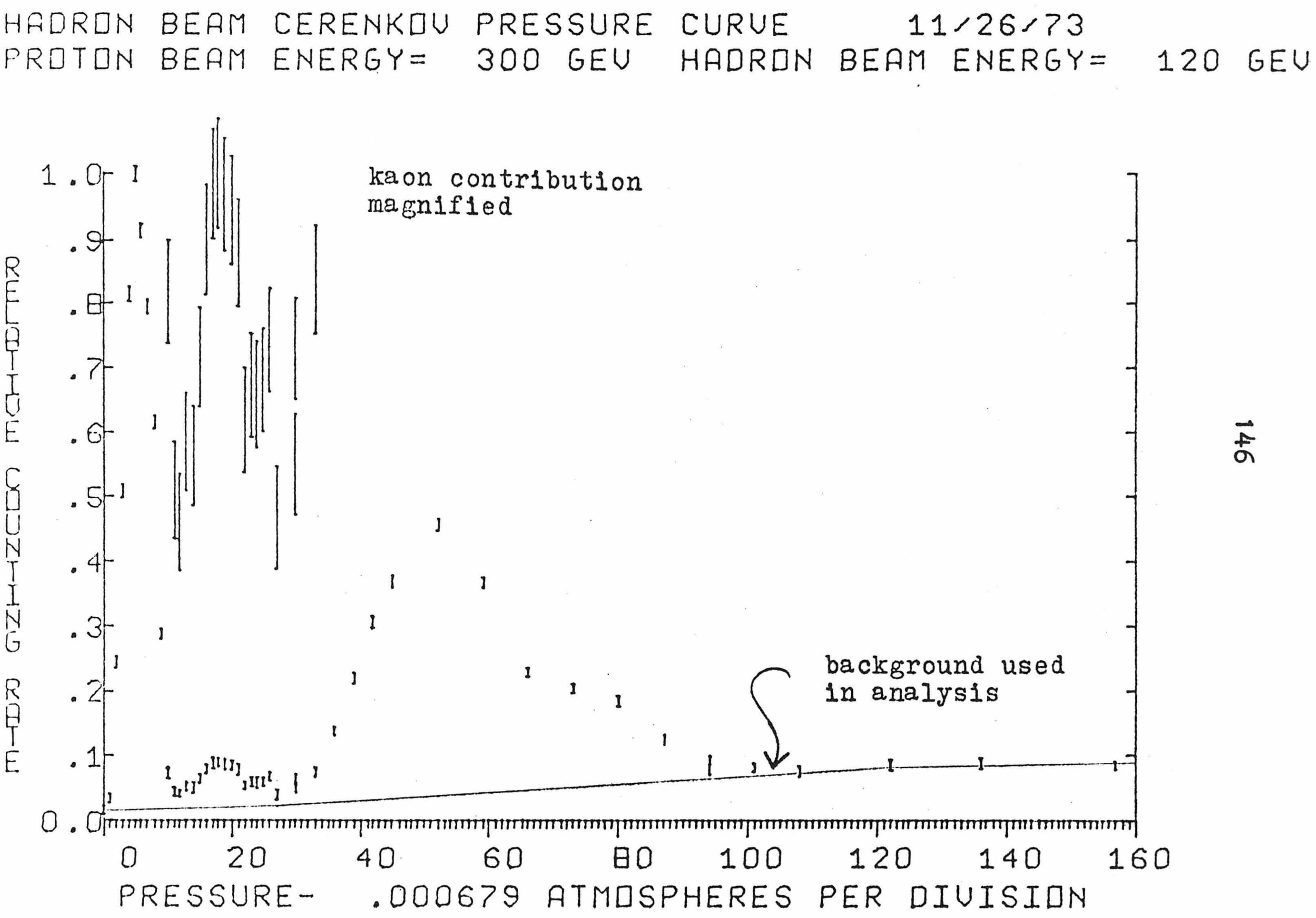

Figure 5.7 Cerenkov pressure curve at 120 Gev (positive) #2

Figure 5.8 Cerenkov pressure curve at 120 Gev (positive) #3

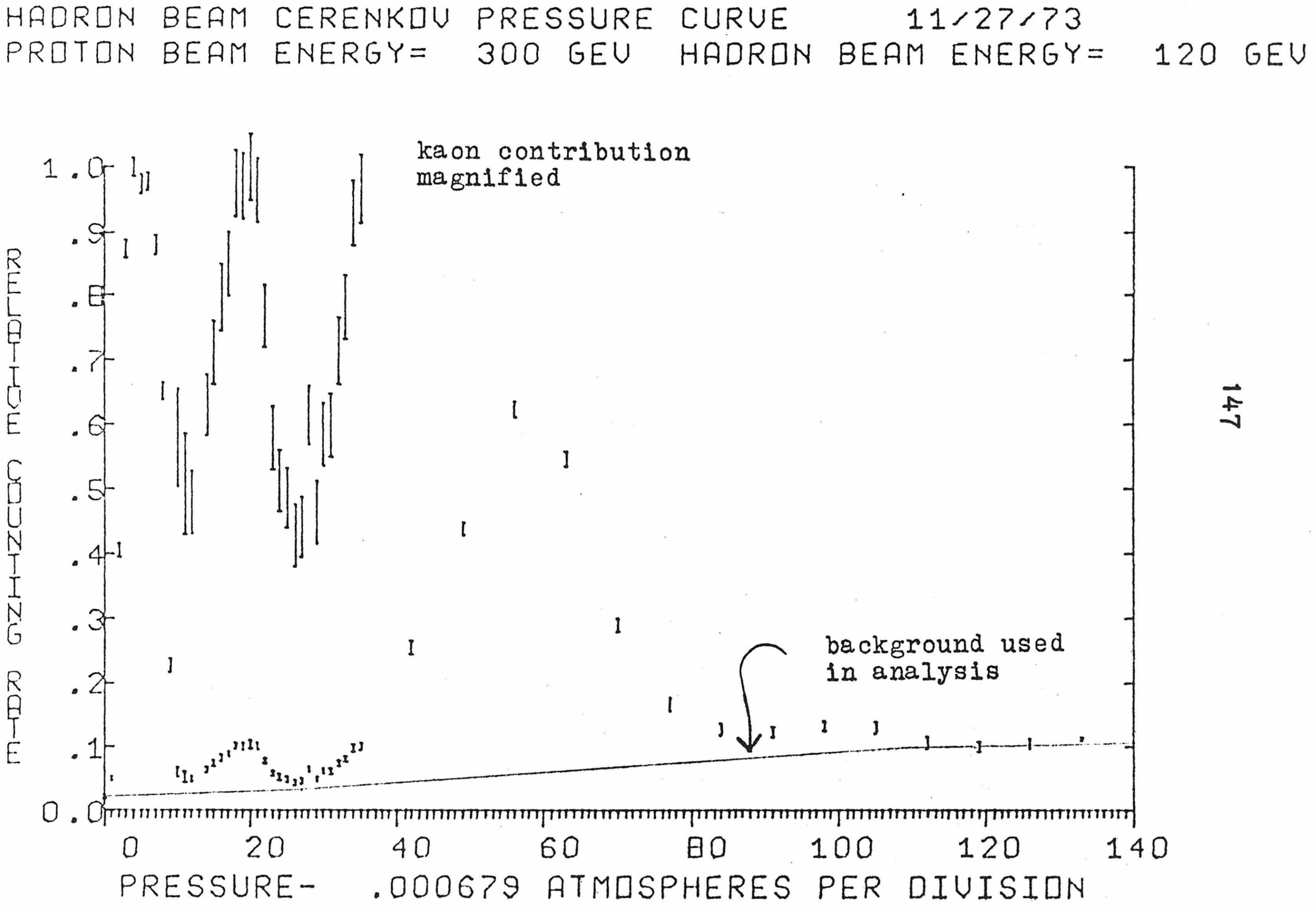

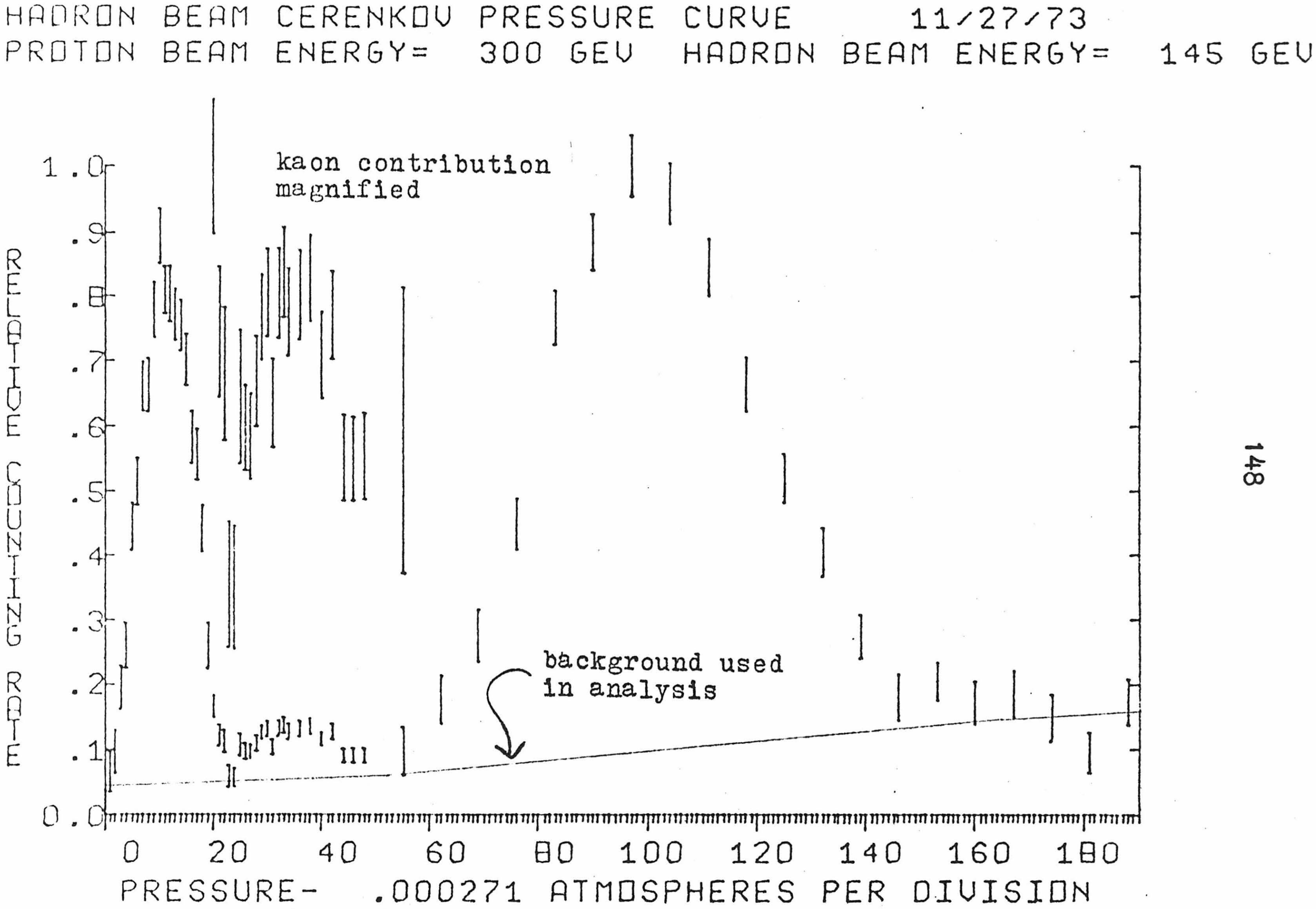

Figure 5.4 Cerenkov pressure curve at 145 GeV (positive)

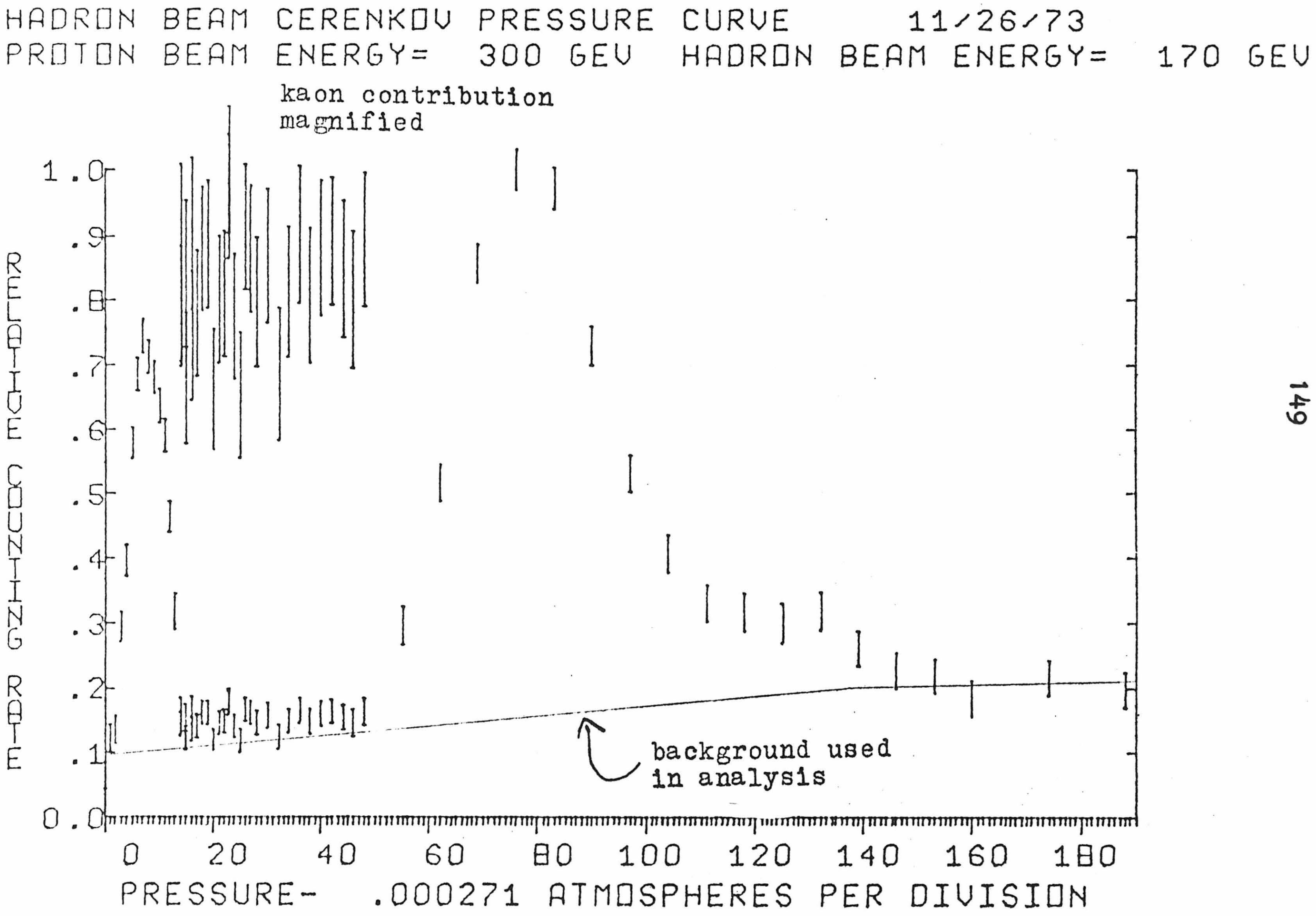

kaon contribution magnified

background used in analysis

Figure 5.10 Cerenkov pressure curve at 170 Gev (positive)

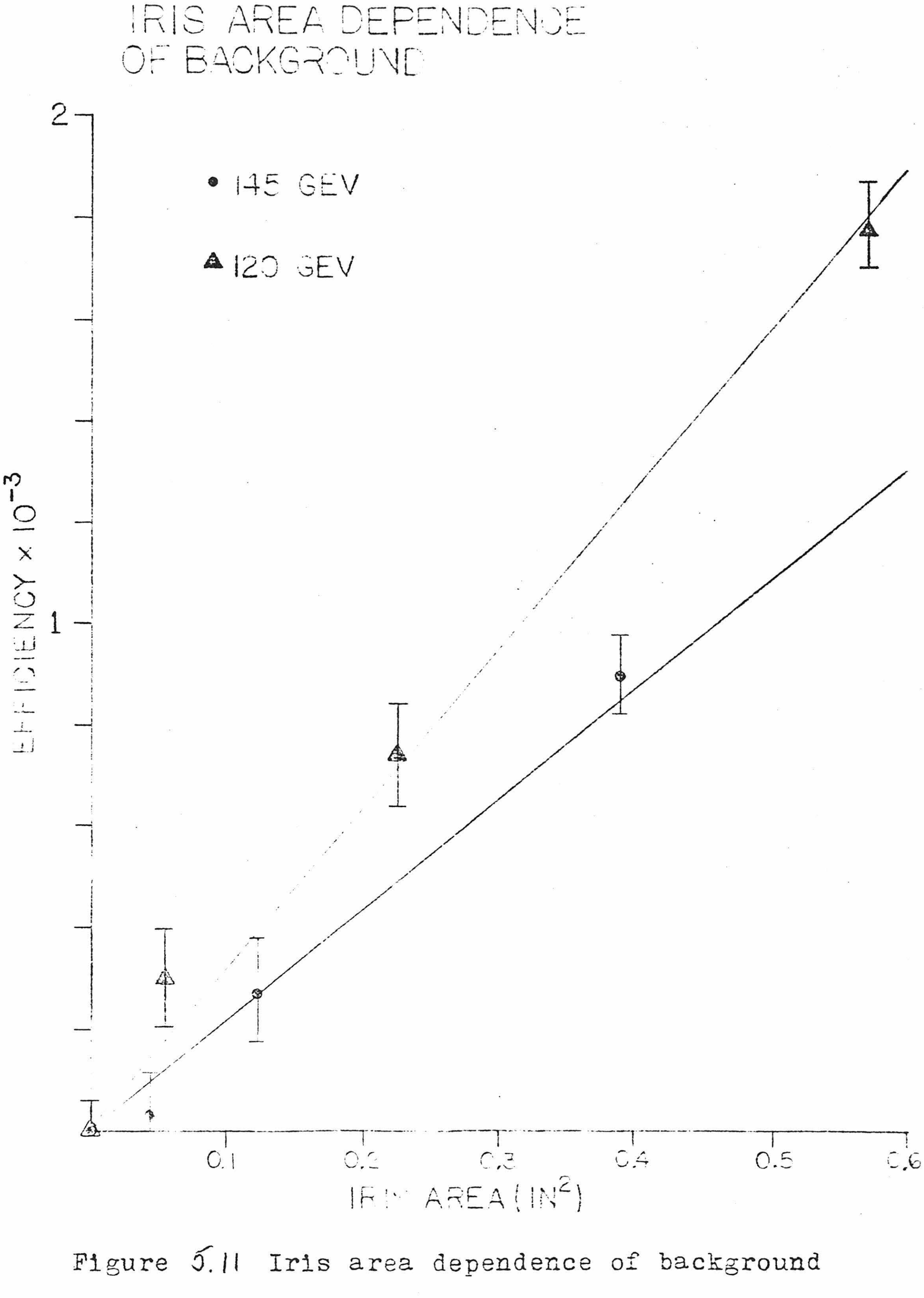

Figure 5.11 Iris area dependence of background

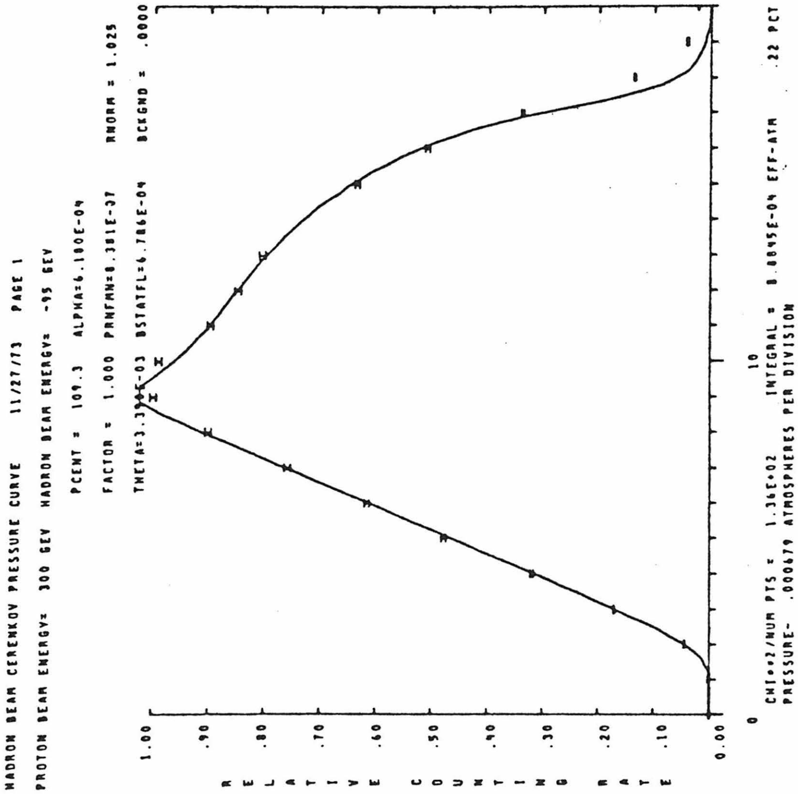

Figure 5.12 Pion pressure curve fit at 95 Gev (negative)

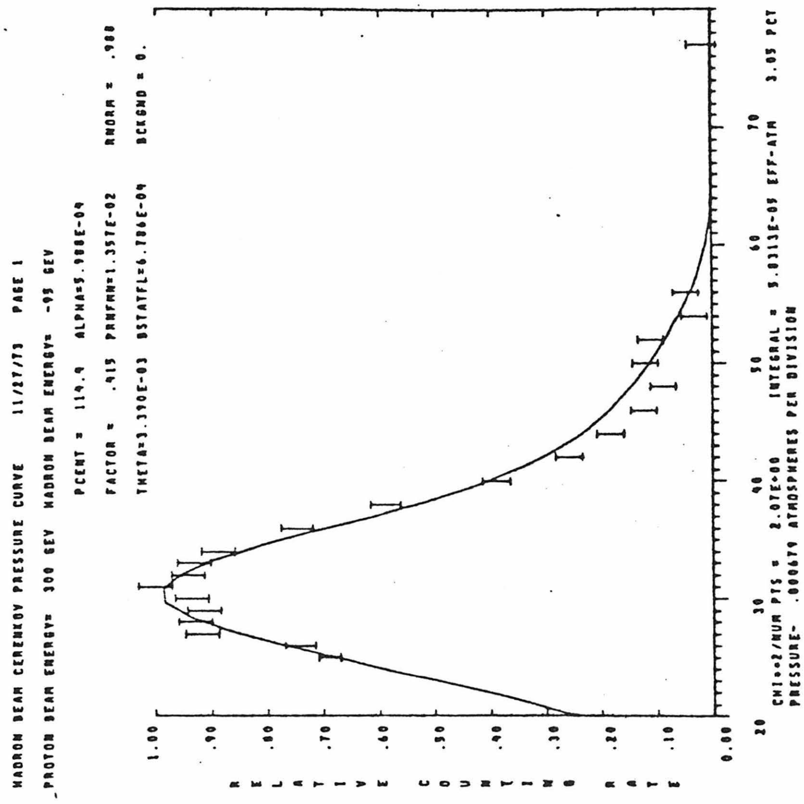

Figure 5.13 Kaon pressure curve fit at 95 Gev (negative)

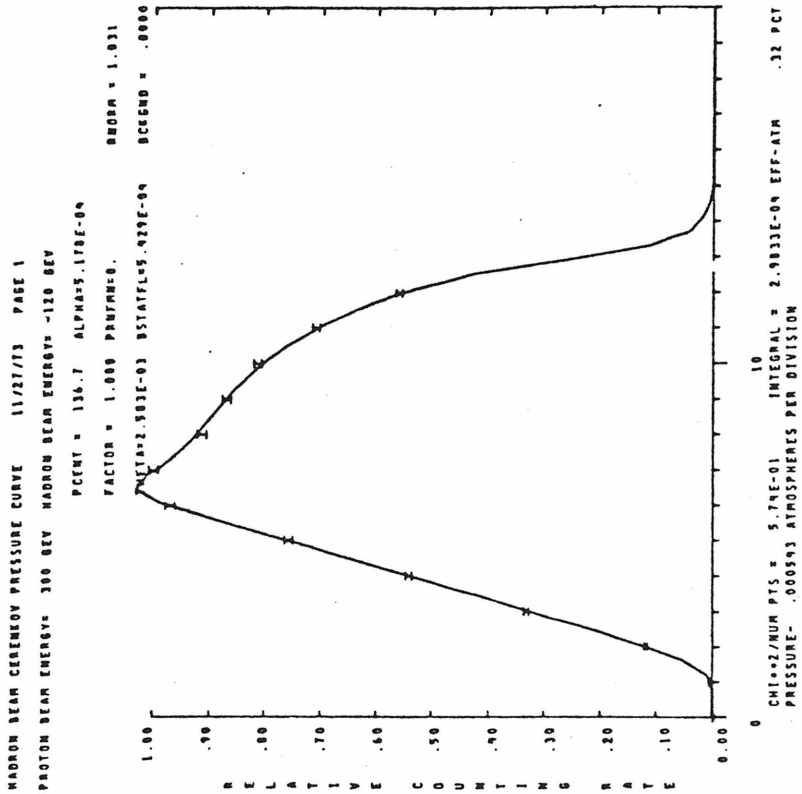

Figure 5.14 Pion pressure curve fit at 120 Gev (negative)

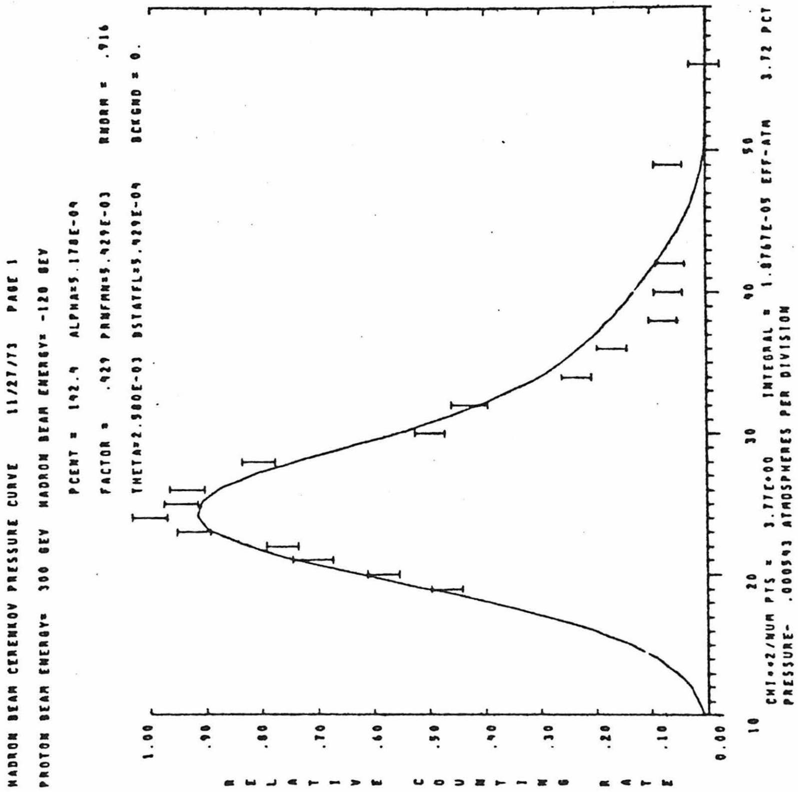

Figure 5.15 Kaon pressure curve fit at 120 Gev (negative)

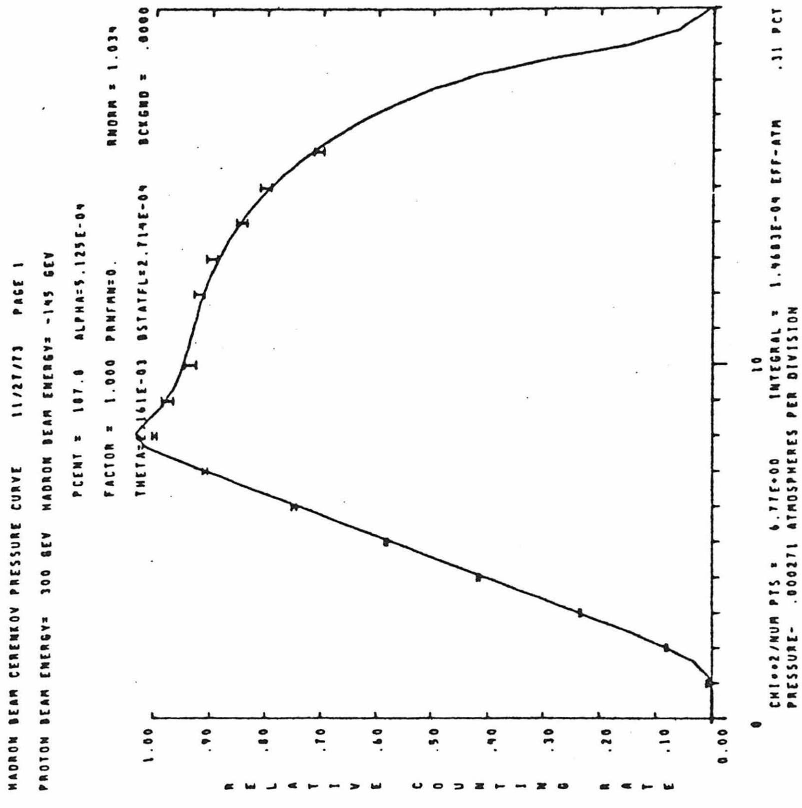

Figure 5.16 Pion pressure curve fit at 145 Gev (negative)

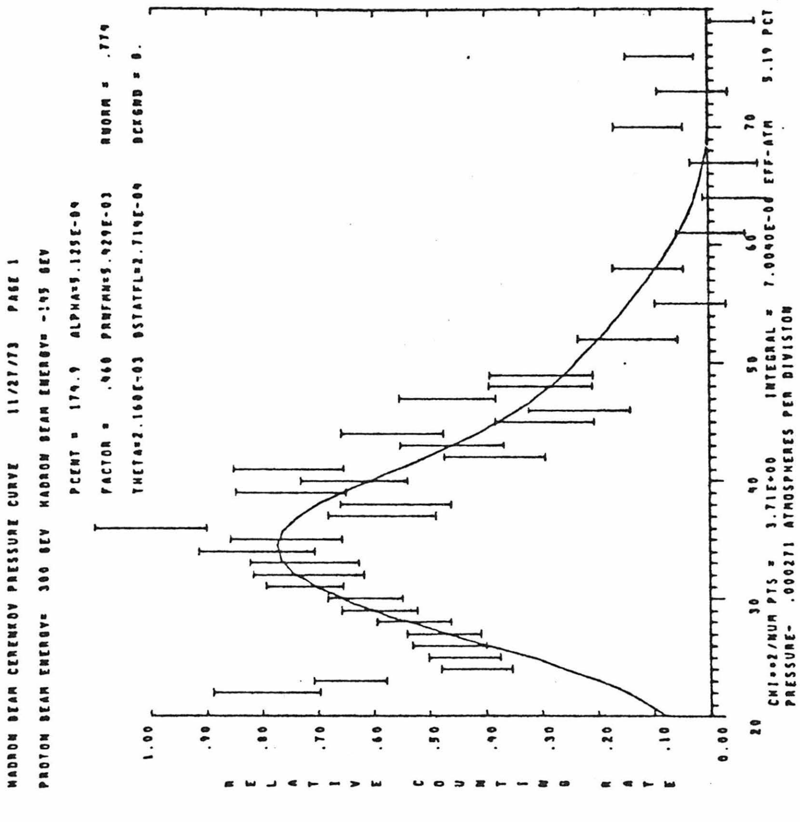

Figure 6.17 Kaon pressure curve fit at 145 Gev (negative)

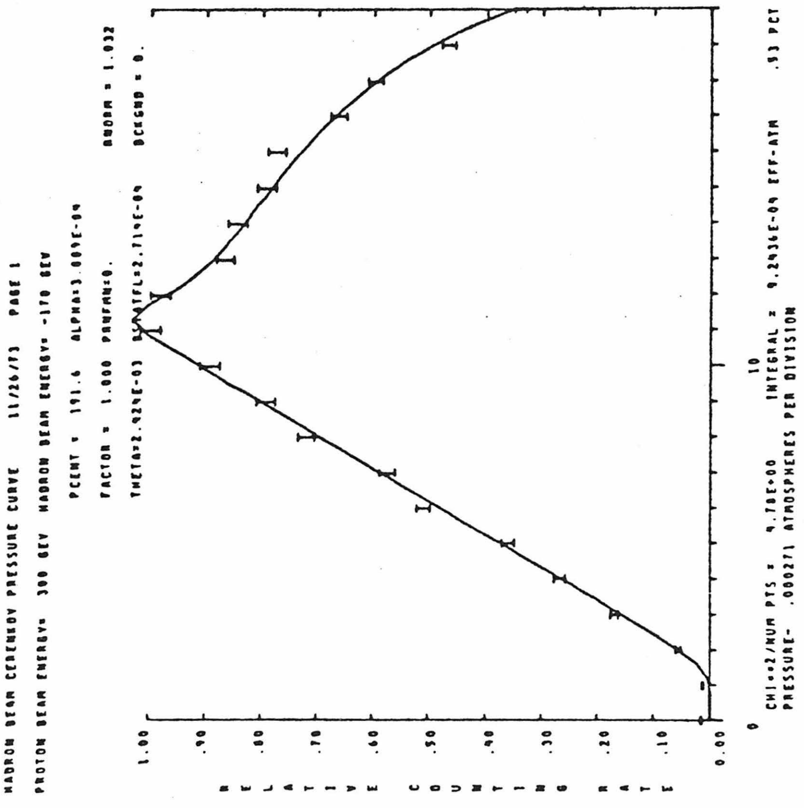

Figure 5.18 Pion pressure curve fit
at 170 Gev (negative)

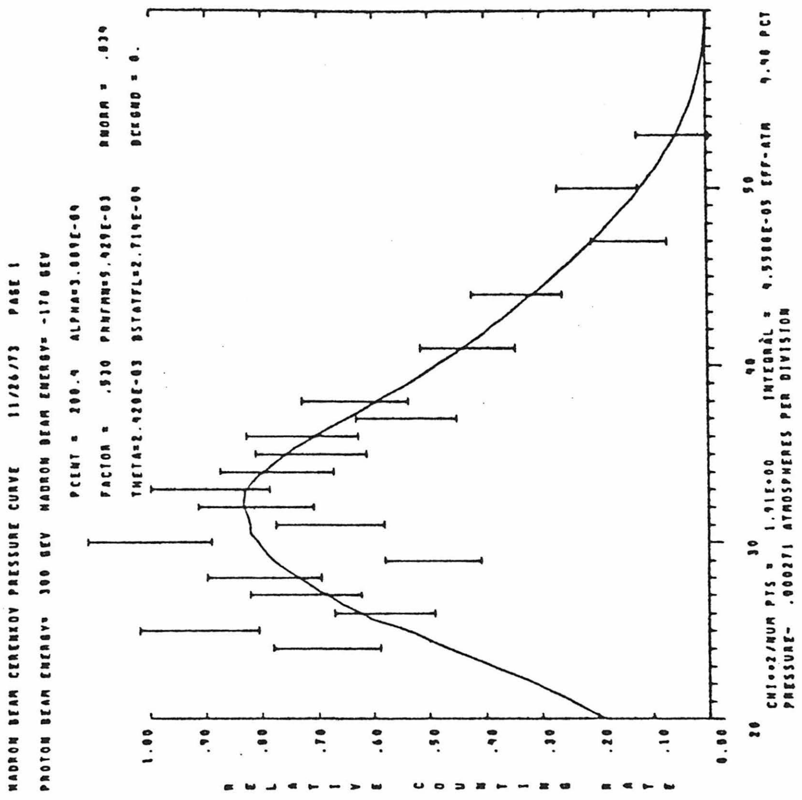

Figure 5.19 Kaon pressure curve fit
at 170 Gev (negative)

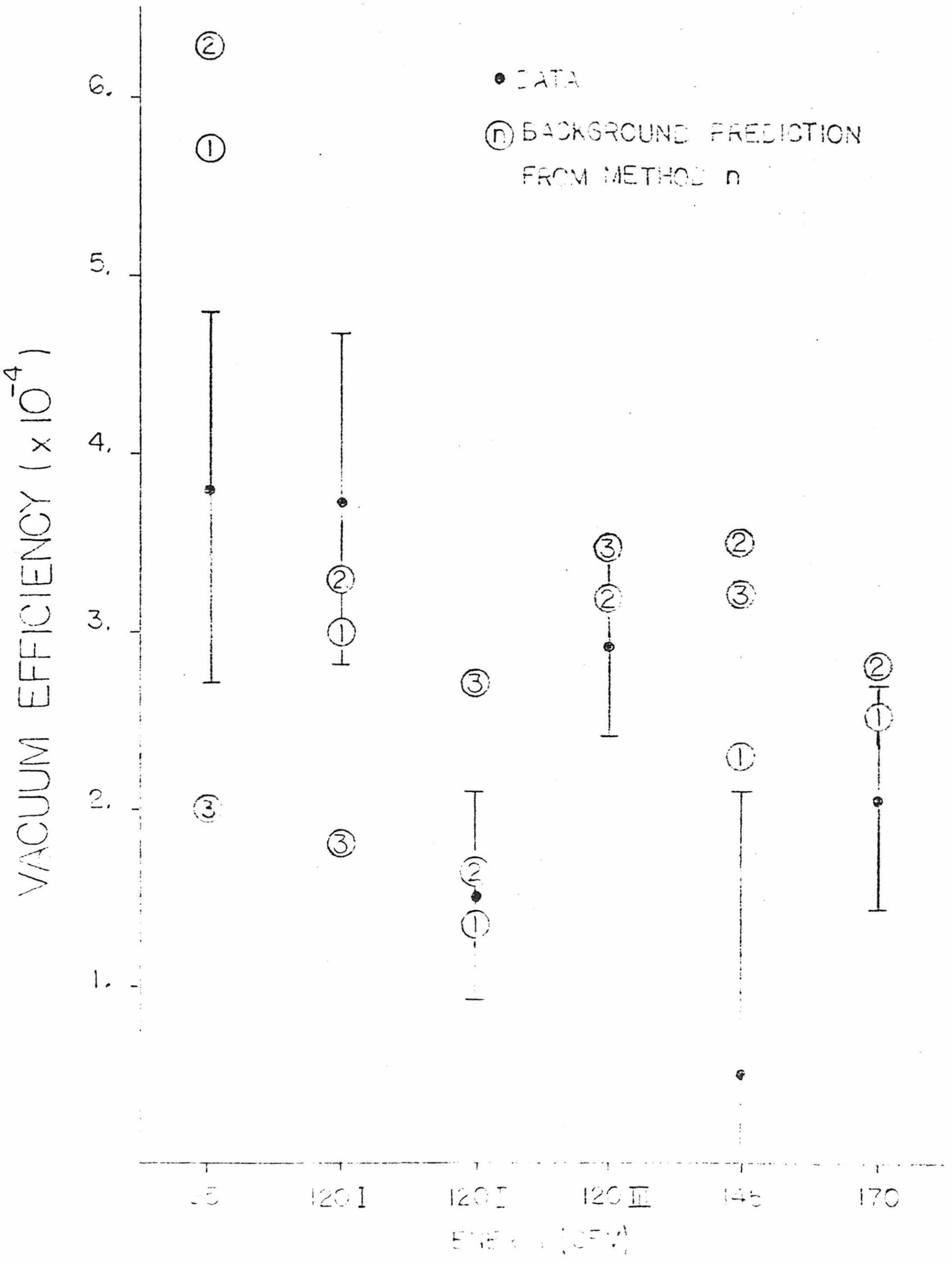

Figure 6.20 Attempts to predict vacuum level efficiency

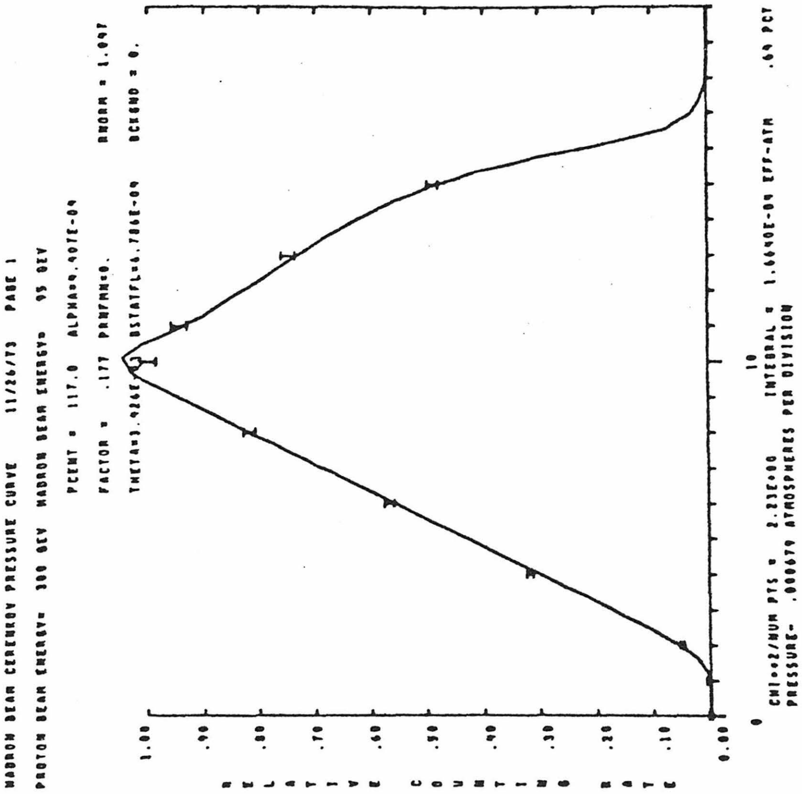

Figure 5.21 Pion pressure curve fit at 95 Gev (positive)

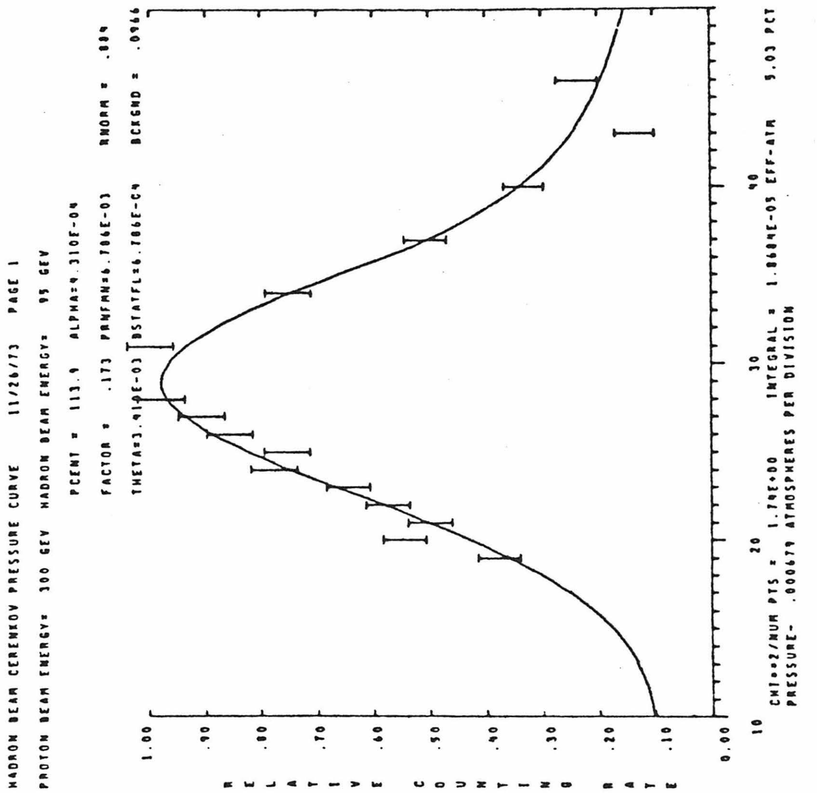

Figure 5.22 Kaon pressure curve fit at 95 Gev (positive)

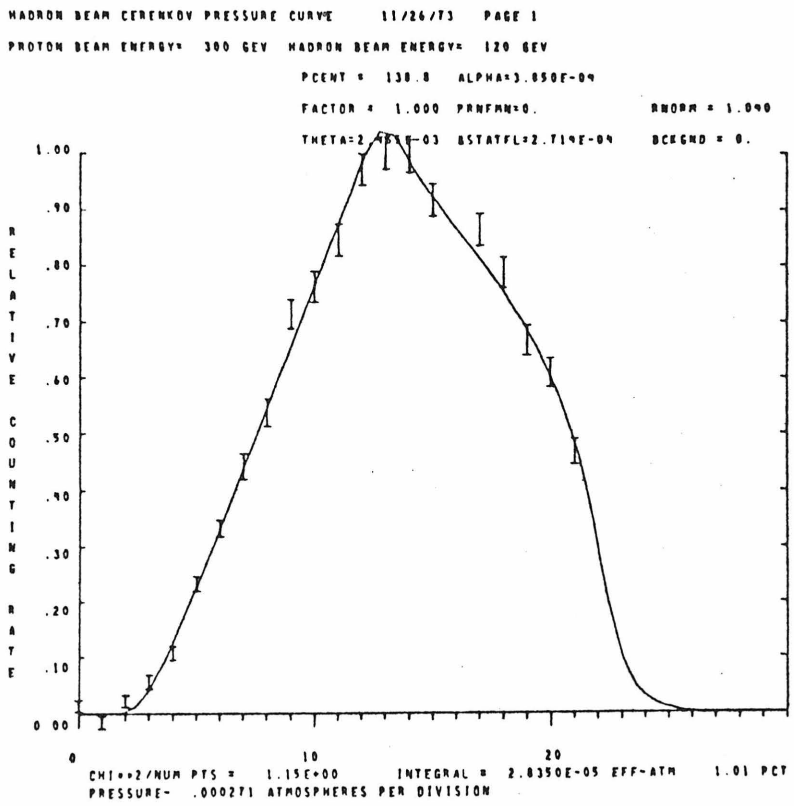

Figure 5.23 Pion pressure curve fit
at 120 Gev (positive) #1

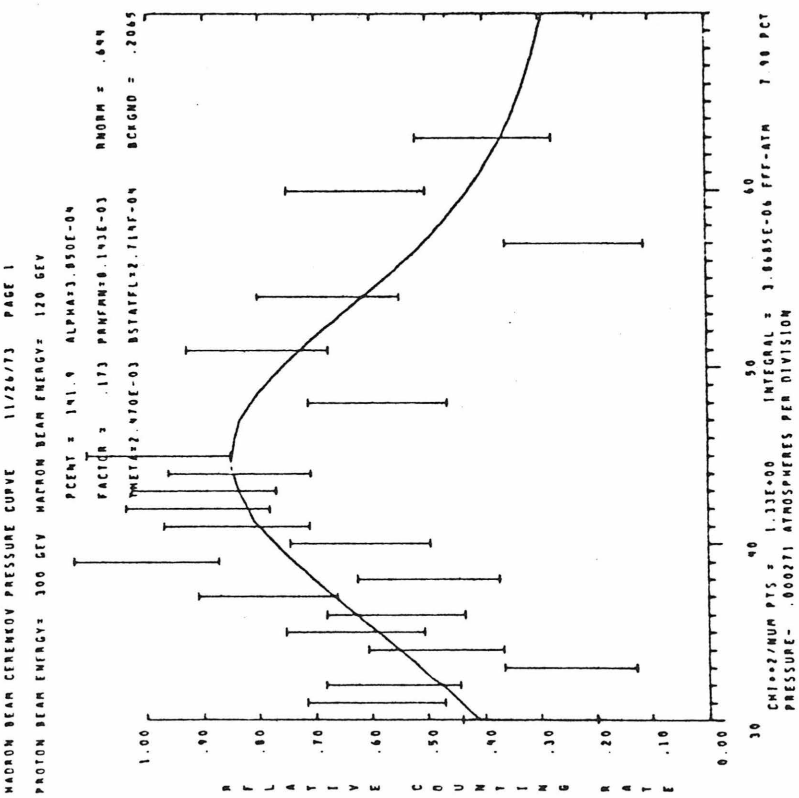

Figure 5.24 Kaon pressure curve fit
at 120 Gev (positive) #1

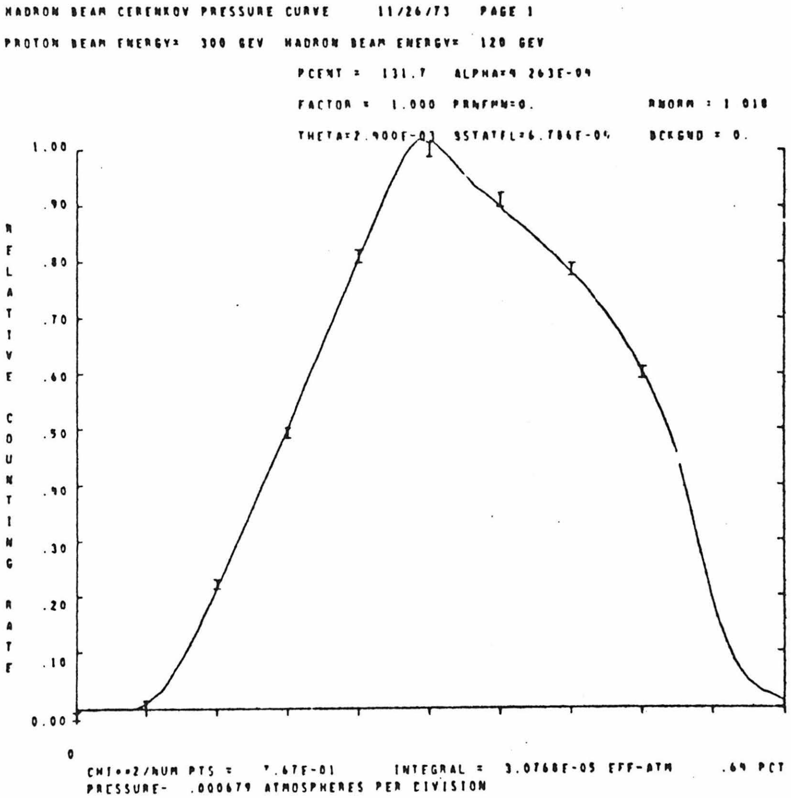

Figure 5.25 Pion pressure curve fit
at 120 Gev (positive) #2

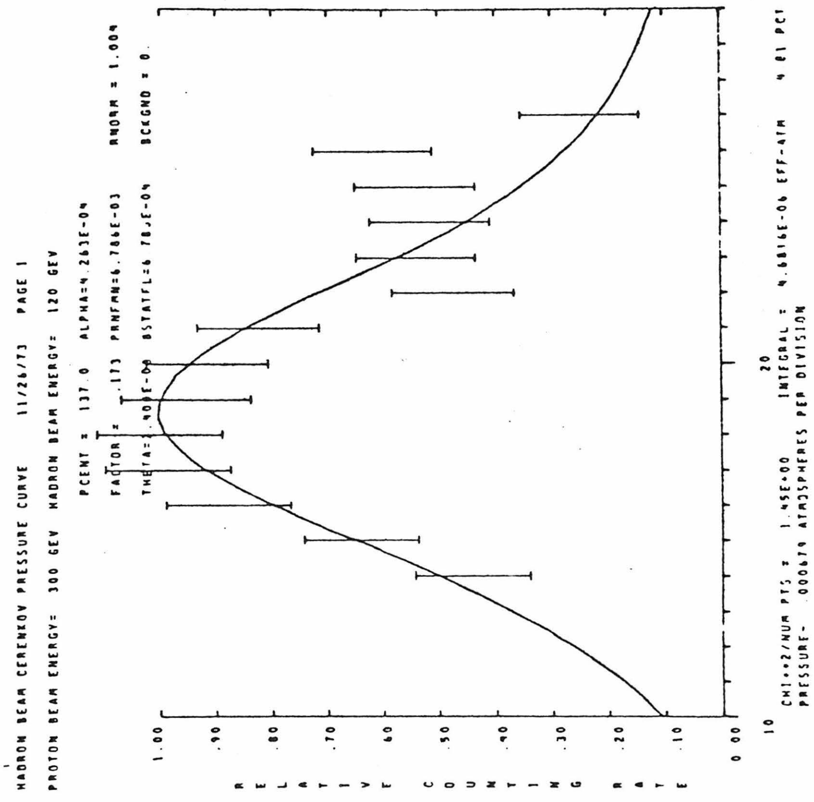

Figure 5.26 Kaon pressure curve fit
at 120 Gev (positive) #2

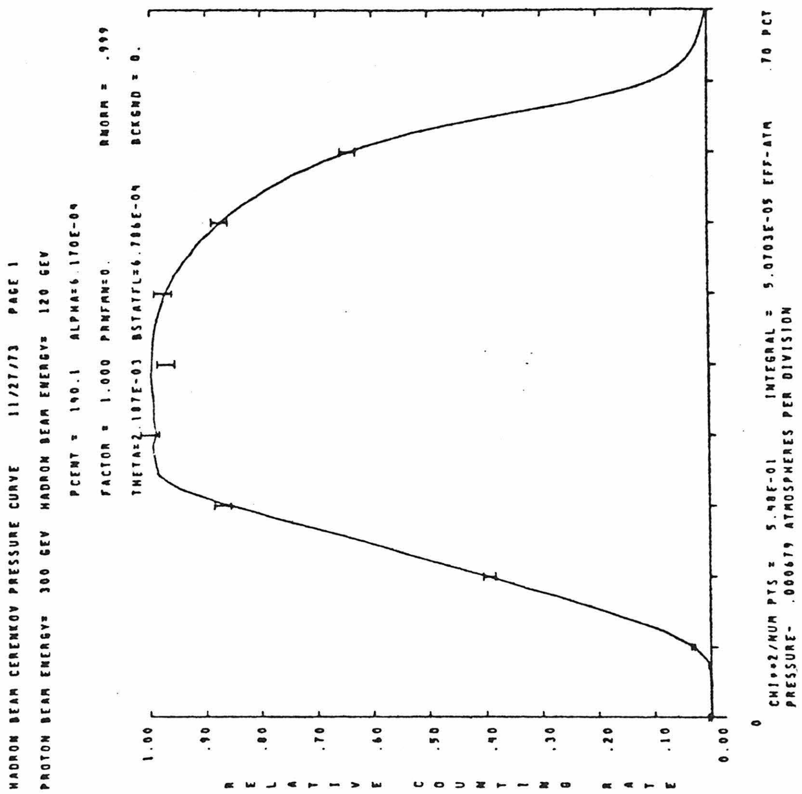

Figure 5.27 Pion pressure curve fit at 120 Gev (positive) #3

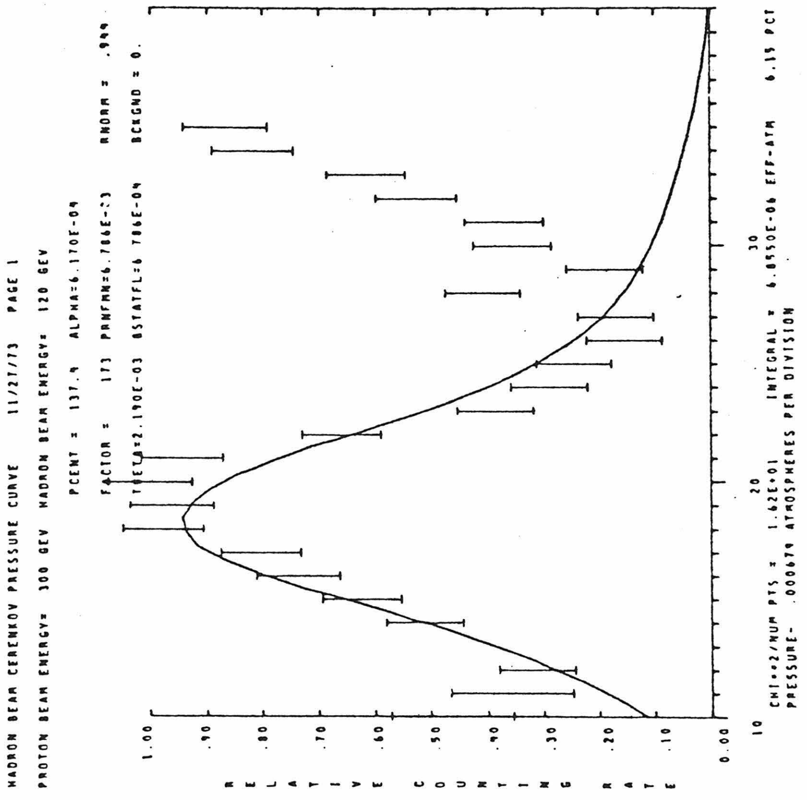

Figure 6.28 Kaon pressure curve fit
at 120 Gev (positive) #3

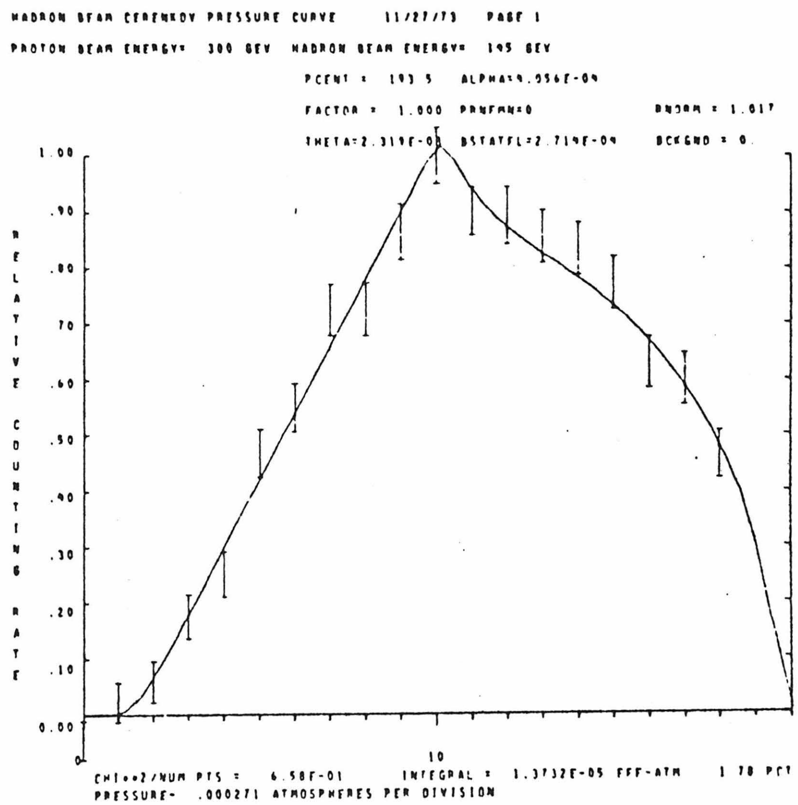

Figure 5.29 Pion pressure curve fit at 145 Gev (positive)

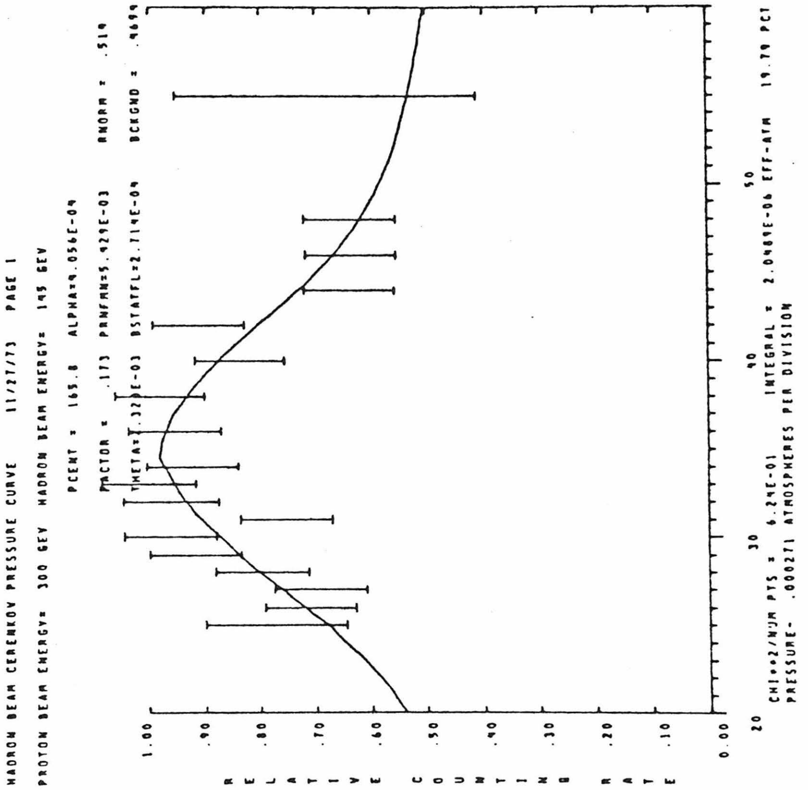

Figure 5.30 Kaon pressure curve fit at 145 Gev (positive)

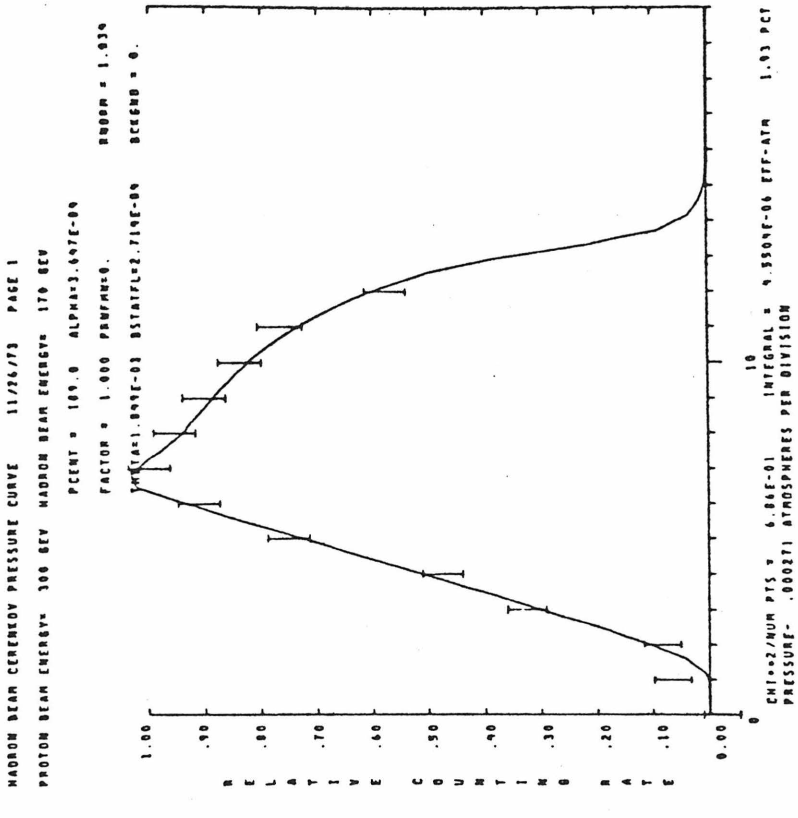

Figure 5.31 Pion pressure curve fit at 170 Gev (positive)

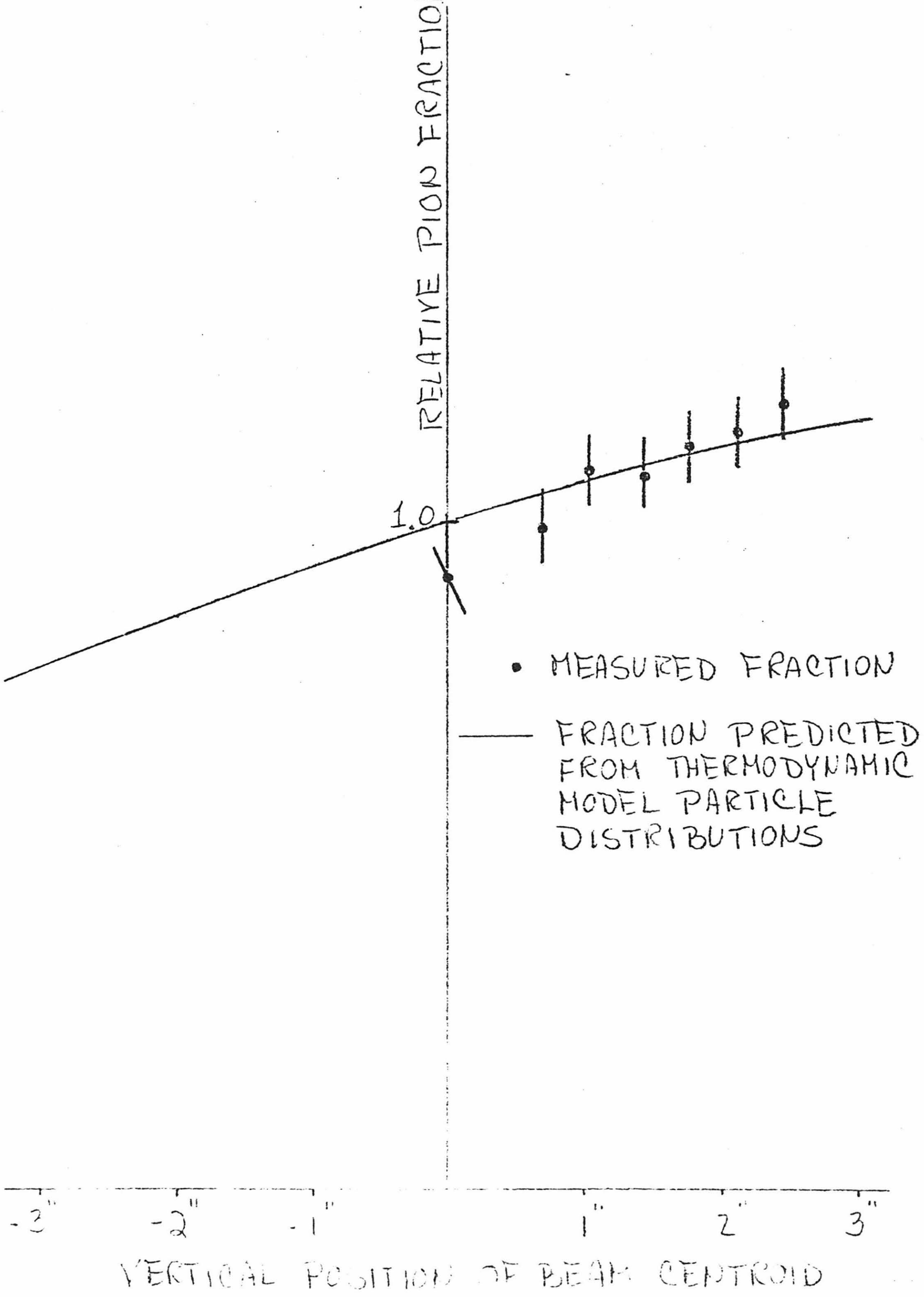

FIG. 5 32 PION FRACTION VS BEAM HEIGHT

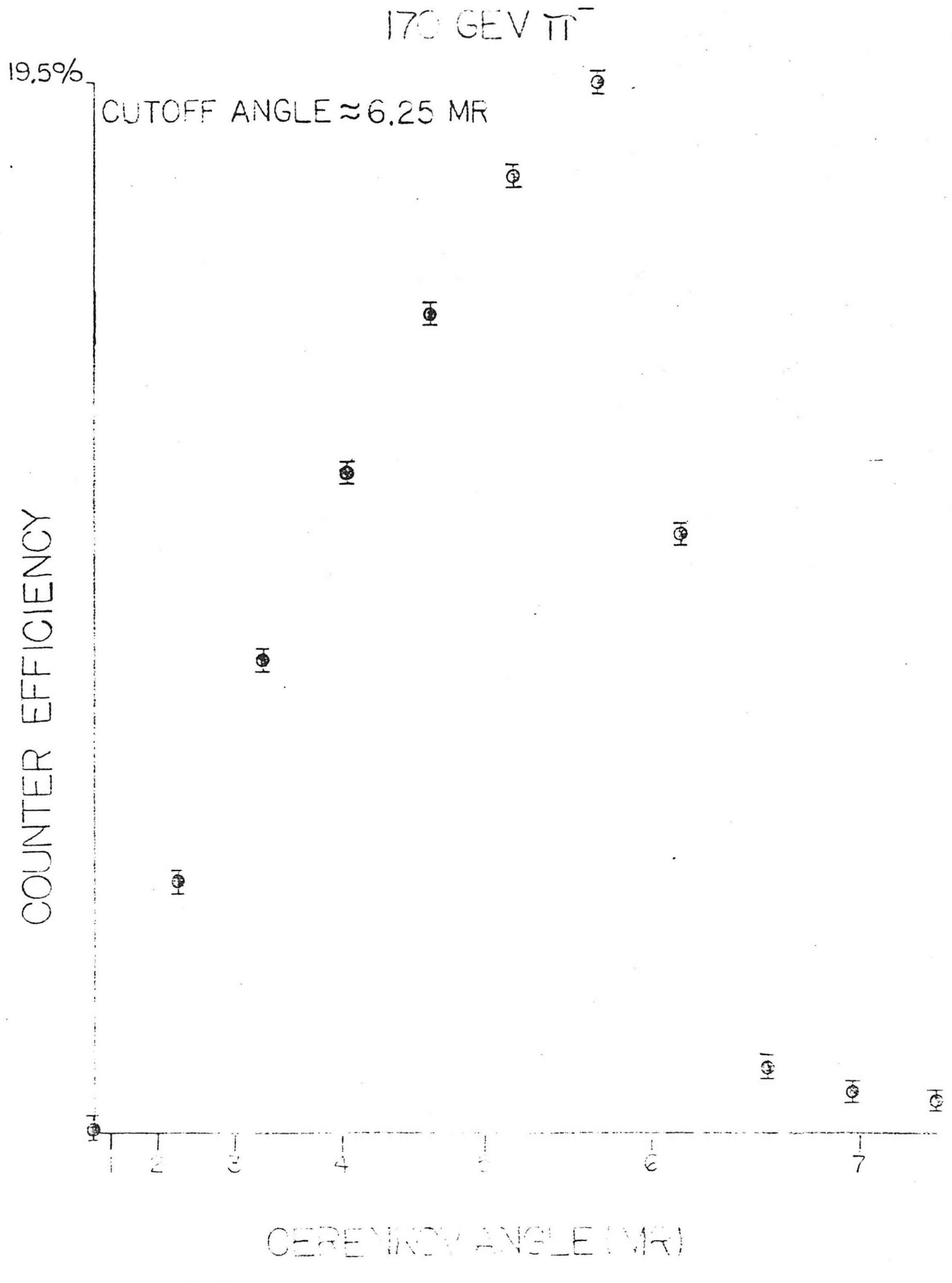

Figure 6.1 170 Gev pion Cerenkov pressure curve

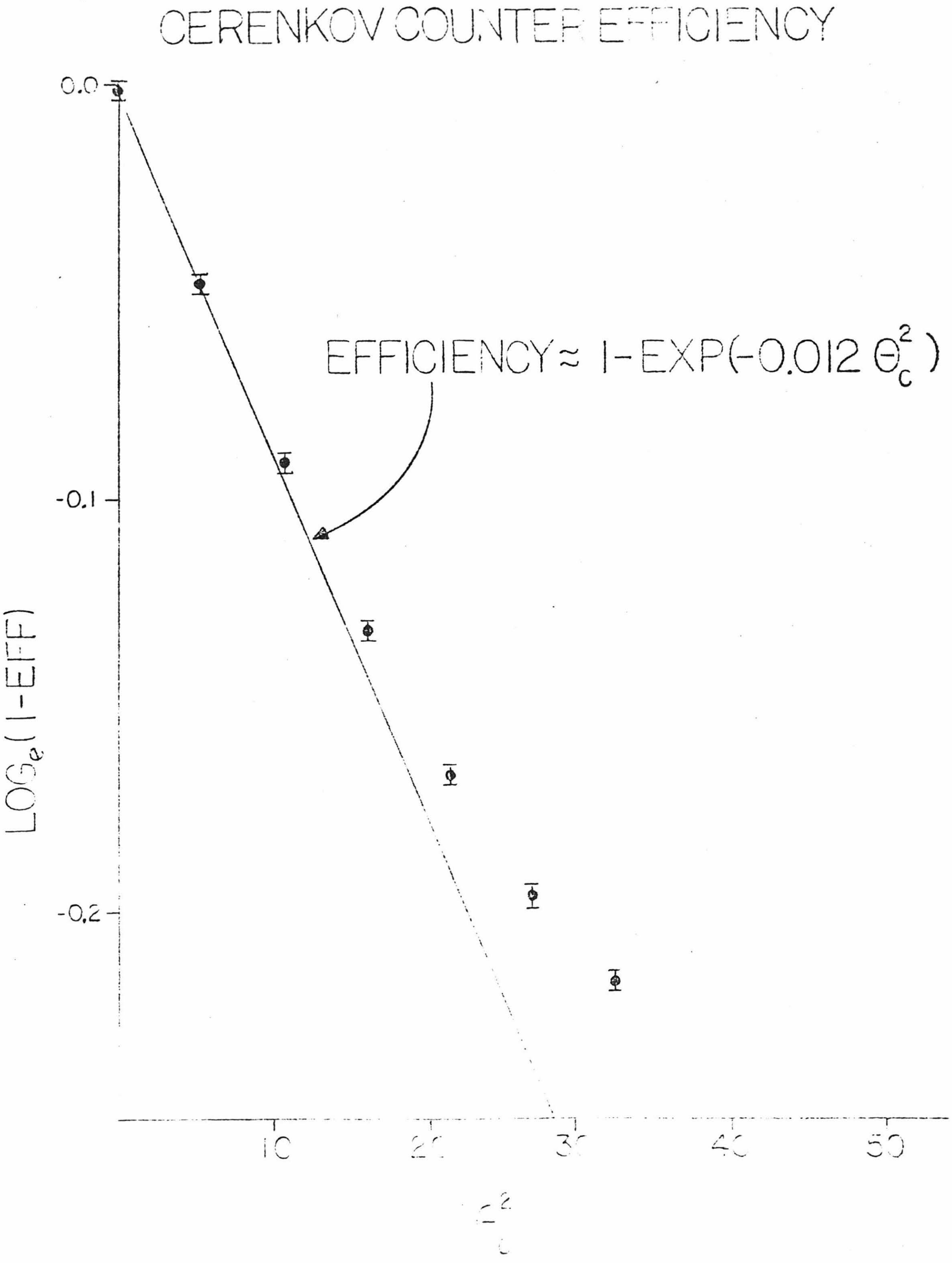

Figure 6.2 Cerenkov counter efficiency versus Cerenkov angle

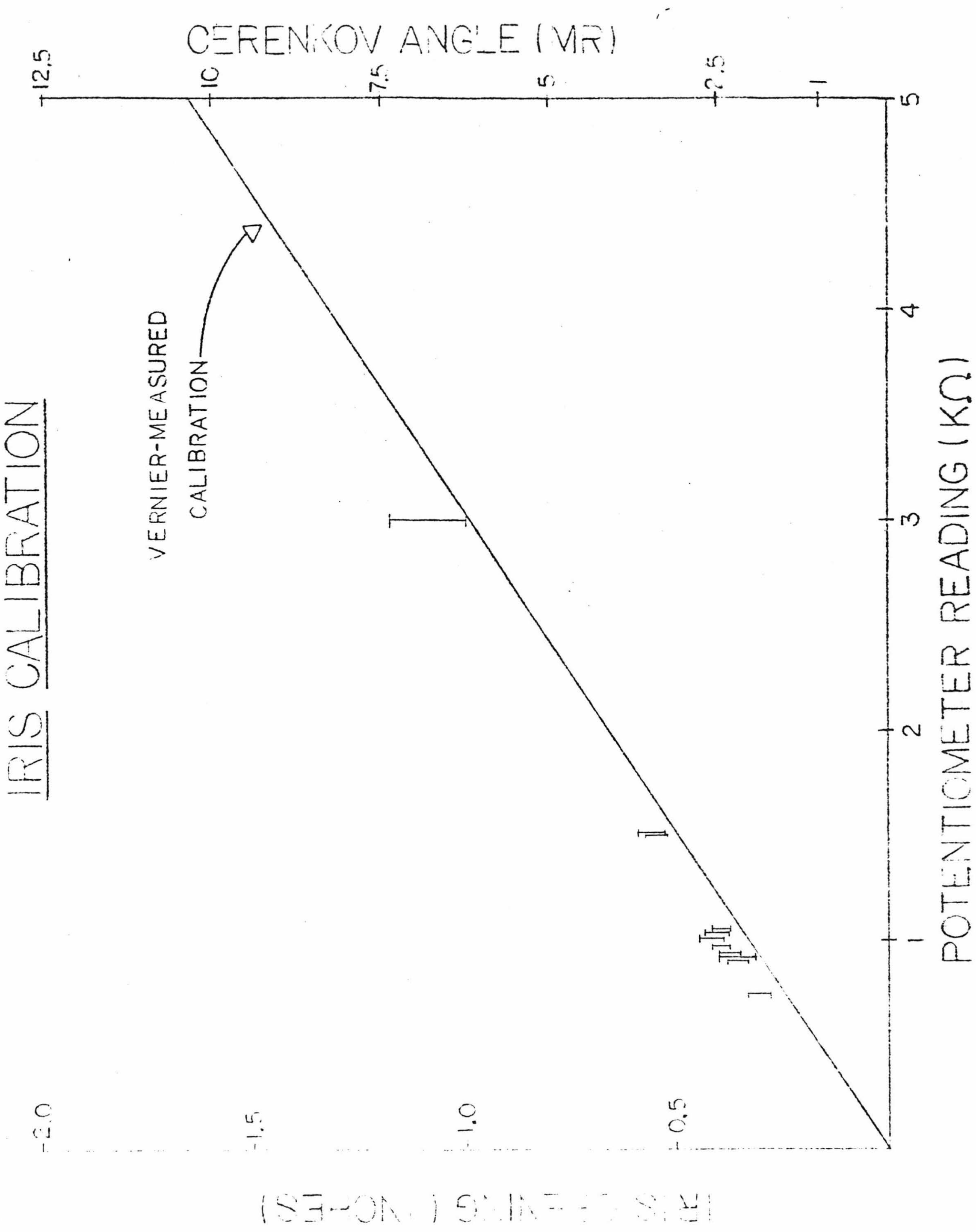

Figure 6.3 Iris calibration

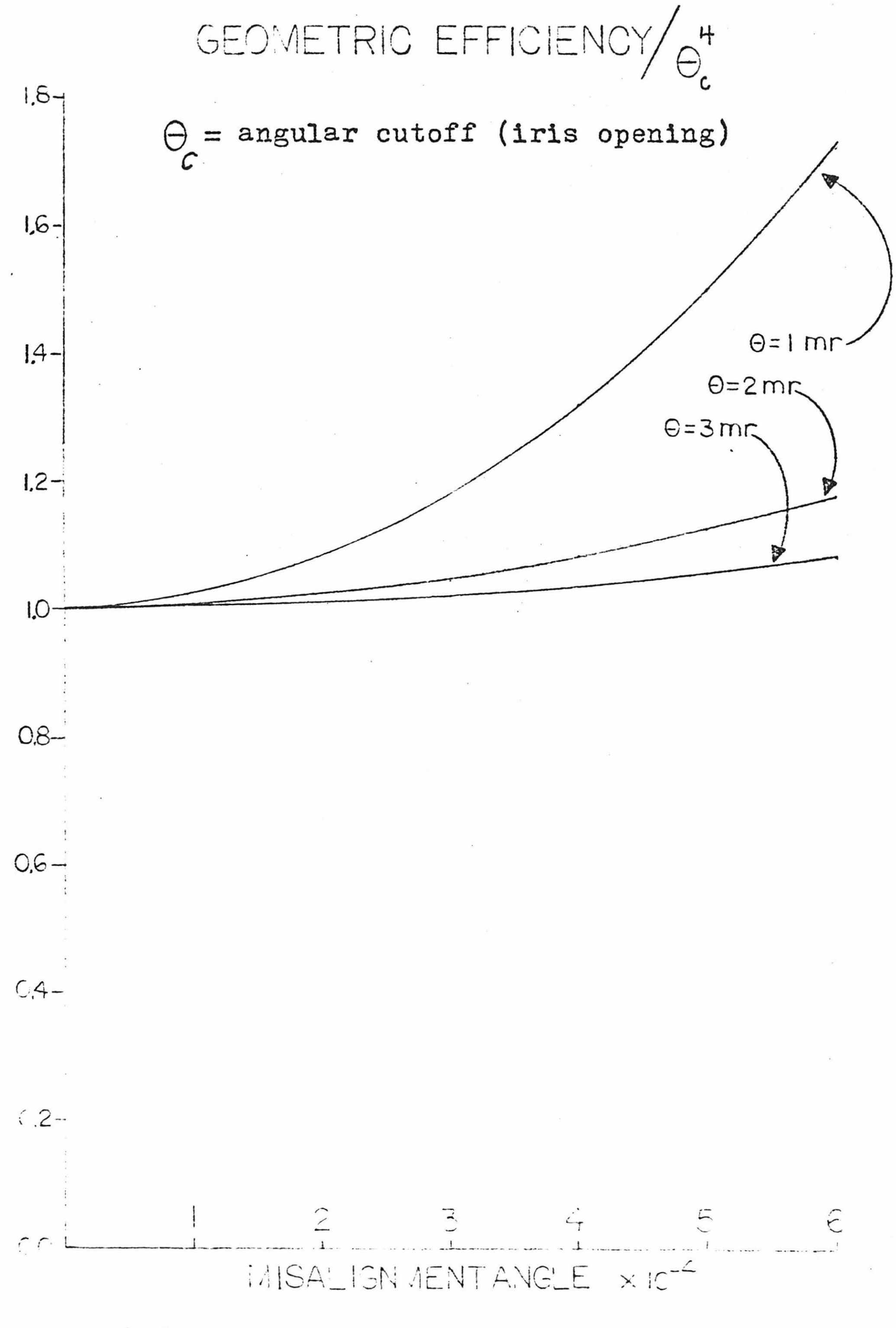

Figure 6.4 Geometric efficiency versus misalignment

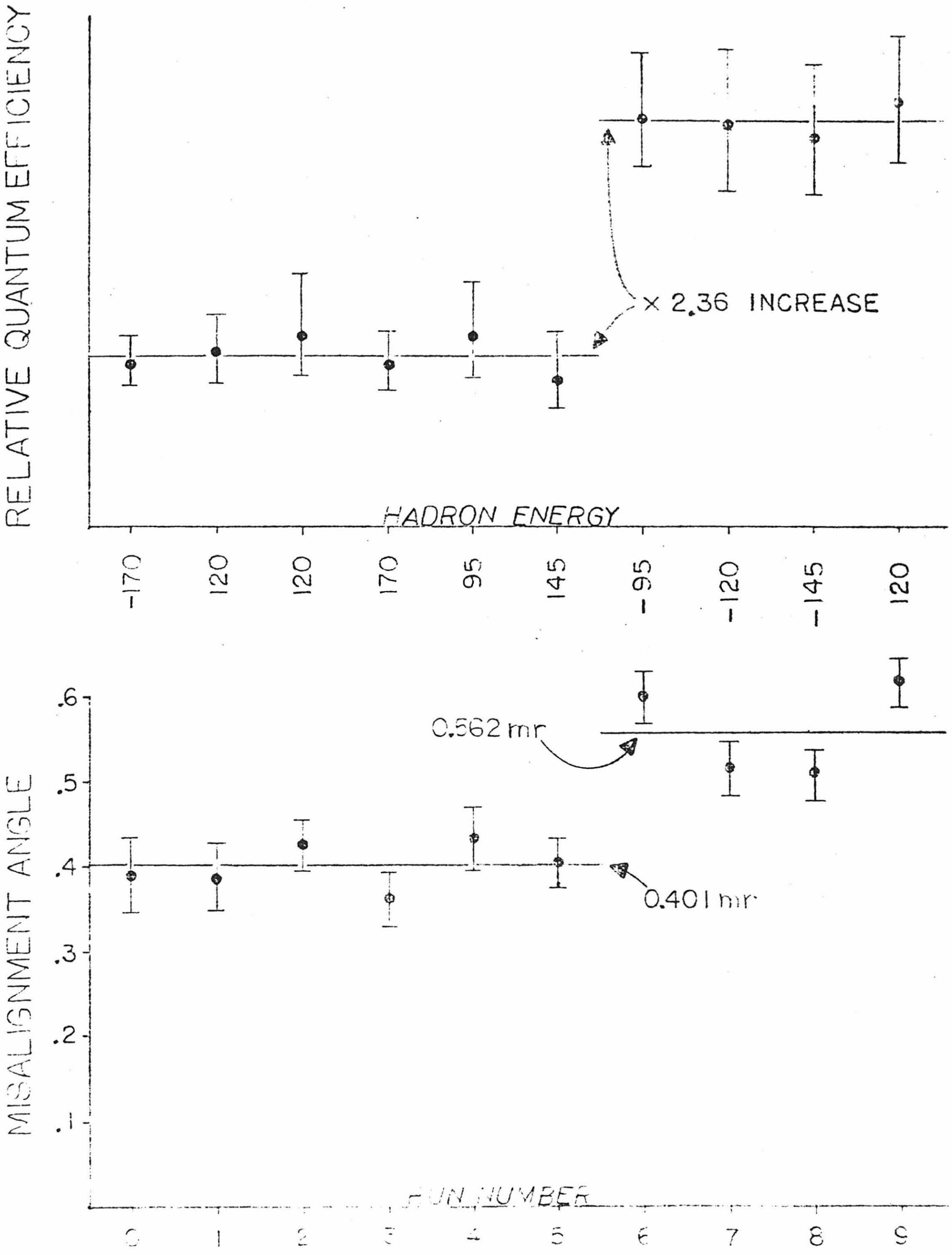

Figure 6.5 Relative quantum efficiency and misalignment angle for each run

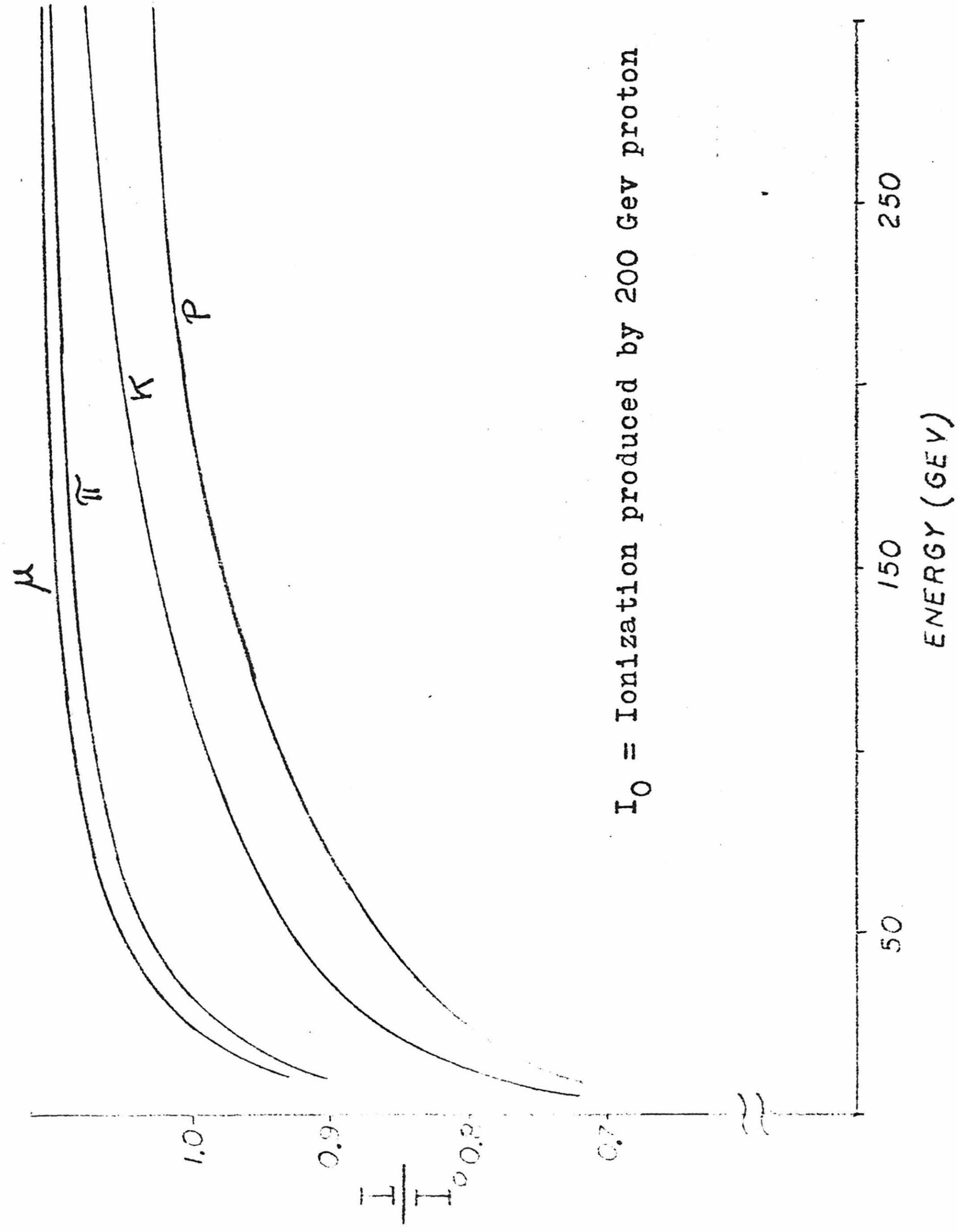

Figure 7.1 Ionization rise versus energy

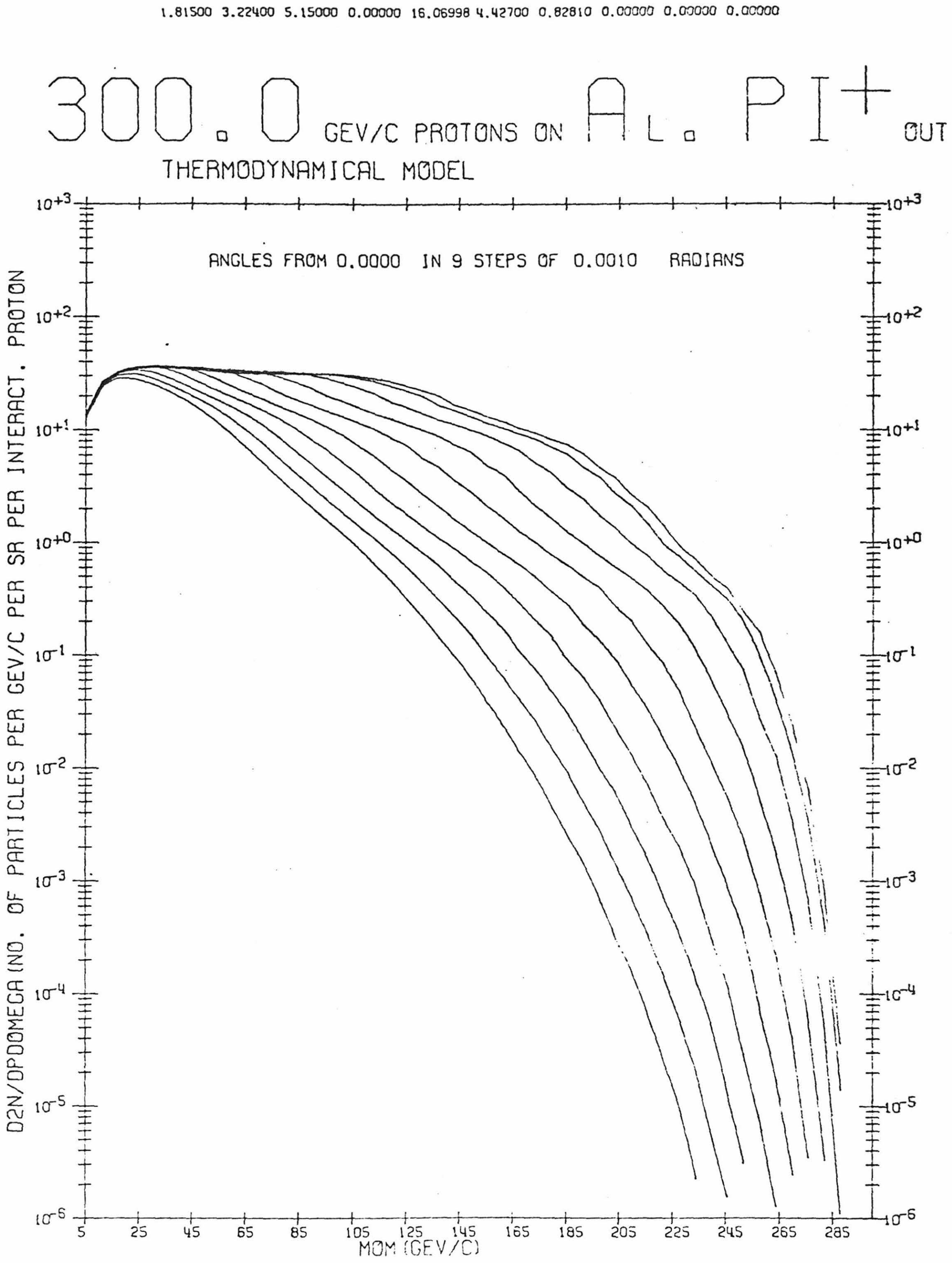

Figure 8.1 Thermodynamic Model prediction for π^+

2.76800 4.95200 0.00000 0.00000 0.00000 0.00000 0.00000 0.00000 0.00000 0.00000

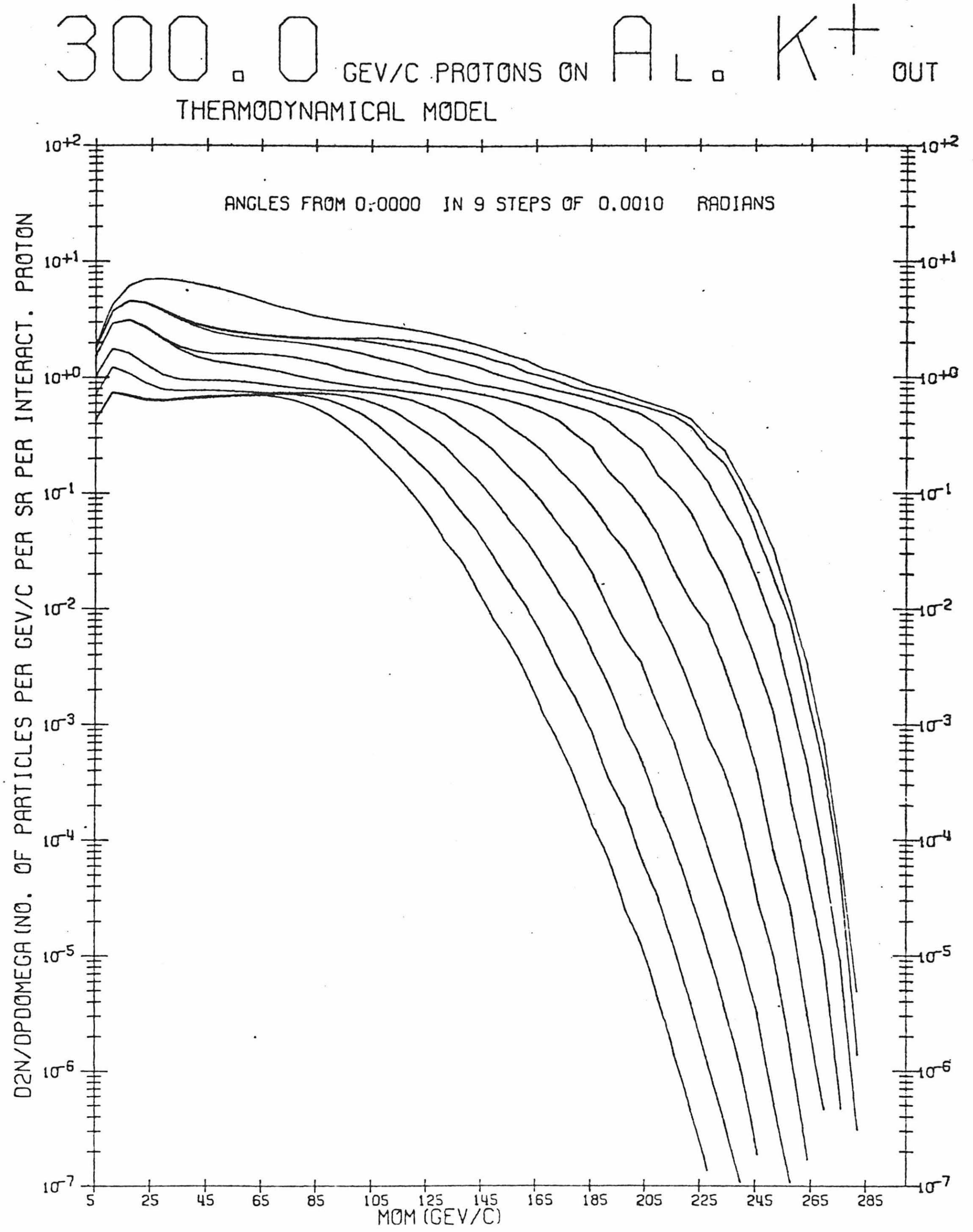

Figure 8.2 Thermodynamic Model prediction for K^+

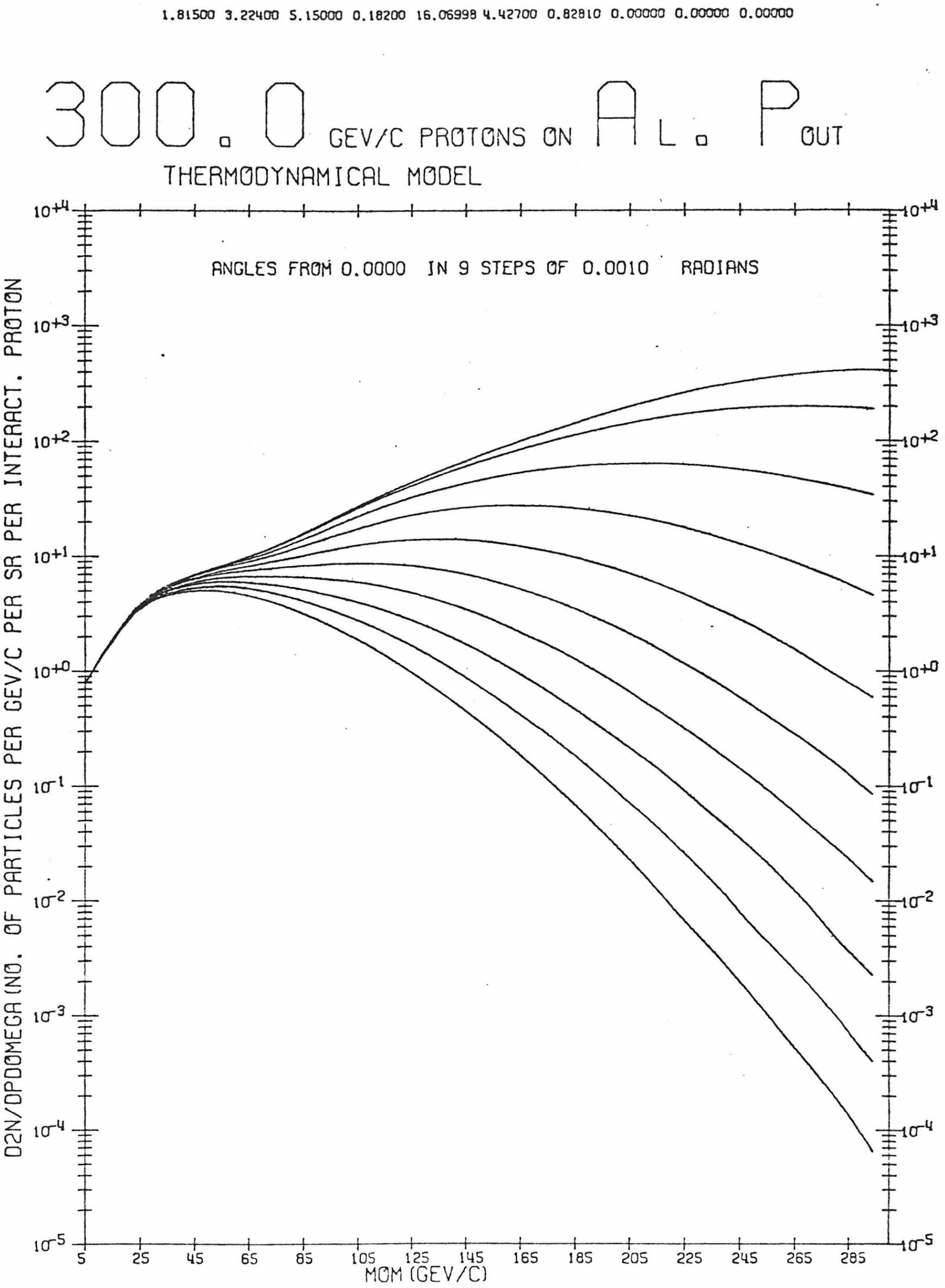

Figure 8.3 Thermodynamic Model prediction for protons

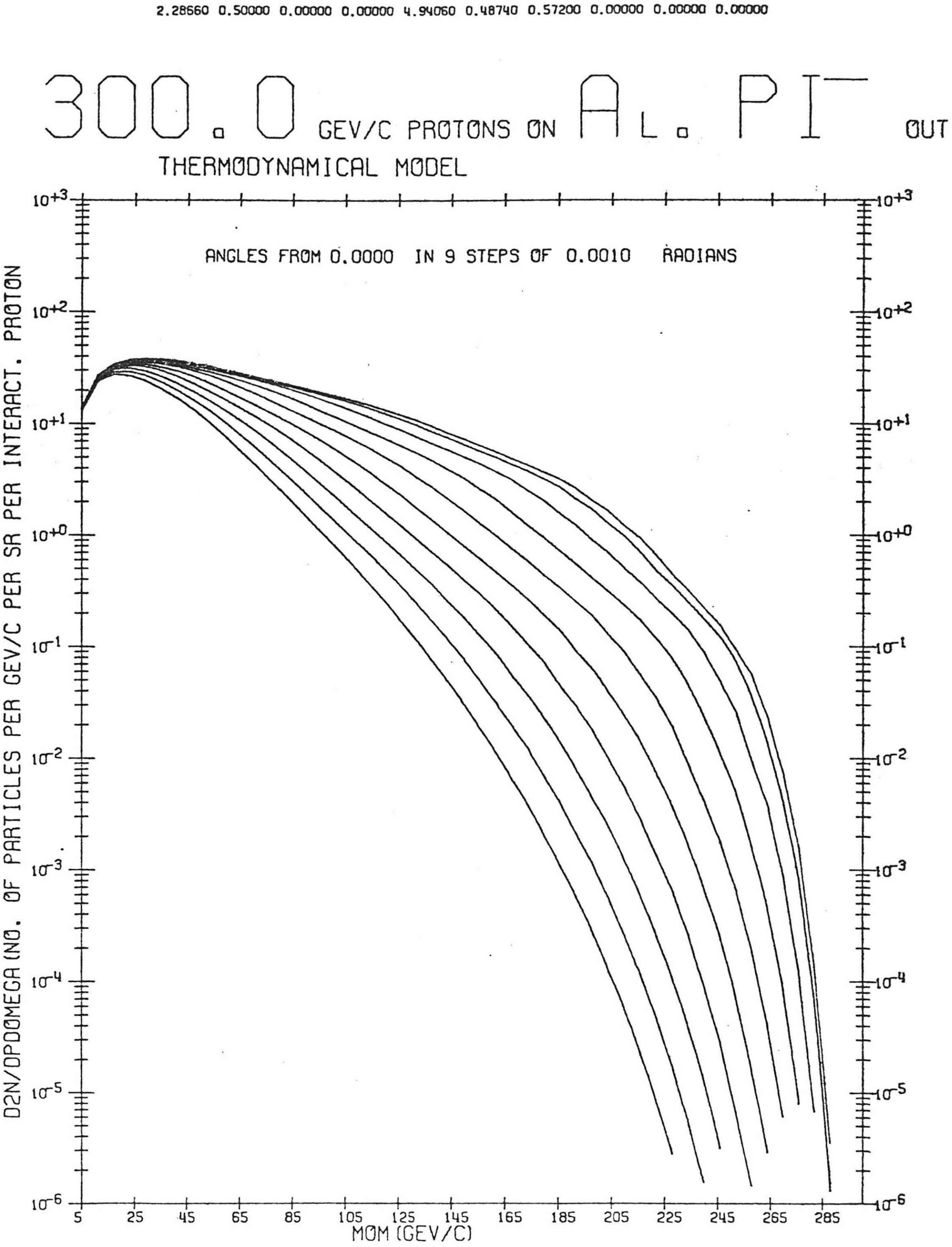

Figure 8.4 Thermodynamic Model prediction for π^-

0.00000 0.00000 5.43450 0.50000 4.94060 0.00000 0.57200 0.00000 0.00000 0.00000

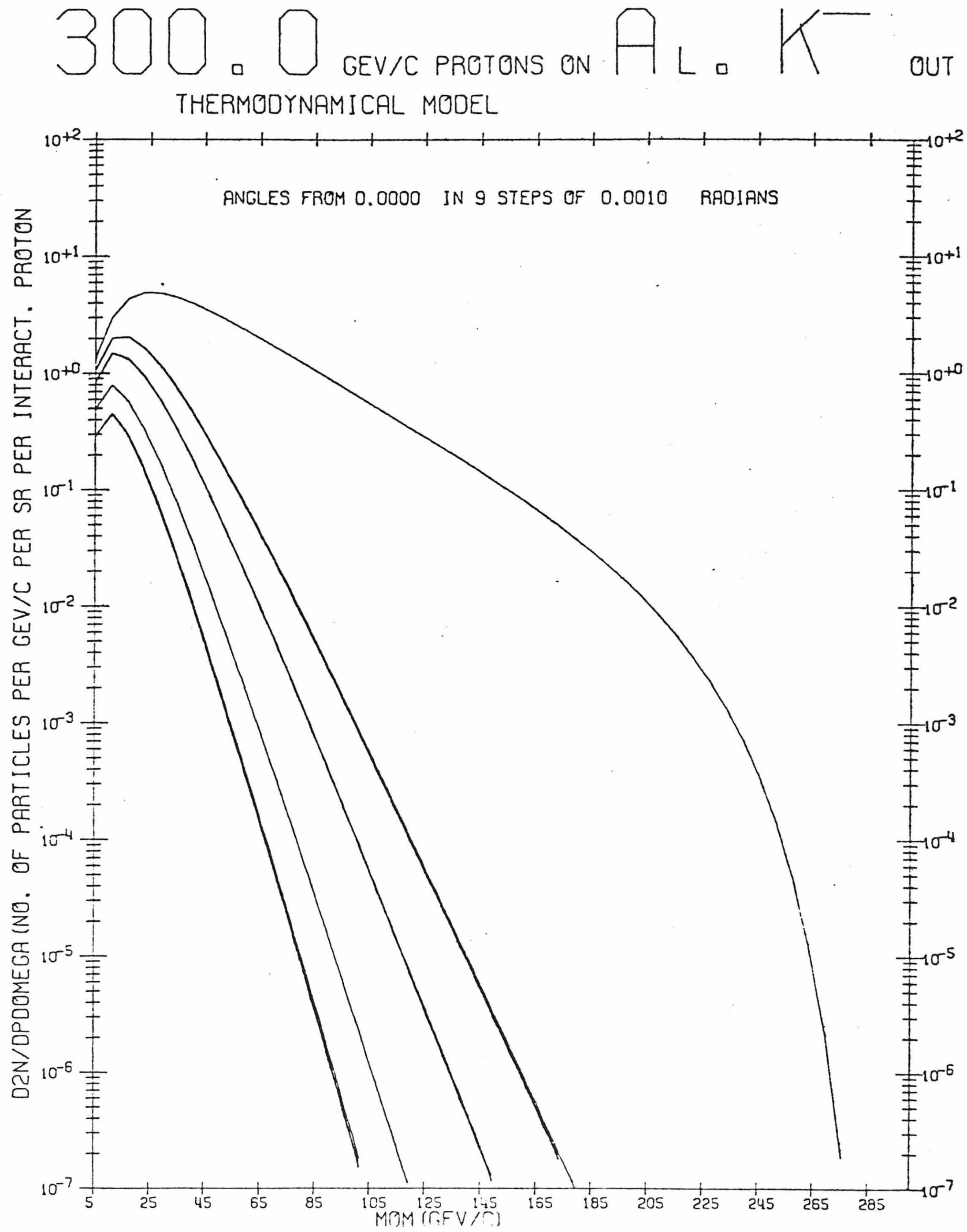

Figure 8.5 Thermodynamic Model prediction for K^-

0.00000 0.00000 6.26170 0.50000 4.94050 0.00000 0.57200 0.00000 0.00000 0.00000

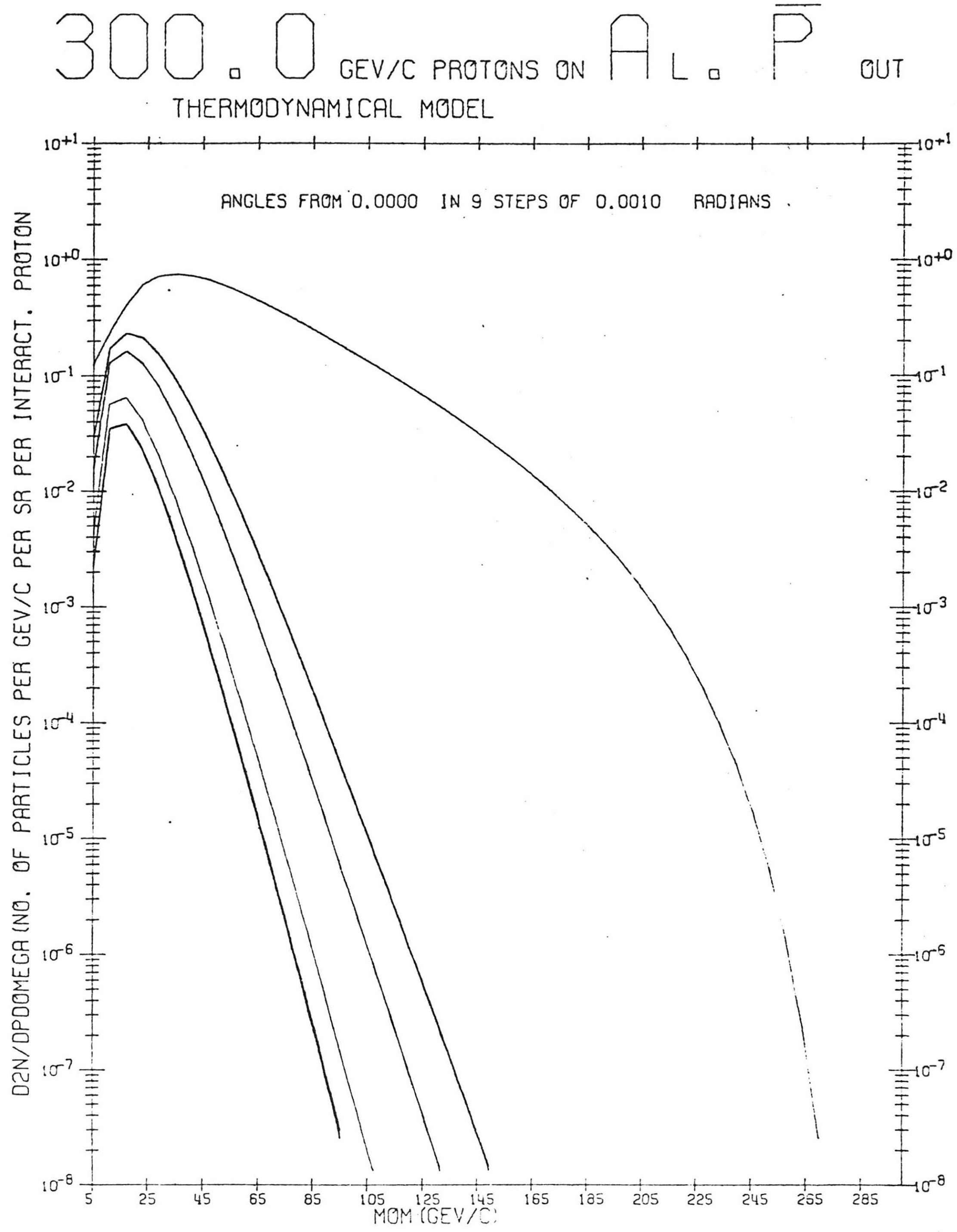

Figure 8.6 Thermodynamic Model prediction for $\overline{P}$

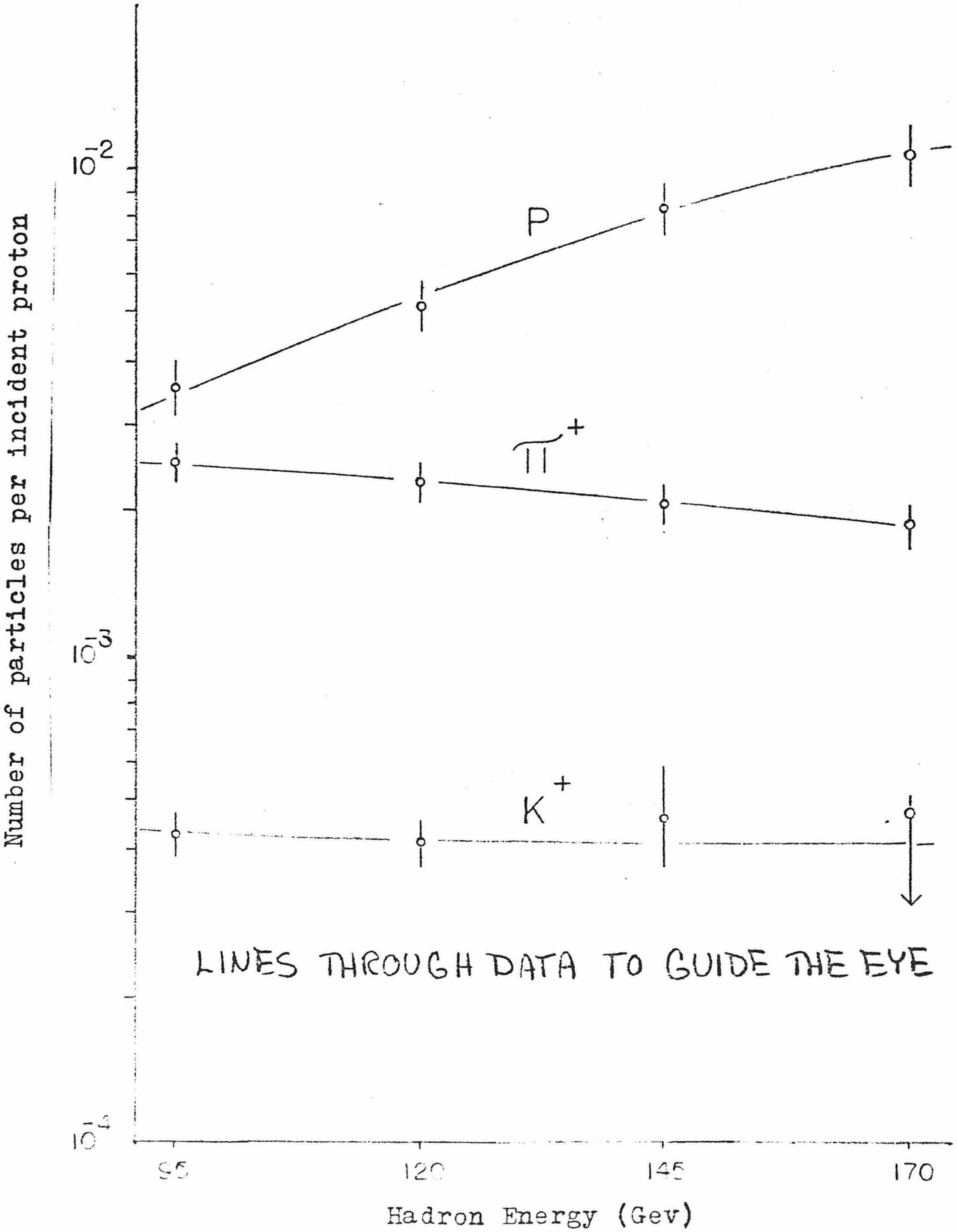

Figure 9.1 Positive particle yields

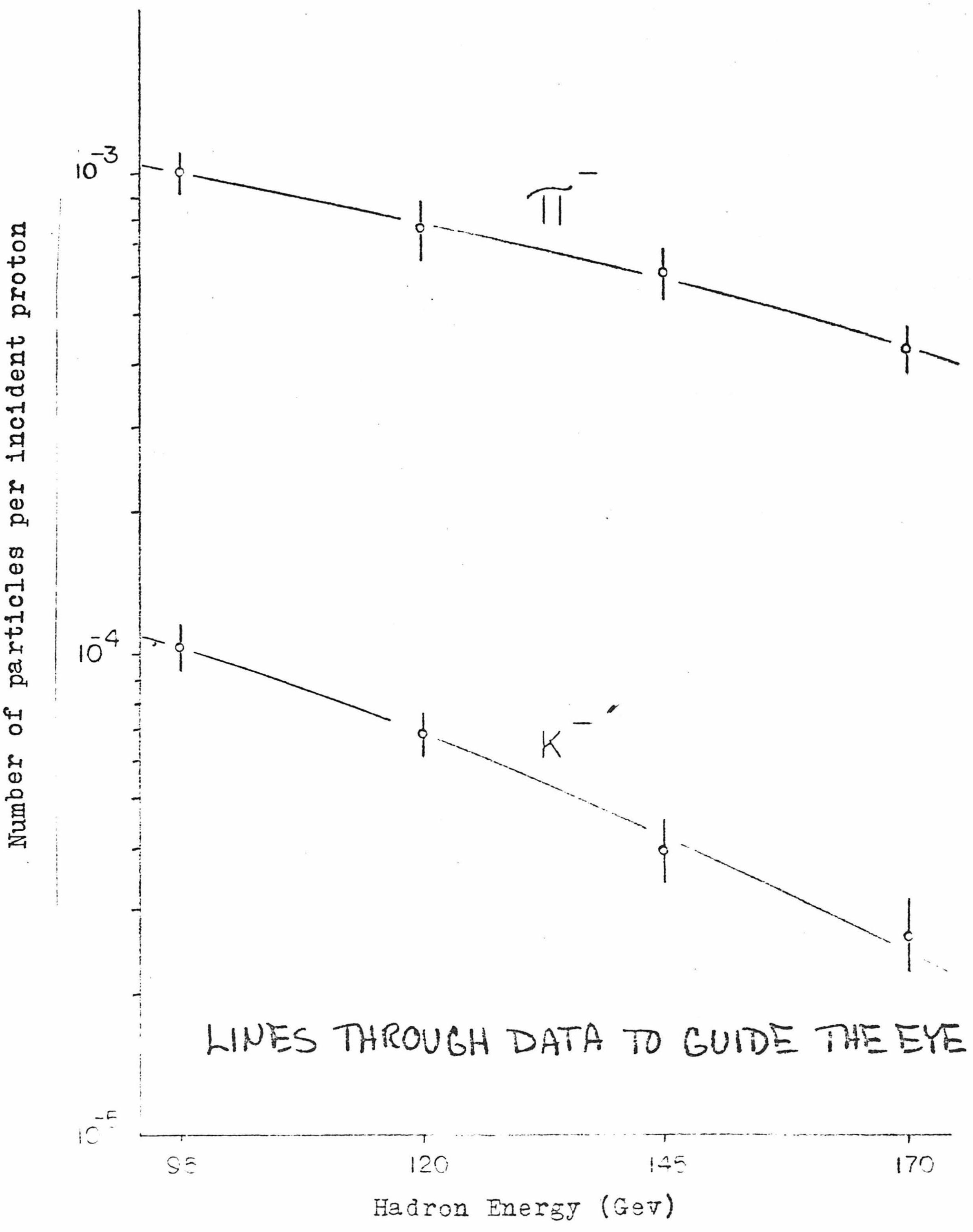

Figure 9.2 Negative particle yields

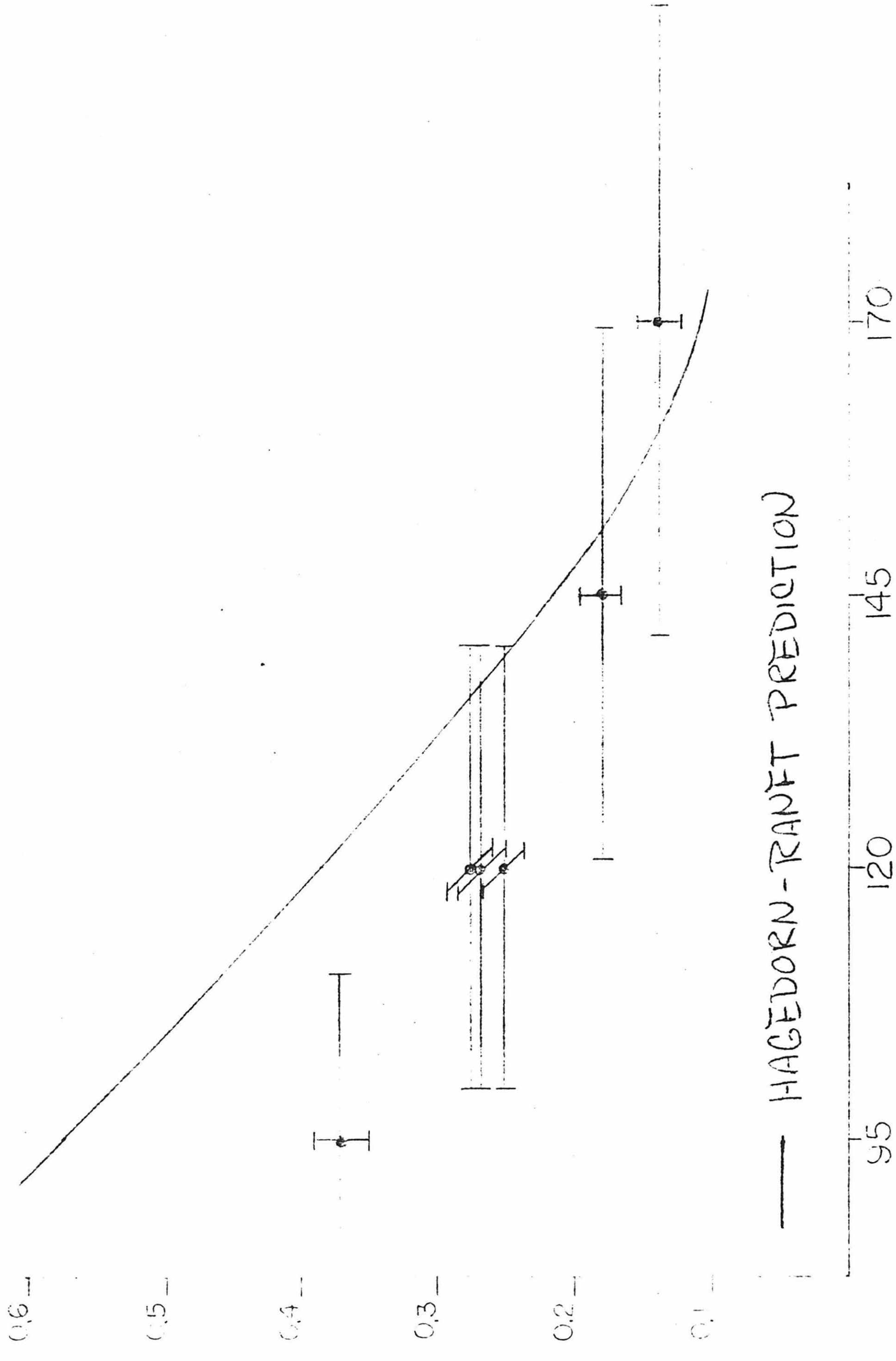

Figure 9.3 π^+ fraction at target

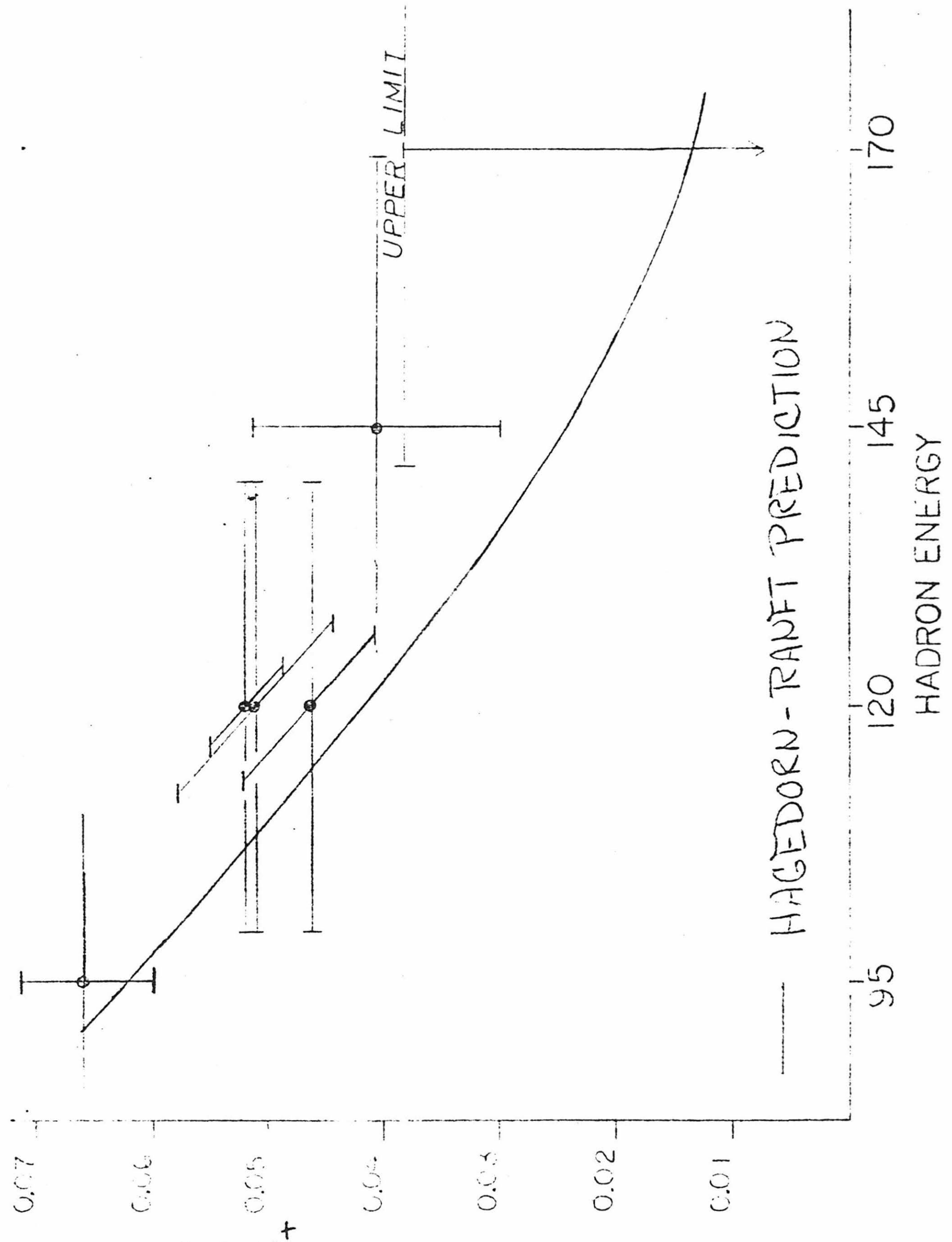

Figure 9.4 K^+ fraction at target

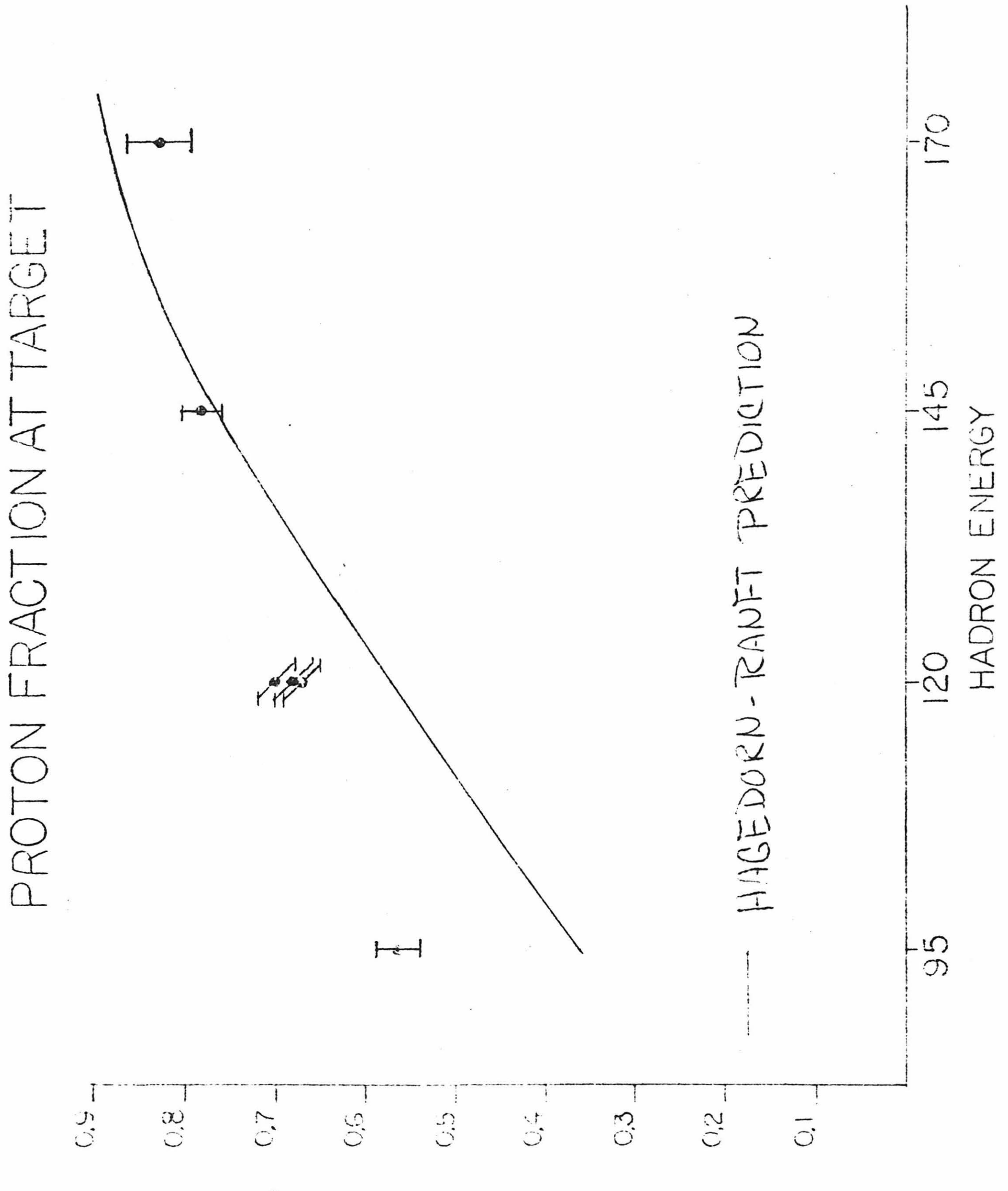

Figure 9.5 Proton fraction at target

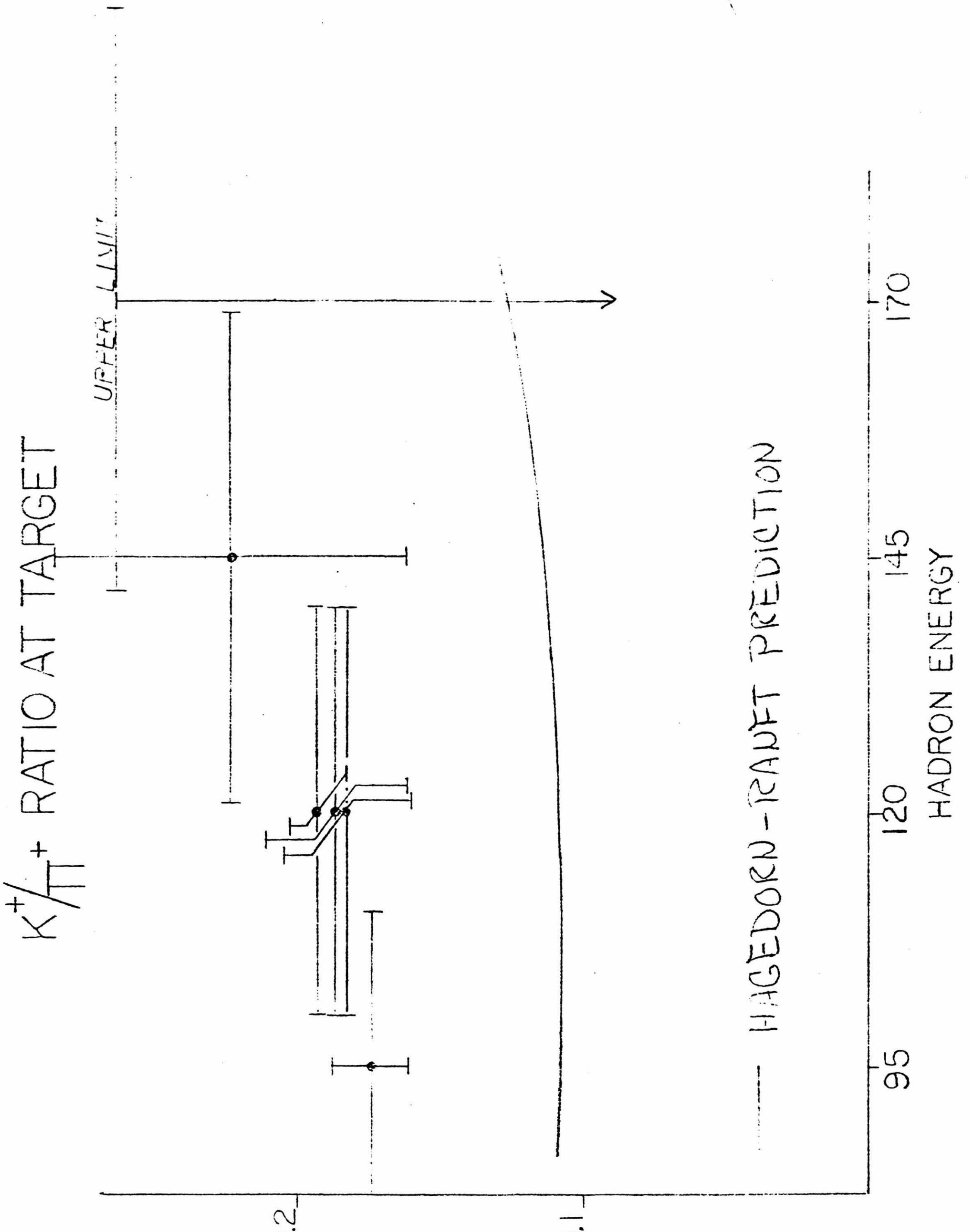

Figure 9.6 K^+/π^+ ratio at target

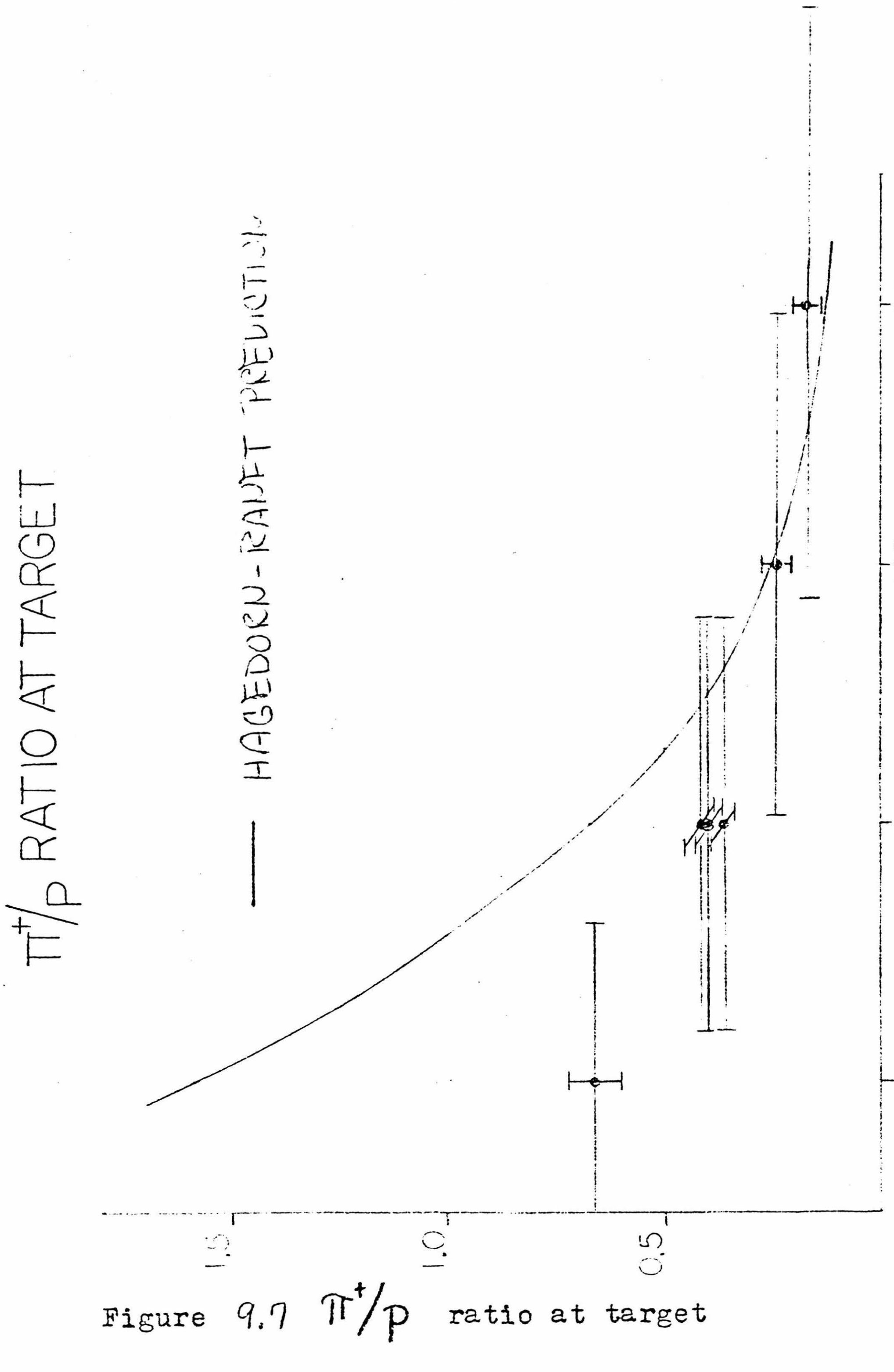

Figure 9.7 π^+/p ratio at target

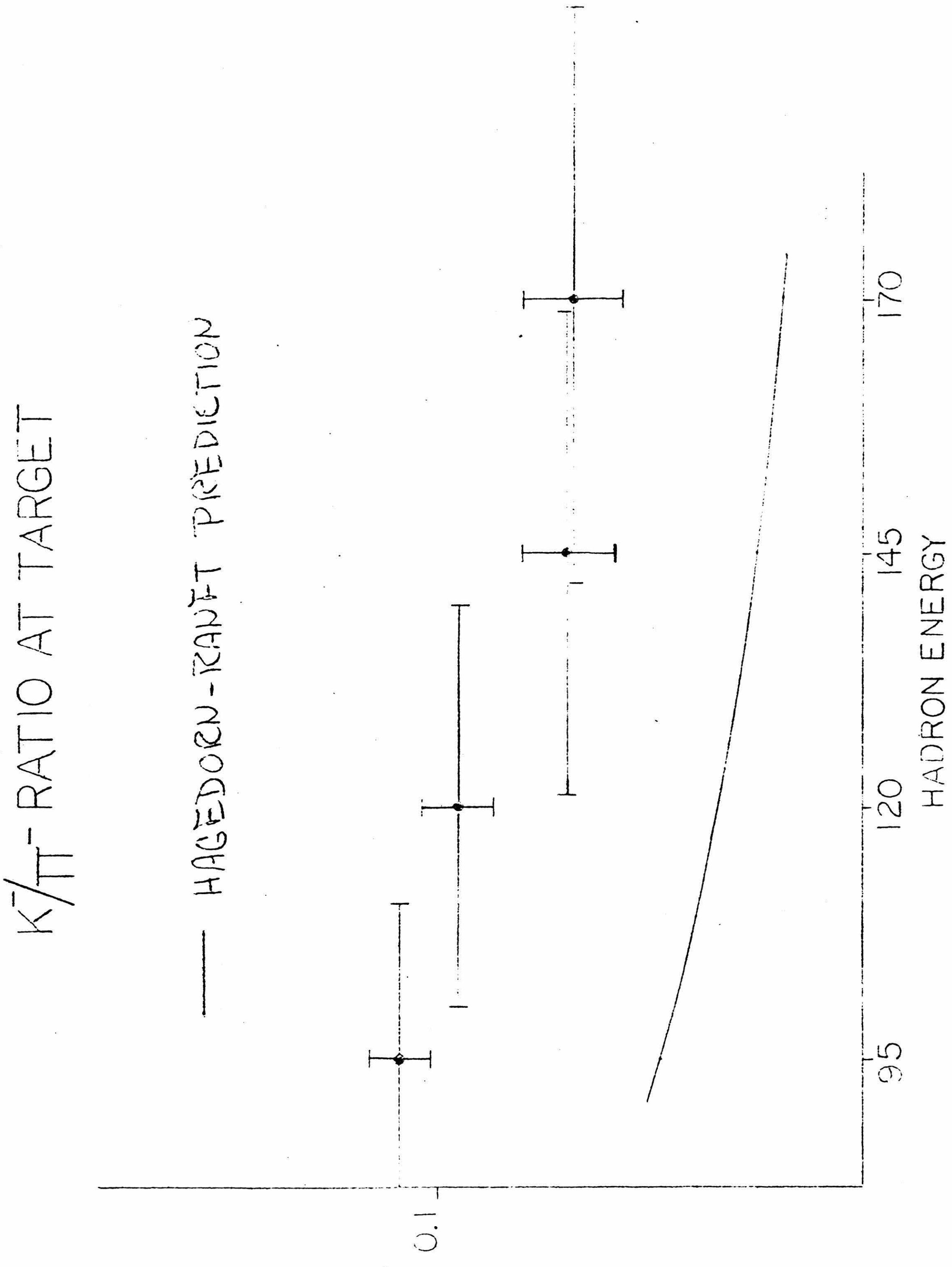

Figure 9.8 K^-/π^- ratio at target

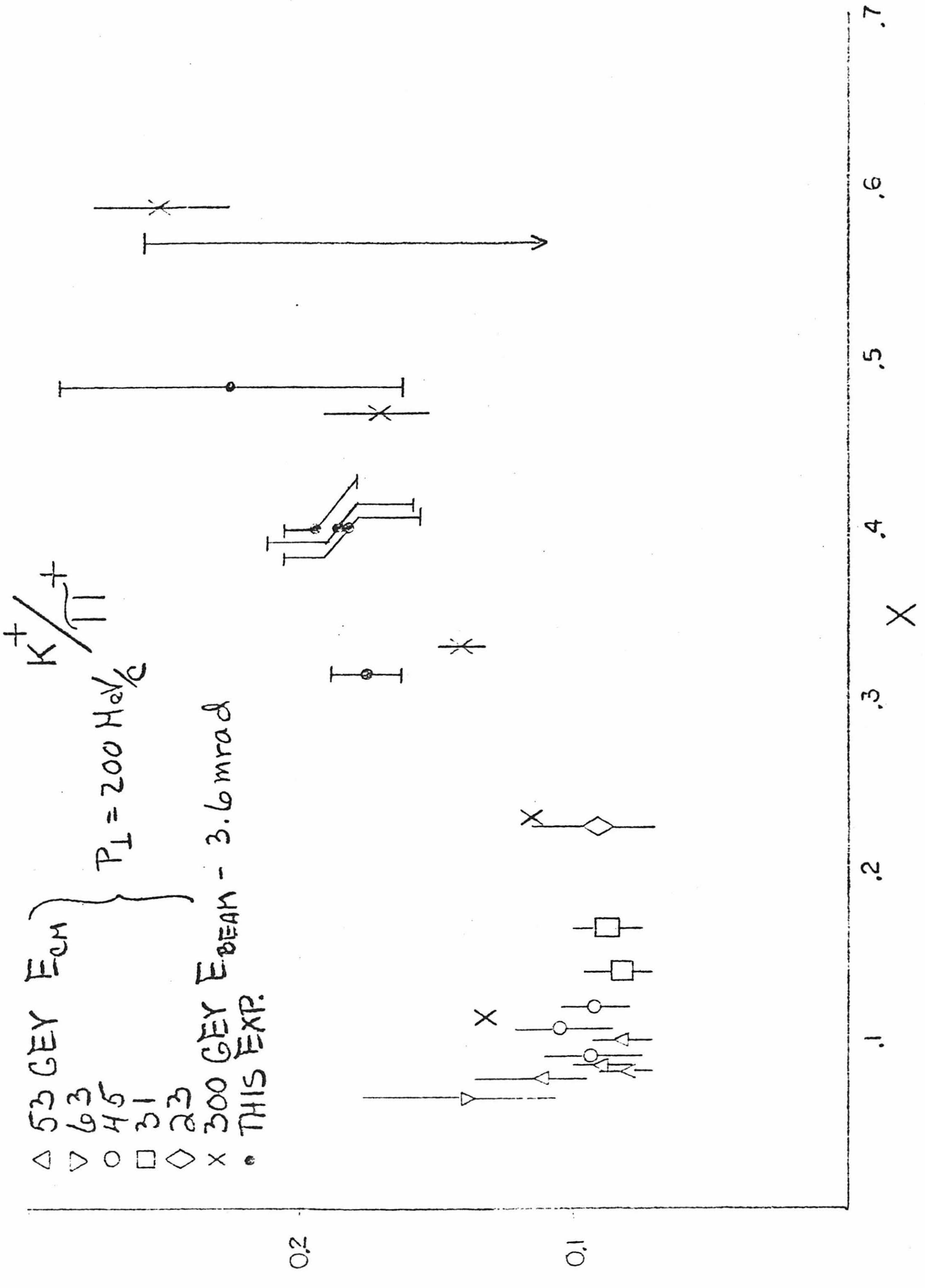

Figure 9.9 Comparison of K^+/π^+ ratios

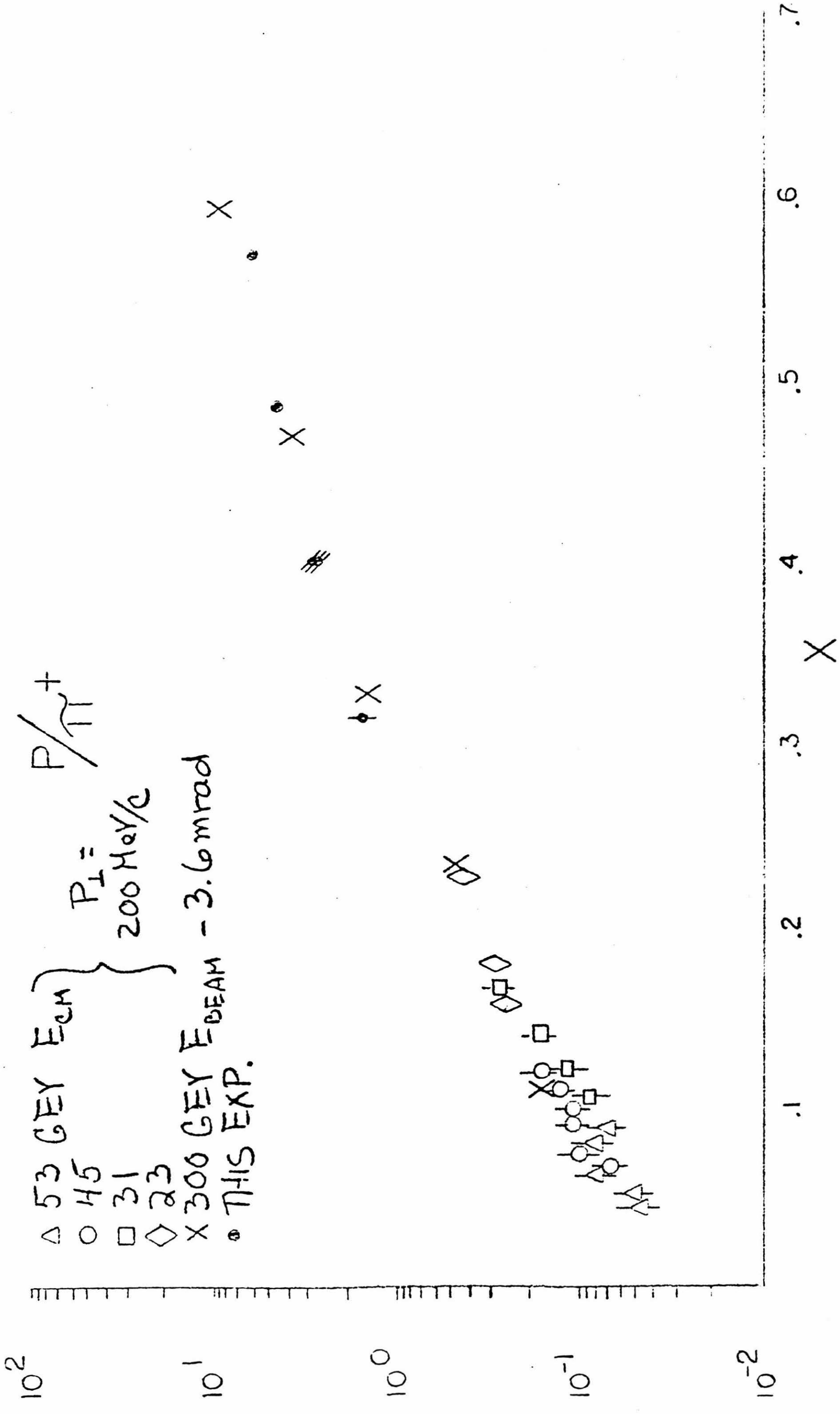

Figure 9.10 Comparison of P/π^+ ratios

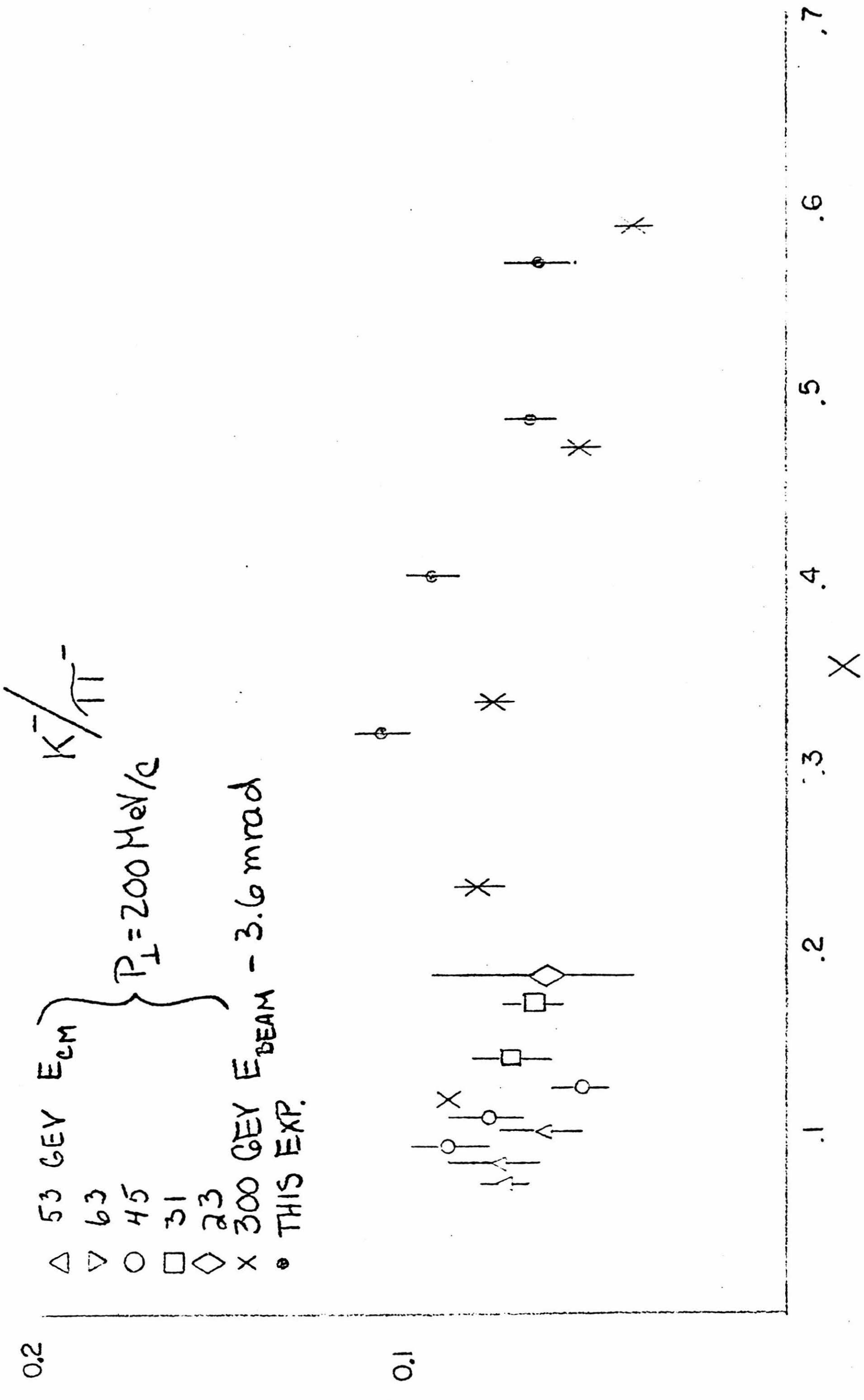

Figure 9.11 Comparison of K^-/π^- ratios

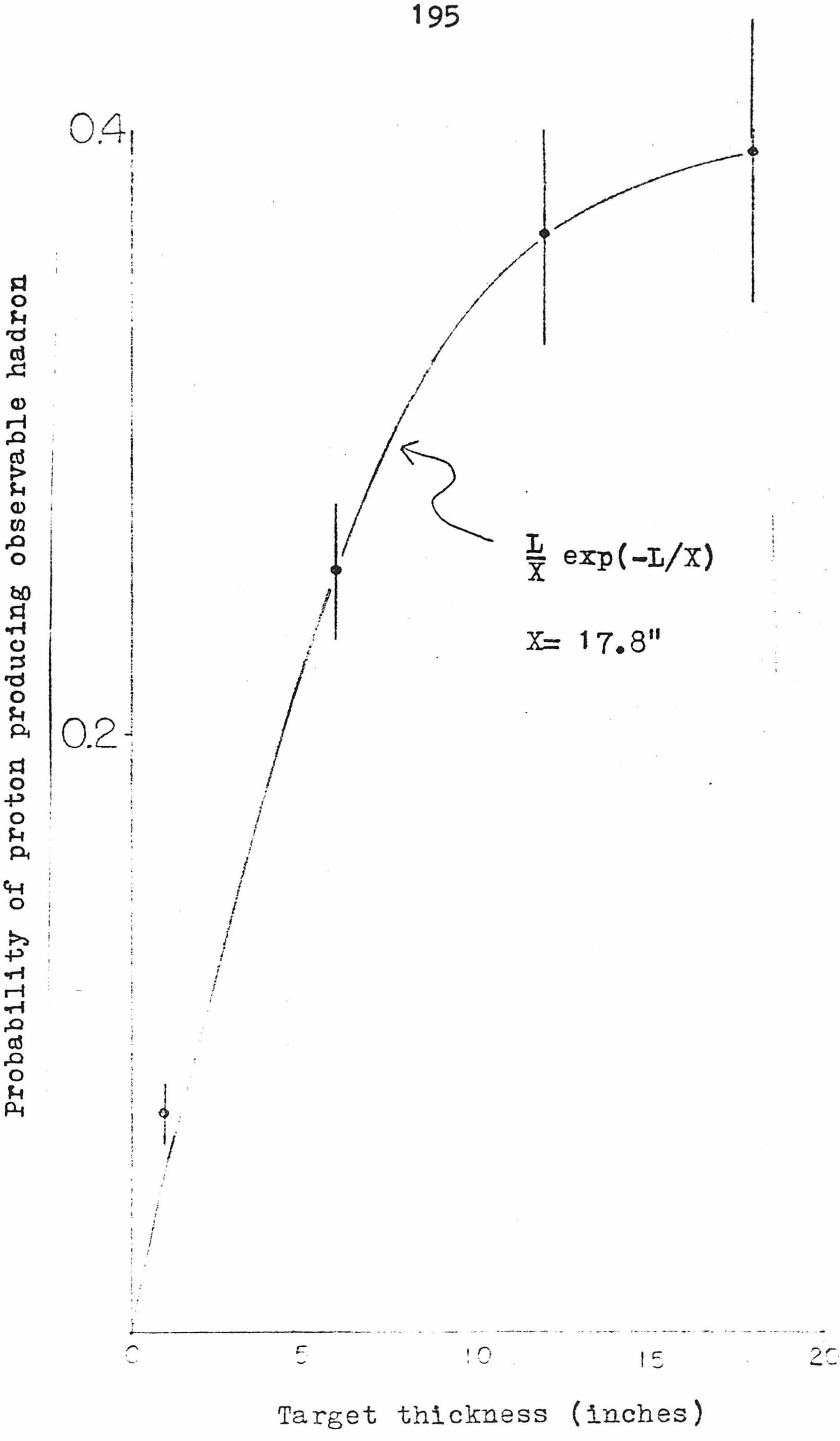

Figure 9.12 Dependence of yields on target thickness

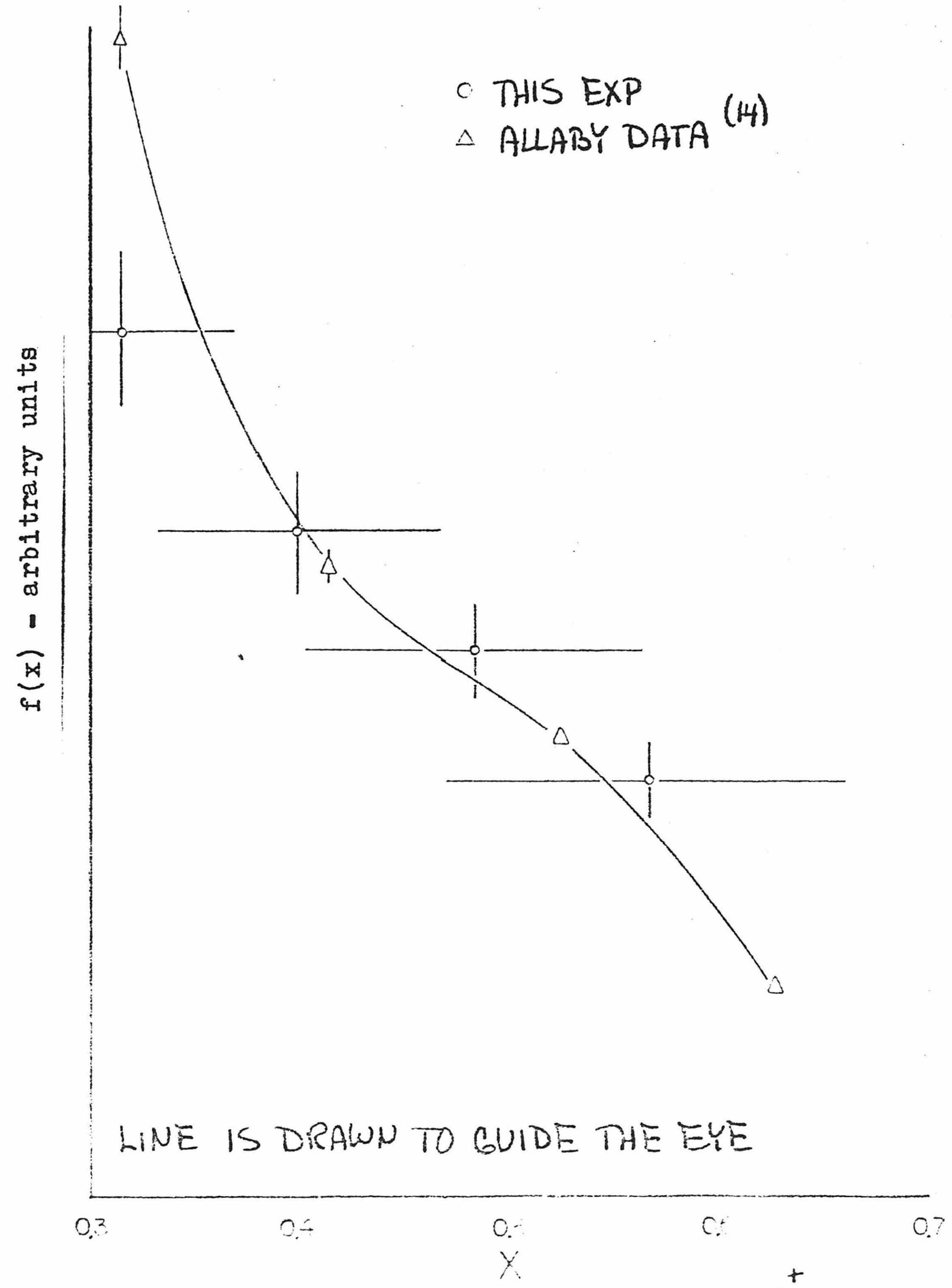

Figure 9.13 Scaling function for π^+

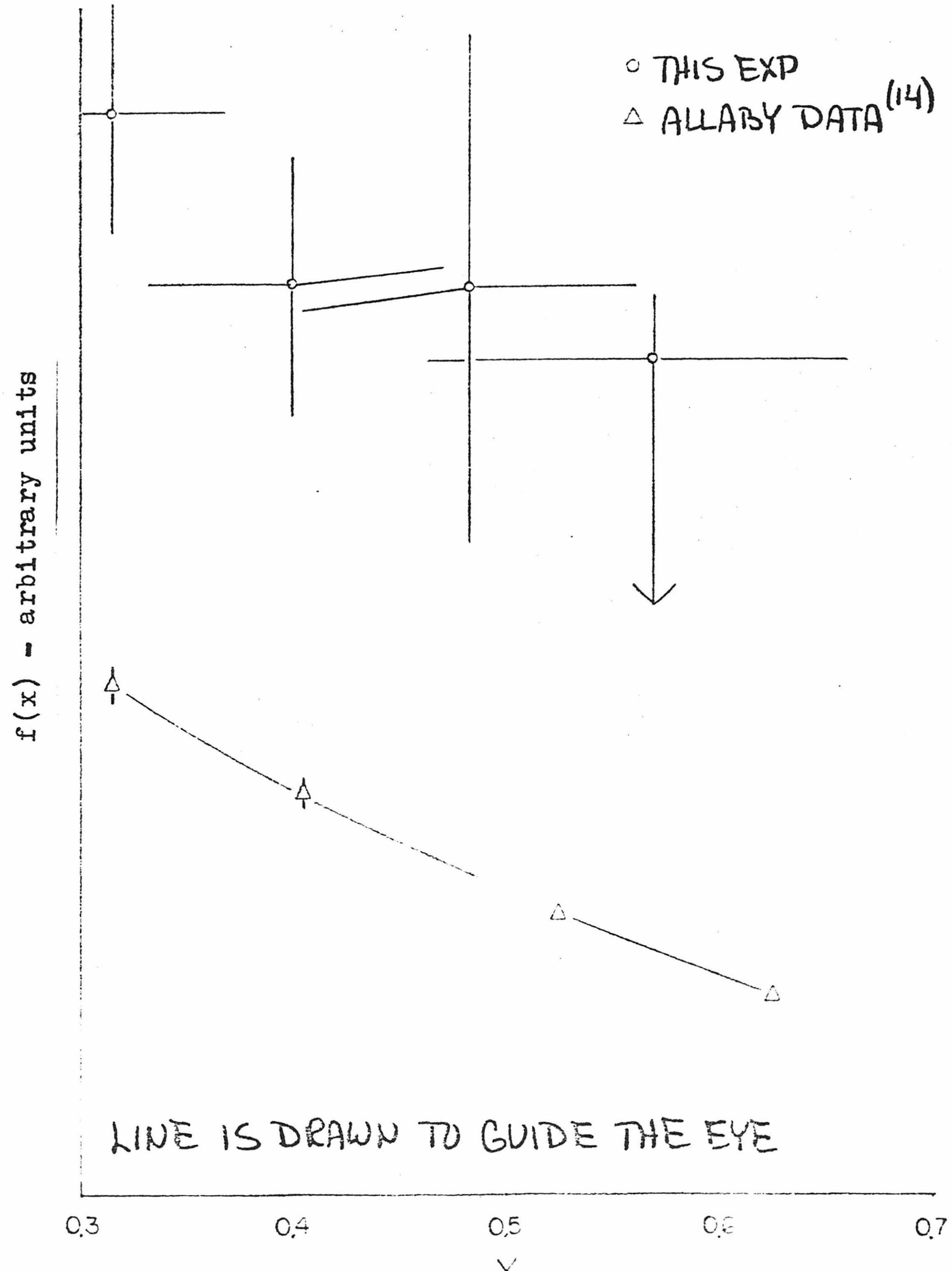

Figure 9.14 Scaling function for K^+

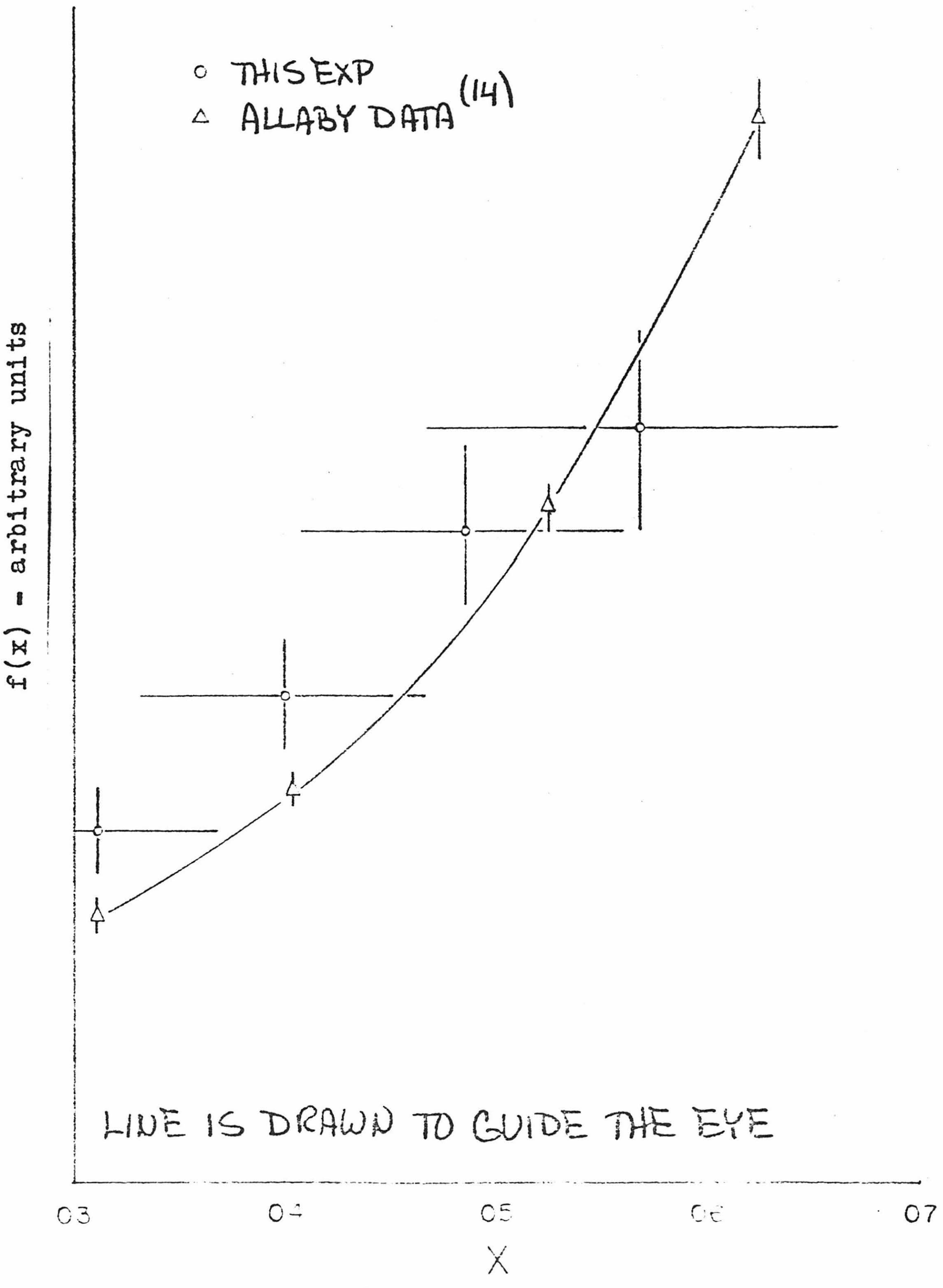

Figure 9.15 Scaling function for protons

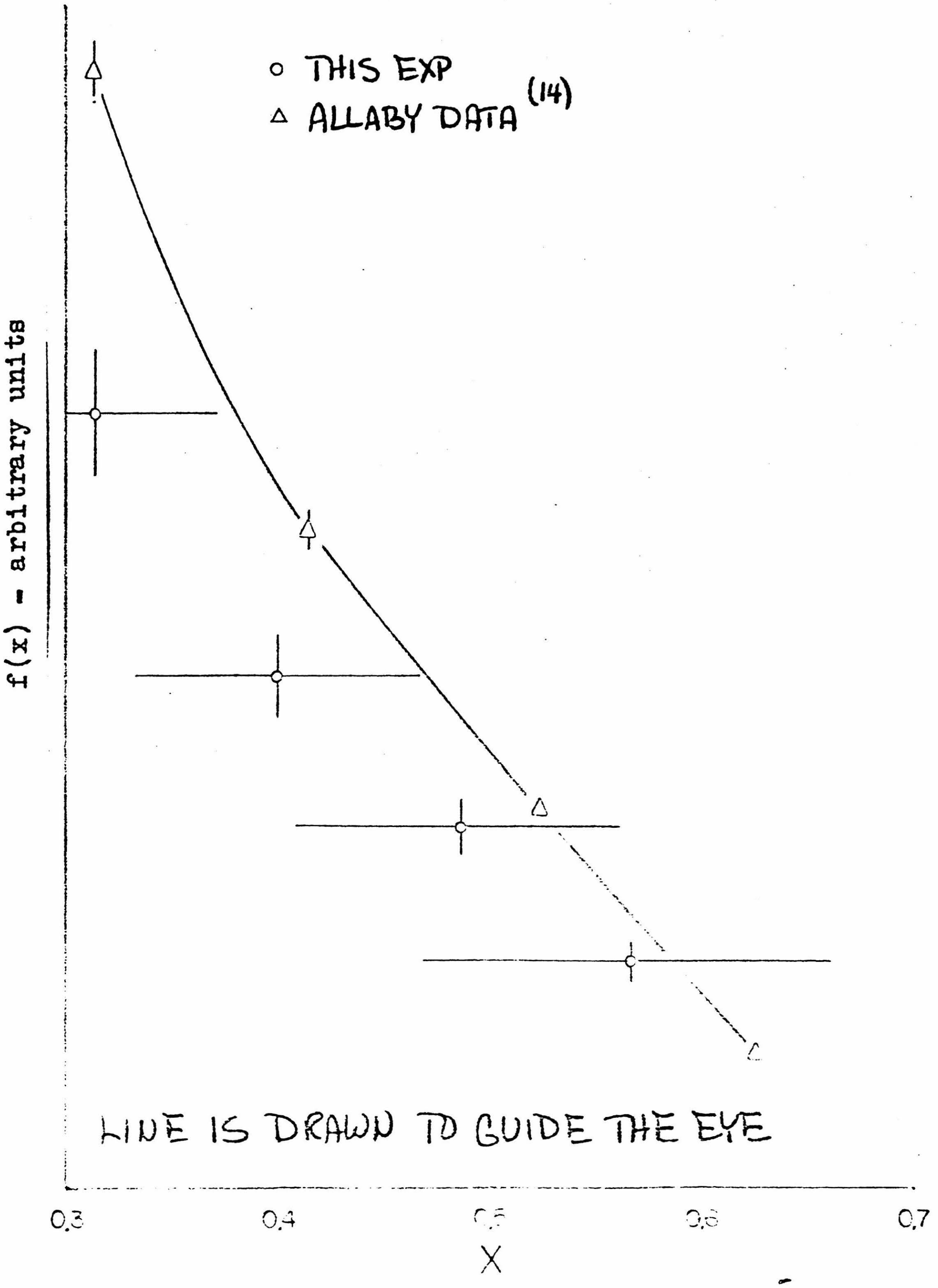

Figure 9.16 Scaling function for π^-

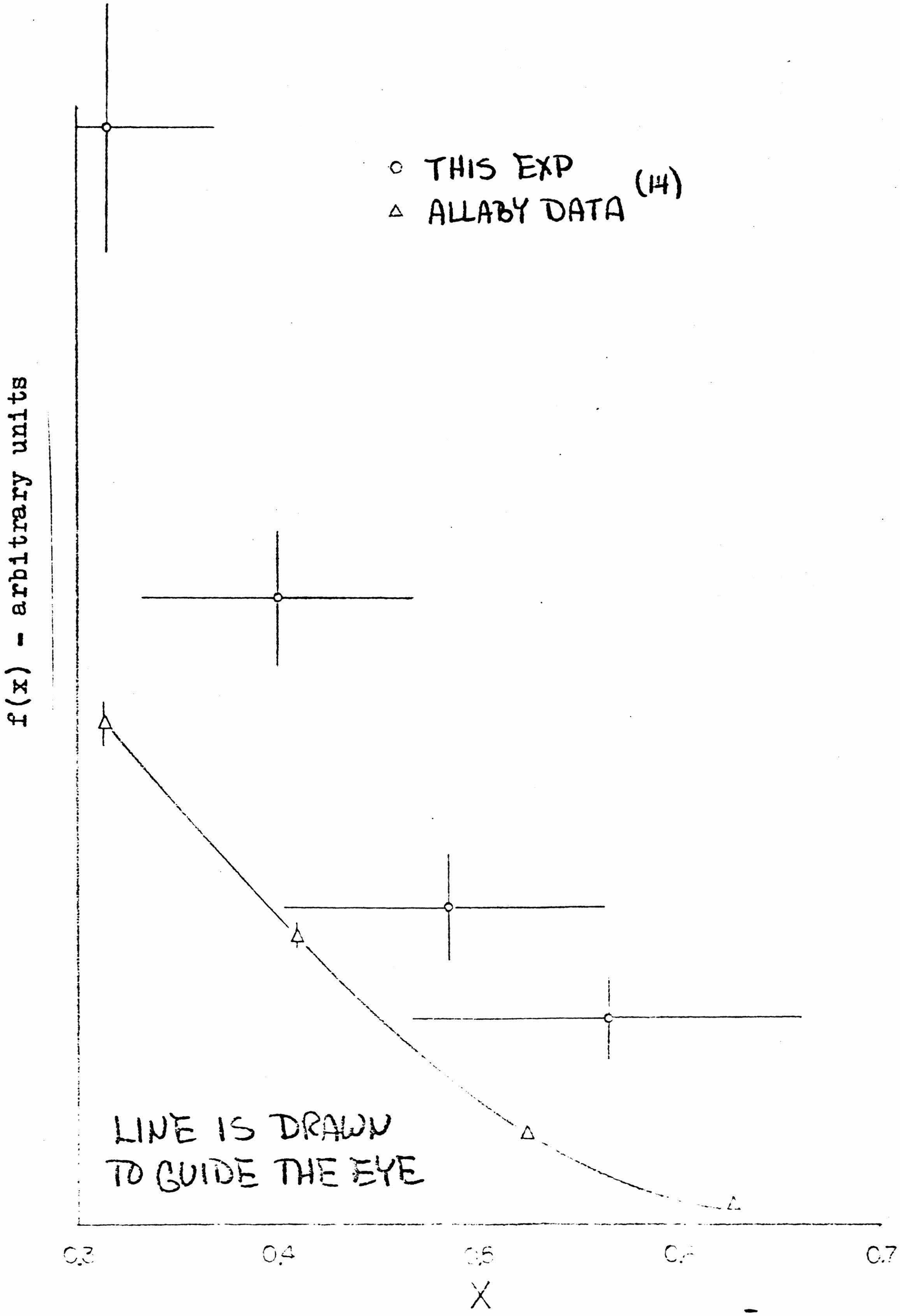

Figure 9 17 Scaling function for K^-

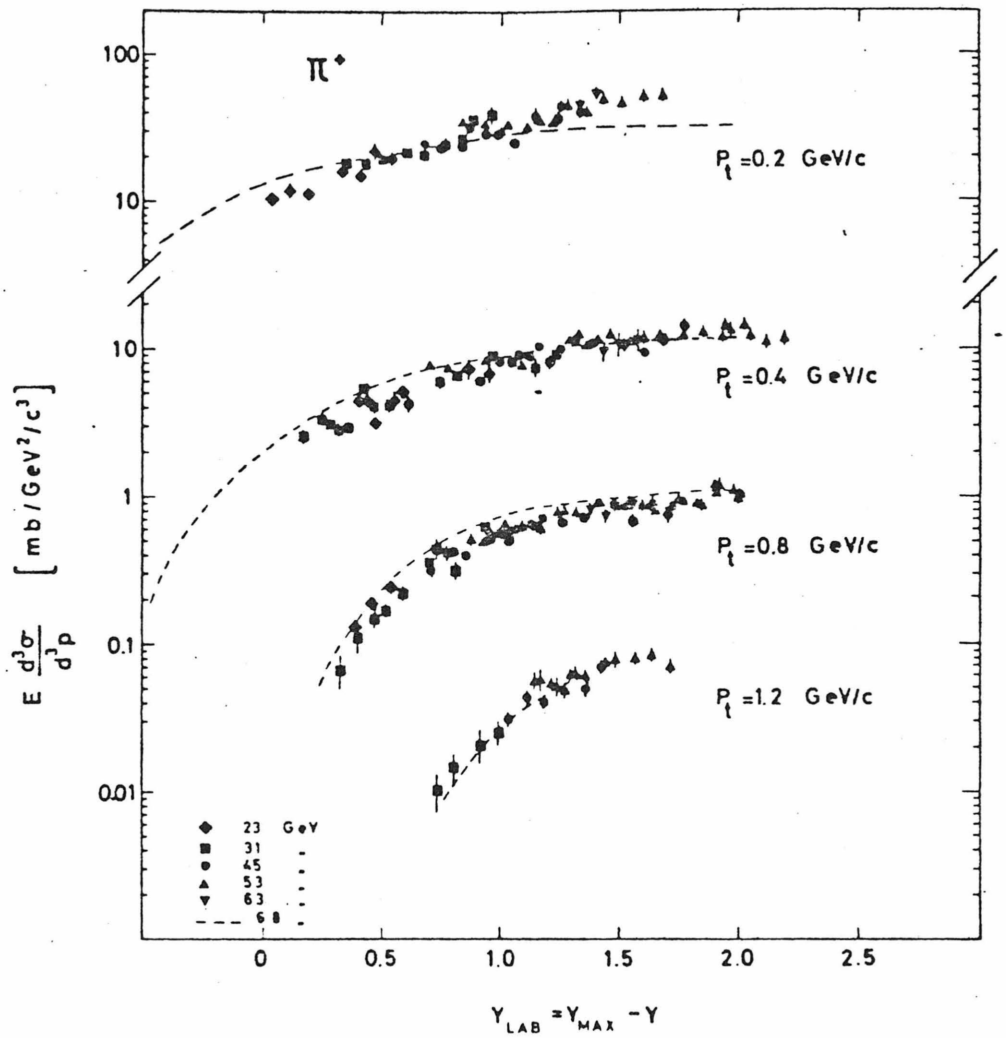

Figure 9.18 Invariant cross section for π^+ measured at ISR

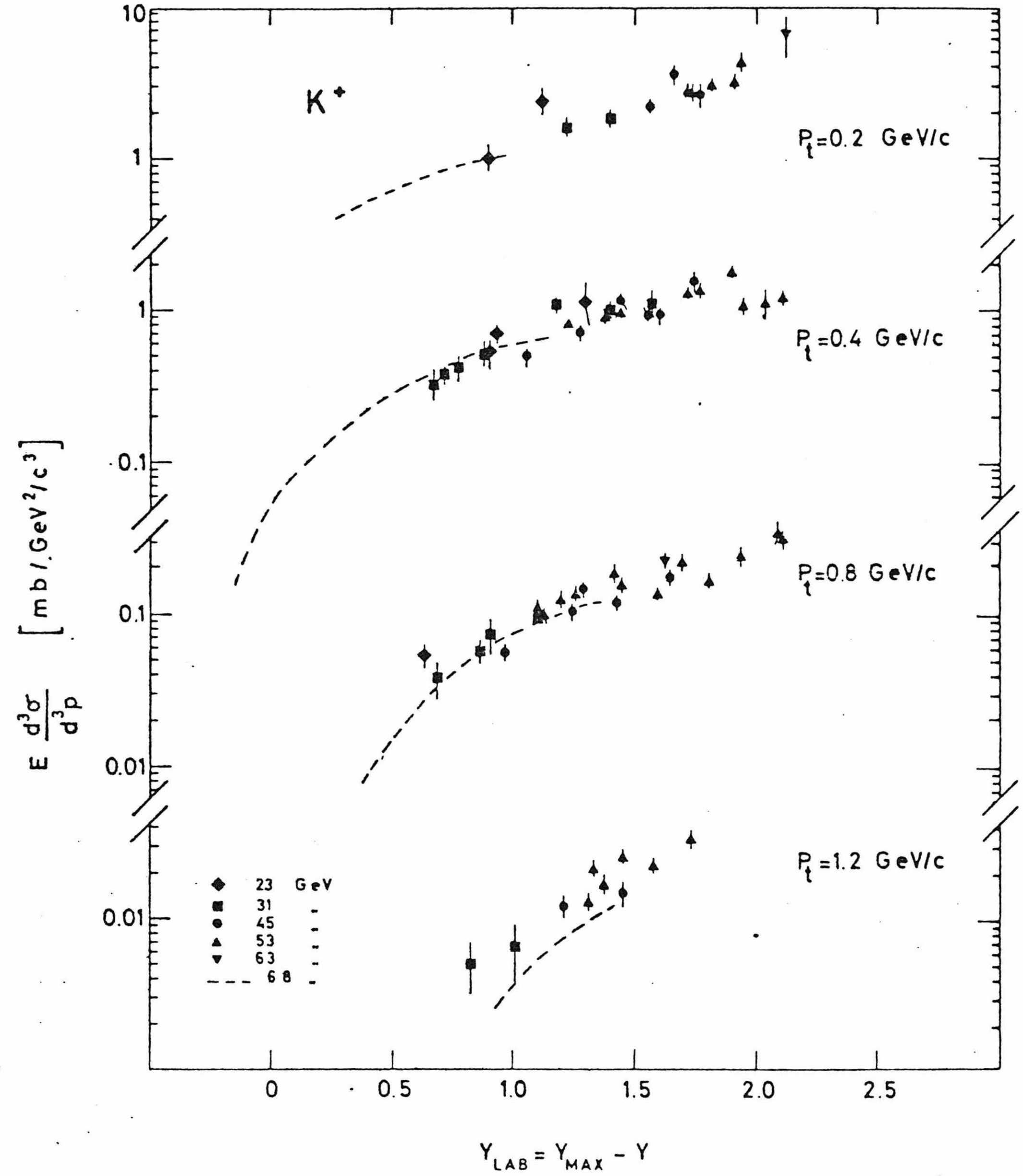

Figure 9.19 Invariant cross section for K^+ measured at ISR

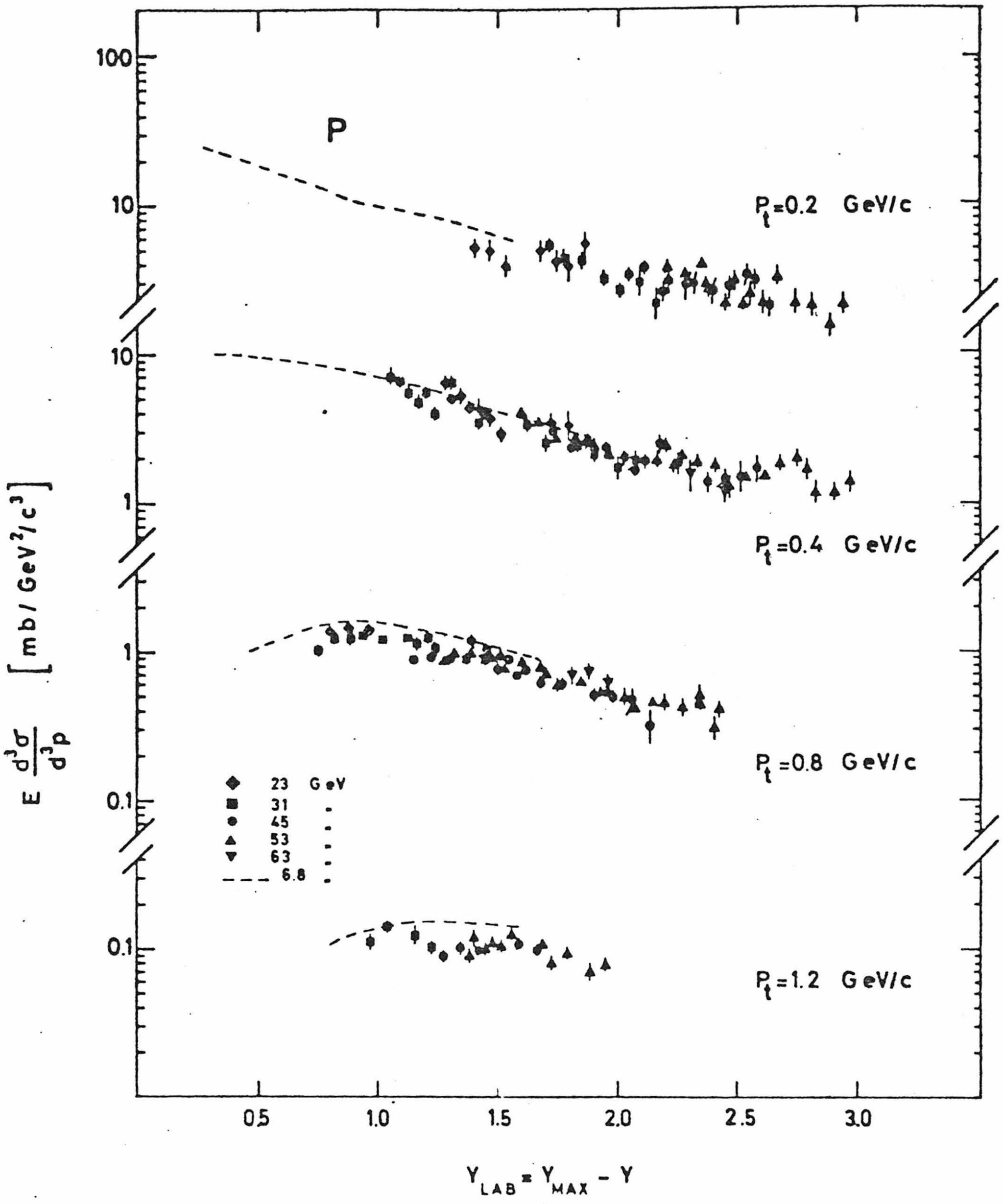

Figure 9.20 Invariant cross section for protons measured at ISR

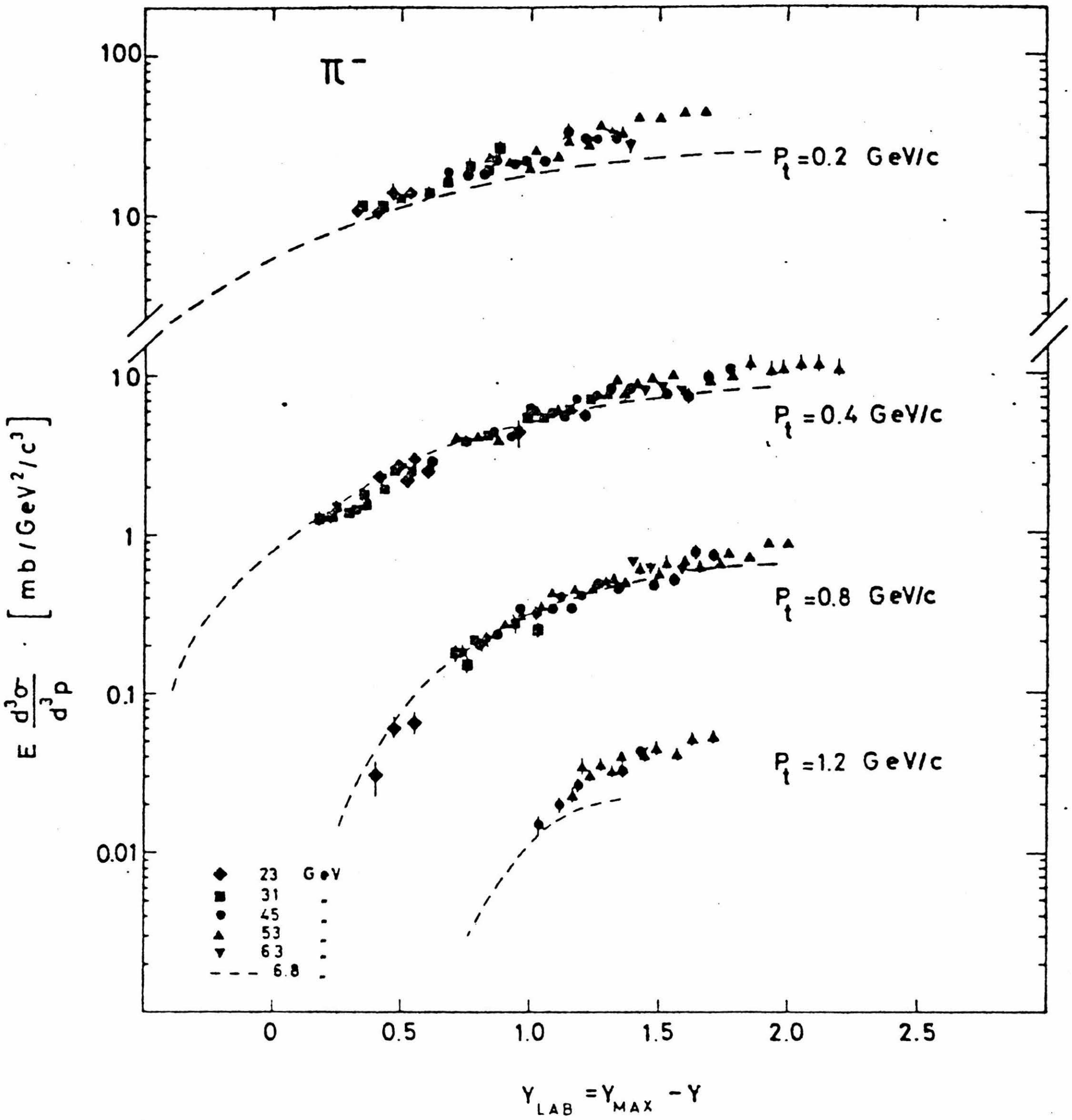

Figure 9.21 Invariant cross section for π^- measured at ISR

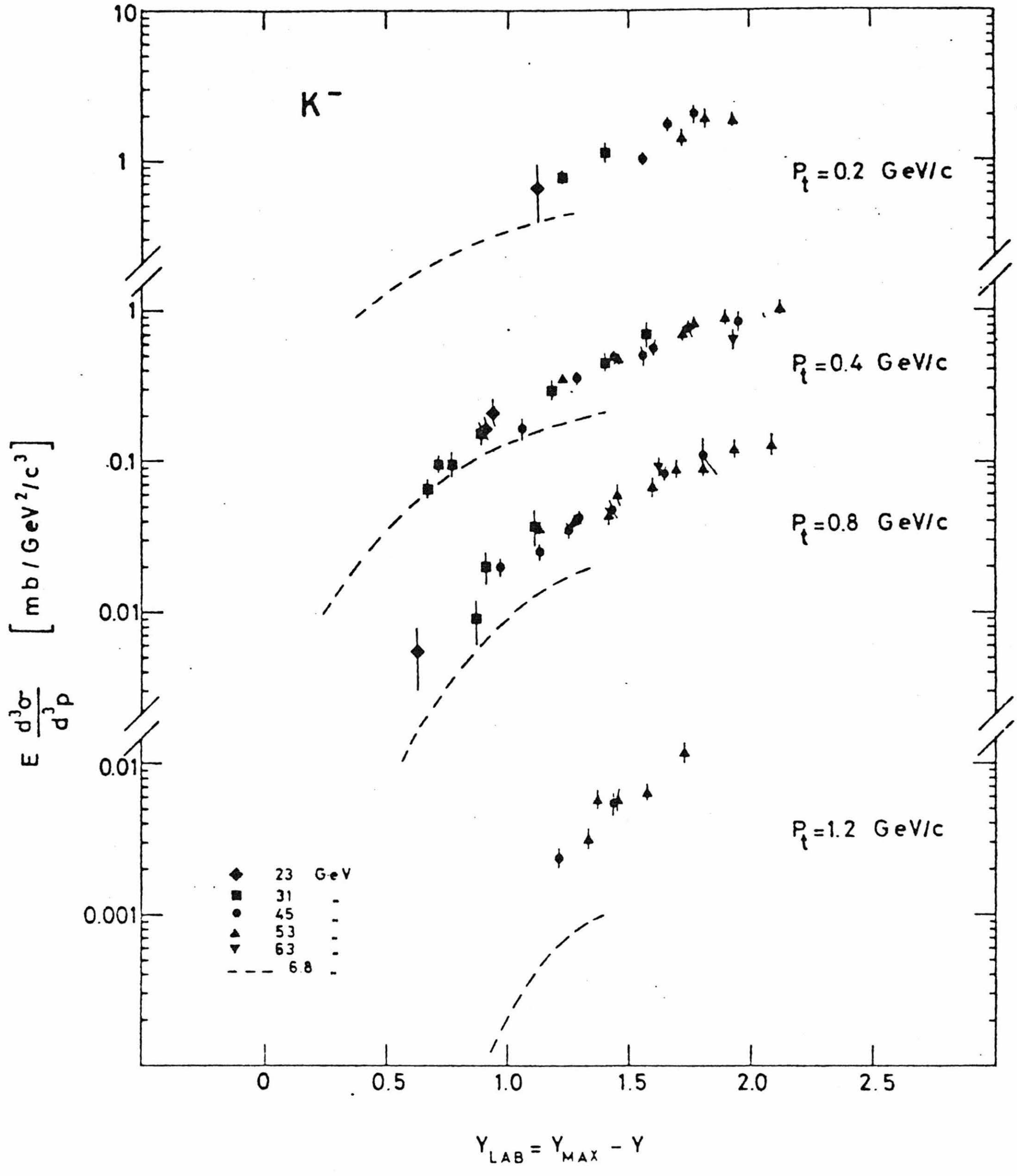

Figure 9.22 Invariant cross section for K^- measured at ISR

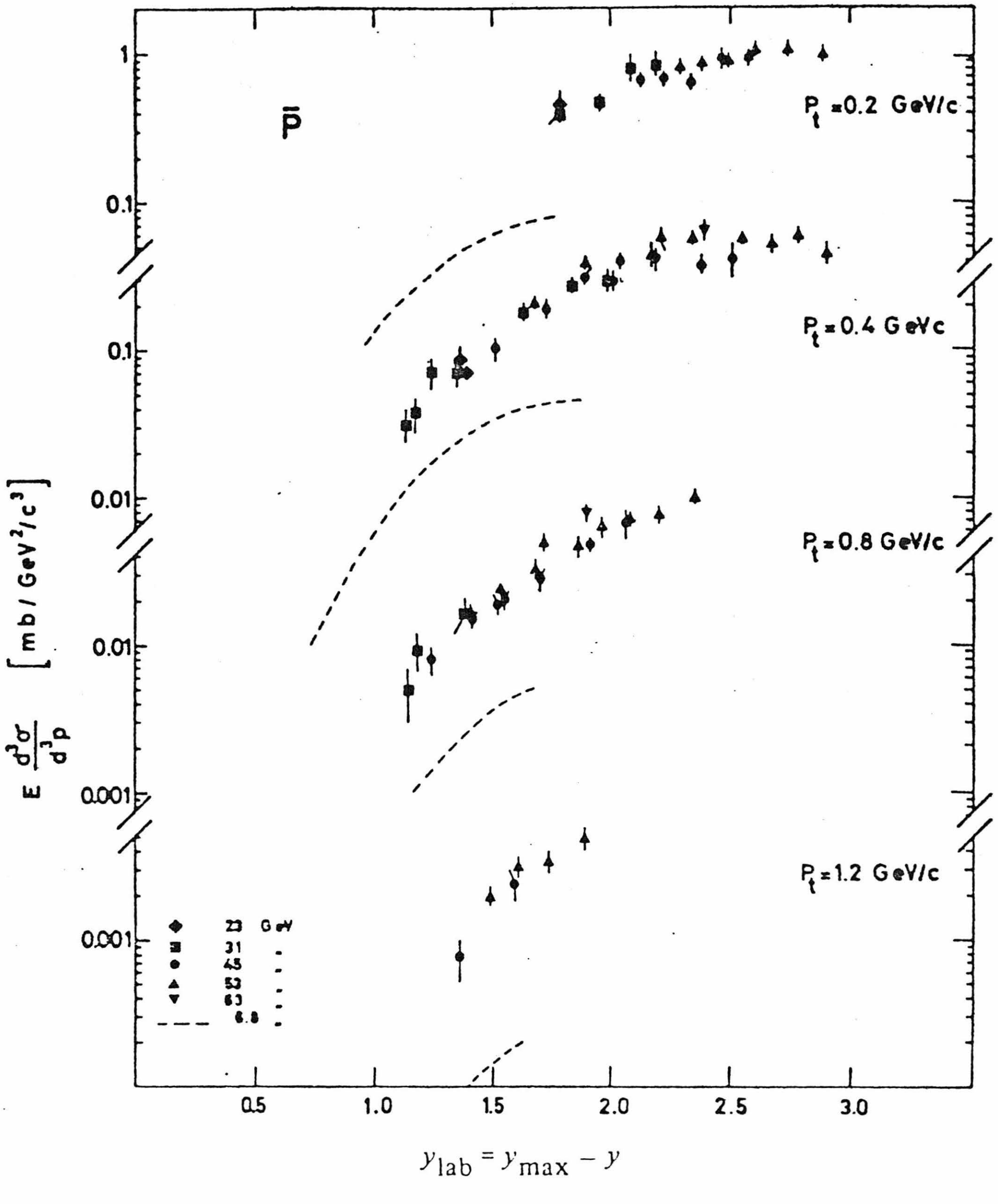

Figure 9.23 Invariant cross section for $\overline{P}$
measured at ISR

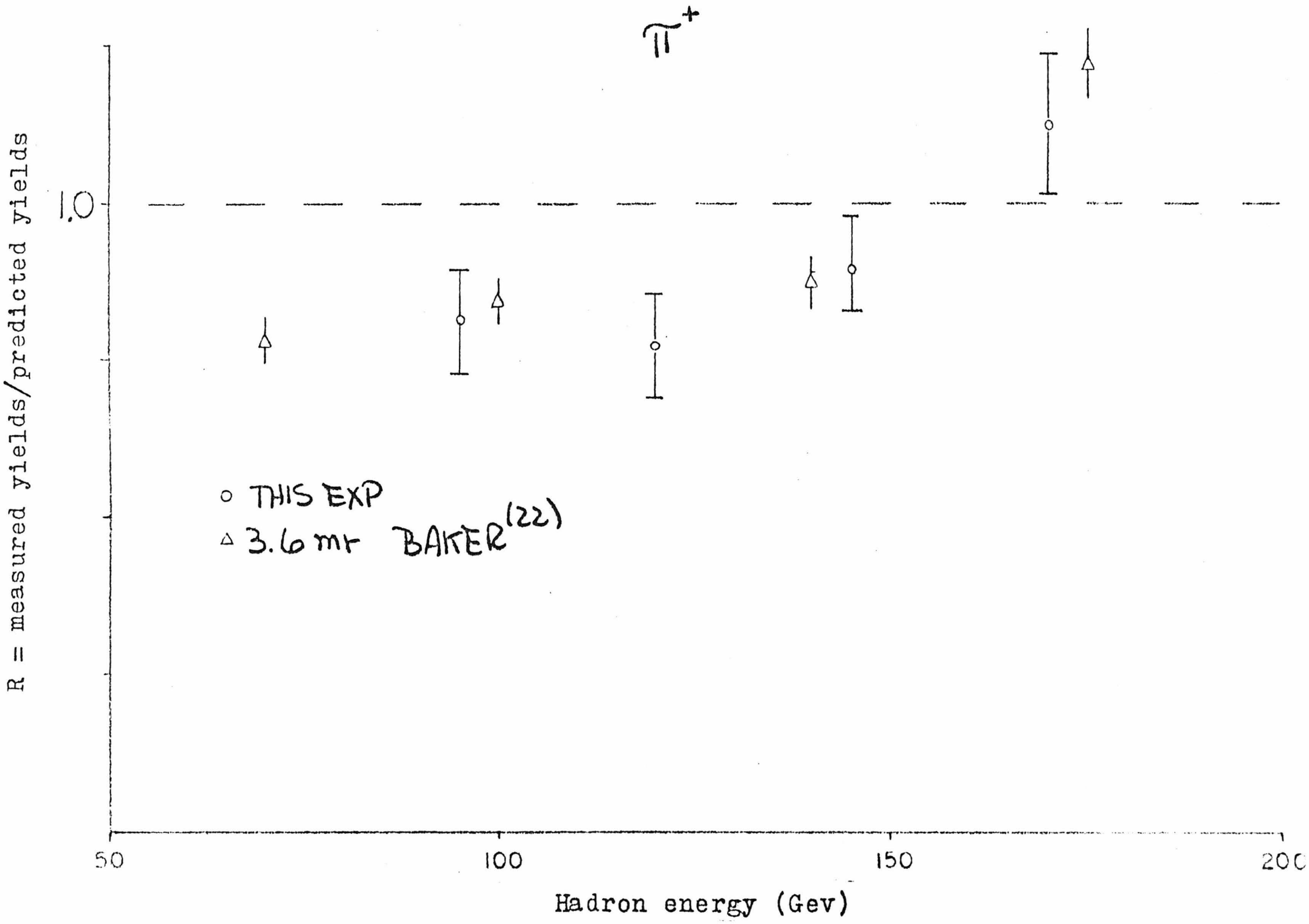

Figure 9.24 Comparison of π^+ yields with Hagedorn-Ranft predictions

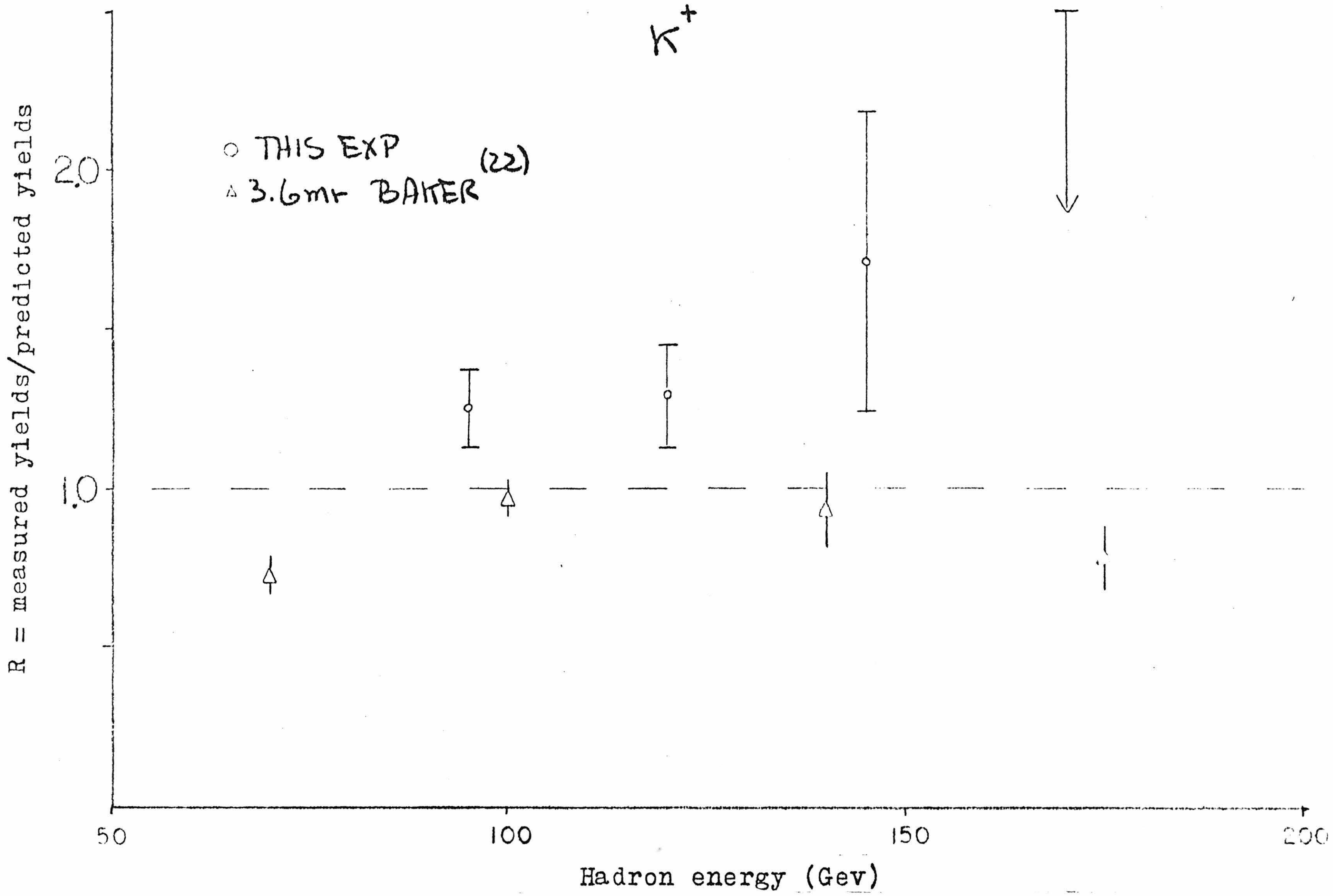

Figure 9.25 Comparison of K^+ yields with Hagedorn-Ranft predictions

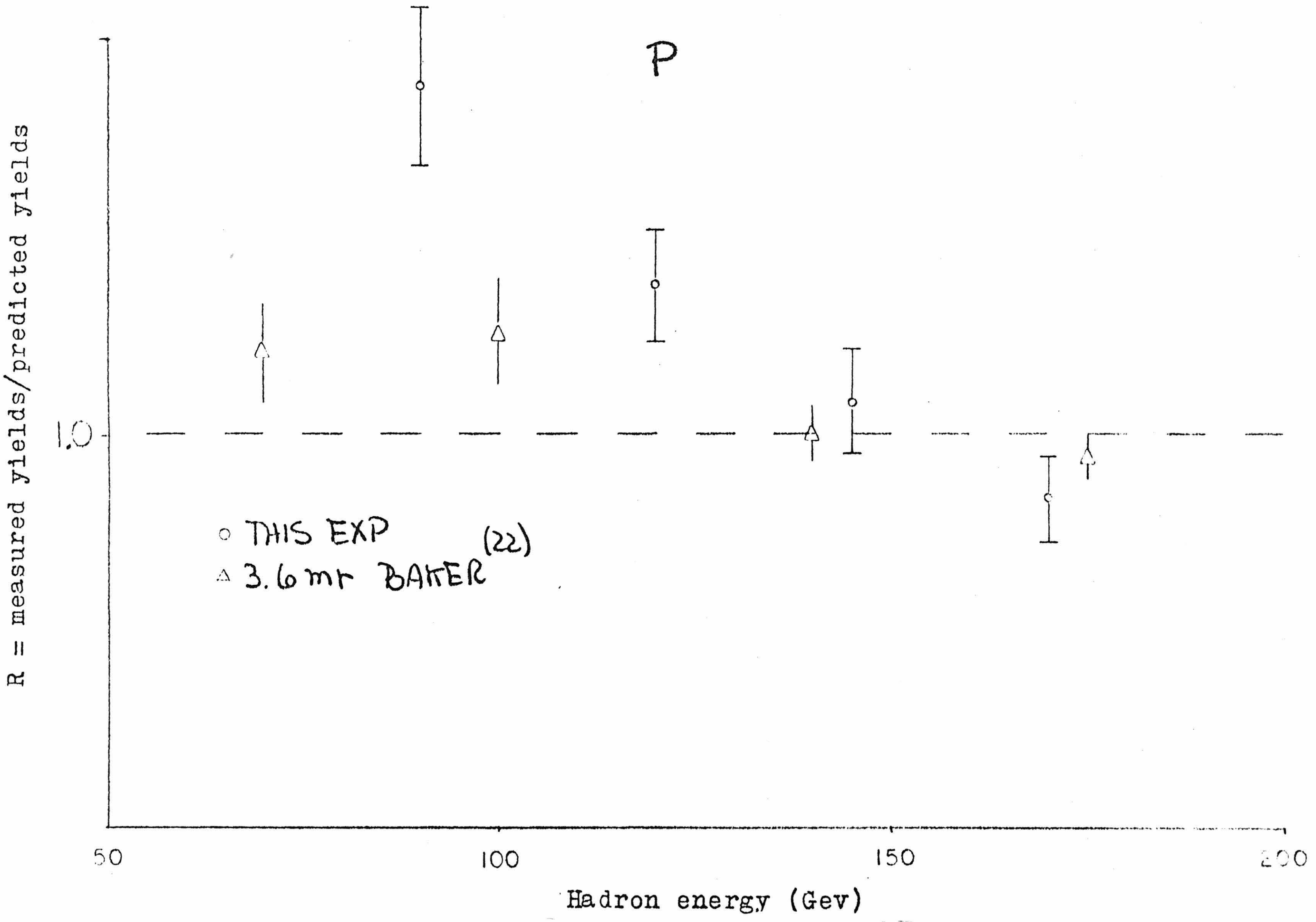

Figure 9.26 Comparison of P yields with Hagedorn-Ranft predictions

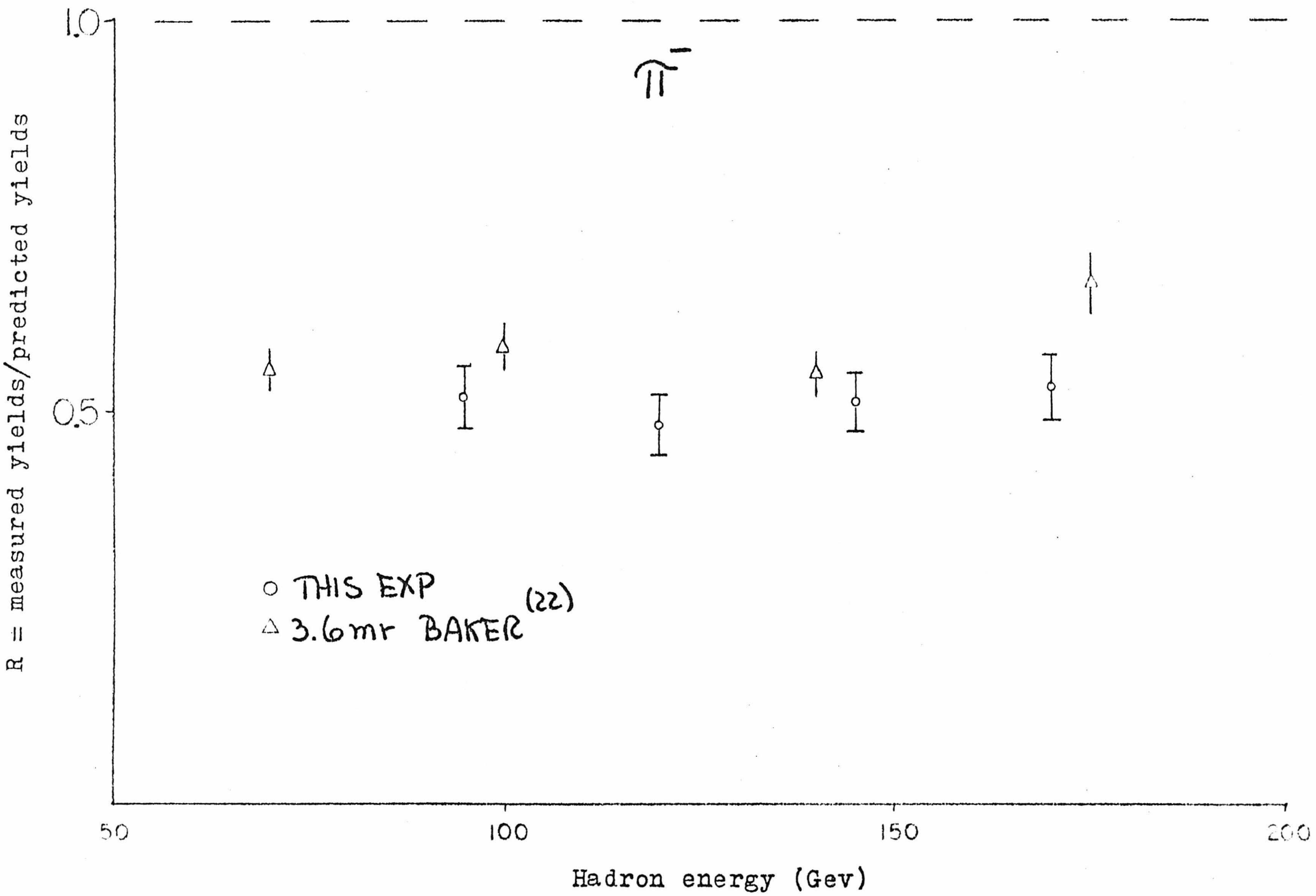

Figure 9.27 Comparison of π^- yields with Hagedorn-Ranft predictions

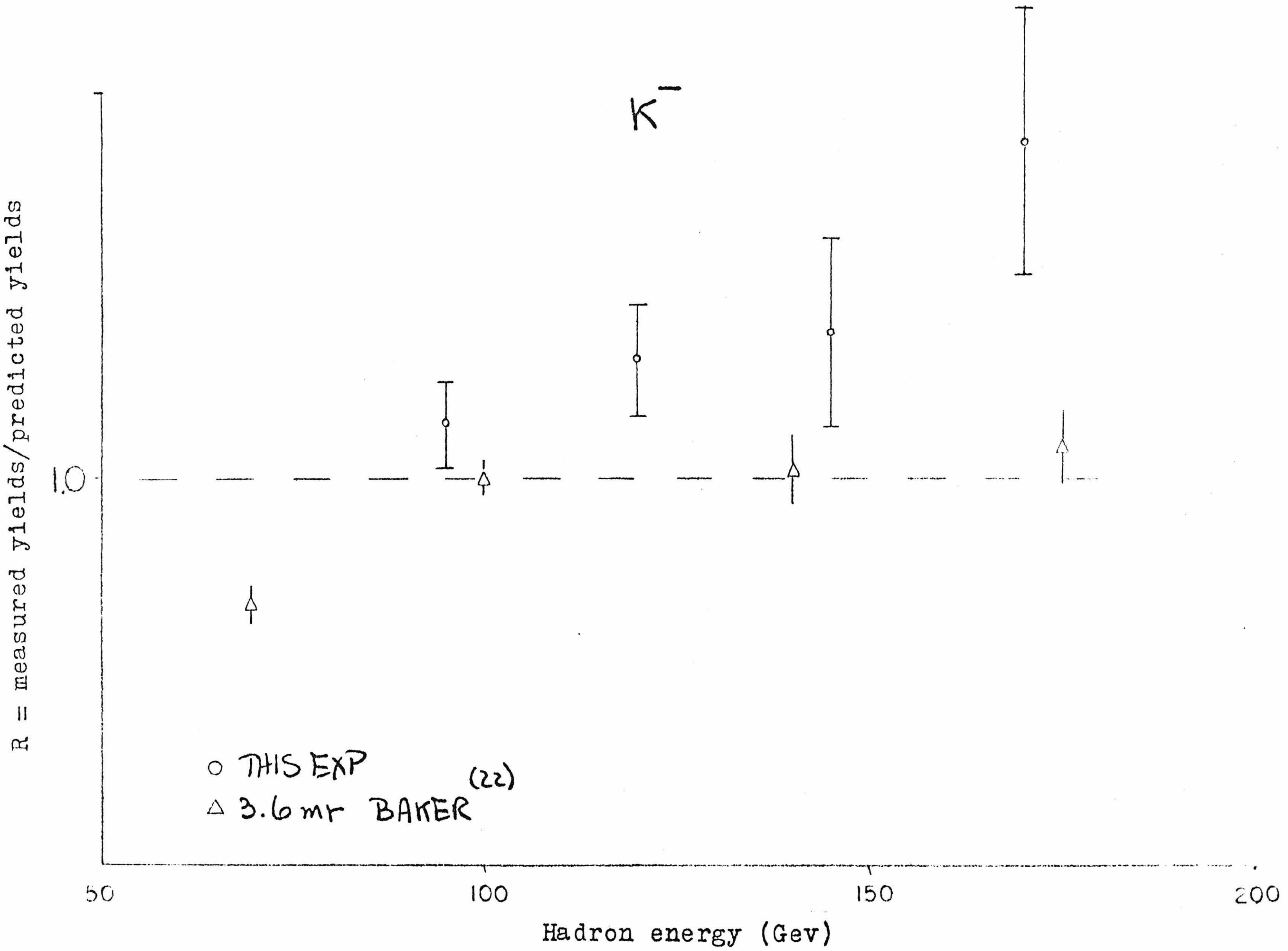

Figure 9.28 Comparison of K^- yields with Hagedorn-Ranft predictions

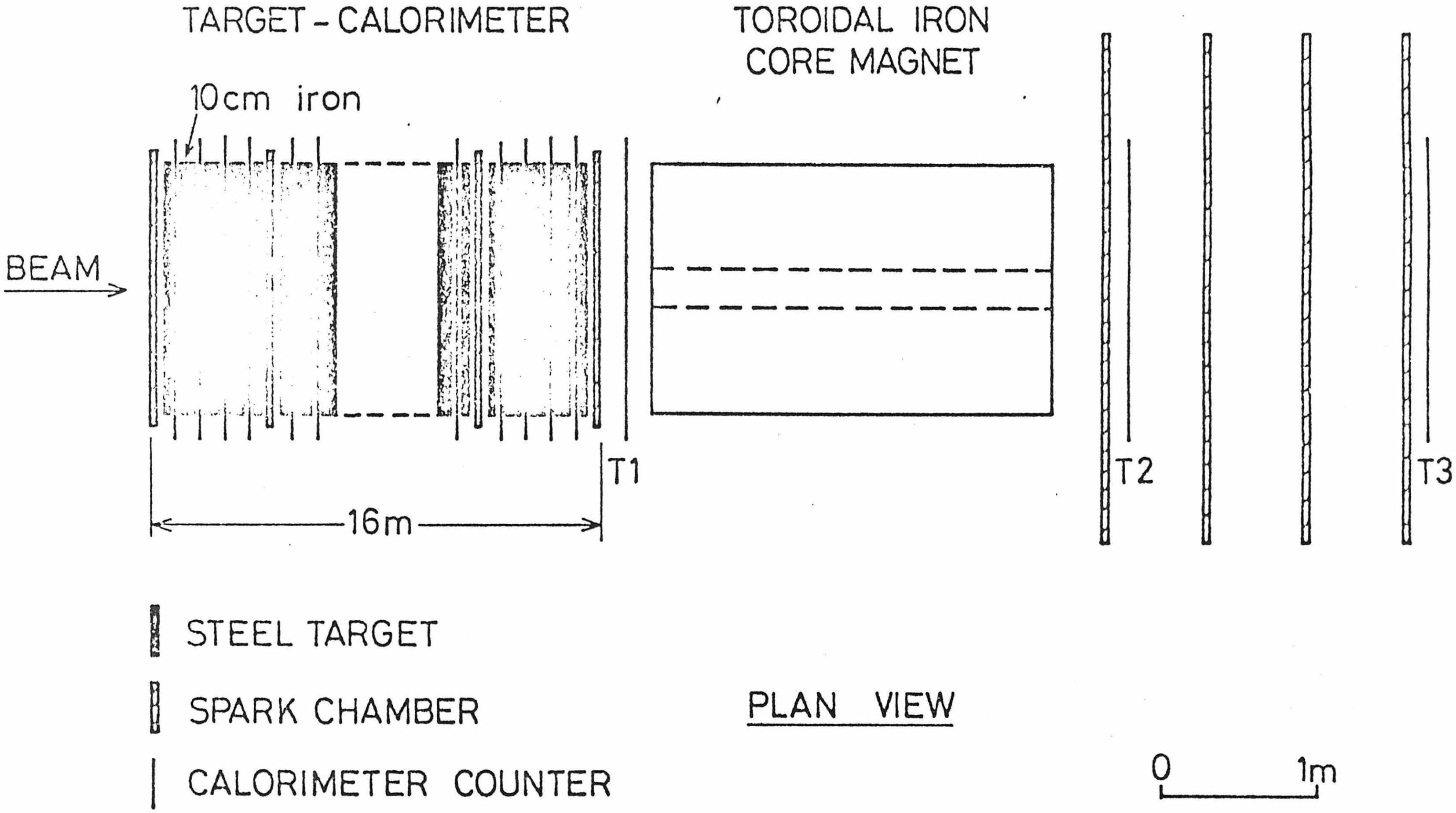

Figure 10.1 Neutrino-detecting apparatus

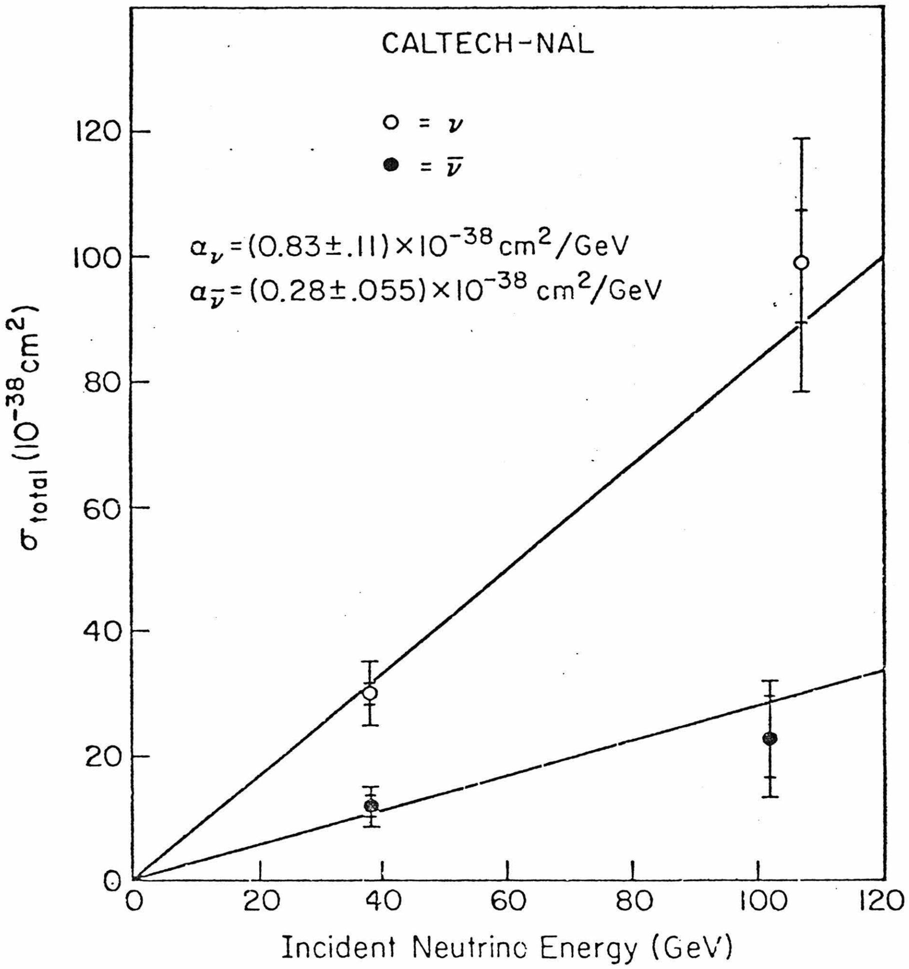

Figure 10.2 Neutrino total cross section
measured in this experiment

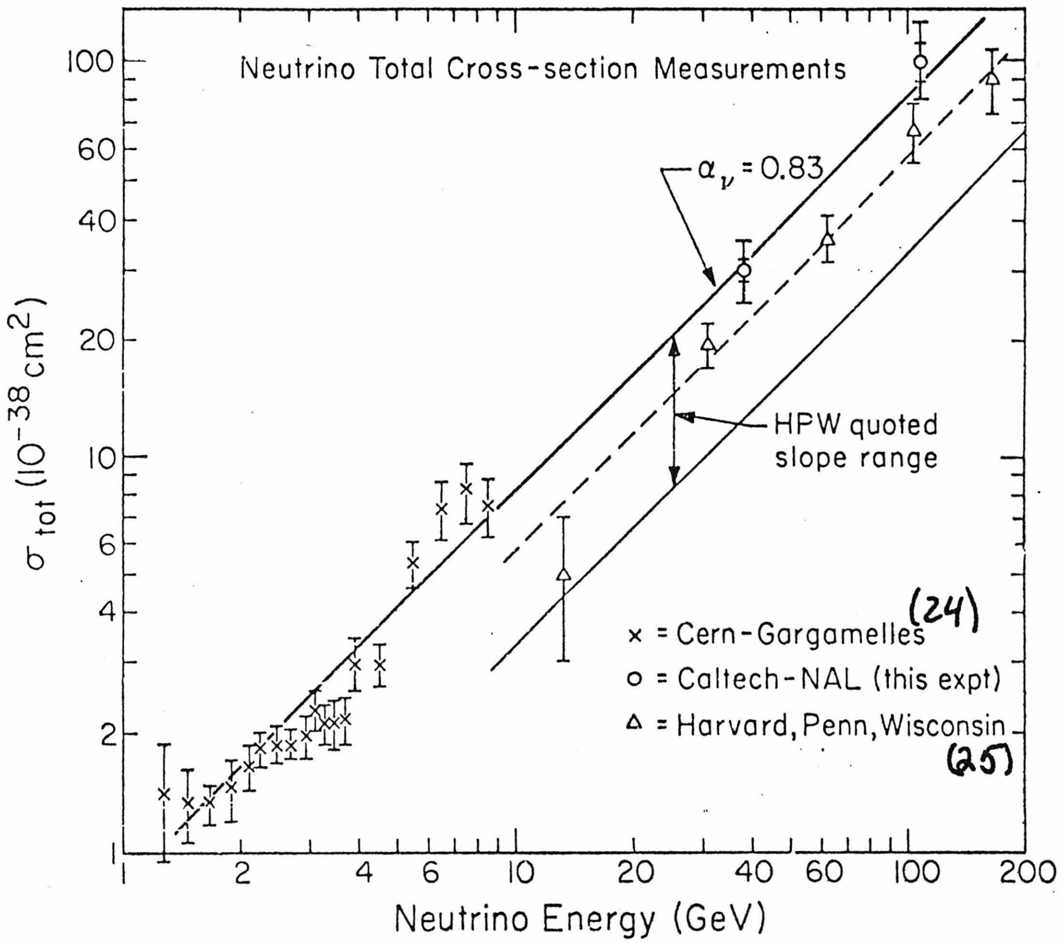

Figure 10.3 Existing data on neutrino total cross section

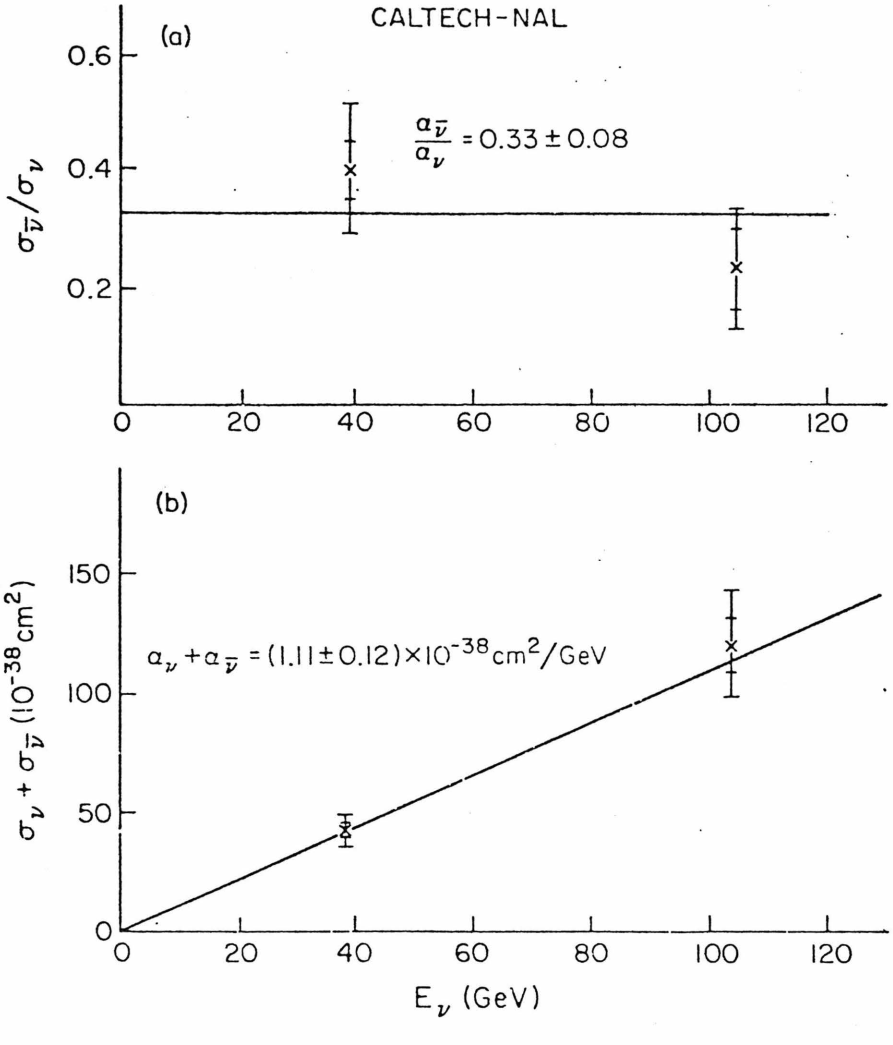

Figure 10.4 Ratio and sum of slope parameters

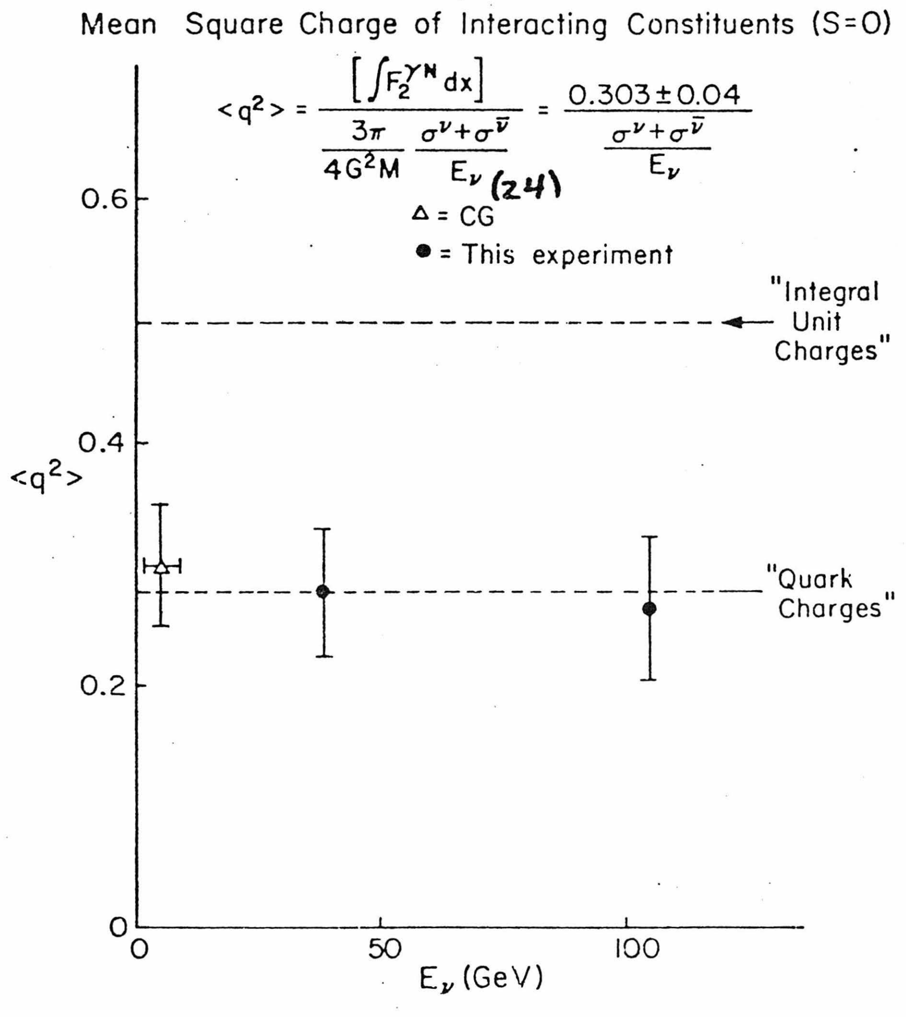

Figure 10.5 Mean-square-charge of interacting constituents

XIV. References

1) E.L. Berger, "Phenomenology of Inclusive Reactions", ANL/HEP 7134, (1971)

2) R.C. Arnold, "Lectures on Inclusive Reactions", ANL/HEP 7139, (1971)

3) G. Cocconi, L.J. Koester, D.H. Perkins, UCRL 10022, p. 167, (1962)

4) G. Trilling, UCID-10148, p. 25, (1966)

5) J.R. Sanford, C.L. Wang, BNL-JRS/CLW-1, (1967)

6) J.R. Sanford, C.L. Wang, BNL-JRS/CLW-2, (1967)

7) J. Benecke, T.T. Chou, C.N. Yang, E. Yen, Phys. Rev 188, 2159, (1969)

8) R. Hagedorn, Suppl. Nuovo Cimento 3, 147, (1965)

9) R. Hagedorn and J. Ranft, Suppl. Nuovo Cimento 6, 169, (1968)

10) R. Hagedorn, Suppl. Nuovo Cimento 6, 311, (1968)

11) R. Feynman, Phys. Rev. Letters 23, 1415, (1969)

12) P. Capiluppi et al., Nuclear Physics B79, 189, (1974)

13) J.V. Allaby et al., Contribution to the 4th International Conference on high-energy collisions, Oxford, vol. 2, p. 85, (1972)

14) J.V. Allaby et al., CERN 70-12, (1970)

15) G. Cocconi, Phys. Rev. 111, 1699, (1958)

16) R. Hagedorn, Astron. and Astrophys. 5, 184, (1970)

17) Yu. B. Bushnin et al., Phys. Letters 29B, 48, (1969)

18) F. Binon et al., Phys. Letters 30B, 506, (1969)

19) J. Ranft, Phys. Letters 31B, 529, (1970)

20) J.V. Jelley, Cerenkov Radiation and Its Applications, p. 22, (1958)

21) RCA technical data sheet accompanying phototube

22) W.F. Baker et al., NAL-Pub-74/13-EXP, (1974)

23) Sciulli, F.J., XVII International Conference on High Energy Physics, IV-105 (1974)

24) T. Eichen, et al., Phys. Lett. 46B, 274, 281 (1973)

25) Benvenutti, et al., PRL 32, 127 (1974)

26) B. Barish et al., CALT-68-452 (1974)

27) J.D. Bjorken, SLAC-PUB-1017 (1972)

28) E.D. Bloom et al., PRL 23, 931 (1969);
G. Miller et al., Phys. Rev D5, 528 (1972)

29) B. Rossi, High Energy Particles (1965)

30) J. Ranft, TUL 37, Karl-Marx-Universität (1970)

31) E. Bloom et al., SLAC-PUB-796, SLAC-PUB-815, SLAC-PUB-907